

Cosmogenic Activation in NaI Detectors for Dark Matter Searches

By
Walter C. Pettus

A dissertation submitted in partial fulfillment of
the requirements for the degree of

Doctor of Philosophy

(Physics)

at the
UNIVERSITY OF WISCONSIN-MADISON
2015

Date of final oral examination: 7 May 2015

The dissertation is approved by the following members of the Final Oral Committee:

Francis Halzen, Professor, Physics

Karsten Heeger, Professor, Yale University, Physics

Reina Maruyama, Assistant Professor, Yale University, Physics

A. Baha Balantekin, Professor, Physics

Matthew Herndon, Professor, Physics

Stefan Westerhoff, Professor, Physics

Delia Tosi, Assistant Scientist, Wisconsin IceCube Particle Astrophysics Center

© Copyright by Walter C. Pettus 2015

All Rights Reserved

COSMOGENIC ACTIVATION IN NAI DETECTORS FOR DARK MATTER SEARCHES

Walter C. Pettus

Under the supervision of

Professor Karsten Heeger at Yale University

Assistant Professor Reina Maruyama at Yale University

Professor Francis Halzen at the University of Wisconsin – Madison

DM-Ice is a direct detection dark matter experimental program driving towards deployment of a quarter-ton scale detector of low-background NaI(Tl) scintillating crystals. The experiment will search for the expected annual modulation signature of the dark matter signal. The definitive detection of dark matter would resolve a long-standing open question in the community and significantly advance our understanding of the universe. Successful achievement of the experimental goals requires that the intrinsic detector backgrounds be minimized and well-characterized.

This work focuses on backgrounds from cosmogenic activation which are impossible to directly quantify using radioassays of detector components. The radioactive isotopes produced by activation may have half-lives of weeks to years and can thus persist over a long period of the physics dataset. The activation of detector components will occur during construction, transportation, or storage at the South Pole (altitude 9,301 ft) prior to deployment.

DM-Ice17, the first-generation experiment, was deployed at a depth of 2450 m under the ice at the geographic South Pole in December 2010. It has collected a stable and continuous physics dataset spanning over three-and-a-half years. The DM-Ice17 data provide compelling evidence of significant production of cosmogenic isotopes, which has been used to validate the simulation of the production based on a known exposure history. This cosmogenic study provides important feedback to the background modeling for the full-scale DM-Ice250 experiment.

Karsten Heeger, Reina Maruyama, and Francis Halzen

*Behold, these are but the outskirts of his ways,
and how small a whisper do we hear of him!
But the thunder of his power who can understand?*

ACKNOWLEDGMENTS

This thesis represents the culmination of more than five years of work on DM-Ice. I would not have learned so much, nor would this analysis have been successfully completed, without the patient instruction, criticism, and support of many people. These remarks will single out only a few of the many people who have taught me so much over these years.

I have had the privilege of naming three faculty members as my advisors during my graduate career – Karsten Heeger, Reina Maruyama, and Francis Halzen. Without their influence this work would never have begun, and so they deserve first credit. The other members of my thesis and preliminary committees also deserve note – Baha Balantekin, Matthew Herndon, Dan McCammon, Delia Tosi, and Stefan Westerhoff. Their review of my work from an external perspective served to stimulate discussion and prompt further investigation.

Along my educational path leading to this point, the contagious excitement of several mentors rubbed off on me which drove me to pursue this career. Michael Savina, my first research mentor, and Cyril Slezak, my undergraduate advisor, both prompted me to escape my comfort zone and helped show me that I wanted to get piled higher and deeper. Jeff Hengesbach and Darren Starnes deserve credit for an excellent foundation in high school that started this journey. It would also have not been possible without the disciplined education provided by the physics department at the University of Wisconsin–Madison, the physics and chemistry departments at Hillsdale College, and the science and math departments at the Webb Schools.

My peers and colleagues have been responsible for many engaging discourses over the years, through which I have become a more effective scientist. Foremost among this number is the DM-Ice local group – Matt Kauer, Antonia Hubbard, and Zack Pierpoint – with whose analyses my own has become entwined and from whom I have learned so much. The other members of the Heeger and Maruyama groups, as well as the community at the Wisconsin IceCube Particle Astrophysics Center (WIPAC), have encouraged a broadening of my physical intuition as well as contributing to the editing process of this document.

The smooth operation of the detectors was made possible through the several IceCube DAQ experts – John Kelley, Chris Wendt, and Mark Krasberg. Whenever the system did something truly unexpected, they selflessly contributed their time and systems knowledge to help me diagnose problems. In completing the cosmogenics analysis, Vitaly Kudryavtsev of the University of Sheffield has provided invaluable guidance

at various stages to make the study more robust. The cosmogenic simulation incorporated several datasets which were made available by their authors – HEAD-2009 activation library from Yury Korovin and epoch 2010 geomagnetic rigidities from Margaret Shea and Donald Smart.

Much of my graduate career has been made possible because of support from the Stewardship Science Graduate Fellowship of the Department of Energy’s National Nuclear Security Administration. This fellowship, administered by the Krell Institute, has facilitated the free pursuit of this thesis work, afforded many enrichment opportunities, and facilitated discourse with the other fellows which has in turn broadened my own perspective.

The staff at the WIPAC, Wright Lab, and Krell Institute deserve special mention for keeping the wheels turning. Without their careful attention to detail, I would have been buried under paperwork or never have gotten paid. Instead they make everything work like magic and liberate the absent-minded physicists to stick their heads in the clouds or play with their cool toys.

Most importantly throughout this endeavor has been the support of my family and friends. Guilhem Ribeill, Zack DeLand, and Amanda Kruse were always there in Madison to enliven the drab moments, throw a frisbee, or give an excuse to eat chips and queso. Truly we all took that test, and probably would have failed it were it not for study sessions under Guilhem’s tutelage. My family has been consistent in their encouragement and unfailing in their love, it is thanks to you that I always had a stable foundation and never lost perspective. To Katie (and Teddy), the completion of this saga is a testament to your forbearance and endurance. Rejoice! It’s finally over.

TABLE OF CONTENTS

	Page
ABSTRACT	i
LIST OF FIGURES	ix
LIST OF TABLES	xiv
1 Introduction	1
1.1 Outline	3
1.2 Author’s Contributions	5
2 Overview of Dark Matter	7
2.1 History of Dark Matter	7
2.2 Constraints from Cosmology	9
2.2.1 Cosmic Microwave Background	10
2.2.2 Large Scale Structure	11
2.2.3 Big Bang Nucleosynthesis	12
2.2.4 Type Ia Supernovae	14
2.3 Direct Observation	15
2.4 Dark Matter Models	16
2.4.1 Modified Physical “Laws”	16
2.4.2 Baryonic Dark Matter	17
2.4.3 Hot Dark Matter	17
2.5 Beyond Standard Model Particles	18
2.5.1 Axions	18
2.5.2 Weakly Interacting Massive Particles	19
2.5.2.1 WIMP Miracle – Thermal Freeze-Out Relic	20
2.5.2.2 Prospects for WIMP Detection	21
3 Direct Detection WIMP Searches	24
3.1 Galactic WIMP Dynamics	24
3.2 WIMP Interactions	25
3.2.1 Spin-Independent Scattering	26
3.2.2 Spin-Dependent Scattering	27
3.2.3 Inelastic Dark Matter	28
3.3 Search Techniques	28
3.3.1 Recoil-Type Identification	29
3.3.2 Annual Modulation	30
3.3.3 Directional Sensitivity & Diurnal Modulation	31
3.4 Status of Current Experimental Searches	32
3.4.1 Semiconductor Detectors	33
3.4.2 Noble Gas Detectors	37

	Page
3.4.3 Inorganic Scintillator Detectors	39
3.4.3.1 DAMA, Sodium Iodide, & Annual Modulation	40
3.4.4 Bubble Nucleation Detectors	43
3.4.5 Directional Detectors	43
3.5 Prospects for Future Searches	44
3.6 Background Concerns for Direct Searches	45
4 Overview of Cosmogenic Activation	47
4.1 Cross Sections	48
4.2 Cosmic Ray Fluxes	50
4.2.1 Neutron Flux Spectrum	52
4.2.2 Altitude Dependence	53
4.2.3 Location and Temporal Dependence	54
4.2.3.1 Solar Activity	54
4.2.3.2 Geomagnetic Rigidity	55
4.3 Activation Mechanisms	56
4.4 Calculating Activation Rates	56
5 The DM-Ice17 Experiment	59
5.1 DM-Ice17 Detectors	59
5.1.1 Optical Components	60
5.1.2 Electronics & Digitization	62
5.1.3 Pressure Vessel and Assembly	65
5.1.4 Construction	66
5.2 South Pole Science	66
5.2.1 IceCube Neutrino Observatory	68
5.2.2 Ice Drilling	69
5.2.3 Ice Properties	70
5.3 Experiment History	70
6 DM-Ice17 Performance and Operations	72
6.1 Detector Operation	72
6.2 Run Schedule	73
6.3 Run Parameters	74
6.3.1 Sampling Rate	74
6.3.2 Photomultiplier Tube High Voltage	76
6.3.3 Trigger Threshold	77
6.3.4 Coincidence Window	79
6.4 Livetime	80
6.4.1 Deadtime	80
6.4.2 Run Transition Downtime	84
6.4.3 Acute Downtime	87
6.5 Monitoring	88
6.5.1 Temperature	89
6.5.2 Pressure	91

	Page
6.5.3 PMT High Voltage	92
6.5.4 Trigger Rate	93
6.6 Calibration	95
7 DM-Ice17 Data	97
7.1 Waveform Corrections	97
7.1.1 Baseline	98
7.1.2 Pedestals	98
7.1.3 Droop Correction	101
7.2 Cuts and Associated Noise	102
7.2.1 Software Local Coincidence	103
7.2.2 Electromagnetic Interference	103
7.2.3 Thin Pulses	105
7.2.4 SPE-Like Noise	106
7.3 Energy Spectrum	107
7.3.1 Energy Calibration	107
7.3.2 Gain Stability	108
7.3.3 Energy Resolution	110
7.3.4 Single Photoelectron Response	112
7.3.5 Comparison to Simulation	114
7.3.5.1 Background Model	115
8 Activation of DM-Ice17	119
8.1 Exposure History	119
8.1.1 Air Shipment	119
8.1.2 Total Exposure	122
8.2 Activation Rate Expectation	124
8.2.1 Activation Codes	124
8.2.1.1 NaI Crystals	125
8.2.1.2 Quartz Lightguides	128
8.2.2 Steel	128
8.3 Cosmogenic Activation Products Observed in DM-Ice17 Data	131
8.3.1 Activation Products in the Low-Energy Spectrum	131
8.3.1.1 Iodine-125 Rate Analysis	134
8.3.2 Activation Products in the High-Energy Spectrum	137
8.3.2.1 Manganese-54 Rate Analysis	139
8.3.3 Simulation Agreement	140
8.4 Comparison to Other NaI Detectors	145
8.5 Summary	149
9 Future DM-Ice Experimental Stages	151
9.1 DM-Ice250	151
9.1.1 Experimental Concept	151
9.1.2 Geometry	152
9.1.3 Intrinsic Background	155

	Page
9.2 DM-Ice250 Cosmogenic Discussion	157
9.2.1 Cosmogenic Impact	157
9.2.2 Cosmogenic Exposure and Mitigation Strategies	161
9.3 DM-Ice Research and Development	163
9.4 Summary	165
10 Conclusion	166
LIST OF REFERENCES	168
GLOSSARY	181
APPENDIX Portable Muon Detector	185

LIST OF FIGURES

Figure	Page
1.1 Observed modulation signal by DAMA experiment.	1
1.2 Tension in comparing dark matter experimental results.	2
2.1 M33 galactic rotation curve.	9
2.2 Constraints on the composition of the Universe and observational complementarity.	10
2.3 Cosmic microwave background power spectrum.	11
2.4 Baryon acoustic oscillation in galactic distribution.	12
2.5 Light element abundance and BBN agreement.	13
2.6 Supernovae evidence for dark energy.	14
2.7 Train-wreck cluster and bullet cluster observations.	15
2.8 Theoretical dark matter candidates.	18
2.9 Axion experimental status.	19
2.10 Dark matter production as a thermal relic.	20
2.11 Dark matter particle interaction modes.	21
2.12 Complementarity of WIMP search techniques.	22
3.1 Example WIMP recoil spectrum.	27
3.2 Dark matter experimental signals.	29
3.3 Recoil-type identification	30
3.4 Dark matter annual modulation.	31
3.5 Dark matter diurnal modulation.	32
3.6 Status of current direct detection dark matter searches.	33
3.7 Annual modulation signal observed by DAMA.	41

Figure	Page
4.1 Production cross section of ^{125}I	49
4.2 Production of secondary cosmic rays in the atmosphere.	50
4.3 Variation in cosmic ray flux with altitude.	51
4.4 Cosmic neutron flux spectrum.	52
4.5 Cosmic ray flux parameterization.	53
4.6 Eleven year solar cycle and anti-correlation with cosmic ray flux.	55
4.7 Geomagnetic rigidity contours for Epoch 2010.	56
4.8 Effect of decay time on cosmogenic production of radionuclides.	58
5.1 DM-Ice17 detector environment.	59
5.2 DM-Ice17 sensitive detector.	61
5.3 Block diagram of DM-Ice17 digitizers and data transfer.	63
5.4 South Pole station facilities.	67
5.5 DM-Ice17 location within IceCube array.	68
6.1 Example delayed waveform trigger.	75
6.2 Effect of sampling rate on waveform leading-edge clipping.	75
6.3 Commissioning trigger rate instability	76
6.4 Threshold selection from commissioning noise spectrum.	78
6.5 Local coincidence trigger window.	79
6.6 Distribution of waveform maximum versus local coincidence trigger window.	80
6.7 Detector exposure and downtime.	81
6.8 Hit deadtime determination from data.	82
6.9 Hit deadtime throughout dataset.	83
6.10 Recorded event rate and associated deadtime throughout dataset.	85
6.11 Run uptime and run transition downtime.	86
6.12 Daily physics uptime fraction over dataset.	87
6.13 Daily average monitored mainboard temperature.	90

Figure	Page
6.14 Mainboard re-thermalization following power outage.	91
6.15 Daily average monitored mainboard pressure.	92
6.16 PMT high voltage deviation from set point.	93
6.17 Det-2b trigger rate and PMT high voltage deviation.	93
6.18 Daily average monitored trigger rate.	94
6.19 Det-2b trigger rate fluctuation.	95
7.1 Example pedestal waveforms.	99
7.2 Binwise pedestal variation.	99
7.3 Pedestal susceptibility to environment and setting changes.	100
7.4 Model droop effect on waveforms.	101
7.5 Low-energy noise event spectra.	103
7.6 Local coincidence window and event pairing.	104
7.7 Example electromagnetic interference (noise) waveform.	104
7.8 Electromagnetic interference (noise) event identification.	105
7.9 Example thin pulse (noise) waveform.	105
7.10 Thin pulse (noise) event identification.	106
7.11 Example scintillation waveforms.	107
7.12 DM-Ice17 calibrated energy spectra.	109
7.13 Gain stability over physics dataset.	109
7.14 Energy resolution function.	111
7.15 SPE height determination.	112
7.16 PMT non-coincident rate determination.	113
7.17 PMT non-coincident rate stability.	114
7.18 Simulation visualizations of DM-Ice17 geometry.	115
7.19 Simulation-data comparison of beta/gamma region.	116
7.20 Simulation-data comparison of alpha region.	117

Figure	Page
8.1 Activation due to air shipment of detectors and components.	121
8.2 Activation history for detector components prior to deployment.	122
8.3 Simulated spectrum from sodium iodide activation.	127
8.4 Simulated spectrum from all activation products.	128
8.5 Simulated spectrum from quartz activation.	129
8.6 Simulated spectrum from steel activation.	131
8.7 Decay scheme of ^{125}I	132
8.8 Simulated spectrum of activated ^{125}I in NaI crystal.	132
8.9 Low-energy data residual.	133
8.10 Observed decay of ^{125}I in DM-Ice17.	136
8.11 Simulated spectrum of activated ^{54}Mn in steel pressure vessel.	137
8.12 High-energy data residual.	138
8.13 Observed decay of ^{54}Mn in DM-Ice17.	140
8.14 Simulation fit to high-energy data residual.	141
8.15 Simulation fit to medium-energy data residual.	143
8.16 Simulation fit to low-energy data residual.	144
8.17 Simulated cross section and differential production rate comparison.	147
8.18 Simulated cross section and differential production rate comparison for ^{113}Sn	148
8.19 Cosmogenic activation contributions to ^{113}Sn rate in DM-Ice17 by exposure stage.	150
9.1 Science potential of full-scale DM-Ice.	152
9.2 Schematic of proposed DM-Ice250 module.	153
9.3 Proposed DM-Ice250 deployment.	154
9.4 Simulated background spectrum for DM-Ice250.	156
9.5 Simulated background spectrum for NaI crystals of DM-Ice250.	157
9.6 Simulated spectrum from sodium iodide activation in DM-Ice250S.	159
9.7 Decay of cosmogenic background over time.	160

Figure	Page
9.8 Cosmogenic rate in 2–6 keV region.	160
9.9 Cosmogenic activation contributions to DM-Ice250S by exposure stage.	162
9.10 DM-Ice37 detector configurations.	164
Appendix	
Figure	
A.1 Profile schematic of South Pole RodWell.	186
A.2 Muon detector schematic.	188
A.3 Muon detector single optical assembly.	189
A.4 Muon detector single paddle assembly.	190
A.5 Muon detector completed package.	191
A.6 Amplifier transimpedance parameter effect on waveforms.	193
A.7 Muon detector spectrum for all channels after PMT gainmatching.	194
A.8 Trigger threshold effect on spectra.	194
A.9 Coincidence spectra from trigger mask alterations.	195
A.10 Overburden locations and muon detector operation at the South Pole.	196
A.11 Example spectrum from muon detector.	199
A.12 Calibration source data.	200
A.13 Comparison of muon spectra from all locations.	200

LIST OF TABLES

Table	Page
3.1 List of current direct detection experiments and future plans.	34
5.1 DM-Ice17 detector components and vendors.	60
6.1 Hit deadtime values for each DM-Ice17 MB.	83
7.1 DM-Ice17 PMT calibration functions.	108
7.2 Contamination of DM-Ice17 detector components.	116
7.3 Contamination levels of DM-Ice17 NaI crystals.	118
8.1 Summary of flight activation.	120
8.2 Summary of storage activation.	123
8.3 NaI crystal activated isotopes.	126
8.4 Quartz lightguide activated isotopes.	129
8.5 Steel composition comparison.	130
8.6 Steel pressure vessel activated isotopes.	130
8.7 Fit values for ^{125}I peak.	135
8.8 Comparison of NaI cosmogenic activation rates.	146
9.1 Simulated contamination of DM-Ice250 detector components.	155
9.2 NaI cosmogenic activation rates used for DM-Ice250 simulation.	158
9.3 Reduced baseline exposure scenario for DM-Ice250S.	162
A.1 Components of Cosmic Ray Detector	187
A.2 Relative rates measured by muon detector.	201

Chapter 1

Introduction

The current cosmological understanding posits a universe that is comprised of 26.5% dark matter [1, 2], a substance which has eluded definitive explication for over 80 years [3]. The field of direct dark matter detection has driven rich and productive scientific exploration for nearly three decades [4, 5]. Spurred on in the quest to detect a rare interaction processes, many detector technologies and search strategies have vied for preeminence [6].

Within this milieu, only the DAMA experiment has reported a positive detection claim (see Fig. 1.1). With 1.33 ton-yr of data collected between the DAMA/NaI and DAMA/LIBRA phases, the best-fit modulation amplitude measured is 0.0112 ± 0.0012 counts/day/keV/kg, a $9.3\text{-}\sigma$ result. The period and phase of the DAMA modulation are both consistent with the expectation for a dark matter signal [7]. The modulation signal persisted between the DAMA experimental phases despite the entire detector and electronics apparatus having been upgraded and replaced in between.

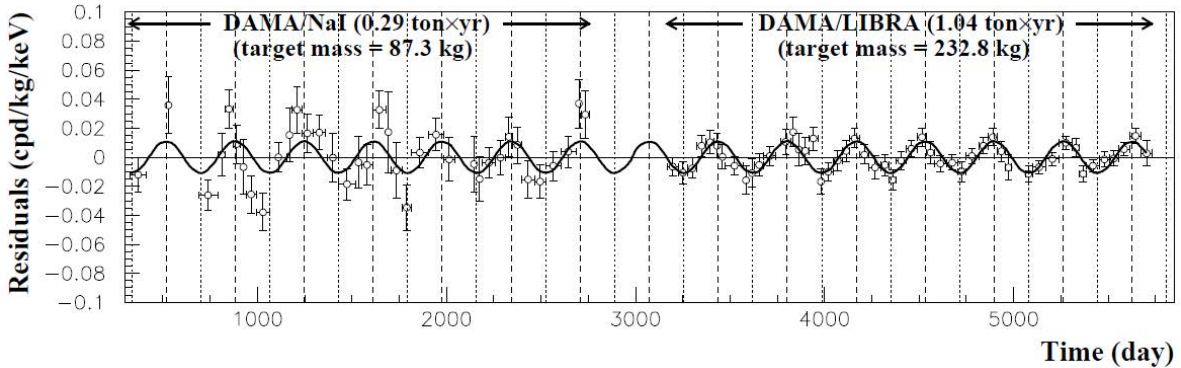


Figure 1.1: Observed modulation signal in 2–6 keV region by DAMA/NaI and DAMA/LIBRA interpreted as evidence for dark matter [8]. The observed modulation over 14 annual cycles has non-zero amplitude ($9.3\text{-}\sigma$) and the observed phase and period match the prediction for dark matter.

Meanwhile, other experiments have continued to measure null results, generating exclusion limits that strongly disfavor the complete DAMA-preferred parameter space (see Fig.1.2) [9, 10, 11, 12, 13]. The DAMA iodine-recoil region (at ~ 50 GeV dark matter mass) is even excluded by experiments also using iodine targets [14, 15].

Low-significance signal excesses previously observed [16, 17, 18] in other experiments have all since been excluded by newer results either by the same collaborations or by others operating the same target material [12, 13]. As the leading experiments continue to improve sensitivity across all mass ranges by increasing the target mass, decreasing the intrinsic backgrounds, and lowering the detector thresholds [6], the DAMA signal becomes increasingly disfavored for any theoretical dark matter model. At the same time, no explanation for the DAMA signal apart from dark matter has withstood scrutiny [19, 20].

Responding to this prolonged tension, a new suite of experiments is seeking to directly test the DAMA signal claim [21, 22, 23]. These new experiments all aim to repeat the DAMA annual modulation measurement with the same target material and detector technology, they differ only in their implementation and plans to eliminate any systematic uncertainty. Of these experiments, DM-Ice is unique in its proposal to operate detectors in the Southern Hemisphere, planning for a deployment in the South Pole ice [22].

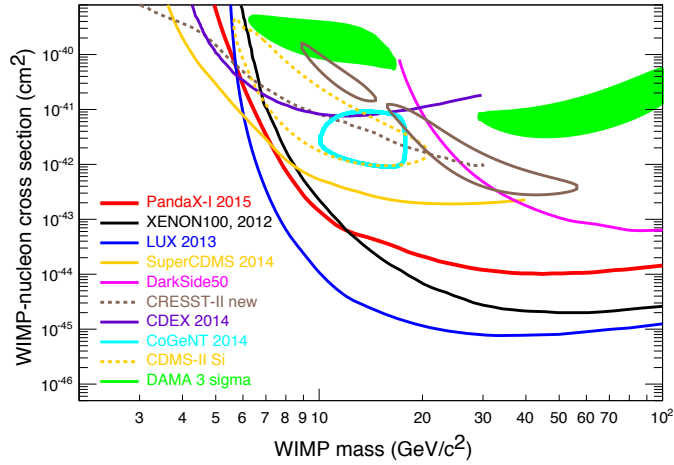


Figure 1.2: Comparison of results from direct detection dark matter experiments in spin-independent WIMP parameter space in 2015 [11]. The DAMA-preferred dark matter regions (green shaded regions) are strongly disfavored under standard dark matter interaction assumptions. The other dark matter candidate regions (teal, brown, dotted-yellow outlined regions) based on signal excesses of other experiments have all since been excluded by the same experiment or another experiment using the same target material.

DM-Ice17 is the first experimental phase of the DM-Ice experimental program, with 17 kg of target mass deployed between two detectors modules buried 2450 m in the South Pole ice. Over a continuous three-and-a-half year physics dataset, the detectors have achieved 99% uptime. Based on the data collected, DM-Ice17 has demonstrated the stability of the environment, as well as the ability to remotely calibrate and operate low-background dark matter detectors buried in the South Pole ice [24].

An important component of the DM-Ice17 goals was the assessment of the radioactive backgrounds experienced by detectors in this environment due to intrinsic contamination, environmental impurity, and cosmogenically-activated radioisotopes. The intrinsic contamination is controlled by screening of detector materials prior to construction and following clean assembly procedures. The environmental impurity has been assessed by sampling and counting the drill water and demonstrated to be a negligible contribution to the total background. The cosmogenically-activated background induced by exposure to elevated cosmic ray fluxes during shipment to and storage at the South Pole is the only background that cannot be directly estimated before deployment; instead it must be simulated after the exposure history is determined. All radioactive backgrounds have been included in the detector Monte Carlo simulation and agreement has been demonstrated with DM-Ice17 data.

In this thesis analysis of DM-Ice17 data, a significant presence of six cosmogenic isotopes in the crystal and pressure vessel is identified persisting months to years past deployment. The accurate measurement of the abundance of these isotopes validates the activation model for DM-Ice17 as well as future South Pole deployments. Projecting the activation observed in DM-Ice17, a reasonable estimate can be made for the total activation expected for future deployments as well as the impact this additional background will have on the physics potential of these experiments. In order to mitigate the effects of this background, strategies are discussed to reduce the total exposure.

The cosmogenics analysis also produces positive feedback to the low-level analysis chain for DM-Ice17 and other remotely-operated detectors. The decaying isotopes analyzed in residual spectra provide background-free features which can then be matched to simplified simulation predictions. These spectral features can be used to assess the quality of the energy calibration and resolution. This method is in contrast to the standard analysis of the approximately static intrinsic radioactive backgrounds which requires assumptions about the underlying background spectrum shape at the peak locations.

1.1 Outline

This thesis can be roughly divided into four broad categories. The background physics motivating the DM-Ice experiment and behind cosmogenic activation are discussed in Chapters 2–4. The DM-Ice17 experiment, its data, and the low-level analysis which are prerequisites for the cosmogenics analysis are discussed in Chapters 5–7. The cosmogenics measurements and simulation performed for this analysis

are discussed in Chapters 8–9. Supplemental materials supporting the activation mitigation for future deployments are included in the appendix. A more detailed chapter breakdown is as follows:

- [Chapter 2](#) introduces dark matter within the context of the standard cosmological model of the universe and establishes the motivation for the ‘weakly interacting massive particle’ (WIMP) dark matter that DM-Ice searches for.
- [Chapter 3](#) explores the mechanisms allowing direct detection of dark matter and the current status of the experimental field.
- [Chapter 4](#) reviews cosmogenic activation and calculations of its cumulative effects. In this context cosmic ray fluxes on Earth and their variation in time and space are discussed.
- [Chapter 5](#) describes the DM-Ice17 detectors up to deployment. Their components are each detailed, the design and construction process are outlined, and the experimental environment and deployment in the South Pole ice are discussed.
- [Chapter 6](#) demonstrates the operational settings, performance, and stability of the DM-Ice17 detectors. The 99% uptime and stability of all monitored detector quantities are demonstrated in this chapter.
- [Chapter 7](#) provides the low-level analysis chain which processes the raw DM-Ice17 data into calibrated energy spectra used in the cosmogenic analysis.
- [Chapter 8](#) details the cosmogenic simulation expectation based on the known DM-Ice17 exposure history and the search for cosmogenic isotopes in DM-Ice17 data. The agreement between data and simulation are discussed in the context of validating the model uncertainty and expanding the established activation results from other experiments.
- [Chapter 9](#) discusses the prospects for a full-scale DM-Ice experiment. The physics potential, experimental overview, and total background simulation of these detectors is provided. The effects of cosmogenic isotopes on the physics potential of a full-scale detector are outlined, as well as possible mitigation strategies. Current R&D work is introduced in the context of advancing cosmogenic activation analysis and demonstrating the feasibility of the full-scale DM-Ice experiment.
- A [Glossary](#) serves double-duty in expanding acronyms and explicating terminology.
- [Appendix A](#) introduces the portable muon detector operated at the South Pole in January 2012 and discusses the measurement results from various proposed storage locations for short-term shielding prior to deployment of future detectors.

1.2 Author's Contributions

I had the privilege of joining DM-Ice in Spring 2010, when the planning phases for DM-Ice17 deployment were still underway. This allowed me to witness and even participate in every phase of the experimental process. As the first graduate student on the project, I was afforded the opportunity to take on more varied roles during the entire experience. DM-Ice has remained a small project, but the low-level data processing underlies all high-level analyses, including the cosmogenics work presented here; the processing is also built on critical contributions from Matt Kauer, Antonia Hubbard, and Zack Pierpoint. The entire analysis has formed under the watchful guidance of Reina Maruyama and Karsten Heeger.

During the DM-Ice17 design and construction phase in 2010 all tasks were focused on the immediate issue of ensuring the detectors would be done on time. A series of my initial projects involved characterizing or optimizing the various detector components – temperature cycling of NaI crystals, pulse characteristics and signal response of photomultiplier tubes (PMTs), settings optimization and noise reduction of mainboard electronics, stability of PMT high voltage supplies, and pulse shaping of PMT voltage dividers. Much of this work escapes the scope of this thesis as the outcome was rejected components not included in DM-Ice17 or any future detector. In parallel to component testing, I participated in the iterative design review and modification process with the engineers at the Physical Sciences Laboratory (PSL). During the detector assembly, there were daily trips out to PSL to assist in the ‘nuts and bolts’ of the process. Thanks to the cooperative effort and a great undertaking by the staff at PSL, the deadline arrived and two fully functional detectors were shipped off to the South Pole, exactly as planned.

Following the deployment of DM-Ice17, I was charged with operation of the detectors. It is therefore a great source of pride that our detectors have achieved an incredible 99% over the three-and-a-half year dataset. The detectors operate on a simplified version of the IceCube DAQ which has remained unchanged, but the user interface wrapper scripts have been extensively rewritten during my tenure to customize for DM-Ice’s use. The operation and performance of the detectors is described in detail in Chap. 6.

In 2013, much of my emphasis was shifted towards simulation, and I inherited upkeep and operation of DMIceSim, the Geant4 Monte Carlo simulation framework. This simulation package was originally designed for NaIAD by Matt Robinson of University of Sheffield and updated into its current form for DM-Ice by Lauren Hsu of Fermilab. My primary contributions to the simulation were implementation of the precise DM-Ice17 geometry, streamlining of event generation for more efficient calculations, and production and validation of all DM-Ice17 simulation dataset. As the DM-Ice family of experiments has grown, the simulation geometries have grown apace as I implemented the new experimental configurations. The intrinsic background simulation for DM-Ice17 is addressed in Sect. 7.3.5, the cosmogenic background simulation is discussed in Chap. 8, and both intrinsic and cosmogenic background simulations are projected in Chap. 9.

The primary analysis of this thesis, modeling of cosmogenic exposure, prediction of activation, and analysis of cosmogenic isotopes, is entirely my work. The results for DM-Ice17 are presented in Chap. 8, with a discussion of future impact provided in Chap. 9.

The muon detector project presented in App. A was a self-contained project executed around my work at the South Pole in January 2012. I was responsible for all aspects of the work – design, construction, operation, and analysis. Engineering assistance from Tom Wise and Jeff Cherwinka, especially in crunch-time leading up to the ship date, helped bring the project together.

As the DM-Ice experimental program moves forward into the R&D phase preparing for the full-scale experiment, the timeline has started over at the beginning again. I have taken a lead role in establishing test setups at two underground sites – a shallow site at Fermilab and at a deep site at Boulby. My primary responsibilities in the R&D program have been PMT testing, detector assembly, data acquisition coding, and experiment operations.

It has been an incredible opportunity to participate in the entire experimental process once, and then to lead in initiating the process anew under very different circumstances. For DM-Ice17, existing components from many disparate places were brought into a cohesive whole by many participants on an abbreviated timescale to seize on a critical window of opportunity. For the R&D detectors, all new components are being brought together in a staged approach over a long time by a few people to systematically improve the setup until it can reach the design requirements. The new apparatus has come with its own not-insignificant set of challenges, but also has provided the opportunity to apply forward a few of the lessons learned over five years with DM-Ice17.

Chapter 2

Overview of Dark Matter

The scientific conception of dark matter can be traced back over eighty years [3]. The scientific consensus on the subject is remarkably poor, however, despite decades of observing the effects of and searching for dark matter. This deficiency ought to be shocking, as there is no shortage of subject material to study – dark matter abounds throughout the universe, accounting for nearly 85% of all matter in the universe, and possibly as much as 95% of the matter in galaxies.

A wide range of observations contribute to our understanding of the effects of dark matter on the universe and the need for its existence. These varied techniques can be used to build a consistent cosmological model partitioning the universe into 68.5% dark energy, 26.5% dark matter, and only 5.0% ordinary matter [1, 2]. The dark matter is accepted to be a yet-undiscovered particle (or particles), but its identification has remained elusive to experimental searches. Theoretical models meanwhile abound with predictions of particle physics beyond the Standard Model which generate a zoo of candidates, providing little definitive guidance.

“Weakly interacting massive particles” (WIMPs) are a leading theoretical candidate to account for dark matter. Searches employing widely diverging techniques from the fields of collider physics, astronomy, and nuclear physics are currently underway to measure this piece of the cosmos.

2.1 History of Dark Matter

It was through the lens of history that Eugene Wigner commented on the “unreasonable effectiveness of mathematics” at describing the natural world [25]. Rigorous application of the law of universal gravitation which Wigner singled out has had a pivotal roll in identifying ‘dark’ objects at scales from within the Solar System to throughout the galaxy. The predictions of unseen objects have often been so advanced that decades elapsed before their direct confirmation could be provided.

In the mid-19th century, several famous demonstrations were provided of such identification by mathematical extrapolation from precise observations on perturbations in the behavior of an object. Friedrich Bessel is credited as the first for his 1844 analysis of Sirius and Procyon which predicted unseen binary companions [26]. Bessel did not live to see the optical confirmation of the white dwarf companions he predicted

– Sirius B was not observed until 1862 by Alvan Graham Clark and Procyon B until 1896 by John Martin Schaeberle. Only two years after Bessel’s yet-unverified binary star predictions were published, the discovery of Neptune brought the search back within the confines of the Solar System. In 1846, Urban Le Verrier was able to predict the location of the unknown planet to within 1° , a precision which allowed Johann Galle to identify it with only one night of observation.

The first use of the term “dark matter” in scientific literature may be attributed to Dutch astronomer Jacobus Kapteyn in 1922 [27] as astronomers attempted to understand the matter density in the vicinity of the Solar System and the position of the sun relative the galactic center. These observations were based on the velocity dispersion of nearby stars, and so they continued to improve as star catalogs of distances and luminosity expanded and gained accuracy. Such observations reached a consensus with Jan Oort’s conclusion that stars could account for nearly all the local matter density within the uncertainties of the abundance of faint objects [28].

History tends to credit Fritz Zwicky as being the first person to accurately postulate the existence of dark matter as a result of his observations of the Coma cluster of galaxies in 1933. By inferring the mass from the luminosity and applying the virial theorem, he concluded that the relative speeds were much too great to be bound gravitationally by the visible matter alone. His estimation was “dark matter” would need to be approximately 400 times more abundant than the visible matter in order to reconcile the observation [3].

In order to obtain information of the distribution of dark matter throughout a galaxy, the rotation of the galaxy is a very useful probe. Oort noted in his observations of galaxy NGC 3115 in 1940 that the mass and light emission distributions did not directly correlate [29]. With the advent of radio measurements, the rotation curves of galaxies could be mapped to greater distances from the core by studying the HI neutral hydrogen line of the gas. The rotation curve of M33 observed by Louise Volders in 1959 with this technique showed a rotational velocity profile remained leveled off out to ~ 6 kpc in disagreement with expected rotational dynamics [30].

The connection from the anomalous galactic rotation curves to dark matter was finally made by Vera Rubin and Kent Ford in their observations of M31 (Andromeda galaxy) in the 1960’s [31]. Rubin’s analysis had the advantage of Ford’s superior instrumentation which extended the observable galactic profile to much larger radii, which enhanced the anomalous pattern they observed relative to earlier measurements. Rather than velocities decreasing at large radii as $r^{-1/2}$, her velocity profile leveled off out to the furthest radii with detectable signal. Repeated measurement of other spiral galaxies, particularly NGC 3198, M31, and M33 have all continued to observe the same phenomenon with greater precision (see Fig. 2.1).

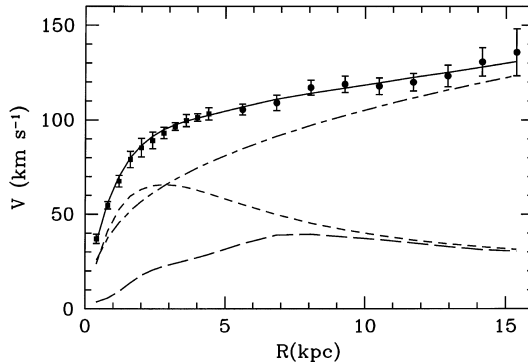


Figure 2.1: Measurement of the rotation curve of M33 (points) compared with the best-fitting model (continuous line) [32]. After an initial sharp rise in velocity at small (< 2 kpc) radii in the densest star region, the rotation curves characteristically flatten out or even continue increasing despite the absence of significant amounts of visible matter. The mass in the stellar disk (short-dashed line) and hot gas (long-dashed line) cannot account for the galactic rotational velocity, requiring an additional mass component be provided by a dark matter halo (dot-dashed line).

2.2 Constraints from Cosmology

While the galactic rotation curves help to visualize the mass shortage from luminous matter, they are an inadequate probe for quantifying the total dark matter abundance of the universe. Accurate constraints on the dark matter contribution to the mass-energy of the universe are obtained from a combined analysis of many different cosmological observables. The standard cosmological model, Lambda-Cold Dark Matter (Λ CDM), is this concordance model built on the complementarity of different measurement techniques (see Fig. 2.2). The Λ CDM model includes a cosmological constant (Λ , a specific implementation of dark energy), cold dark matter, and an inflationary phase at the beginning of the cosmic time.

The primary observables to constrain the six fitted parameters of Λ CDM include the cosmic microwave background (CMB), baryon acoustic oscillations (BAO), Big-Bang nucleosynthesis (BBN), type Ia supernovae, and gravitational lensing. The current best estimates for the Λ CDM parameters of radiation (Ω_γ), baryonic matter (Ω_b), dark matter (Ω_c), and dark energy (Ω_Λ) fractions of the universe from the combination of multiple CMB observations are: [1, 2]:

$$\begin{aligned}
 \Omega_\gamma &= (5.46 \pm 0.19) \cdot 10^{-5} \\
 \Omega_b &= 0.0499 \pm 0.0022 \\
 \Omega_c &= 0.265 \pm 0.011 \\
 \Omega_\Lambda &= 0.685^{+0.017}_{-0.016} .
 \end{aligned}
 \tag{2.1}$$

These measurements are consistent with a ‘flat’ ($\Omega = 1$) universe, and indicate that the dark energy dominance will only strengthen as the universe continues to expand.

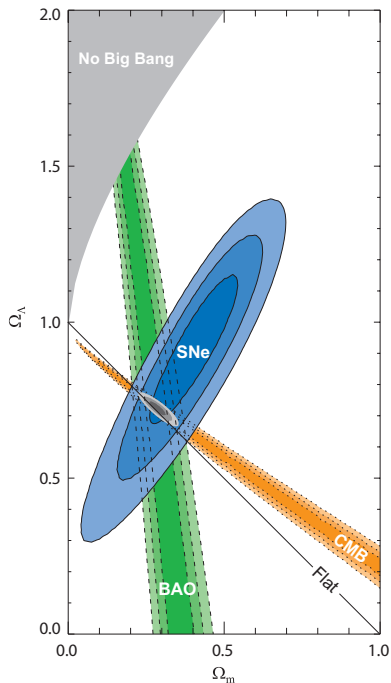


Figure 2.2: Constraint on the composition of the universe in dark energy (Ω_Λ) and matter (Ω_m , the sum of baryonic and dark matter) [33]. A complementarity exists between supernovae (SNe), cosmic microwave background (CMB), and baryon acoustic oscillation (BAO) observations different cosmological observables allowing a more precise determination of the matter and dark energy fractions.

2.2.1 Cosmic Microwave Background

The cosmic microwave background (CMB) was accidentally discovered in 1964 by Arno Penzias and Robert Wilson of Bell Labs as an undesired excess antenna temperature [34]. It is isotropic to 1 part in 100,000 and follows a thermal black-body spectrum of temperature 2.7255 K [35]. The CMB is a useful probe of cosmology because the photons which constitute it decoupled when the universe cooled to ~ 3000 K and are imprinted with the quantum fluctuations of the nearly-homogeneous early universe.

The full-sky CMB has been mapped most recently by the Planck satellite with sufficient precision to resolve the seventh acoustic peak (see Fig. 2.3) [35]. Ground-based experiments, such as the Atacama Cosmology Telescope (ACT) and South Pole Telescope (SPT) map the CMB over smaller portions of the sky but with greater angular precision, thereby accessing higher- ℓ modes (smaller angular scales) of the power spectrum. The observations from different experiments overlap for much of the power spectrum and show excellent consistency and agreement with the Λ CDM model. The quoted Λ CDM-derived composition of the universe (see Eqn. 2.1) combine four CMB datasets – the Planck satellite 15.5-month temperature data [35],

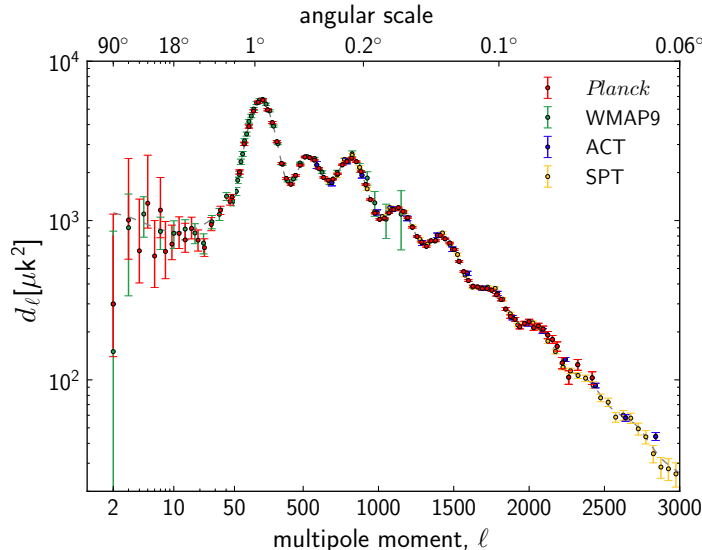


Figure 2.3: The cosmic microwave background temperature angular power spectrum with Λ CDM fit [35]. Full-sky satellite surveys WMAP9 and Planck provide the highest precision measurements at large angular scales (low ℓ) while deeper ground-based surveys ACT and SPT extend the measurement to small angular scales (high ℓ). The experiments agree well in the overlap region of $500 < \ell < 2500$.

the WMAP 9-year polarization data [36], and constraints on foregrounds from the high- ℓ CMB measurements from ACT [37] and SPT [38].

The current generation of ground based telescopes is placing increased focus on measuring the polarization of the CMB, particularly for the B-mode (“curl” component). The B-mode polarization of the CMB power spectrum contains signatures of gravitational lensing at high- ℓ and of gravitational waves at low- ℓ , both of which have implications for cosmology. While the lensing signature has been measured to high significance [39, 40, 41, 42], contamination from dust foregrounds has been demonstrated to exceed the signal at large angular scales [43] masking any direct detection of gravitational waves [44, 40, 45].

2.2.2 Large Scale Structure

Surveys of the distribution of galaxies in the universe provide a sensitive probe to cosmology by mapping out the growth of structure in the universe and the cosmic expansion history. By measuring the distance between galaxies, these surveys uncover a “standard ruler” - a length scale with a statistically significant excess in the matter power spectrum or galactic distribution (see Fig. 2.4). This phenomenon traces back to the very early universe when photon pressure of overdense regions drove oscillations which continued until recombination, when the photons decoupled and the baryons were left as a shell around the original perturbation. The matter at the center of the perturbation and sound horizon served as gravitational seeds

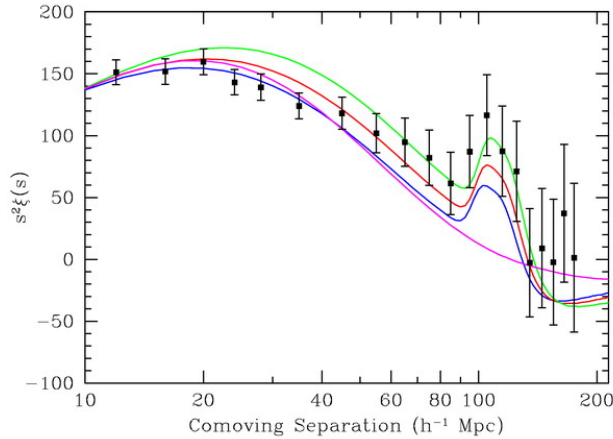


Figure 2.4: First observation of baryon acoustic peak in large scale correlation of sampled galaxies [46]. The amplitude of the peak at comoving separation of 100 Mpc/h constrains the baryonic abundance while the broad shoulder at smaller separation constrains the dark matter abundance. Models drawn include best-fit to only dark matter (magenta) and fixed baryonic matter with varying dark matter (green, red, blue).

for galaxy formation, which is reflected as a distance scale of 150 Mpc in today’s universe. The clustering observed in large scale structure stems from the same oscillations which gave rise to the acoustic peaks in the CMB power spectrum [2].

Because galaxy surveys target a small region of the sky in angle and redshift, the surveys complement each other. Baryon acoustic oscillation (BAO) surveys agree well with CMB-only fits to Λ CDM [47, 48, 49, 50, 51], providing marginal improvement in the uncertainty of the calculated parameters. They provide critical clarity when combined with other cosmological probes in constraining the dark energy equation of state and the total curvature.

2.2.3 Big Bang Nucleosynthesis

As the primordial universe expanded and cooled, there was a brief time window during which the light elements (up to beryllium) could be formed. These processes were sensitive to both the baryon density (high enough to provide sufficient probability of interaction) and the photon density (low enough to not break apart the newly-formed nuclei).

After the universe cooled to allow the quarks to combine into hadrons, weak interactions allowed free conversion between neutrons and protons controlled only by the mass difference. The expansion of the universe froze-out this conversion at $t \sim 1$ s or $T \sim 1$ MeV, but the instability of the deuterium nucleus (the first step of nucleosynthesis) required further cooling to $T \sim 0.1$ MeV before its formation could occur. By this time, the entry conditions had $n/p \sim 1/7$.

Because ${}^4\text{He}$ is the light element with the lowest binding energy per nucleon, big bang nucleosynthesis (BBN) resulted in a universe with most of the neutrons bound into helium, 75% ${}^1\text{H}$ and 25% ${}^4\text{He}$ (by mass). The remaining light element abundances ($\sim 0.01\%$ ${}^2\text{H}$, $\sim 0.001\%$ ${}^3\text{He}$, $\sim 10^{-10}$ lithium and beryllium) can fluctuate significantly depending on the initial conditions, and are thus probes of η , the baryon-to-photon ratio.

BBN can be directly probed by measuring the light element abundances in low metallicity (very old) stars. The deuterium abundance measurement provide the dominant constraint on η (see Fig.2.5). For measurements of other light element abundances, the error is dominated by systematics of the measurement (${}^4\text{He}$ and ${}^7\text{Li}$) or stellar nucleosynthesis (${}^3\text{He}$). The η value obtained from these measurements are in good agreement with that derived from CMB (measured independently from its effect on the damping tail of the power spectrum) except for ${}^7\text{Li}$, whose observed abundance is at least a factor of 2 lower than predicted.

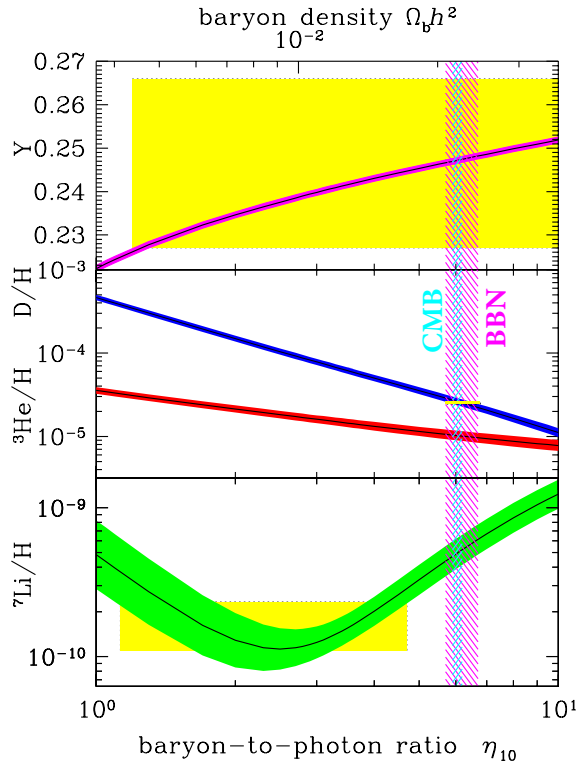


Figure 2.5: Light element abundances predicted by BBN and agreement with CMB observations [2]. The vertical bands represent the predicted baryon-to-photon ratio, η , from the CMB damping tail (cyan) and combined BBN from light element abundances (magenta). Deuterium abundance measurements drive the combined BBN η estimate as systematic uncertainties dominate the measurements of other isotopes. The light element abundance measurements agree for all isotopes except ${}^7\text{Li}$.

The agreement between CMB and BBN probes is significant because BBN is a probe of the universe at a much earlier time (~ 3 min) than the CMB ($\sim 400,000$ yr) [2].

2.2.4 Type Ia Supernovae

In order to determine the rate of expansion of the universe, astronomers must be able to map the distance and redshift of objects out to hundreds of megaparsecs from the Earth. The cosmic distance ladder is built up from objects with well-defined luminosity and spectra, particularly cepheid variables and type Ia supernovae. Measurement of type Ia supernovae enables a direct measurement of the Hubble constant, the rate of expansion of the universe.

The thermonuclear explosion which constitutes a type Ia supernova arises from mass accretion by a carbon-oxygen white dwarf from its binary companion until it reaches the Chandrasekhar mass. The brightness of the nova event makes them excellent probes out to $z \approx 1$ and the mechanism makes them a “standard candle.” Surveys of type Ia supernovae out to redshifts of ~ 1 by the Supernova Cosmology Project [52] and High- z Supernova Search Team [53] provided smoking gun evidence for an accelerating universe, necessitating a dark-energy dominated cosmological model (see Fig. 2.6).

The derived value of the Hubble constant from supernova observations alone is $H_0 = 72.0 \pm 3.0$ km/s/Mpc [54]. This value is in moderate tension with the best-fit of CMB-only data of 67.3 ± 1.2 km/s/Mpc [1, 2]. The discrepancy between these methods results in CMB data preferring a smaller dark energy fraction of the universe and correspondingly larger fractions of dark matter and baryons.

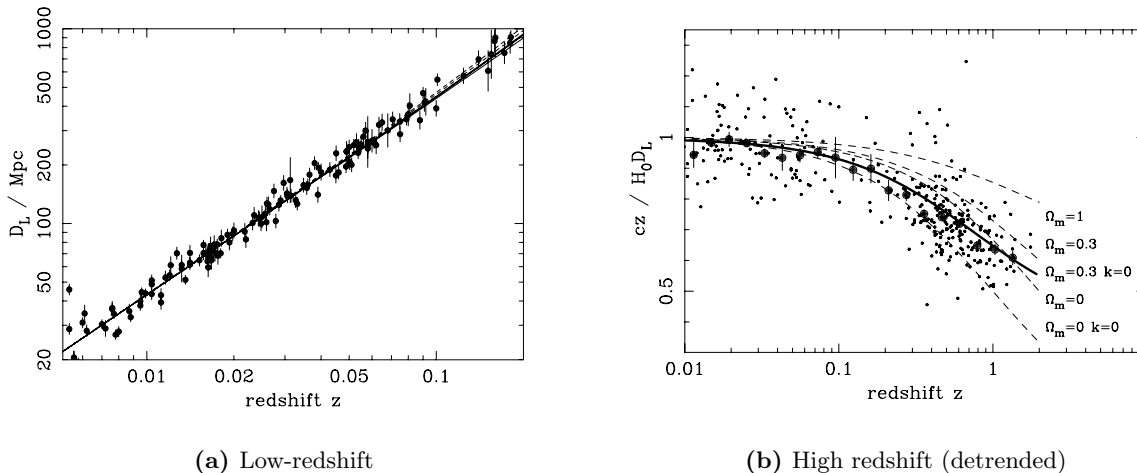


Figure 2.6: Observation of type Ia supernovae at low (left) and high (right) redshift [2]. The high redshift data has been detrended of the linear behavior to demonstrate its deviation from expected behavior in the absence of dark energy. The data is well modeled by including a dark energy component (solid line) comprising 70% of the universe.

2.3 Direct Observation

Given the abundance of dark matter in the universe, it should produce a signature capable of detection by direct astronomical observation. Mergers of galaxy clusters are a promising place to look because the aftermath of these collisions has the potential to have displaced the components from their equilibrium state. The observations can be made in different frequency ranges, and can also be analyzed for gravitational lensing to reveal how the luminous, gaseous, and matter regions behave differently as a result of the different forces experienced. Searches for such objects has thus far yielded inconclusive results.

An object commonly claimed to provide direct empirical proof of dark matter is 1E 0657-558, nicknamed the ‘Bullet Cluster.’ Observations of this object taken with X-rays and optical instruments reveal striking features when overlaid (see Fig. 2.7a). The Chandra X-ray observation shows the hot plasma clustered in the center, while the gravitational lensing inferred from the Hubble Space Telescope optical image places the mass of the cluster distributed on either side. The dark matter-driven explanation given is that we are viewing the aftermath of a collision, in which the dark matter and galaxies passed through each other and the plasma was impeded by electromagnetic interactions and became entangled in the center [55].



(a) Optical image of the 1E 0657-558, the ‘bullet cluster,’ from Magellan telescopes with overlay of the X-ray regions from Chandra (red) and mass regions inferred from Hubble (blue) [56].



(b) Optical image of Abell 520, the ‘train wreck cluster,’ from HST and CFHT with overlay of the luminous regions from CFHT (yellow), X-ray regions from Chandra (green), and mass regions inferred from Hubble (blue) [57].

Figure 2.7: Overlay images of the bullet cluster and the train wreck cluster. In both clusters, the luminous regions and X-ray regions have separated following the merger. In the bullet cluster the mass remained with the luminous regions, but in the train wreck cluster the mass regions inferred from lensing are separated from both the luminous and X-ray regions.

A counterexample is provided in the Abell 520, nicknamed the Train Wreck Cluster, another galaxy cluster resulting from a merger (see Fig. 2.7b). Observations with Chandra (X-ray) and the Canada-France-Hawaii Telescope (optical) indicated an unexpected mass distribution relative to the luminous regions, which were confirmed with the Hubble Wide Field Planetary Camera 2. In this merger, the luminous regions dominated by the galaxies have passed through unimpeded again, and the X-ray emitting plasma is impeded in the center, but the mass was also found to be concentrated in the center [58].

An analysis of all known cluster mergers with optical and X-ray data (including both the bullet and train wreck clusters) has demonstrated that the displacement of the mass, luminous, and X-ray regions is compatible with a dark matter explanation and in considerable tension with a no dark matter model [59]. Although the motion of the components of the train wreck cluster seem in contradiction to expectation, their behavior is consistent within statistical fluctuations. Simulations even suggest that existence of objects like the bullet cluster is consistent Λ CDM cosmology and new wider and deeper surveys may discover more candidate cluster mergers [60, 61].

2.4 Dark Matter Models

The magnitude of the “dark matter puzzle” has led to the proposal of a wide range of theoretical solutions. To clarify this zoo of explanations, a brief introduction to and counterargument of a few of the popular models is given here. These explanations range from modifying the laws of physics, known dark astronomical objects, Standard Model particles, and beyond the Standard Model physics.

2.4.1 Modified Physical “Laws”

As no particle has yet been measured which will satisfy the evidence as dark matter, many scientists have suggested an incomplete knowledge of the laws of physics as the explanation. Instead of building experiments to search for exotic particles, they turn to mathematical manipulations of existing physical laws to explain some of the observed signatures.

One of the oldest of these models is modified Newtonian dynamics, or MOND, first postulated by Mordehai Milgrom [62] in the 1980’s. In this model, the Newtonian force law is modified for small accelerations:

$$\mathbf{F} = m\mathbf{a} \times \mu(a/a_0) \tag{2.2}$$

$$\mu(x \gg 1) \approx 1, \quad \mu(x \ll 1) \approx x$$

This modification leaves terrestrial accelerations unchanged ($a_0 \approx 2 \times 10^{-10} m/s^2$ in the original formulation), but could have profound impact on orbital behavior on galactic scales. In this formulation, combining the rotational acceleration ($a = v^2/R$) with the modified gravitational acceleration ($a^2/a_0 = GM/R$) gives the desired flat rotational velocity curve for galaxies $v = \sqrt[4]{GMa_0}$. MOND has the additional benefit of

correctly predicting the ratio of the first two peaks of the CMB power spectrum *a priori*, but then has difficulty explaining the third peak amplitude (whereas Λ CDM is a model with enough flexibility in its six parameters to get the right answer, but without any justification for the parameter values).

Interest in MOND persists to the present day, with modifications such as Tensor-Vector-Scalar (TeVeS) making the theory fully relativistic [63]. A limitation that MOND-like theories will always have is in explaining observational unusual galaxy-cluster phenomena such as either the train wreck or bullet clusters, as they provide no method for separation of mass.

2.4.2 Baryonic Dark Matter

In the observations by Kapteyn and Oort of the solar vicinity, the discrepancy was largely attributed to astronomical objects which emit little or no radiation (*e.g.*, black holes and dwarf stars). These so called Massive Compact Halo Objects (MaCHOs) would not have appeared in any optical images, but could be distributed throughout the galactic halo to account for the unseen mass. Even for objects as small as $10^{-7} M_{\odot}$, these objects do produce a signature observable to microlensing experiments, so their concentration can be inferred from imaging distant objects through the halo. For larger white dwarfs of $\sim 1 M_{\odot}$, additional constraints come from D and ^4He abundance that must have been produced by the progenitor star [64]. Because of these constraints, many theorists would limit the possible contribution of MaCHOs or any baryonic dark matter candidate to be $< 1\%$.

2.4.3 Hot Dark Matter

Before embarking on a quest for unknown particles and objects to satisfy our need for dark matter, it is worthwhile to review the particle physics we already understand. A candidate particle ought to be neutral (or else we would have observed its interaction with photons) and not composed of quarks (or else it would alter BBN). A search within the standard model reveals the neutrino to be a tantalizing candidate for dark matter, the only particle which interacts only the weak and gravitational forces. Because of their small mass and interaction cross section, neutrinos in the early universe will travel at ultra-relativistic speeds and have a very long free-streaming length. Neutrinos are therefore classified as a candidate of “hot dark matter.”

Neutrinos as dark matter cause tension with cosmological observations because their long free-streaming length. In the CMB, they would be expected to smooth out the anisotropies, which places a bound on $\Omega_{\nu} < 1.5\%$. In terms of large scale structure, they would again smooth out clumpsiness and force structure to form top-down, which is in tension with the observation that our galaxy is older than the Local Group.

2.5 Beyond Standard Model Particles

In the absence of acceptable explanations of dark matter within the Standard Model framework, theories have expanded the search to invoke new physics. The particles investigated (see Fig. 2.8) are beyond the scope of the Standard Model of particle physics, but are theoretically-motivated to answer some of the open questions of the field.

A complete treatment of all these candidates is best left to a more theoretical discussion [65], so this discussion will only focus on candidates being tested by current experiments. The two candidate particles, axions and weakly interacting massive particles, are also among the most strongly theoretically motivated dark matter candidates.

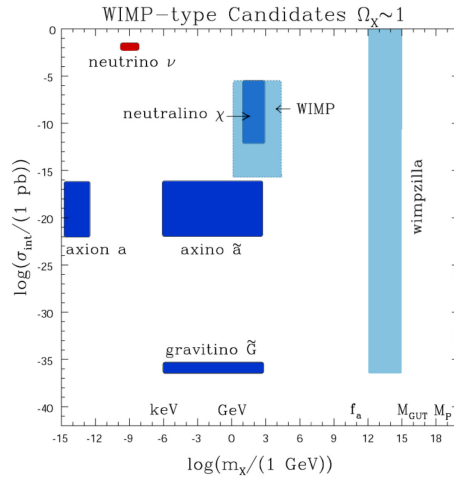


Figure 2.8: Parameter space illustrating some of the theoretically-motivated weakly interacting dark matter candidates [66].

2.5.1 Axions

Axions are a theoretical particle that come about as a consequence of a new symmetry proposed in 1977 by Peccei and Quinn as a solution to the strong-CP problem in quantum chromodynamics [67]. This proposed symmetry gives rise to a light pseudoscalar boson as predicted by Weinberg [68] and Wilczek [69] (who gave the axion its name).

Experimental attempts to search for axions focus mainly on helioscopes and microwave cavities, with each having sensitivity to different sub-eV mass ranges (see Fig. 2.9). The best limits for helioscopes come from the CAST experiment, probing model space for axion masses from 0.1–1 eV [70]. The best limits

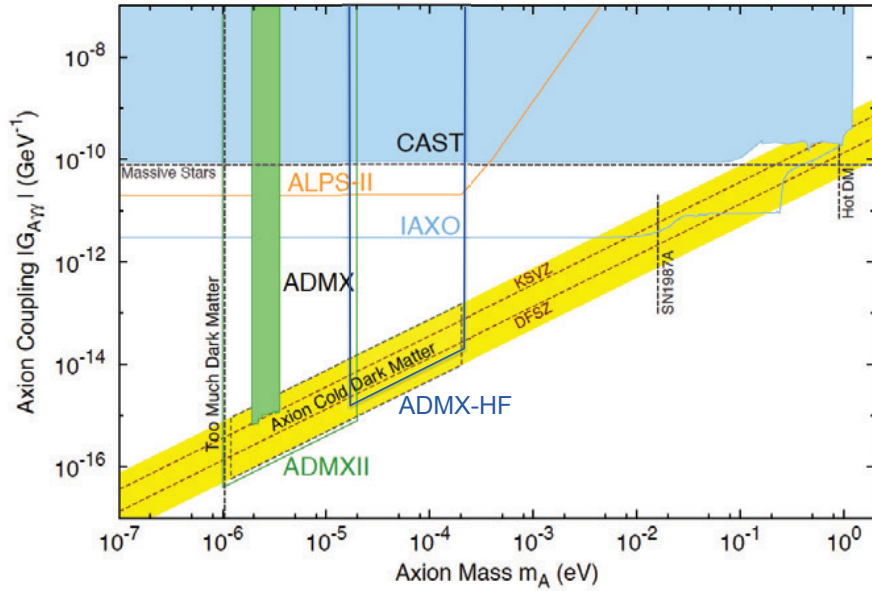


Figure 2.9: Axion parameter space tested by current and future experiments [72]. The yellow band is the theoretical prediction for any Peccei-Quinn axions, while axion dark matter candidates are theorized to be of lighter mass (< 1 meV). Much of the allowed parameter space will be tested by next generation experiments ADMXII, ADMX-HF, and IAXO.

for microwave cavities come from the ADMX experiment, probing model space for axion masses from $3.3\text{--}3.5\ \mu\text{eV}$ [71]. Next generation experiments ADMXII, ADMX-HF [72], and IAXO [73] seek to cover much of the preferred axion parameter space.

2.5.2 Weakly Interacting Massive Particles

Experimental limitations force any experiment to choose which dark matter particle and mass range it will have sensitivity to, so the remainder of this thesis will focus on ‘weakly interacting massive particles’ (WIMPs) as its dark matter candidate. The WIMP is a product of new physics at the weak scale, and so its predicted mass lies is of order $m_{weak} \sim 10\ \text{GeV} - 1\ \text{TeV}$.

Early interest in WIMPs was partly fueled by the elegance of the “WIMP miracle” argument for its production. The flexibility of production via the WIMP miracle yields numerous theoretical models which generate WIMP-like candidate particles, with supersymmetry (the neutralino) and extra dimensions (Kaluza-Klein dark matter) being the most commonly cited. The predicted signatures of WIMP dark matter are tantalizing close to the discovery thresholds of direct detection, indirect detection, and collider searches [65].

2.5.2.1 WIMP Miracle – Thermal Freeze-Out Relic

If WIMPs exist and are stable, they could have been naturally produced as a thermal relic by freeze-out as the universe expanded and cooled (see Fig. 2.10). The evolution of the number density of thermal relic particles (n_χ) is governed by the Boltzmann equation:

$$\frac{dn_\chi}{dt} = -3Hn_\chi - n_\chi^{eq}n_{\bar{\chi}}^{eq} \langle \sigma_{\chi\bar{\chi}\leftrightarrow q\bar{q}}v \rangle \left(\frac{n_\chi n_{\bar{\chi}}}{n_\chi^{eq}n_{\bar{\chi}}^{eq}} - \frac{n_q n_{\bar{q}}}{n_q^{eq}n_{\bar{q}}^{eq}} \right) \quad (2.3)$$

where $H = \dot{a}/a$ is the Hubble parameter, n^{eq} is the thermal equilibrium dark matter number density, and $\langle \sigma_{\chi\bar{\chi}\leftrightarrow q\bar{q}}v \rangle$ is a thermally averaged annihilation cross section to a specific standard model particle (q) times velocity. Making the assumption that dark matter is in particle-antiparticle equilibrium, and that the standard model particles are being repopulated through other channels so $\frac{n_q n_{\bar{q}}}{n_q^{eq}n_{\bar{q}}^{eq}}$ is approximately unity, the Boltzmann equation simplifies to:

$$\frac{dn_\chi}{dt} = -3Hn_\chi - \langle \sigma_A v \rangle (n_\chi^2 - (n_\chi^{eq})^2) \quad (2.4)$$

The first term ($-3Hn_\chi$) accounts for dilution by expansion of the universe, while the second term ($\langle \sigma_A v \rangle (n_\chi^2 - (n_\chi^{eq})^2)$) has been summed over all channels to account for dark matter annihilation to SM particles (n_χ^2) and SM particle annihilation to thermal relics ($(n_\chi^{eq})^2$).

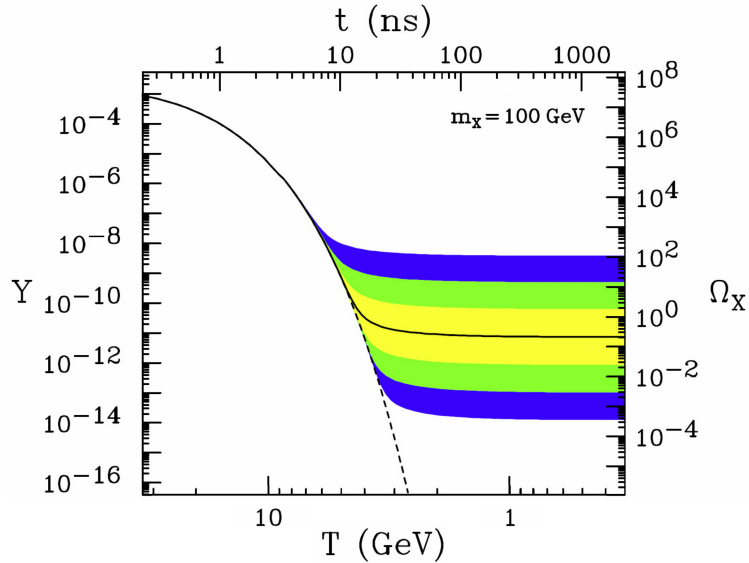


Figure 2.10: The comoving number density Y (left) and resulting thermal relic density (right) of a 100 GeV thermal relic as a function of temperature T (bottom) and time t (top) [65]. The solid contour is for an annihilation cross section that yields the correct relic density, and order-of-magnitude differences in cross section are shaded. The dashed contour is the number density of a particle that remains in thermal equilibrium.

As the universe expands and dilutes the thermal relic number density, the second term of the Boltzmann equation becomes vanishingly small and so thermal relic annihilations effectively cease, causing the number of thermal relic particles to “freeze out.” With a constant number of thermal relic particles, it is more instructive to think of the comoving thermal relic density (Y_χ , with the thermal relic density normalized by the entropy density) or thermal relic contribution to the mass-energy of the universe (Ω_χ). Solving the Boltzmann equation gives:

$$\Omega_\chi \sim \frac{x_f T_0^3}{\rho_c M_{Pl}} \langle \sigma_{Av} \rangle^{-1} \quad (2.5)$$

where x_f is the ratio of the thermal relic mass to freeze-out temperature, T_0 is the present temperature of the universe, ρ_c is the critical density (=1 for a flat universe), and M_{Pl} is the Planck mass. The thermal relic density is therefore insensitive to its mass, and inversely proportional to its annihilation cross section $\langle \sigma_{Av} \rangle$. If a thermal relic particle is the sole contributor to the dark matter mass-energy of the universe, then $\langle \sigma_{Av} \rangle \approx 10^{-26} \text{ cm}^3 \text{ s}^{-1}$. Since the cross section of weak interactions scales as α^2/m_χ^2 , this implies a particle with a mass of $\sim 100 \text{ GeV}$.

2.5.2.2 Prospects for WIMP Detection

Any interaction of dark matter can be imagined as an initial and final state each with two particles. Assuming a conserved quantum number preventing dark matter decay into standard model particles, two of these states must involve the dark matter and two involve a standard model particle. There are three unique permutations of this interaction corresponding to collider production, indirect detection, and direct detection, as depicted in (see Fig. 2.11). Because these different search techniques probe different observables of dark matter, the parameter space may be explored in an orthogonal and complementary way (see Fig. 2.12).

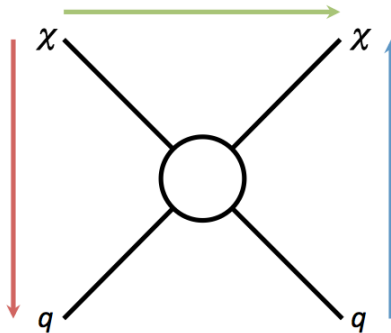


Figure 2.11: Possible interactions of dark matter (χ) with standard model particle (q). Three unique permutations of the interaction exist indicated by arrows for collider production (red), indirect (blue), and direct (green).

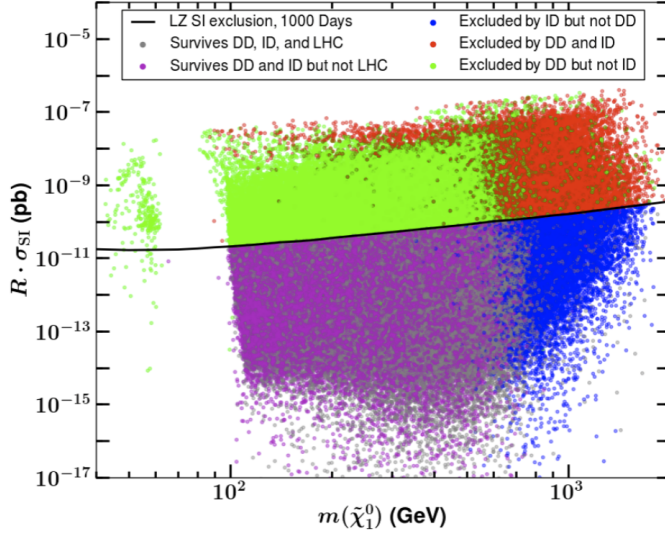


Figure 2.12: Sensitivity of different search techniques to pMSSM (phenomenological minimal supersymmetric standard model) WIMPs [74]. A combination of collider, direct, and indirect experiments results in an increased total sensitivity to dark matter models because of the complementarity of the search techniques.

Collider searches have the cleanest signal at lepton colliders, where a mono-jet ($\chi\bar{\chi}j$) or mono-photon ($\chi\bar{\chi}\gamma$) signal can be looked from jet or photon production by initial state radiation. At hadron colliders like the LHC and Tevatron, the mono-jet and mono-photon signals are obscured because the quarks do not have a definite initial energy. Instead, an indirect signal is looked for via jets with missing energy following pair production of dark matter [75, 76, 77].

Indirect searches target unexplained excess production of particles coming from dark matter pair annihilation. Even though the rate of dark matter annihilation has diminished to the point it has no significant impact on the total number density, we may still observe signatures of annihilation from regions of higher local density such as the galactic center or the sun. Indirect searches with neutrinos (*e.g.*, Super-K) and photons (*e.g.*, Chandra, XMM-Newton, Fermi) can provide pointing information if a discovery is made. Searches for positron or antiproton (*e.g.*, PAMELA, Fermi, AMS-02) excesses look for a spike in the energy spectrum characteristic of pair production-annihilation $\chi\bar{\chi} \rightarrow e^+e^-$ or $\chi\bar{\chi} \rightarrow p\bar{p}$. The sensitivity of these search techniques to dark matter is dependent on the couplings to quarks and leptons and decay channels, leaving flexibility in the interpretation of any single measurement.

Indirect dark matter searches have returned interesting results for dark matter particle masses from keV to TeV scales. A line feature at 3.5 keV in single [78] and stacked [79] galaxy analysis from XMM-Newton and Chandra X-ray observatories suggests a possible decay of 7 keV sterile neutrinos. An excess in the positron fraction above 10 GeV, first measured by the PAMELA satellite in 2009 [80] and further

confirmed and extended by Fermi-LAT [81] and AMS-02 [82], allows interpretation of TeV-scale decaying or annihilating dark matter as well as millisecond pulsars [83, 84]. An excess in the gamma ray spectrum around 2 GeV from an extended region near the galactic center measured by Fermi [85] could arise from dark matter annihilations of mass 10–50 GeV [86, 87, 88]. Fermi-LAT has also observed a $3.3\text{-}\sigma$ bump in its galactic center data centered at 133 GeV with low global significance and inconsistent with expectation of the instrument response [89]; further data has lowered the significance of the excess [90]. While these signals present tantalizing hints, without further confirmation they lack clear interpretation as dark matter.

Direct searches rely on the dark matter particles coming to us and depositing energy through an interaction inside the detector. They are discussed in greater detail in the next chapter.

Limits obtained from indirect dark matter searches provide a more direct probe of the thermal relic cross section of the WIMP miracle (see Sect. 2.5.2.1), with the dwarf spheroidal searches by Fermi-LAT constraining WIMP dark matter for masses below 100 GeV [91]. Both indirect and collider searches provide stronger limits than direct searches for spin-dependent WIMP couplings and spin-independent WIMP couplings (see Sect. 3.2) for low-mass WIMPS [75, 76, 77, 92]. Significant allowance for model dependence must be made when comparing these calculations.

Chapter 3

Direct Detection WIMP Searches

Standard galactic models of dark matter predict a ‘WIMP halo’ extending throughout the galaxy, with Earth’s motion through the galaxy drawing it through this halo and providing a consistent flux of WIMPs to terrestrial detectors. Monolithic direct detection dark matter experiments have been built to search for the rare WIMP interactions, with different target nuclei providing better sensitivity for different scattering models. These experiments utilize a suite of techniques to optimize their rejection of all backgrounds in order to definitively identifying the dark matter signal of interest. This chapter frames the scientific goals of the DM-Ice experimental program within the current field tension between the positive signal claim of the DAMA experiment and exclusion limits of many others.

3.1 Galactic WIMP Dynamics

The expected signal observed in direct detection dark matter detectors is dependent on the dynamics of WIMPs in the local region of the galaxy. These local astrophysical WIMP parameters, including the density and velocity distribution, are constrained by a combination of halo simulations and extrapolation from stellar observations. Since both the event rate and energy spectrum of direct detection experiments are impacted by these astrophysical parameters, a common set of standard values are assumed to achieve a relatively model-insensitive comparisons of experimental results.

WIMPs are known to be distributed throughout the galaxy in order to match the observed effects on galactic rotation, with the standard assumption of an isothermal spherical WIMP halo with local WIMP density of $\rho_0 = 0.3 \text{ GeV/cm}^3$. Recent analyses have estimates varying over $0.23\text{--}0.47 \text{ GeV/cm}^3$, with preference for a value closer to 0.4 GeV/cm^3 after accounting for enhancements near the disk [93, 94, 95]. Large uncertainty remains in the shape of the halo profile towards the galactic center, which can significantly impact indirect searches, but the local density can be derived independent of this error [96].

The velocity (v) of the WIMPs is assumed to follow a non-rotating Maxwell-Boltzmann distribution:

$$f(v) = Nv^2 \exp\left(-\frac{v^2}{v_0^2}\right) \quad , \quad (3.1)$$

where v_0 is the most probable speed. It is typically assumed to 220 km/s ($v_{rms} = 270$ km/s) to match the International Astronomical Union's value for galactic disk rotation [97], although recent analyses prefer higher values by 5–20% [98, 99]. The velocity distribution is truncated at the escape velocity of $v_{esc} = 544$ km/s, determined by measurements of high velocity stars in the Milky Way [100].

3.2 WIMP Interactions

The signal of a direct detection experiment is the recoil energy (E_r) deposited as the WIMP scatters off a target nucleus in the detector. Under the assumption of elastic scattering, the recoil energy may be solved kinematically:

$$E_r = \frac{m_\mu^2 v^2}{m_n} (1 - \cos \theta) \quad , \quad (3.2)$$

where v is the velocity of the WIMP relative to the nucleus, θ is the scattering angle in the center-of-mass frame, and m is a mass term for the WIMP (χ) or target (n). The WIMP-target reduced mass, $m_\mu = (m_\chi m_n)/(m_\chi + m_n)$, conveniently simplifies the above relation.

Because the WIMPs are not mono-energetic, but follow a Maxwell-Boltzmann distribution of velocities, it is necessary to integrate over this distribution. The differential rate (dR/dE_r) of WIMP elastic scatterings off nuclei in the detector is given by:

$$\frac{dR}{dE_r} = N_n \frac{\rho_0}{m_\chi} \int_0^{v_{esc}} d\mathbf{v} f(\mathbf{v}) v \frac{d\sigma}{dE_r} \quad (3.3)$$

where N_n is the number of target nuclei in the detector, ρ_0 is the local WIMP density, $d\sigma/dE_r$ is the WIMP-nucleus differential cross section, and v_{esc} is the escape velocity of WIMPs in the galaxy. The parameters of WIMP density and velocity are determined from astrophysics (see Sect. 3.1). The velocity distribution, $f(\mathbf{v})$, must be modified from the rest-frame Maxwell-Boltzmann to include the sun's rotation about the galactic center, the sun's peculiar velocity with respect to the disk rotation, and Earth's rotational velocity about the sun (see Sect. 3.3.2).

The scattering rate of Eqn. 3.3 provides no consideration of instrumental effects. A lower integration limit can be imposed because any physical detector will have an energy threshold (E_{th}) below which it does not trigger and collect signals. This minimum velocity (v_{min}) can be derived from maximizing Eqn. 3.2 when $\cos \theta = -1$:

$$v_{min} = \sqrt{\frac{m_T E_{th}}{2m_\mu^2}} \quad . \quad (3.4)$$

Real detectors must also consider the trigger efficiency, which is typically a rapidly varying function near the energy threshold.

The particle physics of WIMP-nucleus scattering enters Eqn. 3.3 in the final term, the scattering cross section ($d\sigma/dE_r$). The most common WIMP models (*e.g.*, SUSY) predict the cross section will be dominated

by scalar (spin-independent) and axial-vector (spin-dependent) couplings. The differential cross section is most often written in terms of the momentum transfer, q ($q^2 = 2m_T E_r$), with both spin-independent and spin-dependent terms. To leading order, it is:

$$\frac{d\sigma}{dq^2}(q^2, v) = \frac{1}{4\mu^2 v^2} (\sigma_{SI}^0 F_{SI}^2(q) + \sigma_{SD}^0 F_{SD}^2(q)) \Theta(q_{max} - q) \quad (3.5)$$

where σ_{SI}^0 (σ_{SD}^0) is the zero momentum transfer spin-independent (spin-dependent) cross section, $F^2(q)$ is the appropriate form factor, and Θ is the Heaviside step function. The presence of the form factor in Eqn. 3.5 accounts for the finite size of the nucleus; $F^2(q) \approx 1$ for small momentum transfer, but decreases as the de Broglie wavelength of the momentum transfer becomes comparable to the size of the nucleus [101].

Target nuclei have different sensitivity to spin-independent and spin-dependent scattering depending on the nuclear spin and number of nucleons. Different experiments therefore select target nuclei to enhance one or both of these interactions [102].

3.2.1 Spin-Independent Scattering

The spin-independent, or scalar, coupling arises from coherent scattering of a WIMP with the nucleus. This provides a critical enhancement to the cross section with increasing target nucleus mass (number of nucleons):

$$\sigma_{SI}^0 = \frac{4m_\mu^2}{\pi} (Zf_p + (A - Z)f_n)^2 \quad (3.6)$$

where Z ($A - Z$) is the number of protons (neutrons) and f_p (f_n) is the effective coupling to the proton (neutron). The most basic models will typically assume that $f_p = f_n$, which simplifies the spin-independent cross section to $\sigma_{SI}^0 \propto A^2$. In attempts to penalize reconcile experimental results, suggestions of $f_n = -0.7f_p$ have been used to remove spin-independent sensitivity from heavier nuclei (Xe-based experiments currently providing leading sensitivity).

The form factor describing the dependence on momentum transfer may be reduced with reasonable accuracy to an exponential form:

$$F(q) \approx e^{-q^2/q_0^2} \quad (3.7)$$

where q_0 is related to the size of the nucleus.

The combined effect of Eqn. 3.6 and Eqn. 3.7 is that all target nuclei show a similar exponential spectrum, but with normalizations defined by the A^2 enhancement favoring xenon (see Fig. 3.1). However, the exponential penalty for large momentum transfer affects xenon the most strongly causing its spectrum to fall off more quickly. The current generation of direct detection experiments places greater emphasis on spin-independent interactions because the A^2 enhancement allows them to probe more extreme cross sections. [103]

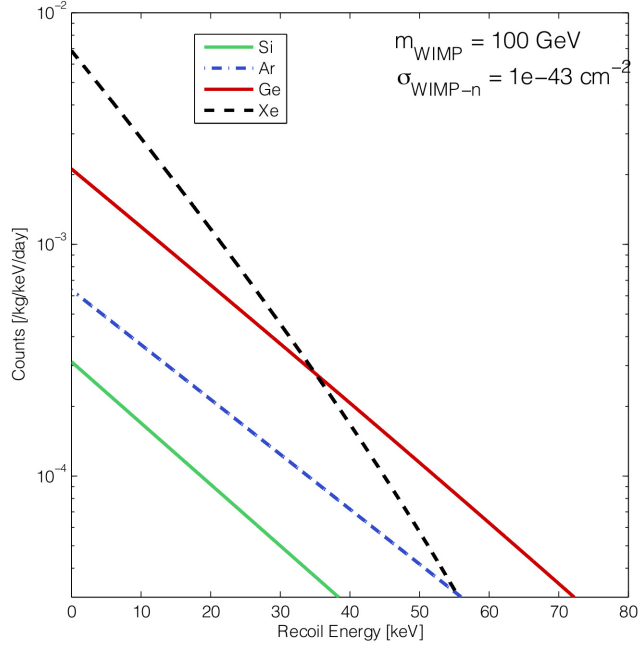


Figure 3.1: Differential WIMP recoil spectrum for four illustrative target nuclei based on a WIMP mass of 100 GeV and a WIMP-nucleon cross section $\sigma = 10^{-43} \text{ cm}^2$ [102]. All targets exhibit an exponential spectrum, with xenon enjoying the largest low-energy rate due to the A^2 cross section enhancement.

3.2.2 Spin-Dependent Scattering

The spin-dependent, or axial-vector, coupling arises from interaction of a WIMP with the total spin of the nucleus:

$$\sigma_{SD}^0 = \frac{32m_\mu^2 G_F^2}{\pi} J(J+1)\Lambda^2 \quad (3.8)$$

where G_F is the Fermi constant, J is the total spin of the nucleus, and

$$\Lambda \equiv \frac{1}{J} (a_p \langle S_p \rangle + a_n \langle S_n \rangle). \quad (3.9)$$

Here $\langle S_p \rangle$ ($\langle S_n \rangle$) is the average spin contribution from the proton (neutron) group. and a_p (a_n) is the effective coupling to the proton (neutron). Many models allow a_p and a_n to differ by a factor of a few, making a simplification similar to the spin-independent case impossible.

For many models, the spin-dependent coupling to a proton is larger than the spin-independent ($\mathcal{O}(10^2 - 10^4)$ for a MSSM neutralino), but the spin-independent scattering will still dominate. The spin-independent scattering is greatly enhanced A^2 factor. The spin-dependent scattering must rely on $\mathcal{O}(1)$ $\langle S_p \rangle$ and $\langle S_n \rangle$ terms, and often suffers from the presence of some isotopes with zero spin [101].

Since the form factor again punishes large momentum transfer, it is advantageous to select a light nucleus with nuclear spin. Flourine is a commonly used target for spin-dependent work because, ^{19}F has $\sim 100\%$ natural abundance, is low-mass (high spin/mass ratio), and forms a variety of molecules with carbon. [103]

3.2.3 Inelastic Dark Matter

Inelastic dark matter provides a modification to the above treatment should elastic scattering be impossible for the dark matter. It was first suggested to resolve the tension between a positive claim (DAMA) and the claimed exclusion of that result by another (CDMS) [104].

This model posited a doublet of WIMP states, χ_- and χ_+ , where χ_+ is slightly heavier by a mass splitting δ . If scattering is only allowed for χ_- upscattering into the χ_+ state, an additional kinematic constraint is imposed on the WIMP interactions:

$$\delta < \frac{\beta^2 m_\chi m_n}{2(m_\chi + m_n)} \quad , \quad (3.10)$$

where m_n and m_χ are the masses of the target and WIMP. This constraint increases the minimum considered WIMP velocity (v_{min}) of Eqn. 3.4 to:

$$v_{min} = \frac{1}{\sqrt{2m_n E_{th}}} \left(\frac{m_n E_{th}}{m_\mu} + \delta \right) \quad , \quad (3.11)$$

where E_{th} is the energy threshold and m_μ is the WIMP-target reduced mass.

The effect of inelastic dark matter was to penalize lighter targets by increasing the minimum velocity to produce detectable signals and thereby reducing the total event rate. With the increasing sensitivity of experiments with high-mass xenon targets, the simple models of inelastic dark matter have been excluded.

3.3 Search Techniques

When energy is deposited in a detector, it can be read out as one of three types of signals - light, charge, or heat. The light signal is available in scintillators (inorganic crystals and noble gases in dark matter searches), transparent materials whose band structure (for crystals) or molecular states (for liquids) allows the excitations to emit photons, and receives typically $\mathcal{O}(1)\%$ of the deposited energy. The charge signal is available in materials with impurity densities small enough to permit charges to be drifted long distances (semiconductors, noble gases, and gaseous detectors), and receives typically $\mathcal{O}(10)\%$ of the deposited energy. The remainder of the deposited energy is directed into elementary excitations which can be read out as heat by bolometers, this requires the detectors to be cryogenically cooled to eliminate thermal noise interference. Experiments take advantage of all possible signal channels, often combining two (see Fig. 3.2), as the field presses towards ever-increasing sensitivity.

The challenges of definitively attributing a signal to dark matter for a direct detection experiment include the non-unique spectral form (exponential to low energy, see Fig. 3.1) and the very low count rate. The

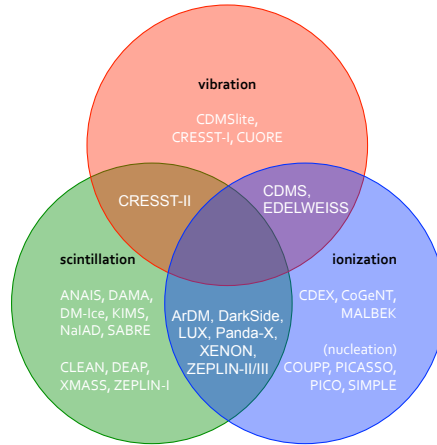


Figure 3.2: Different signals collected by major dark matter experiments. Experiments collecting multiple signals can employ recoil type identification to reduce the background rate.

exponential spectrum forces experiments to examine the lowest-energy region where threshold and detector effects may be poorly understood and calibration is most difficult.

Experiments increase their sensitivity by exploiting expected features of the dark matter signal from both particle physics and astrophysics. Particle interactions predict that dark matter should scatter off the nucleus (as opposed to the electron cloud) giving a specific energy signature. The astrophysical model of the dark matter distribution predicts an anisotropy in the WIMP arrival direction from solar motion through the galaxy and rate modulations from the earth’s orbit and rotation.

3.3.1 Recoil-Type Identification

When an incident particle scatters off an atom, this can be do either to an interaction with the nucleus (a ‘nuclear recoil’) or the electron cloud (an ‘electron recoil’). The type of recoil causing the scattering will effect the rate and ratio of energy deposited into each of the three signal channels. Electron recoils are typically dominant when the interaction is electromagnetic, namely for charged particles (*e.g.*, α ’s, β ’s, μ ’s) and photons. For neutral particles without electromagnetic interactions (*e.g.*, neutrons and WIMPs), the reduced mass (m_μ term) of the cross section (see Eqn. 3.6 and Eqn. 3.8) suppresses scattering off the electron cloud, resulting in a nuclear recoil.

Recoil-type identification is a powerful tool to constrain backgrounds, because the dominant intrinsic radioactive contaminants (ubiquitous ^{40}K and ^{232}Th -, ^{235}U -, and ^{238}U -chains, as well as specific radioactive isotopes of the target material) produce mostly γ (or X-ray) and β radiation in the low-energy region of interest (ROI). An effective discrimination of electron-recoils in a detector limits the backgrounds to rarer neutrons, typically from heavy-element fission or spallation by alphas or muons. Additionally, α and μ events

may possess a unique pulse signal shape because their stopping power (dE/dx) is different from electrons; understanding these backgrounds at higher energy can improve the simulated expected spectrum in the ROI.

Discrimination between the recoil types can be achieved by any detector with two different measurements of energy deposition. This is most effectively employed in detectors which measure more than one signal channel (see Fig.3.2), where one channel is used as the energy calibration and discrimination power is achieved in a multi-variate space (see Fig. 3.3). In detectors which only measure one channel, discrimination is still possible through pulse-shape discrimination (PSD, *i.e.*, analyzing the timing structure of the signal readout).

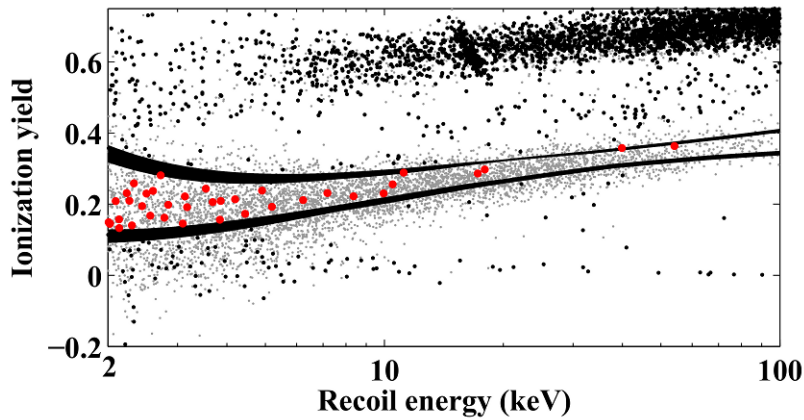


Figure 3.3: Recoil-type identification to define signal band (outlined in black) and reject backgrounds for CDMS detectors [105]. Large red dots are WIMP candidate events, black dots are rejected events, and gray shows neutron calibration points.

3.3.2 Annual Modulation

Since the modeled WIMP halo is non-rotating, the velocity of a target nuclei in the detector (\mathbf{v}_n) causes a shift in the Maxwell-Boltzmann velocity distribution of the WIMPs (Eqn. 3.2 has dependence on the relative WIMP velocity):

$$\mathbf{v}_n = \mathbf{v}_{disk} + \mathbf{v}_{sun} + \mathbf{v}_{orb} + \mathbf{v}_{rot} \quad (3.12)$$

where $v_{disk} = 220$ km/s is the galactic disk rotation speed, $v_{sun} = 18$ km/s is the sun's peculiar velocity relative to the disk, $v_{orb} = 29.8$ km/s is the earth's orbital speed, and v_{rot} is the earth's rotational speed at the location of the detector (0–0.46 km/s). This equation can be simplified (see Fig. 3.4) by ignoring the small effect of v_{rot} , and combining the remaining terms into a constant and a time-varying velocity:

$$v_n = v_S + v_{orb} \cos(\omega(t - t_0)) \cos(\theta). \quad (3.13)$$

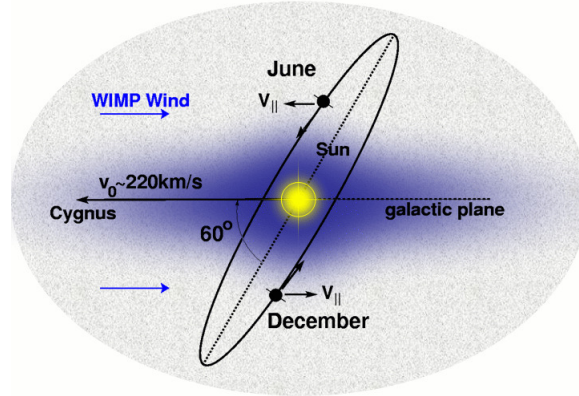


Figure 3.4: Illustration of Earth’s relative velocity to WIMP wind giving rise to annual modulation in dark matter signal [106].

Here there is a “WIMP wind” coming from the constellation Cygnus from the Sun’s reference frame (v_S , combining v_{disk} and v_{sun} terms from Eqn. 3.12, taken to be equal to $v_{disk} = 220$ km/s in most analyses). This is modified by the orbital velocity of Earth (v_{orb}), but only the component in the plane of the galactic motion is relevant ($\cos(\theta)$, where $\theta = 60^\circ$). The orbital velocity contribution modulates throughout the year ($\cos(\omega(t - t_0))$ with 1 yr period ($\omega = 2\pi/365.25$ day) and June 2 phase ($t_0 = 152.5$ days).

This relative velocity produces a varying shift in the Maxwell-Boltzmann velocity distribution for the WIMPs, which in turn changes the recoil spectrum. This shifted distribution gives rise to an approximately sinusoidal variation in the detected WIMP signal ($S(t)$) throughout the year:

$$S(t) = S_0 + S_m \cos(\omega(t - t_0)) \quad (3.14)$$

where S_0 is the average WIMP signal, and S_m is the modulation amplitude. The modulation amplitude can be approximated as the ratio of velocities in Eqn. 3.13:

$$S_m \approx \frac{v_{orb} \cos(\theta)}{v_S} = 0.07. \quad (3.15)$$

3.3.3 Directional Sensitivity & Diurnal Modulation

Also as a result of the effective “WIMP wind” mentioned above in Sect. 3.3.2, the nuclear recoils caused by WIMP scattering events in a detector will not be isotropic, but should have a preferred direction (see Fig. 3.5). The laboratory measurement of this effect will be convoluted with the diurnal modulation from the Earth’s rotation about its axis, so every event trajectory must be converted out of the lab frame into the galactic frame.

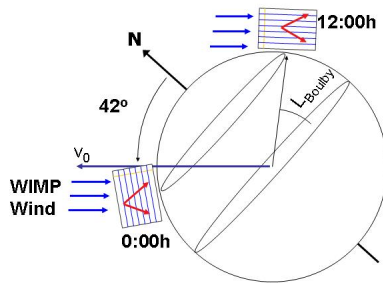


Figure 3.5: Illustration of diurnal variation in preferred recoil direction of WIMP scatters at the location of the Boulby mine in England [106].

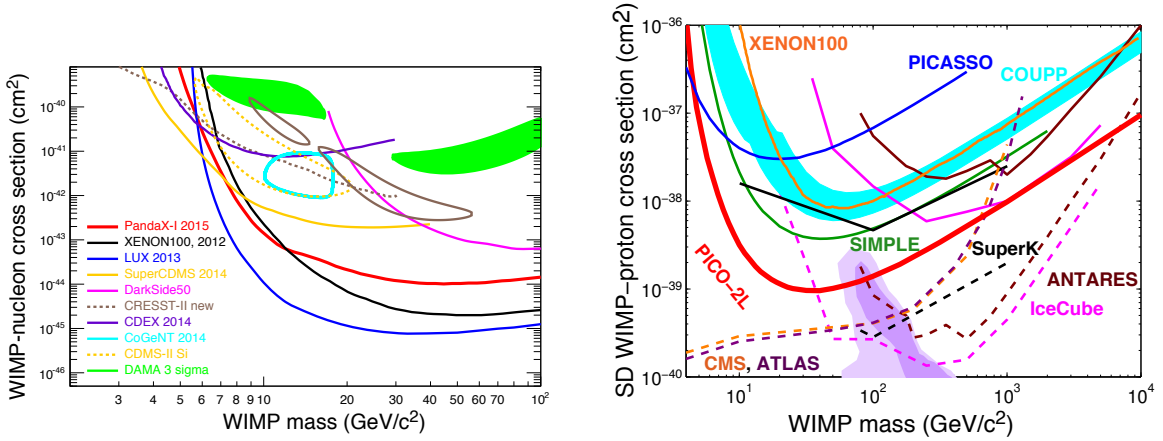
Because the WIMP scatters are not necessarily head-on, the scattering will smear the effect somewhat, and the directional preference must be reconstructed statistically. The annual velocity modulation discussed in the previous section will also slightly sharpen or reduce the scattering anisotropy.

3.4 Status of Current Experimental Searches

The past decade has seen an explosion in the type, number, and scale of direct detection dark matter experiments. This has been accompanied recently by a building controversy as several experiments (using different target nuclei and technologies) have released claims for excesses of signal over known background, with possible interpretation as WIMP signals. These claims are in tension with the leading exclusion limits from other experiments, prompting reanalysis of data sets and discussion into experimental systematics.

The signal claims come from the DAMA (NaI(Tl)), CoGeNT (Ge PPC), CRESST-II (CaWO₄), and CDMS (cryogenic Si) experiments. Although the signal claims do not all overlap under the basic WIMP assumptions, they do all point to a low-mass (~ 10 GeV) WIMP as shown in Fig. 3.6a. This has refocused the emphasis of new experiments in the field towards lowering energy thresholds and understanding low-energy effects in order to gain sensitivity to the preferred parameter space.

In the spin-independent parameter space, the traditional goal was to drive to lower cross-sections at ~ 100 GeV (a typical supersymmetric WIMP mass), requiring extreme background rejection through recoil-type identification. Cryogenic semiconductors (CDMS and EDELWEISS) had led the field by this benchmark until overtaken in 2011 by dual-phase liquid xenon detectors (XENON and LUX). Investigation of the low-mass signal anomalies has shifted the emphasis to lowering the energy threshold even at the cost of higher background, and opened the field to a wide variety of new technologies including germanium PPCs, bubble chambers, and silicon CCDs.



(a) The spin-independent WIMP parameter space showing preferred regions for CDMS-Si, CoGeNT, CRESST, and DAMA experiments, as well as exclusion limits of LUX, XENON100, PandaX, SuperCDMS, and other experiments [11].

(b) The spin-dependent WIMP parameter space showing exclusion limits from COUPP, PICASSO, PICO, SIMPLE, and XENON100 direct detection experiments, as well as model-dependent limits from indirect and collider searches [107].

Figure 3.6: Current exclusion limits on WIMP parameters in cross section-mass parameter space for spin-independent (a) and spin-dependent (b) scattering.

In the spin-dependent parameter space, not all targets have the nuclear spins required for sensitivity (since many experiments focused on A^2 gains in spin-independent results when choosing targets). The initial lead was held by inorganic scintillators (NaI in DAMA and CsI in KIMS), but this has given way over the last five years to bubble nucleation experiments (PICO, COUPP, PICASSO, and SIMPLE). Difficult to compare because of their model-dependent nature, the limits from indirect and collider searches allow for more stringent limits in spin-dependent parameter space.

The current direct detection experiments are summarized in Tab. 3.1 and discussed in detail in the following sections.

3.4.1 Semiconductor Detectors

Semiconductor detectors have been an attractive technology for the field of dark matter on account of their excellent energy resolution of the ionization signal and mature purification and fabrication processes allowing low intrinsic background. Since the early 1990's, germanium detectors have contributed to the search for dark matter, utilizing detectors from neutrinoless double beta-decay experiments (IGEX and Heidelberg-Moscow) as well as newly fabricated detectors (COSME and CDMS). Semiconductor detectors

Table 3.1: List of current direct detection experiments and future plans.

Technology	Current Generation	Location	Status (Sensitive Mass)	Future
Semiconductor Detectors				
Cryogenic Ge	SuperCDMS	Soudan, USA	running 9.3 kg [12]	SuperCDMS-SNOLAB (200 kg)
	CDMSlite	Soudan, USA	collected 6 kg-day [108]	
	EDELWEISS-III	Modane, France	running 29 kg [109]	EURECA (with CRESST)
Ge PPC	CoGeNT	Soudan, USA	running 440 g [16]	C-4 (~ 5 kg) [110]
	MALBEK	Kimballton, USA	running 455 g [111]	
	CDEX-1	Jinping, China	running 994 g [112]	CDEX-10 (~ 10 kg) [113]
Si CCD	DAMIC@SNO	SNOLAB, Canada	running 5 g [114]	DAMIC100 (~ 100 g)
Noble Gas/Liquid				
Dual-Phase Xe	XENON1T	Gran Sasso, Italy	installing 2.2 ton	XENON-nT (~ 7 ton)
	LUX	Sanford, USA	running 370 kg [9]	LZ (8.6 ton)
	PandaX	Jinping, China	running stage Ia (120 kg) [11]	stage II (ton-scale)
Liquid Xe	XMASS-1	Kamioka, Japan	running 835 kg [115]	R&D for XMASS-1.5 (5 ton)
Solid Xe	-	-	R&D [116]	
Dual-Phase Ar	ArDM	Canfranc, Spain	gas-only commissioning [117]	ton-scale dual-phase
	DarkSide-50	Gran Sasso, Italy	running 50 kg [118]	DarkSide-G2 (multi-ton)
Liquid Ar	DEAP-3600	SNOLAB, Canada	installing 3600 kg [119]	
Liquid Ar/Ne	miniCLEAN	SNOLAB, Canada	constructing 500 kg [120]	CLEAN (45 ton)
Liquid He	-	-	R&D [121]	
Inorganic Scintillators				
NaI(Tl)	DAMA/LIBRA	Gran Sasso, Italy	7-year 250-kg complete [7]	PMTs, DAQ upgrade
	ANAIS-25	Canfranc, Spain	running 25 kg [122]	ANAIS (250 kg) [21]
	DM-Ice17	South Pole	running 17 kg [24]	DM-Ice (250 kg) [22]
	KIMS-NaI	Yangyang	running [23]	250 kg
CsI(Tl)	KIMS	Yangyang, Korea	running 103.4 kg [23]	
CaWO ₄	CRESST-II	Gran Sasso, Italy	running 2.4 kg [123]	EURECA (with EDELWEISS)
Bubble Nucleation				
CF ₃ I	COUPP-60	SNOLAB, Canada	running 60 kg [15]	COUPP-500 (~ 500 kg)
C ₄ F ₁₀	PICASSO	SNOLAB, Canada	900 g run complete [124]	with COUPP
C ₂ ClF ₅	SIMPLE-II	LSBB, France	215 g complete [125]	increase target
C ₃ F ₈	PICO-2L	SNOLAB, Canada	running 2L [107]	PICO-30L
Directional				
CF ₄	DMTPC	WIPP, USA	R&D	
	NEWAGE	Kamioka, Japan	R&D	
CF ₄ +CHF ₃	MIMAC	Modane, France	R&D	
CF ₄ +CS ₂	DRIFT-IIId	Boulby, UK	0.8 m ³ at 40 torr [126]	DRIFT-III (8 m ³)
	D ³		R&D	
Xe	NEXT	Canfranc, Spain	R&D [127]	
Ag+Br+C(N,O)	Nuclear Emulsion	LNGS	R&D	
DNA	-	-	proposed	

can be configured in different ways to offer competitive sensitivity to high-mass (cryogenic detectors), low-mass (PPCs), and very-low-mass (CCDs) WIMPs. Additionally, both silicon and germanium are available targets for most detector technologies.

Cryogenic Semiconductors

Cryogenic semiconductor detectors run at < 100 mK, notably CDMS and EDELWEISS, achieve background rejection by implementing recoil-type identification through measuring both the phonon and ionization signals in their detectors (as shown in Fig. 3.3). Timing information from both ionization and phonon signals can be used as an additional parameter to remove noise from the data sample. A design challenge for these detectors is interleaving of electrodes to effectively isolate surface events and provide a uniform response in the fiducial volume. These detectors have focused on low-mass WIMP sensitivity due to the difficulty in scaling the detector array size to match the sensitivity of xenon experiments.

The EDELWEISS-III experiment consists of an array of germanium detectors with a mass of 800 g each (600 g fiducial mass) [109]. The SuperCDMS experiment consists of an array of 15 germanium detector with a mass of 600 g each (400 g fiducial mass) [12]. Both experiments have significantly surpassed their previous-generation results [128, 129, 18] using only a subset of the full experimental exposure.

The final silicon result of CDMS-II was significant in finding an excess of signal over the expected background, with a possible low-mass WIMP interpretation [18]. A dark matter interpretation of this result is strongly disfavored by the SuperCDMS data, but a definitive test must await the upcoming SuperCDMS SNOLAB experiment which will include new silicon detector capable of testing this in the same target. The CDMS-II germanium detectors were also analyzed to search for an annual modulation in the signal, which yielded a null result [105]. A potential signal in the CDMS-II low-energy germanium region from an external maximum likelihood analysis [130] has also been attributed to background after analysis of the full dataset [131].

The CDMS collaboration has also demonstrated a lower analysis threshold of ~ 170 eV and thereby low-mass WIMP sensitivity can be obtained by running the same detectors at higher bias voltages (69 V instead of 4 V for SuperCDMS iZIP detectors) and only collecting phonon signals. The prompt phonon signal is enhanced by the additional phonons produced from the work done drifting the electrons and holes in the applied field. The high field configuration sacrifices measurement of the ionization signal, and only currently allows readout on one side which limits the fiducialization and background rejection capability of CDMSlite. Despite these shortcomings, a single detector run for 6.3 kg·day exposure was able to provide the strongest limits below 6 GeV, showing great promise for this method with higher exposure and greater understanding of backgrounds [108].

P-Type Point Contact Detectors

An alternative semiconductor detector design is the p-type point contact (PPC) detector developed over the last decade. The point contact (as opposed to a traditional coaxial design) design allows for greater rejection of multi-site background events. The low capacitance (~ 1 pF) gives this detector excellent energy resolution and enables thresholds of 400 eV (demonstrated in running experiments) with development goals to lower thresholds as low as 100 eV. These detector only collect the ionization signal, and so they are limited by the passive background reduction and are only significant for low-mass WIMPs. They must be cooled to operate, but only to liquid nitrogen temperatures, as no phonon signal is collected.

All PPC detector research has been focused on creating germanium detectors. CoGeNT, using a 440 g detector, has reported an unexplained exponential spectral feature which may be interpreted as a ~ 10 GeV WIMP, as well as low-significance modulation [16]. A similar exponential spectral feature seen in the data of MALBEK, a 455 g detector, was due to ^{210}Pb contamination near the sensitive region [111]. The removal of this contamination now allows MALBEK to claim exclusion of the preferred CoGeNT parameter space, although the interpretation of this data is contested [132]. CDEX-1 is also currently operating a 994 g detector which may shed further light once a larger dataset is released [112].

Silicon CCD technology has made a late appearance in the dark matter direct detection world, but offers sensitivity to very-low-mass WIMPs. The DAMIC experiment initially ran with a 0.5 g CCD Designed for the Dark Energy Camera at a shallow site and achieved the best limits for < 4 GeV WIMPs. Key to their success is the very low energy threshold – 40 eV due to $2 e^-$ RMS noise (7.2 eV). The fine pixelization of the CCD also allows for recoil identification to reject muons and gammas (track-like) as well as alphas (diffuse blobs) from the desired nuclear recoils.

Semiconductor Future

The current generation of semiconductor detectors have all been small (< 1 kg/detector) with fiducial volume cuts providing a significant decrease in the useful mass. The next generation experiments all target larger detectors with a higher fiducial volume percentage while increasing background rejection.

Both EDELWEISS-III and SuperCDMS-Soudan are still collecting data in their current configurations and expect improvement in the final release. The long-term forecast for EDELWEISS is a combined collaboration with CRESST (discussed below) to form the EURECA collaboration and achieve a tonne-scale cryogenic experiment. SuperCDMS received US funding for scaling to a next-generation experiment to operate at SNOLAB (6000 m.w.e. overburden instead of 2100 m.w.e. at Soudan), and has put significant R&D effort into further increasing the individual detector size to 1.38 kg and scale the total size to 200 kg.

The original SuperCDMS plan only involved germanium detectors, but the recent CDMS-II silicon result has motivated the reintroduction of the silicon target. The SuperCDMS experimental program must also balance the demand to run detectors in CDMSlite mode to gain sensitivity to low-mass WIMPs.

The current generation of PPC detectors is very limited by exposure and ability to check results across multiple detectors. The CoGeNT collaboration has been engaged with Canberra (detector fabrication company) in R&D for larger detectors with lower energy threshold and backgrounds. The next phase of CoGeNT will consist of four such detectors with a total mass of 4 - 5 kg, referred to as C-4 [110]. The CDEX collaboration has plans to scale up their setup to a 10-kg scale experiment (CDEX-10) and possibly a ton-scale experiment (CDEX-1T) with unclear timeline [113].

Since their published result, DAMIC has increased the sensitive mass to 5 g in 5 CCDs and moved to a deeper location at SNOLAB. The new CCDs utilize different packaging in an attempt to reduce the intrinsic backgrounds of the setup. Additional R&D is being performed to attempt to lower the noise level of the CCDs, with $0.2 e^-$ RMS noise (0.72 eV) proposed as possible, which would enable the threshold to drop to ~ 4 eV. The next planned phase will be DAMIC-100, where the individual CCDs are scaled up to 4 g each (based on designs for the BigBOSS spectrograph) and a full array of 100 g is installed at SNOLAB [114].

3.4.2 Noble Gas Detectors

Although joining the field more recently, liquid noble gas detectors have scaled in mass quickly to contribute field-leading sensitivity. All the noble gas elements have scintillation and electron drift properties, allowing background rejection through two-signal measurements. Because the target is kept in the liquid phase, recirculation systems allow continued purification of the target to reduce background and improve electron drift lifetime. In order to run the detectors with a liquid phase, it is necessary to cool all the noble gases, necessitating cryogenic systems and PMTs with low-temperature operation.

For spin-independent WIMP searches, xenon offers a promising target because of its large nucleus (and thus A^2 scaling). Early experiments (ZEPLIN and then XENON10) demonstrated the technology for dual-phase liquid xenon detectors, with the current generation (XENON100, LUX, and PandaX) now providing the leading limits for spin-independent scattering. The bulk of these detectors is a liquid xenon volume in which an energy deposition will emit a prompt scintillation signal (S1). An electric field (~ 1 kV/cm) across the liquid volume drifts the electrons up to the gaseous region where a larger field (~ 10 kV/cm) generates a second proportional electroluminescence signal (S2). The PMTs used in these experiments must be specialized for the 178 nm peak emission of xenon scintillation. Full position reconstruction of all events is achieved by combining the xy information from the hit pattern in the PMT arrays with the z information from timing between S1 and S2 signals. The 3-D position reconstruction allows for a fiducial volume to be

imposed to take advantage of the self-shielding nature of the liquid xenon and reduce backgrounds from the cryostat.

The LUX experiment holds the world-leading limits for spin-independent sensitivity [9], with further data expected to improve the total limit soon. The former world-leading limits of XENON100 experiment [10] remain competitive, and the PandaX experiment is also scaling up their sensitivity [11]. Spin-dependent sensitivity of XENON100 is comparable to that of many bubble nucleation detectors of the same era [133].

The XMASS experiment also attempts to take advantage of a xenon target for its A^2 enhancement and self-shielding properties, but only as a single-phase (liquid) experiment. In addition to the convenience of not needing electric field management, the 4π PMT coverage allows the insertion of a quartz window between the PMT and sensitive volume to decrease the effect of PMT glass contamination. The XMASS-1 detector contains 835 kg of liquid xenon, but the fiducial mass is only 100 kg. Because they collect only the scintillation signal, the PMT coverage needs to be very high, with 62% of the detector surface covered by 642 PMTs [115].

The same dual-phase principle is also being applied to argon by the DarkSide [118] and ArDM [117] experiments. Efforts with argon received attention later because it receives less A^2 enhancement than xenon. The argon scintillation light is peaked at 128 nm, which requires coating of windows and detector walls with wavelength shifters (such as TPB) but then allows for standard PMTs to be used. Natural argon also has the presence of cosmogenic ^{40}Ar , which limits the low-energy sensitivity or requires specially extracted depleted argon.

Argon can also be run as a single-phase (liquid) target with background discrimination achieved by using pulse-shape discrimination (PSD). The principle of PSD is that scintillation light is produced from two different excited states, singlet and triplet, which have different decay times; electron and nuclear recoils will produce ratios of the two states which produce different pulse timing structure. As with XMASS, experiments pursuing single-phase argon need to maximize light-collection, and so they have selected spherical geometries with 4π PMT coverage. The DEAP-3600 experiment is currently installing such an experiment to contain 3600 kg (1000 kg fiducial) of liquid argon, hoping to be the first experiment to reach ton-scale fiducial [119]. The miniCLEAN experiment is also under construction, which would be able to switch between liquid argon and liquid neon targets, with plans to contain ~ 500 kg [120].

Noble Gas Future

LUX and the dual-phase liquid xenon experiments hold the leading dark matter sensitivity, but argon targets hope to demonstrate comparable sensitivity for high-mass WIMPs. The demonstrated scalability of the technologies is leading a drive into multi-ton scale, with XENON1T under construction, and XENONnT, LZ (US funding promised), and PandaX stage2 all in the planning stages.

For sensitivity to low-mass WIMPs, XMASS has demonstrated a sub-keV energy threshold, which could shed light on the regions of interest from the positive signal experiments.

The NEXT collaboration is also pursuing R&D on a gaseous xenon because the best energy resolution of xenon can be achieved in its gas phase. If they can make columnar recombination work, NEXT will gain a boost in sensitivity from directional reconstruction [127].

Xenon in the solid phase offers the intriguing possibility of collecting all three signals from a single target, and thereby an improved background rejection. R&D work towards realizing this detector is ongoing at Fermilab [116].

The emphasis on low-mass WIMP searches also brings liquid helium to consideration as a target. Its lower electron drift speed and very long-lived triplet states make multi-signal analysis more challenging, but the light mass target makes a low energy threshold more feasible. No significant work has been performed since the HERON and MACHe3 detectors over a decade ago, but a group at Berkeley and Yale has studied the concept [121].

3.4.3 Inorganic Scintillator Detectors

Inorganic scintillators take advantage of well-characterized detector technology with a long history to attack the dark matter problem. Years of experience with crystal growth make detector construction comparatively cheap, so this presents a scalable detector design. Additionally, these detectors can be operated at room temperature (although changing the temperature may improve the light output) and are low maintenance. Common scintillators used include NaI, CsI, and CaWO_4 , all of which include at least one heavy nucleus giving excellent spin-independent sensitivity, as well as some nuclei with spin-dependent sensitivity as well.

Selection of clean crystals through powder purification and repeated crystal growing is necessary to achieve the low intrinsic background required for the experiment. The virtue of scalability allows large arrays of crystals to be assembled so that an anticoincidence requirement can be imposed to reduce backgrounds from radioactivity.

Thallium-doped sodium iodide (NaI(Tl)) was the first of these scintillators to be implemented in dark matter searches by the DAMA and then NaIAD experiments in the 1990's. The wavelength of peak emission for NaI at 415nm is well matched to most (bi-alkali photocathode) PMTs, and the light yield of 38 photons/keV is high among inorganic scintillators. The NaIAD experiment was able to use pulse-shape discrimination to perform recoil-type identification and reduce their background, but the effectiveness of the technique diminished at low energies, ending by 4 keV. The DAMA experiment has measured an annual modulation in their signal, which they interpret as a dark matter signal at $9\text{-}\sigma$. Resolving or confirming

the DAMA observation has renewed interest in NaI scintillators with the recent efforts of both ANAIS and DM-Ice collaborations, and the status of is discussed in greater detail below in Sect. 3.4.3.1.

A less direct verification of the DAMA result has been attempted by the KIMS experiment, using CsI(Tl) scintillators. With this different target, KIMS gained advantages in total light yield (65 photons/keV) and less hygroscopic crystals, as well as possessing both target nuclei with large A^2 enhancements. The drawbacks to their test is that CsI can only directly detect the DAMA claim if it is due to iodine recoils, and CsI(Tl) has a higher scintillation wavelength requiring PMTs with special green-enhanced photocathodes (reducing the collected light to approximately the level of NaI). The scintillator response also produces pulses with longer decay times allowing easier PSD, but requiring longer digitizing windows. The KIMS experiment now consists of 12 crystals with total mass 103.4 kg. KIMS has not reported any signal, which as early as 2007 constrained the DAMA result for WIMP scattering off the iodine nucleus. Their spin-dependent limits were field-leading when published [14], but have since been surpassed by bubble nucleation detectors.

The CRESST collaboration entered the field operating cryogenic detectors and collecting the phonon signals from sapphire (Al_2O_3) detectors, but when upgrading to their CRESST-II phase opted for cryogenic scintillating CaWO_4 crystals. The two-signal readout allowed for background rejection through recoil-type identification in which the nuclear recoil bands for each target nucleus (Ca, W, and O) are somewhat offset so some information about which nucleus was scattered off is available. Based on data from eight sensitive detectors with ~ 2.4 kg total mass released in 2011, an excess of events was discovered at $> 4\sigma$. After attempts to reduce the α and neutron backgrounds, a second run was started with the same detectors. Data from a single new detector with lower threshold is sufficient to exclude the low-mass dark matter region of the previous result [123].

3.4.3.1 DAMA, Sodium Iodide, & Annual Modulation

Among dark matter experiments, DAMA is the only one which has claimed a discovery of dark matter. The other experiments with signal excesses, while projecting the WIMP parameters which are capable of producing the observed signal, speak in guarded language which does not claim discovery. The signal DAMA is interpreting occurs in the low energy region ($2-6 \text{ keV}_{ee}$) and has been observed to modulate over 14 annual cycles.

The DAMA experiment can be divided into two experimental phases - DAMA/NaI and DAMA/LIBRA. DAMA/NaI operated from January 1996 to July 2002 with nine 9.70 kg detectors. The experiment was then completely overhauled with new crystals and PMTs to reach DAMA/LIBRA, which operated from September 2003 to September 2010 with 25 detectors of the same mass but lower background ($\sim 1 \text{ count/day/kg/keV}$).

The signal measured by DAMA shows consistency over all 14 annual cycles (see Fig. 3.7). The modulation is only seen in the low energy region ($2-6 \text{ keV}$), with higher energy ranges consistent with no modulation.

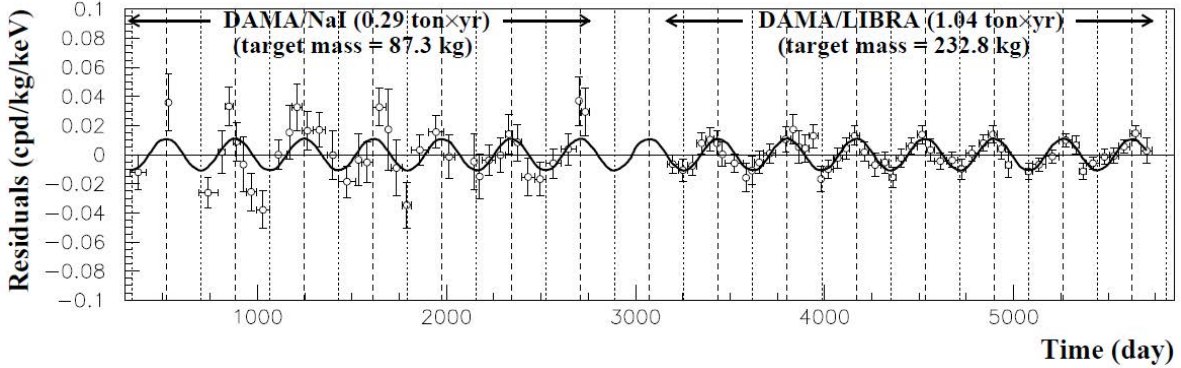


Figure 3.7: DAMA-observed signal modulation in 2–6 keV energy range over complete DAMA/NaI and DAMA/LIBRA-phase1 datasets [8]. The statistical significance of the modulation measurement is $9.3\text{-}\sigma$.

Allowing both the period and phase to float still provides fits consistent with the dark matter theory ($T = 0.998 \pm 0.002$ yr and $t_0 = 144 \pm 7$ days for 2–6 keV range). The quoted significance of $9.3\text{-}\sigma$ is based on the amplitude of the 2–6 keV fit ($A = 0.0112 \pm 0.0012$ counts/day/kg/keV) [7].

The DAMA result has faced the greatest scrutiny because it is the longest-standing, highest significance, and the collaboration has not released data for external reanalysis. Despite attempts, no single explanation has been suggested which clearly explains the observed signal.

The best known modulating background is the cosmic ray muon signal, the strength of which is correlated with the effective temperature of the upper atmosphere and thus with season. The dark matter signal is predicted to peak around June 2nd ($t_0 = 152.5$), and DAMA has measured $t_0 = 144 \pm 7$ in the 2-6 keV interval, with the other energy ranges fitting to $t_0 = 134 \pm 6$ and 140 ± 6 . While these phases may be troublingly early (particularly for the 2 - 4 keV range), the most precise measurement of the muon phase has been measured by Borexino as $t_0 = 179 \pm 6$ [134], a $4\text{-}\sigma$ discrepancy (and a larger discrepancy for the other energy ranges).

A secondary product of cosmic ray muons, the spallation neutrons, have also been considered as a possible background source. The DAMA collaboration has performed an analysis of the multiple-hit events, and found the modulation amplitude to be within $1\text{-}\sigma$ of null for all signal energy ranges. It has also been hypothesized that NaI(Tl) crystals, when receiving a large energy deposition, may store a part of the energy to be reemitted later as a delayed phosphorescence signal. In this way a single muon could create events in multiple crystals but the phosphorescence signal would lack a timing signature which could be vetoed by a muon system or anticoincidence cut. Additionally, because of the nature of the phosphorescence signal, this could naturally create lower energy signals. This hypothesis is somewhat undermined because the DAMA-observed modulation leads the muon signal rather than trails it (and has done so consistently).

Other potential modulation sources that have been suggested include temperature, radon, N₂ gas flush rate, hardware noise rate, and energy calibration. The DAMA collaboration claims to have monitored all of these quantities over each annual cycle of DAMA/LIBRA and found the fitted modulation amplitude consistent with zero (the highest significance discrepancy being -1.3σ [19]).

DAMA has begun taking data in DAMA/LIBRA-phase2 configuration, which utilizes the same low-background crystals but with a lower energy threshold from using higher quantum efficiency PMTs and quieter electronics. This may resolve concerns with the unusual spectral shape DAMA has observed (peaked at ~ 3 keV instead of exponential).

Because of DAMA's incomplete data release policy and the significance of their claim, there is interest in replicating the result in a different location with different systematics. A coordinated R&D effort is underway by the ANAIS [21], DM-Ice [22], and KIMS [23] collaborations all with the goal of replicating the DAMA experiment with similar backgrounds for a definitive test. A second approach is being taken by the SABRE collaboration which seeks to obtain significantly lower backgrounds before running their experiment [135].

ANAIS currently is operating 25 kg of NaI in Canfranc, and have demonstrated a factor of 10 reduction in ⁴⁰K levels relative to previous-generation crystals. The ²¹⁰Pb rates are much higher than allowable, indicating a probable radon contamination during crystal growing [122]. R&D crystals of DM-Ice and KIMS [23] are obtaining similar contamination levels, sparking interaction with the crystal growing vendors to drive down the background of future crystals.

The DM-Ice approach is unique among these experiments in planning for a Southern Hemisphere (specifically at the South Pole) deployment. Operating in the Southern Hemisphere will alter the systematic uncertainties by reversing the seasons, thereby removing possible backgrounds and providing a more definitive test. The current phase of the experiment, DM-Ice17, is operating two separate detectors with a combined crystal mass of 17 kg [24] and is discussed in Chap. 5. Present R&D work and future phases are discussed in Chap. 9.

Inorganic Scintillator Future

The CRESST-II experiment with its second run at lower backgrounds will soon release their full dataset, which should further confirm the exclusion of the earlier signal excess. Future work by CRESST is focused on the low-mass region by lowering the detector threshold.

DAMA underwent PMT and DAQ upgrades following their 7-year DAMA/LIBRA data run and has worked to lower their threshold below 2 keV. The DAMA/LIBRA-phase2 experiment has already collected almost four years of data, but no plan for data release has been announced. Lower threshold data could illuminate the dark matter spectra DAMA observes, which some have claimed shows abnormal shape.

The R&D work of ANAIS, DM-Ice, KIMS, and SABRE will determine the feasibility of these experiments. If the necessary background levels can be achieved, growth toward 250 kg array(s) will be swift and a test of DAMA will be possible within two years. Present R&D work and future phases are discussed in Chap. 9.

3.4.4 Bubble Nucleation Detectors

Although very different in appearance, bubble chambers and superheated droplet detectors bear similarities in technique and sensitivity. These experiments utilize molecules with large abundances of ^{19}F to probe the spin dependent WIMP scattering case. SIMPLE (C_2ClF_5) [125] and PICASSO (C_4F_{10}) [124] are both superheated droplet detectors and COUPP (CF_3I) [15] is a bubble chamber. PICO, a newly-formed collaboration of COUPP and PICASSO, has focused on C_3F_8 for improved sensitivity both to spin-dependent scattering and low-mass spin-independent scattering [107]. The newest results from PICO significantly surpass the previous generation experiments (see Fig. 3.6b).

Tuning the pressure and temperature of these setups allows for operation in a metastable state which is insensitive to electron recoils, thus eliminating the largest source of background. Additional background reduction has been obtained by using acoustic sensors to distinguish between alpha and neutron-like events. Imaging of the nucleation event can further eliminate multiple scatter events (from neutrons) resulting in a nearly background-free sample.

Bubble Nucleation Future

As the bubble nucleation technique allows for a nearly background-free measurement, these experiments are limited by the statistics they can acquire, and so they are all scaling to larger target masses.

COUPP has already upgraded their SNOLAB setup from a 4-kg chamber to a 60-kg chamber. Within a half-year of running, COUPP60 is expected to jump two orders of magnitude in spin-dependent limits, surpassing the IceCube and SuperK indirect search limits even with more generous production mechanisms. COUPP60 will also be competitive in spin-independent limits, surpassing the current XENON100 limit. A further upgrade to COUPP500 may keep pace with the scaling of noble gas detectors, depending on the implementation timeline.

3.4.5 Directional Detectors

Detectors aiming to have sensitivity to the direction of WIMP recoils gain sensitivity from the unique directional signature. If found, a few tens of events should give sufficient statistics for a definitive detection of dark matter.

The challenge for this class of detectors is that most are low-density gaseous detectors in order to allow tracks of detectable length to develop. This generates difficulties when scaling the detector size to achieve

a competitive target mass. All five detectors focus on spin-dependent scattering and use CF_4 as the target nucleus, but differ in their drift techniques (*e.g.* some use CS_2 as a carrier gas) and readout technology (*e.g.* MWPCs for DRIFT, GEMs for D³).

An untested method of obtaining directional sensitivity is columnar recombination. This property of gaseous xenon is being investigated by the NEXT prototype detectors.

Another method for directional detection being investigated is nuclear emulsion. The detector has no timing ability, so the emulsion is exposed for a pre-determined length of time before being recovered and read out; this forces the detector to be housed in a mount which can keep constant galactic orientation throughout the day. During readout, the emulsion is scanned for tracks as short as 100 nm. The technology has the advantages of high density (relative to gaseous directional detectors) and cost of scalability (\$1500/kg), but further R&D is necessary to demonstrate its effectiveness.

3.5 Prospects for Future Searches

Dark matter detectors continue to increase in size and improve background rejection, releasing order-of-magnitude improvements in WIMP limits (by cross-section) every year or two for standard WIMP masses (~ 100 GeV). As these limits continue to improve, the space theorists have labelled as preferred in cmSSM (supersymmetry) models is reduced.

A new background from solar neutrinos is now approaching these experiments as they lower their limit to $\sim 10^{-46}$ cm^2 . Coherent scattering of solar neutrinos will begin to generate tens of detectable events up to the maximum recoil energy (T_{max})

$$T_{max} = \frac{2E_\nu^2}{m_T + 2E_\nu} \quad (3.16)$$

which will affect target nuclei with lighter masses (m_T) more strongly. The events can be removed from the analysis by imposing an artificially higher energy threshold, which will reduce the sensitivity to low-mass WIMPs.

The next generation of experiments is receiving a great deal of emphasis on understanding the signal hints that have been published. Because complicated particle physics interactions could lead to different behavior in different targets, verification from detectors with the same target is desired, as well as new experiments with strong sensitivity to the ~ 10 GeV WIMPs.

While DAMA/LIBRA-phase2 may shed some light on the spectrum, ANAIS and DM-Ice are looked to for resolution of NaI. CoGeNT will be checked by C-4 and CDEX10 using the same detector design, as well as CDMSlite and low-threshold analyses of SuperCDMS and EDELWEISS-III. CRESST-II is the only cryogenic scintillator experiment, so hopefully the background reductions before the new run are sufficient

to shed light on their first result. CDMS-II (Si) is the only experiment without a direct check in progress, but DAMIC-100 or SuperCDMS-SNOLAB silicon detectors may eventually resolve the issue.

3.6 Background Concerns for Direct Searches

In order to positively identify the weak dark matter signal, it is necessary for these experiments to drive their backgrounds as low as possible. Typical backgrounds for dark matter experiments include events from radioactivity in the materials used, radioactivity in the experimental environment, environmental fluctuations which effect detector response, and cosmic ray muons and spallation products of muons. A stepped approach is taken to reducing backgrounds in these experiments: wherever possible the backgrounds are eliminated through experimental design and construction, then careful data analysis cuts can further reduce background in data processing.

Since cosmic ray muons originate in the atmosphere and then shower down to earth, the simplest reduction technique is to move the experiment to a deep underground laboratory (> 2000 m.w.e. overburden). This use of the earth as a passive shield will reduce the muon flux by many orders of magnitude, and make a rare event search possible, but as a further reduction an active veto system can be built around the detector which will trigger on any muon event (the muon is recorded and a deadtime window is imposed on the dataset). The cosmic ray muons can also produce secondary particles, spallation neutrons, which will interact with the detector; this is a more problematic background because the nuclear recoil signal will mimic the desired dark matter signal and neutrons are harder to shield against. The passive defense against this neutron background is to add shielding layers specifically to moderate the neutrons, proton-rich materials like polyethylene to thermalize the neutrons and then layers with high neutron-capture cross-sections like cadmium. It is also possible to veto some neutron events through data analysis by looking for multiple-scatter events in the detector.

The radioactive background of the environment is unavoidable because of the radioactive isotopes naturally present in the surrounding bedrock which is providing shielding from cosmic ray muons, but its effects are typically mitigated by a layered shielding design surrounding the experiment. Lead is an efficient shielding material because of its high density, but its own radioactive isotope of ^{210}Pb will problematically survive processing (other radioactive isotopes of lead from ^{238}U , ^{235}U , and ^{232}Th chains have half-lives less than one day and will quickly decay away). Because of the lifetime of ^{210}Pb ($t_{1/2} = 22.2$ years), lead which has been extracted centuries prior will have decayed down to have negligible rates. For this reason, detectors will be designed with an outer layer of normal lead, an inner layer of ancient Roman lead, and a very inner layer of OFHC copper; each layer shielding the one outside. A common environmental radioactive background presenting a different challenge because of its gaseous nature is radon, which is part of the decay chain of both ^{238}U (^{222}Rn , ^{218}Rn) and ^{232}Th (^{220}Rn). Radon is typically controlled by keeping enclosures airtight and

constantly circulating high purity N_2 gas. The final control against environmental backgrounds is through a fiducial volume cut - detectors with position reconstruction can tag events occurring near the surface and remove them prior to analysis. The fiducial volume cut thus eliminates events which are more likely caused by external radiation, and also events where detector edge effects might impact the energy reconstruction.

Detectors using PMTs to collect photon signals must also combat the added backgrounds from the PMT glass. This is mitigated either by using lightguides (often quartz, sometimes acrylic) to distance the PMTs from the sensitive region or by replacing the glass with more radiopure quartz, but both methods incur additional cost.

The circuit boards and digitizing electronics must also be isolated from the sensitive region of a detector, as these components will often leach radon gas. A compromise must be made in the design to limit the distance analog signals must travel while also isolating the potential source of background.

Radioactive decays which occur inside the detector are impossible to add shielding against and will occur inside the fiducial volume, making it important to have undergone rigorous material screening and purification to drive the internal contamination as low as possible. Data analysis cuts do allow for some reduction - alpha, gamma, beta, and neutron events all exhibit different energy deposition profiles, and so event identification through pulse shape and multi-channel analyses can provide additional discriminating power. Additionally, imposing an anticoincidence requirement between detectors eliminates multiple-scatter neutron events and backgrounds triggering multiple detectors.

Finally experimental condition fluctuations in temperature and humidity can alter the detector response. Changes in the detector response can affect the energy calibration, the noise rate, and the energy threshold. These effects, if unaccounted for, will ruin data sets and destroy the sensitivity of an experiment.

While the above backgrounds are common to all rare event searches (neutrinos as well as dark matter), the individual experiments will have additional concerns for reading out the recoil energy based on their specific design. Readout electronics will have their own unique noise signatures, and detector types have unique dark rates.

Chapter 4

Overview of Cosmogenic Activation

Transmutation of atoms by exposure to cosmic rays is known to occur in both the atmosphere and the ground. The prevalence of light elements in the air (78% ^{14}N and 21% ^{16}O) results in production of mostly light products; ^{14}C is the most common example being produced by neutron capture on nitrogen ($^{14}\text{N}(n,p)^{14}\text{C}$). In terrestrial soil, significant abundances of heavier elements (*e.g.*, ^{28}Si , ^{40}Ca) allows for greater production of heavier products (*e.g.*, ^{26}Al , ^{36}Cl) [136, 137]. Radioactive products of cosmic ray exposure present an additional source of background for detectors that must be thoroughly characterized.

These cosmogenic activation products can be classified into two categories based on the time of activation. Radionuclides produced prior to component fabrication can be controlled by the same purification processes which are used to remove other intrinsic long-lived radionuclides. Radionuclides produced after fabrication cannot be removed, so they must be controlled by limiting cosmic ray exposure or including cooling time in the experimental plan. The same activation physics applies to all products of cosmogenic activation, but the analysis of this thesis will focus on the shorter-lived radionuclides produced after fabrication, especially during construction, storage, and shipment of the detectors.

Unlike naturally occurring radioactivity, cosmogenically activated isotopes continue to be produced until a detector is located deep underground. Operating an experiment in a laboratory with large overburden therefore helps mitigate not only the prompt cosmic ray background, but also the delayed activation effects.

For an incident particle (x), the production rate (R) for activation of a daughter isotope can be calculated from the cosmic ray flux (ϕ_x) and the activation cross-section (σ_x):

$$R \propto \int \phi_x(E) \sigma_x(E) dE \quad . \quad (4.1)$$

A complete calculation must be performed for every component of the cosmic ray flux (*e.g.*, protons, neutrons, muons), but a practical reduction is to only compute the contribution from incident neutrons, as they account for $\gtrsim 95\%$ of the sea level nucleon flux [138]. Since the cosmic ray flux varies with geographic location, altitude, and time, activation calculations typically perform the integration one to obtain a reference production rate at sea level (R_0) and scale for cosmic ray flux intensity variations.

4.1 Cross Sections

Cross sections must be considered for each target and product isotope of interest. For sodium iodide crystals, each element has only a single isotope with significant abundance, ^{23}Na and ^{127}I . For quartz (SiO_2) lightguides, both elements are dominated by a single isotope, ^{28}Si (92.22%) and ^{16}O (99.76%), with lesser contributions from other isotopes. For steel, it is impractical to perform analysis of individual target isotopes because five elements (Fe, Cr, Ni, Mo, and Mn) have $>1\%$ abundance and five other elements are present in trace quantities in the alloy, with each element typically having four or five stable isotopes. In the case of activation of steel, data from previous activation studies [139] was used to establish the reference activation rate, whereas for sodium iodide and quartz individual production rates were considered from measured and calculated values.

For many target and product combinations, measured production cross section data is available in the EXFOR database¹. This data is generally available for production of product isotopes near in neutron and proton numbers to the target. Additionally, the energy intervals and errors are often quite large. For these reasons, the measured data is not used directly but is used to benchmark the cross section calculations and in error estimation.

Evaluated data libraries based on *ab initio* calculations present a more complete database of activation cross sections. The libraries investigated in this study, covering incident particle energies up to 1 GeV for protons and neutrons, are MENDL-2 [140], MENDL-2P [141], HEAD-2009 [142], ENDF/B-VII.1 [143], and TENDL-2014 [144]. MENDL-2, the ‘Medium Energy Nuclear Data Library,’ contains neutron reaction data for energies up to 100 MeV, produced in 1995 it is also the oldest library referenced. MENDL-2P² contains proton reaction data for energies up to 200 MeV, produced in 1998 it compliments the MENDL-2 data. HEAD-2009³, the ‘High Energy Activation Data Library,’ is a combined library for 150–1000 MeV incident particle energies including proton data from HEPAD-2008, the ‘High-Energy Proton Activation Data,’ and IEAF-2009, the ‘Intermediate Energy Activation File;’ for activation of ^{127}I , the calculations follow the CASCADE model [145]. ENDF⁴, the ‘Evaluated Nuclear Data File,’ contains only <30 MeV neutron activation data for ^{23}Na and ^{127}I ; the B-VII.1 library was released in 2011. TENDL⁵, the ‘TALYS Evaluated Nuclear Data Library,’ contains activation up to 200 MeV for incident neutrons or protons (as well as deuterium, tritium, helium, or gammas); it is updated every year with 2014 being the current release.

The cross sections can also be calculated on the fly using semi-empirical formulae, with the most common being those of Silberberg and Tsao for proton activation [146, 147]. Activation codes [148, 147, 149] which

¹ <http://www.nndc.bnl.gov/exfor/exfor.htm>

² <https://rsicc.ornl.gov/Catalog.aspx?c=DLC>

³ Available from authors, by request.

⁴ <http://www.nndc.bnl.gov/exfor/endl00.jsp>

⁵ <ftp://ftp.nrg.eu/pub/www/talys/tendl2014/tendl2014.html>

desire versatility to perform calculations for any target and product isotope over arbitrarily large energy ranges must use this method. Newer calculations take advantage of more recent modifications to the formulae and exhibit better agreement with data, with factor of two or better errors typical [149].

In this thesis, simple reactions with only one possible production mechanism for the product isotope will be written explicitly (*e.g.*, $^{127}\text{I}(n, 3n)^{125}\text{I}$). Reactions with multiple production channels (*e.g.*, $^{127}\text{I}(p, p2n)^{127}\text{I}$, $^{127}\text{I}(p, dn)^{125}\text{I}$, $^{127}\text{I}(p, t)^{125}\text{I}$) will be simplified (*e.g.*, $^{127}\text{I}(p, x)^{125}\text{I}$).

Production of ^{125}I from a ^{127}I target provides an illustrative example of precisely determining the cross section (see Fig. 4.1). The available experimental data is limited, with two low-energy measurements of neutron activation [150, 151] and two sets of high-energy measurements of proton activation [152, 153] found in EXFOR. The calculations from the evaluated libraries show good consistency, with the proton and neutron libraries reproducing different features below 50 MeV but following similar behavior at high energy. The semi-empirical calculation, produced by ACTIVIA activation code [149], more closely follows the cross sections from the neutron activation libraries, despite being designed for proton activation. This deviation produces a more accurate calculation, as the neutron flux is dominant for energies below 1 GeV.

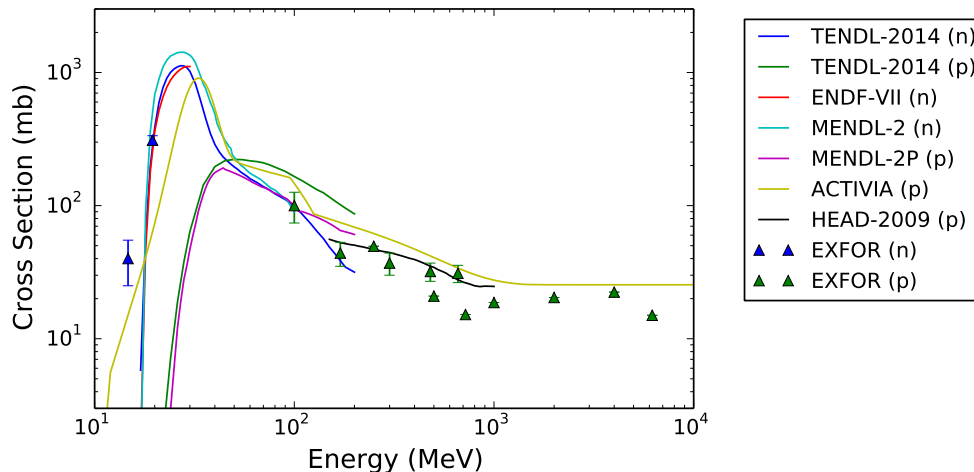


Figure 4.1: Production cross section of ^{125}I for incident protons (p) and neutrons (n) on an ^{127}I target. Proton and neutron activation show very different behavior at low energy (< 50 MeV) but converge at higher energy. Different calculation methods are in good agreement with each other and measurement for this isotope. Experimental data was compiled by EXFOR; evaluated data libraries are TENDL, ENDF, MENDL, and HEAD; semi-empirical calculation is ACTIVIA.

4.2 Cosmic Ray Fluxes

The study of cosmic rays began in 1912 with Victor Hess's discovery of a new ionizing radiation coming down from the heavens. In his work, Hess found that when compared to its level at sea level, this radiation increased with altitude and vanished in underground caves [154]. The cosmic ray flux which Hess observed at the Earth's surface is more precisely composed of secondary cosmic rays, having been produced by particle showers in the atmosphere (see Fig. 4.2).

The dynamics of the secondary cosmic rays are independent of the identity of the primary cosmic ray (79% protons and 15% helium [2]) because the first collision with in the atmosphere will break apart the primary into its constituent nucleons. A cascade is fueled by collisions with and the subsequent breaking apart of atoms in the atmosphere, with each secondary particle having the potential to produce yet more secondaries if its kinetic energy exceeds the binding energy of that atmospheric atoms. Because only the secondary cosmic rays are of significance to activation studies inside the atmosphere, these are referred to as cosmic rays throughout the remainder of this discussion.

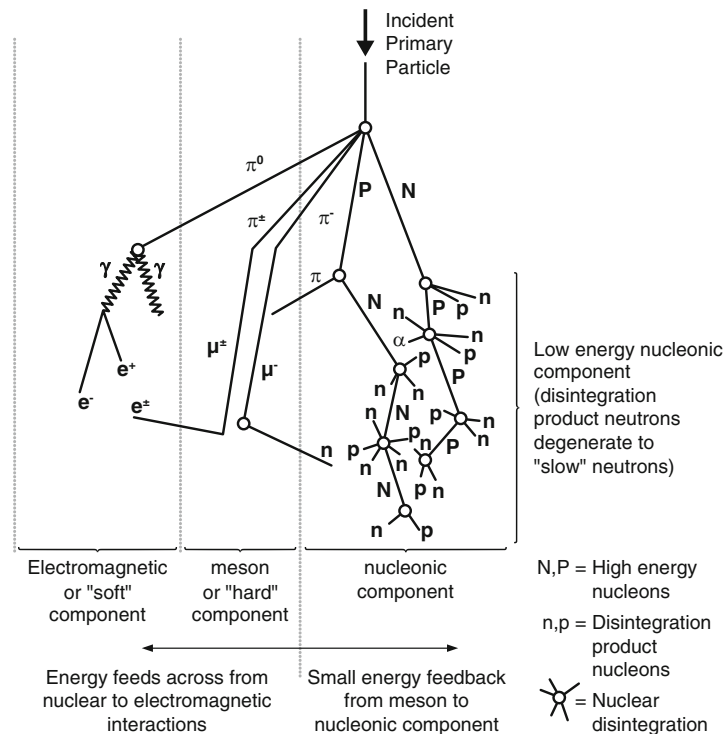


Figure 4.2: Production of secondary cosmic rays in the atmosphere from a single high-energy primary particle [155]. Nucleons with kinetic energy exceeding the binding energy of an atoms can break apart the atom into its constituent nucleons thereby increasing the size of the cascade.

As the shower passes through the atmosphere, it is attenuated, resulting in a maximum total cosmic ray flux at an altitude of ~ 15 km. Because the particles of the shower have different attenuation lengths (~ 136 g/cm² for neutrons and ~ 105 g/cm² for protons), the composition changes with altitude [138] (see Fig. 4.3).

Neutrons, in consideration of cosmogenic activation, are more important than protons because they account for $\sim 95\%$ of activation at sea level. The cosmic ray energies of interest have energies of 10–1000 MeV, with lower energy neutrons being below the threshold energy for activation (see Fig. 4.1) and higher energy neutrons being too rare to produce significant activation. Across this energy range, the neutron flux is approximately constant between sites when the correct scaling factors are applied (see Fig. 4.4) [156].

Studies of neutron flux spectrum by Gordon *et al.* [156] found that it can be scaled from a sea level reference flux (ϕ_0) by using two factors. The first is an altitude factor ($F_{alt}(d)$) which depends only on the atmospheric depth (d , calculable from altitude). The second factor ($F_{BSYD}(R_c, d, I)$) incorporates

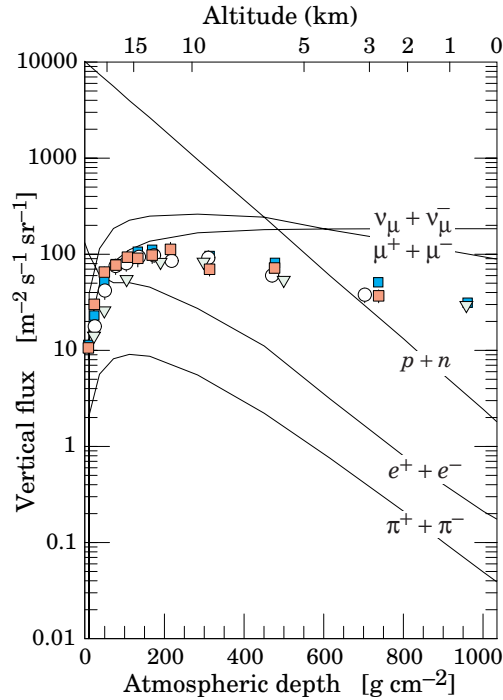


Figure 4.3: Variation in intensity of cosmic ray flux with energy > 1 GeV with atmospheric depth [2]. In the upper atmosphere, the primary electrons and protons quickly range out so below 20 km all significant flux is secondary cosmic rays. The shower components reach their maximum at an altitude of ~ 15 km. Because of the different attenuation lengths, the composition of secondary cosmic rays varies strongly with altitude.

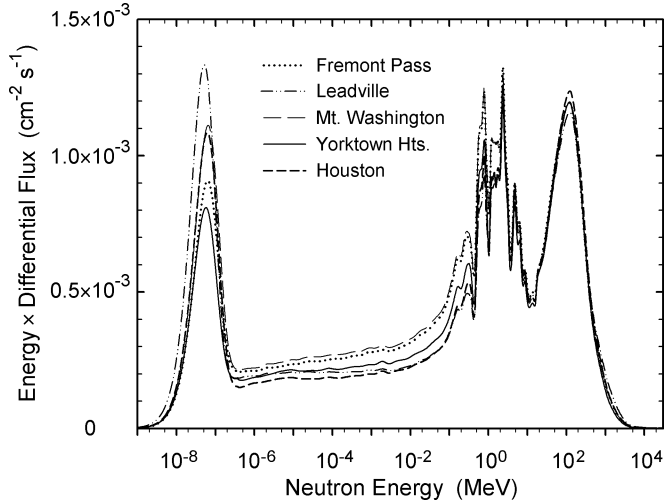


Figure 4.4: Neutron flux spectrum measured at different locations by Gordon *et al.* [156]. Spectra have been scaled by the appropriate factors to remove altitude and geomagnetic rigidity effects. The spectrum above 10 MeV (of interest for cosmogenic activation studies) is approximately constant between all five measurement sites after correction.

dependence on geomagnetic rigidity (R_c), solar intensity (I), and atmospheric depth:

$$\phi = \phi_0 F_{alt}(d) F_{BSYD}(R_c, d, I) \quad (4.2)$$

Using these scaling factors, they will be able to achieve the spectral match shown in Fig. 4.4 between sites spanning 3450 m in altitude and geomagnetic rigidities from 1.5 to 4.7.

4.2.1 Neutron Flux Spectrum

Several competing models of the shape and intensity of the cosmic ray neutron spectrum have been utilized for cosmogenic studies. Although this analysis adopts the model of Gordon *et al.*, comparison with other models is discussed in the context of possible error introduced through flux uncertainty.

The native spectrum utilized by the ACTIVIA code is that of Armstrong [157] and Gehrels [158]; this spectrum has the advantages of simplicity of shape and of including both proton and neutron flux components. Providing a much-needed update, Ziegler *et al.* compiled and fit available data to produce a new standard neutron-only spectrum with higher modeled flux up to 4 GeV [138]. A thorough study by Gordon *et al.* measured the neutron flux to higher precision and at various sites to determine a more accurate functional form and scaling rules [156]. The Gordon flux is in good agreement with PARMA simulation studies [159] of propagating the measured primary cosmic ray flux through the atmosphere (see Fig. 4.5).

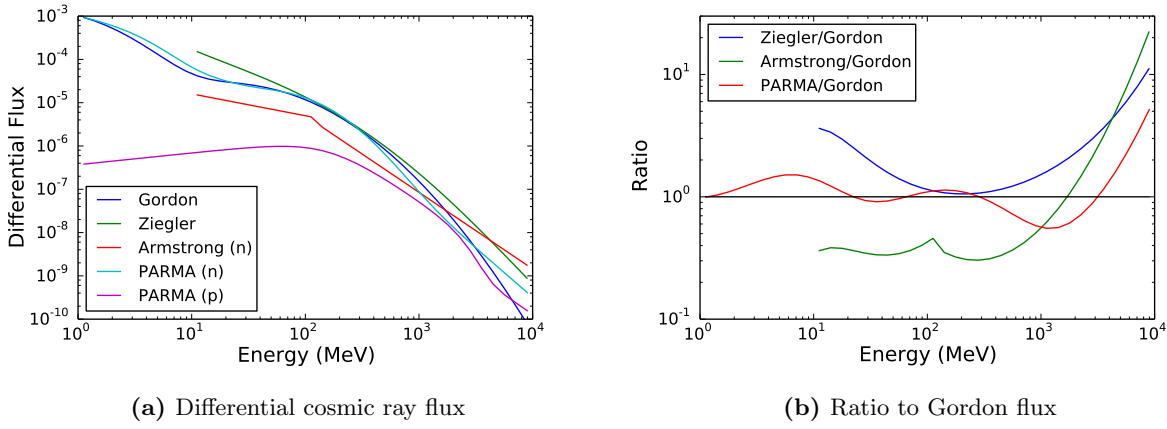


Figure 4.5: Common parameterizations of sea level cosmic ray neutron flux. The older Armstrong model heavily underestimates the flux below 1 GeV relative to all other models and consequently predicts lower activation rates. The selected measured spectrum (Gordon) and simulation (PARMA) agree well in both shape and normalization especially around 100 MeV where most activation occurs. A sea level proton flux is included to demonstrate its sub-dominant contribution to the total flux, and thus total activation, below 1 GeV.

The Gordon spectrum adopted in this thesis has differential flux ($d\phi/dE$) parameterization:

$$\begin{aligned} \frac{d\phi}{dE} = & (1.006 \cdot 10^{-6}) \cdot \exp \left[-0.35 \cdot (\ln(E))^2 + 2.1451 \cdot \ln(E) \right] \\ & + (1.011 \cdot 10^{-3}) \cdot \exp \left[-0.4106 \cdot (\ln(E))^2 - 0.667 \cdot \ln(E) \right] \quad . \end{aligned} \quad (4.3)$$

The units of differential flux are ($\#/cm^2/s/MeV$) and the parameterization has measured validity from $10^{-1} - 10^4$ MeV. The Gordon spectrum is a widely adopted model both for cosmogenic activation studies and as the JEDEC standard for electronics testing.

4.2.2 Altitude Dependence

The dependence of cosmic ray intensity on altitude was one of the first features observed by Hess. The cosmic ray flux scaling ($F_{alt}(d)$) follows an exponential attenuation with atmospheric depth, a measure of the distance travelled weighted by atmospheric density (units of g/cm^2):

$$F_{alt}(d) = \exp \left[\frac{(d_{ref} - d)}{L_n} \right] \quad , \quad (4.4)$$

where $L_n = 131.3 g/cm^2$ is the attenuation length of neutrons (measured for energies above 10 MeV) and $d_{ref} = 1033.7 g/cm^2$ is the atmospheric depth at sea level [156].

The atmospheric depth can be calculated from altitude (h , in km) following the parameterization of Stephens [160]:

$$h = \begin{cases} 44.34 - 11.861 \cdot d^{0.19} & d > 230 \text{ g/cm}^2 \\ 45.5 - 6.34 \cdot \ln(d) & 25 < d < 230 \text{ g/cm}^2 \end{cases} \quad (4.5)$$

This simple model is widely recommended in literature [161] and as part of the JEDEC standard. Only requiring a single piecewise break at an altitude of 11 km (36,000 ft) for the altitudes of interest in this analysis, its calculated atmospheric depth agrees to better than 1% with more complicated models [162].

The effect of the entire atmospheric depth on the cosmic ray flux, 1033.7 g/cm^2 , is equivalent to 10 m of water ($\rho = 1.0 \text{ g/cm}^3$) or 4 m of rock ($\rho \approx 2.7 \text{ g/cm}^3$) shielding. The highest altitudes considered in this study are 40,000 ft (12 km) for commercial flights, corresponding to an atmospheric depth of 191 g/cm^2 .

4.2.3 Location and Temporal Dependence

The second scaling factor of Eqn.4.2 (F_{BSYD}) incorporates spatial and temporal dependence of the cosmic ray flux. It takes the form of a Dorman function:

$$F_{BSYD}(R_c, d, I) = N \left[1 - \exp\left(\frac{-\alpha}{R_c^k}\right) \right] \quad , \quad (4.6)$$

where R_c is the vertical geomagnetic cutoff rigidity, α and k are parameters which vary based on the solar intensity and atmospheric depth, and $N = 1.098$ is a normalization which allows the New York City sea level reference factor to be forced to be 1. The values for α and k for the solar activity minimum assumed in this analysis are:

$$\begin{aligned} \alpha &= \exp[1.84 + 0.094h - 0.09 \exp(-11h)] \\ k &= 1.4 - 0.56h + 0.24 \exp(-8.8h) \quad , \end{aligned} \quad (4.7)$$

where $h = 9.8025 \cdot 10^{-4} \cdot d$ is the barometric pressure, which is proportional to the atmospheric depth (d) [163, 156].

4.2.3.1 Solar Activity

An anti-correlation between solar activity, as measured in number of sunspots, and cosmic ray flux was first observed by Forbush in 1954 [164]. The solar cycle has observed variable periodicity with an average of 11 yr (see Fig. 4.6). During periods of active sun the solar wind increases by multiple orders of magnitude; the distortion of Earth's magnetic field by the solar wind results in and increased shielding against primary cosmic rays [138].

The majority of the particles in the solar wind have too little energy to penetrate Earth's magnetic field and atmosphere to have a direct impact on the cosmic ray flux. The diurnal variation in the cosmic ray

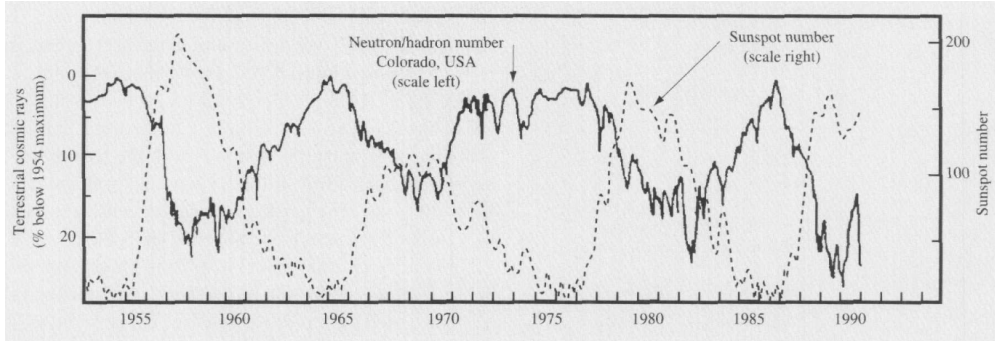


Figure 4.6: Cosmic ray flux anti-correlation with sunspot activity measured over three complete solar cycles [138]. Typical variation in the cosmic ray intensity is $\pm 10\%$.

intensity has been measured to be $< 1\%$, placing a constraint on this direct impact. During solar flares, there is a chance the Earth will pass within the stream of particles from the Sun, which can cause a brief (< 1 day) increase in the cosmic ray intensity of up to a factor of two [165]. The more common effect of solar flares is an increased distortion of Earth’s magnetic field leading to a $\sim 20\%$ peak decrease in the cosmic ray intensity, with lesser effects observed over several days [164]. Both of these potential effects are not considered in this analysis because of their temporally brief nature.

The most recent solar activity minimum was in 2009, with neutron monitors recording an extended and elevated maximum in the cosmic ray flux [166, 167, 168]. Because the solar minimum extended into 2010, all cosmic ray flux scalings in this analysis assume solar minimum conditions for DM-Ice17 (see Chap. 8). Depending on future deployment timelines, the assumption of solar minimum conditions may lead to an overestimate in the activation rate of up to 20% (see Chap. 9).

4.2.3.2 Geomagnetic Rigidity

The variation of cosmic ray intensity is a well-documented effect, with the observed effect strengthening with altitude [169]. This effect has its origin in the Earth’s magnetic field, which provides shielding against low-energy (< 10 GeV) primary cosmic rays at equatorial latitudes. The shielding is measured in units of vertical geomagnetic cutoff rigidity, R_c , a measure of the minimum momentum-to-charge (in GV) for the primary charged particle. The magnetic poles provide no shielding while the equatorial regions provide maximal shielding (see Fig. 4.7)

The geomagnetic rigidity grids are created by computationally-intensive tracing cosmic ray trajectories. This method identifies both a lower cutoff below which no cosmic rays can penetrate, an upper cutoff above which all cosmic rays can penetrate, and an effective cutoff which accounts for partial penetration

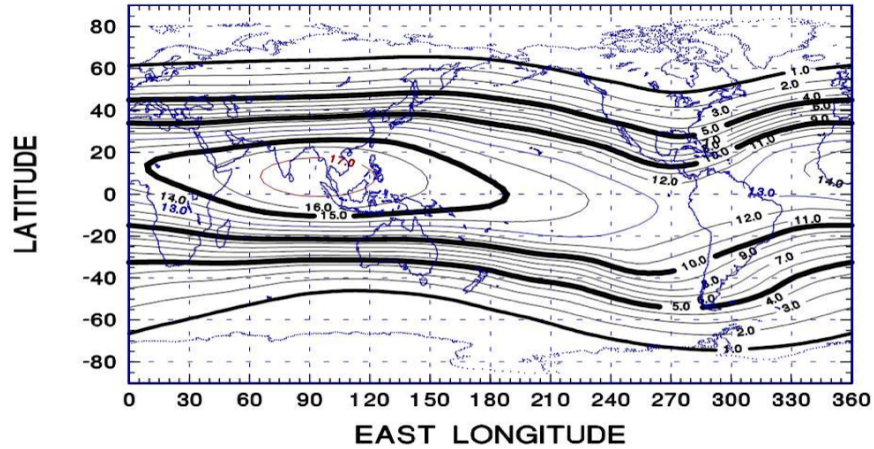


Figure 4.7: Iso-rigidity contours for vertical geomagnetic cutoff rigidities for Epoch 2010 [170]. The shielding effect is maximal near the equator with $R_c > 10$ GV and minimal near the Poles with $R_c \approx 0$ GV.

at intermediate rigidities [171]. Calculations are performed based on the geomagnetic field model which is updated every five years; the 2010 rigidity grid was used for all analysis in this thesis [170].

4.3 Activation Mechanisms

There are two primary processes of cosmogenic activations: capture and spallation. In capture reactions, the daughter produced will be close to the original nucleus in number of both protons and neutrons; the relevant incident particle is captured on the nucleus, which immediately emits some combination of neutrons, protons and photons (but few in number). In spallation, the incident particle causes the nucleus to split into daughter nuclei, and the daughter nuclei are thus further in proton and neutron number from the parent nucleus. Because larger nuclei are often neutron-rich, spallation of these nuclei typically releases a number of neutrons which may then be captured on nearby nuclei.

The DM-Ice17 detectors were shipped to the South Pole fully assembled, meaning that the NaI(Tl) were already surrounded by the steel pressure vessel. In this analysis, the possible effects of the steel pressure vessel on the neutron flux environment of the crystal, both as small additional shielding and as a possible spallation neutron source, are omitted in scaling considerations.

4.4 Calculating Activation Rates

The reference (sea level at New York City) activation production rate, R_0 , can be calculated according to Eqn. 4.1 with inclusion of appropriate unit conversion factors. Commonly used units adopted in this treatment are ($\#/kg/day$) for activation rate, ($\#/cm^2/s/MeV$) for differential flux, and (barns) for cross

section. The necessary unit conversion factors for ^{125}I production in the crystal are (10^{-24} cm²/barn), (86,400 s/day), ($6.022 \cdot 10^{23}$ atom/mol), and (1 mol/0.1269 kg I), (0.8466 kg I/kg NaI).

With the reference production rate established, the production rate at any arbitrary location (R) is calculated:

$$R = R_0 \cdot F_{alt}(d) \cdot F_{BSYD}(R_c, d, I) \quad , \quad (4.8)$$

according to the scaling factors established in Sect. 4.2.2 (F_{alt}) and Sect. 4.2.3 (F_{BSYD}). The range of altitudes considered in this study extends from atmospheric depths of 1033.7 g/cm² at sea level to 191 g/cm² at the highest aircraft altitude, resulting in a F_{alt} scaling factors of up to 600. The range of geomagnetic rigidities considered extends up to R_c values of 15, resulting in F_{BSYD} scaling factors as low as 0.2.

Because all radionuclides produced by cosmogenic activation have half-lives, the rate of change in the abundance (dN/dt) of any isotope is:

$$\frac{dN}{dt} = R - \lambda N \quad , \quad (4.9)$$

where R is the activation production rate, λ is the decay constant ($\lambda = \ln(2)/t_{1/2}$), and N is the abundance of the isotope; the quantity λN is the activity, the total decay rate of the isotope. This differential equation has the solution:

$$N = \frac{R}{\lambda} (1 - e^{-\lambda t}) \quad . \quad (4.10)$$

The exposure history considered for the detectors in this study (see Sect. 8.1) covers a period over a year, and so different isotopes will experience significantly varied decay effects, depending on their half-lives (see Fig. 4.8). For short-lived isotopes like ^{52}Mn only the most recent exposure periods are important as the effects of older periods have decayed away. For long-lived isotopes like ^{54}Mn a significant fraction of the total activity at deployment can be the result of historic exposure.

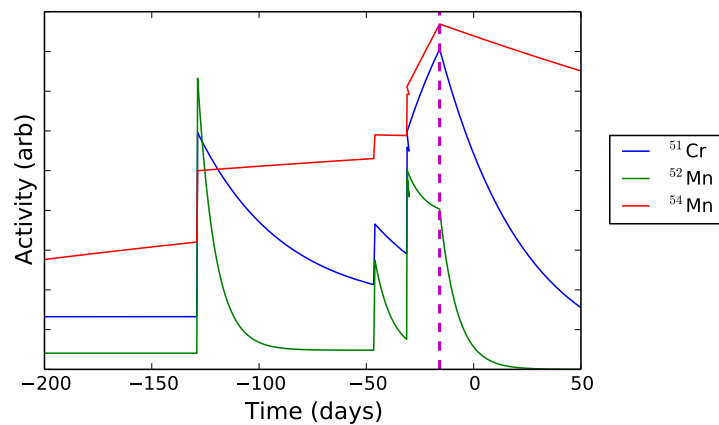


Figure 4.8: Activity of three cosmogenically produced isotopes over the final months preceding DM-Ice17 deployment (dashed purple line). Isotopes from the stainless steel pressure vessel selected to represent a range of half-lives are ^{52}Mn ($t_{1/2} = 5.59$ d), ^{51}Cr ($t_{1/2} = 27.7$ d), and ^{54}Mn ($t_{1/2} = 312$ d). Short-lived isotopes like ^{52}Mn are only impacted by the most recent exposure whereas long-lived isotopes like ^{54}Mn bear the residual effects of the entire exposure history. The x -axis counts from day 1 as 1 January 2011, adopting the same notation as later chapters; the y -axis units have been rescaled to allow display on the same graph.

Chapter 5

The DM-Ice17 Experiment

5.1 DM-Ice17 Detectors

DM-Ice17 is the first direct detection dark matter experiment deployed in the Southern Hemisphere. It consists of two detectors (denoted Det-1 and Det-2) with a combined 17 kg of NaI(Tl) crystal. The detectors were deployed to a depth of 2450 m in the South Pole ice (see Fig.5.1) and have been operating under remotely control since January 2011. A WIMP interaction in the sensitive region will result in the emission of scintillation light by the crystal, which is collected by photomultiplier tubes (PMTs) which are optically coupled to the crystal. Electronics boards digitize the PMT signal *in situ* and send the data over a ~ 3 km cable to a hub located on the surface. The detectors and electronics are protected by a stainless steel pressure vessel, and are encased in ice.

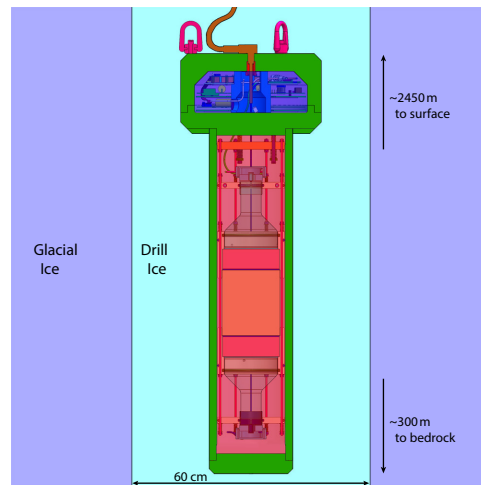


Figure 5.1: DM-Ice17 detector and experiment environment. The detectors are encased in ice at the South Pole deep below the surface; a nearby region of “drill ice” and “glacial ice.” A steel pressure vessel (green) protects the detector components and maintains separate volumes for the optical assembly (red) and electronics (blue).

Table 5.1: List of DM-Ice17 detector components and vendors. The table is divided into sections corresponding to where in the detector the component is found (*i.e.*, Optical Components, Assembly and Pressure Vessel, Electronics), and thus which text section addresses it.

Component	Product / Material	Vendor
Crystal	NaI(Tl)	Bicron/Saint-Gobain
Lightguide	Fused Silica	
PMT	9390-UKB	Electron Tubes Limited (ETL)
PMT Socket	C636KFP	Electron Tubes Limited
Silicone Gel	Q900	Quantum Silicones
Optical Grease	EJ-550	Eljen Technology
Rings & Collars	PTFE	Applied Plastics Technology
Stabilizing O-rings	Buna-N	McMaster-Carr
Assembly Rods	OFHC Copper	Southern Copper & Supply
Mounting Plate	OFHC Copper	Southern Copper & Supply
Pressure Vessel Tube	SAF 2205 Stainless Steel	Sandvik Materials Technology
Pressure Vessel (other)	SA182 Stainless Steel	Gulf Coast Machine & Supply
O-Ring Seal	Ethylene Propylene Rubber	Darcoid Nor-Cal Seal
Backup O-Ring	Parbak	Darcoid Nor-Cal Seal
Electronics Board	Custom	IceCube
High Voltage Supply	9730A + Custom Board	EMCO High Voltage
Isolation Transformer	FTB-1-1*A15+	Mini-Circuits

5.1.1 Optical Components

The crystals, lightguides, and PMTs used in DM-Ice17 were previously operating in the Boulby Underground Laboratory (2805 m.w.e. overburden) as part of the NaIAD experiment. The crystal assemblies were maintained separately in airtight copper boxes filled with dry nitrogen. Following the conclusion of the NaIAD experiment in 2003, the boxes maintained a sealed environment until they were reopened and the required components were recommissioned in 2010 for DM-Ice17. The remaining optical components were machined from clean material to complete the detector assembly.

The DM-Ice17 NaI(Tl) crystals (green in Fig. 5.2), DM80 (Det-1) and DM81(Det-2) in NaIAD publications [172], were selected as the only two encapsulated crystals in the NaIAD array. The crystals were grown by Bicron using the Bridgman-Stockbarger technique and were encapsulated by Saint-Gobain. The crystals are 8.47 kg and have cylindrical geometry with diameter 14.00 cm (5.512 inch) and length 15.00 cm

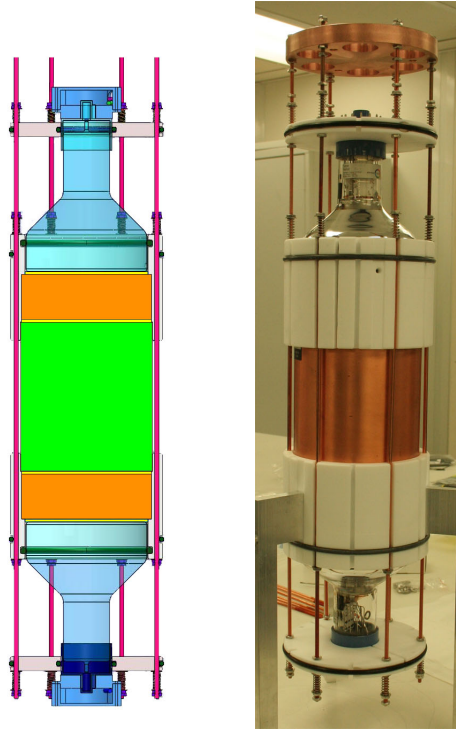


Figure 5.2: Engineering drawing (left) and photograph (right) of DM-Ice17 detector optical components. The sensitive detector, an NaI crystal (green, left), is coupled to two PMTs (blue, left) through quartz lightguides (orange, left).

(5.906 inch). The radial surfaces are wrapped in thin sheets of polytetrafluoroethylene (PTFE) to provide diffusive light reflection. The encapsulation to protect the hygroscopic NaI(Tl) crystal consists of a quartz window coupled to either end of the crystal and a copper housing wrapping the crystal and window. The encapsulation has outer dimensions of diameter 14.6 cm (5.75 inch) and length 16.5 cm (6.51 inch).

The scintillation light of each crystal is measured by two ETL low-background 5 inch 9390-UKB PMTs (blue in Fig. 5.2). These 10-dynode PMTs have typical quantum efficiency of 28% and gain of 7×10^5 at 1000 V. The low-background model features roughly a factor of ten reduction in K/Th/U contamination levels. The outer diameter of the PMT is 13.42 cm, but the active photocathode diameter is only 11.5 cm. The dynode chain voltage and pulse shaping was set by C636KFP voltage divider (9R:R:...:R voltage divider, $R = 330 \text{ k}\Omega$). Since the spectrum of each PMT is recorded separately, the PMTs of Det-1 can be differentiated as Det-1a (upper) and Det-1b (lower); the same naming convention applies to Det-2.

A fused silica lightguide (orange in Fig. 5.2) separates the crystal from its PMT on either side. The lightguides provide shielding to prevent the radioactive decays in the PMT glass from reaching the crystal

and causing a scintillation event. The lightguides have dimensions of diameter 14.4 cm (5.67 inch) and thickness 5.00 cm (1.97 inch).

A $\sim 1/8$ inch thick disk of Q900 silicone gel (yellow in Fig. 5.2) was cast at each optical interface (*i.e.*, between crystal, lightguide, and PMT). Compression of the gel layer allowed for mitigation of mechanical shock transferred to the crystal. Q900 has been demonstrated to be clean and stable for operation in the South Pole ice by IceCube, which used it to optically couple PMTs to pressure housings. The optical coupling of the interfaces was enhanced by applying a thin layer of EJ-550 optical grease.

PTFE (gray in Fig. 5.2) was machined into rings and collars to stabilize the assembly. A PTFE ring encompasses each light guide and accompanying optical interfaces to provide diffusive light reflection and thereby increase light collection. The ring has a length of 10.4 cm (4.10 inch) to allow ~ 1 inch overlap with both the crystal encapsulation and PMT to ensure no light escapes. The inner radius was machined to snugly fit the components and thus is stepped at three different radii. A slit running the length of the the ring allows for different rates of thermal contraction between the PTFE and enclosed optical components.

An additional PTFE component collars the plastic base of each PMT. A Buna-N O-ring (dark green in Fig. 5.2) on the inside of each PTFE component provides coupling to the PMT. A second Buna-N O-ring on the outside of each PTFE component snugly fits in the pressure vessel tube to constrain lateral movement while damping any mechanical shock.

Six threaded copper rods (magenta in Fig. 5.2) sit in vertical grooves machined into the PTFE rings and collars. A series of nuts and springs and nuts apply a compressive force to the optical components to hold them together despite any shocks induced during shipment. The copper rods also ensure alignment of the optical assembly prior to insertion into the pressure vessel. The copper rods rigidly mount the entire optical assembly to a $3/4$ inch OFHC copper plate for incorporation into the pressure vessel.

5.1.2 Electronics & Digitization

The signal from the PMTs and high voltage (HV) to the PMTs are carried from the electronics on shielded RG303 coaxial cable. All cables were produced with the same ~ 1.5 m length to preserve identical signal transit time between PMTs. The signal is passed through a FTB-1-1*A15+ isolation transformer before reaching the mainboard.

The electronics of DM-Ice17 are a subset of those used by IceCube [173] to control their Digital Optical Modules (DOMs), and were rigorously tested by IceCube for remote operation in the South Pole ice (see Fig. 5.3). Each PMT is controlled by a separate set of electronics boards: a DOM mainboard (MB), a delay board, and a HV board. The DOM MB controls the other two boards, communicates with the surface, and receives the PMT signal. The delay board provides a 75 ns delay line to provide time for electronics to

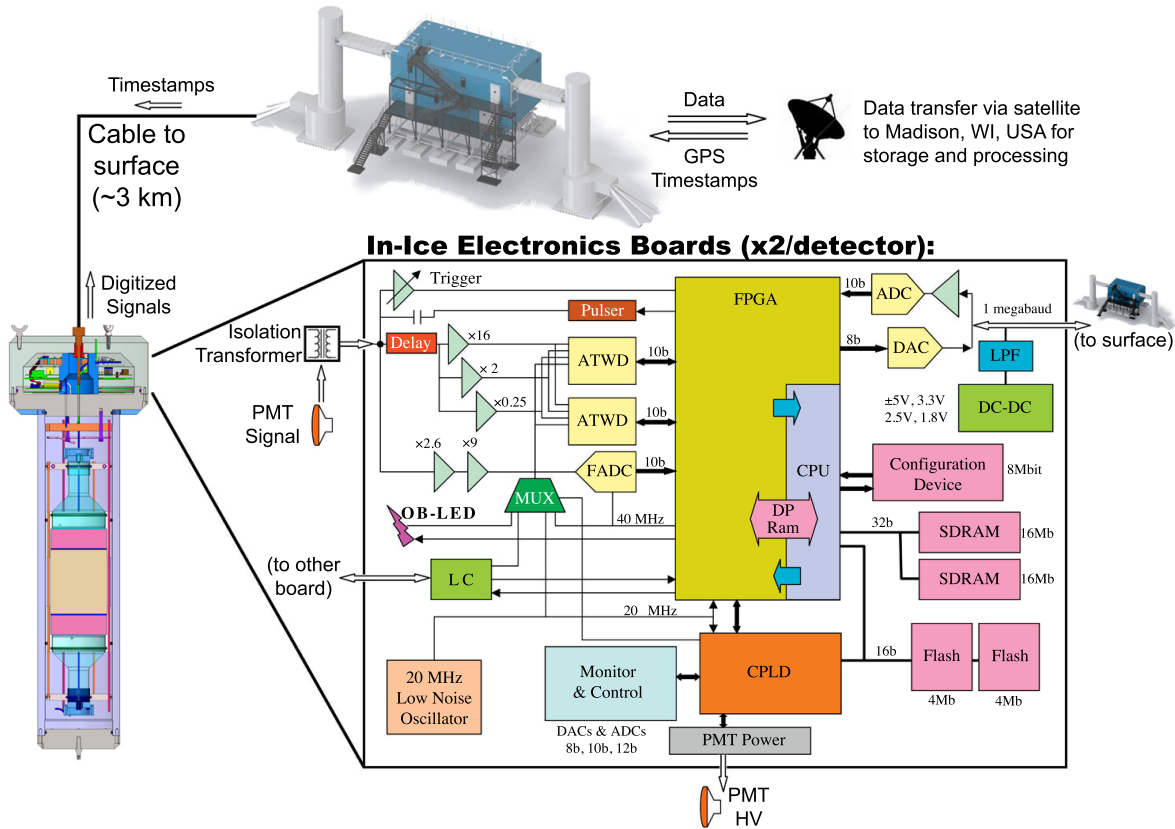


Figure 5.3: Block diagram of single DM-Ice17 and data transfer sequence [24]. Signals from the PMTs are passed through an isolation transformer and then digitized *in situ* by the MBs if they meet the coincidence condition. The digitized events are communicated to the hub which aggregates data from all PMTs into runs. Data are transferred via satellite to the data warehouse in Madison, WI. Event timestamps are established by each MB, which is calibrated to UTC time via a timing protocol with the hub.

respond to a trigger from the discriminator on the DOM MB. The HV board interprets the signal from the DOM MB for the high voltage supply to output a voltage up to 2050 V for the PMT.

The MBs are controlled and powered by a computing hub located on the surface in the IceCube Laboratory (ICL). The hub communicates the run settings to the MB and then receives all the digitized signal and monitoring information encoded in binary payloads. GPS timing is received from an antenna on the ICL and then distributed to every hub; the hub calibrates the 40 MHz MB local clock using a reciprocal active pulsing technique [173] which corrects for the 2500 m (Det-1) or 2995 m (Det-2) cable length. Connection with the hubs is possible via TCP/IP over a satellite during limited pass hours; on-site personnel can connect at any time.

The hub collects the hit, monitoring, and timing records as well as relevant logs for the specified run length (variable, but set to 3600 s for physics runs). The run data is then compressed and sent over the satellite connection for storage and processing in Madison, WI with a ~ 1 day delay.

The Field Programmable Gate Array (FPGA) on the MB is equipped with IceCube’s data acquisition (DAQ) software. Currently running the simplified “testDAQ” version, this enables the MB to coordinate collection of data and monitoring information, participate in timing calibration, and well as run calibration routines.

An analog PMT signal arriving at the MB is split to the discriminator, the Analog Transient Waveform Digitizer (ATWD), and the Flash Analog-to-Digital Converter (FADC). If the discriminator condition is met, it signals the digitizers to capture waveforms and sends a local coincidence (LC) signal to the connected MB. The signal to the ATWD is sent through the 75 ns delay line and is then split into three amplifiers ($\times 16$ gain ATWD0, $\times 2$ gain ATWD1, and $\times 0.25$ gain ATWD2) before being passed to the 128 sampling capacitors of one of the ATWDs, which can be digitized with 10-bit precision over a 2 V dynamic range. The signal to the FADC is passed through a waveform-shaping amplifier ($\times 23.4$ gain) before sampling a record at 40 MHz with up to 256 samples and 10-bit precision. If the LC condition is met, the FPGA signals the digitizers to record the desired length and precision of the waveform.

The DM-Ice17 sampling settings have been chosen within the limitations of the testDAQ software framework to maximize waveform information. The FADC record length is set to its maximum of 255 samples to preserve the longest record length of 6.375 μ s. Although each MB is equipped with two ATWDs to minimize downtime during waveform digitization (~ 30 μ s), testDAQ must select only one ATWD for a run; this advantageously removes any possible electronic baseline effect between the two ATWDs from data. During the physics run, all three ATWD channels collected record lengths of the full 128 sample. During runs to calibrate the single photoelectron (SPE) spectrum and noise, only ATWD0 and FADC records were collected (at maximum record length of 128 and 255 samples). The sampling rate of the ATWD is programmable from 100–500 MHz; for all presented data the sampling rate of all four MBs was ~ 210 MHz for a sample length of ~ 600 μ s. The testDAQ deadtime between successive digitizations was observed to be ~ 900 μ s, much greater than the digitizer downtime.

The HV settings for the PMTs were varied to produce the most stable running conditions, for all data presented here those are {1000, 1000, 1100, 950} V for {Det-1a, Det-1b, Det-2a, Det-2b}. After establishing the HV settings, the trigger threshold was scanned for each PMT to achieve a ~ 0.25 photoelectron hardware threshold. The LC window between the PMTs on the same crystal was set to 800 ns.

The DAQ queries the MB at periodic intervals to measure useful operational parameters. These include environmental temperature and pressure (at the MB) and PMT HV and trigger rate. The monitoring interval

was changed during the physics data run from 2 s period until February 2012 to 60 s after. This change was enacted when a waveform noise was discovered to be correlated with the monitoring sample times.

5.1.3 Pressure Vessel and Assembly

The pressure vessel was designed to protect the optical assembly and electronics from up to 10^5 psi of external pressure and maintain a clean, dry environment (see Sect. 5.2.2). The five stainless steel five steel pieces were machined specifically for DM-Ice17 to provide the necessary strength and dimensions. All seals were modeled after those used in IceCube's drill head (see Sect. 5.2.2) and use O-rings with backups and were bolted to specified tolerance with a torque wrench. Electrical connection into the pressure vessel was established using the same penetrator designed used for IceCube modules.

The tube body (enclosing the optical assembly) was machined to size from stainless steel tube stock. Sandvik SAF 2205 was selected because of its mechanical properties (yield strength (0.2 % offset) ≥ 485 MPa, tensile strength ≥ 680 MPa), the vendor was selected for its history of producing clean steel. The remaining steel components were machined from stainless steel bar stock.

The tube body with endcaps was pressure tested for 48 hrs at > 7000 psi in a water chamber at the University of Wisconsin–Madison Physical Sciences Laboratory (PSL). The pressure chamber could not accommodate the width of the pressure vessel top. The full pressure vessel was also subjected to a helium leak test.

Detector assembly began with the optical components. Three bolts suspend the copper mounting plate from the stainless steel mid-plate of the pressure vessel; a series of springs on these bolts provide mechanical shock damping for the optical assembly. The mid-plate provides structural support and isolates the lower volume containing the optical components from the upper region containing the electronics. The optical components were then lowered into the capped stainless steel tube and the tube and mid-plate were bolted together.

Six holes drilled at 45° angles through the steel mid-plate allow passage of the PMT cables and copper gas purge lines. The cables and copper lines were all potted with RTV silicone epoxy to provide an airtight seal. After the lower volume was flushed with dry nitrogen and the copper lines were crimped and epoxied close to completely isolate the lower gas volume.

The electronics boards were mounted around a hollow cylindrical steel support which allowed the PMT cables to be brought to the top of the board stack and provided structural support to the top of the pressure vessel. After PMT signal and HV connections were made, the pressure vessel top was lowered and the surface cable was connected to the MBs before sealing the detector.

5.1.4 Construction

The detector construction was compressed into a rapid timeline from 7 September–4 November 2010. Due to the time constraint, vendors and materials were selected based on reputation for low radioactive background, but were not pre-screened. During machining, excess material was set aside and later sent to the low-background counting facility at SNOLAB for evaluation.

All construction and machining was performed at PSL, allowing for optimal coordination between the tasks. The steel, copper, and PTFE components each required some degree of machining.

The crystals, lightguides, and PMTs were thoroughly cleaned with acetone, methanol, and deionized water prior to assembly. All other components were cleaned with ultra-high vacuum techniques. The assembly of the optical components was performed in the semi-clean room at PSL previously used for IceCube module assembly.

Custom shipping crates were created for DM-Ice17 to protect the assembly against mechanical and thermal shocks. A sensor located inside the crate monitored temperature, humidity, and shock during the entire shipment. The crates maintain the detector strapped down in its upright orientation and allow space for foam insulation surrounding the steel tube. The base of the crate is a pallet designed to be moveable by forklift during shipment. Removable caster wheels allow the crate to be moved into position for easier detector deployment at the South Pole.

5.2 South Pole Science

The DM-Ice17 detectors are located at a depth of 2457 m under the ice at the geographic South Pole. They are encased in ice at the bottom of two strings of the IceCube detector.

The geographic South Pole has been continuously inhabited since the construction of the original Amundsen-Scott South Pole Station in 1956. Construction of the station was performed by the U.S. Navy in support of the science mission for the upcoming International Geophysical Year (1957–1958). The harsh environment and drifting snow have forced the station to be rebuilt two times to continue supporting work, with the most recent station being dedicated in 2008.

The U.S. National Science Foundation is responsible for overseeing all science activity at the South Pole as part of the U.S. Antarctic Program. The daily operations of the program are coordinated by a private contractor - Raytheon through March 2012 and Lockheed Martin since. Logistic support, supply, and transportation to the South Pole are provided by the U.S. Air National Guard using LC-130 cargo aircraft flying from McMurdo station on the coast. Additional supplies are brought in once or twice per austral summer by the South Pole Traverse following an overland route from McMurdo.

During the austral summer, October to February, the station is bustling with activity and personnel when transportation to and from the South Pole is possible. Then through the dark winter months a smaller crew of 40–50 “winterovers” operates the experiments and keeps the station running. Communication with the Pole is limited in nature because the Pole is not visible from geostationary orbits; older satellites in very inclined orbits are contracted by the NSF to provide the limited communication and data transfer. These satellites, from the geostationary operation environmental satellite (GOES-3), Skynet (NATO-IVB), and tracking and data relay satellite (TDRS-6) systems provide intermittent coverage spanning a period of 12 hours per day.

The South Pole is a unique location for a wide range of science activities because of its remoteness, altitude (9301 ft), thick ice sheet, and atmospheric qualities. Support facilities for the different science programs are arranged around the station to minimize backgrounds for each observation (see Fig. 5.4). The Atmospheric Research Observatory (ARO) in the “clean-air zone” (upwind of station) makes ground-based and balloon-borne measurements particularly focused on greenhouse gases and ozone layer; it has the longest continuous atmospheric CO₂ record. The South Pole Remote Earth Science and Seismological Observatory (SPRESSO) in the “quiet zone” has seismic instruments buried 300 m in the ice and achieves the quietest seismic sensing environment on the planet; observation of the same seismic event by stations around the globe provides a probe of the Earth’s interior structure.

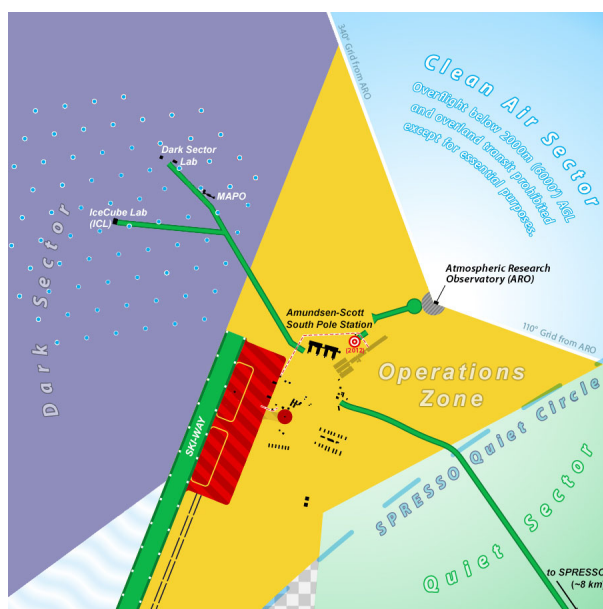


Figure 5.4: Geographic South Pole facilities [174]. The DM-Ice detectors operate in the “Dark Sector” at a depth of 2450 m in the ice under the IceCube array.

The “dark sector” hosts a suite of astrophysics experiments studying the cosmic microwave background (CMB), neutrinos, cosmic air showers, and dark matter. The South Pole is the best location for ground-based observations of the CMB because of the altitude, low atmospheric humidity (high transparency at microwave wavelengths), and incredible atmospheric stability due to the six-month day and night cycle. The current generation of experiments harnessing this environment includes the 10 m dish South Pole Telescope [175] on the Dark Sector Lab and the Keck Array [176] at the Martin A. Pomerantz Observatory (MAPO). The IceCube Laboratory (ICL) provides support to the IceCube Neutrino Observatory, IceTop air shower array, and DM-Ice17 detectors.

5.2.1 IceCube Neutrino Observatory

The IceCube Neutrino Observatory is a 1 km^3 instrumented array (see Fig. 5.5) taking advantage of the $\sim 2.85 \text{ km}$ thick ice sheet [177] and incredible ice purity at the South Pole. It consists of 5160 digital optical modules (DOMs) located on 86 strings and frozen into the ice at depths of 1450–2450 m. The strings are arranged in a grid with inter-string spacing of $\sim 125 \text{ m}$ and the 60 DOMs are evenly vertically spaced 17 m apart. IceCube is designed to be sensitive to neutrinos with energies of $10^{-1} - 10^6 \text{ TeV}$ [178].

The DeepCore subarray, located at the center of IceCube, is designed to increase the sensitivity down to neutrino energies of 10 GeV . It consists of eight strings with mostly higher quantum efficiency DOMs. The

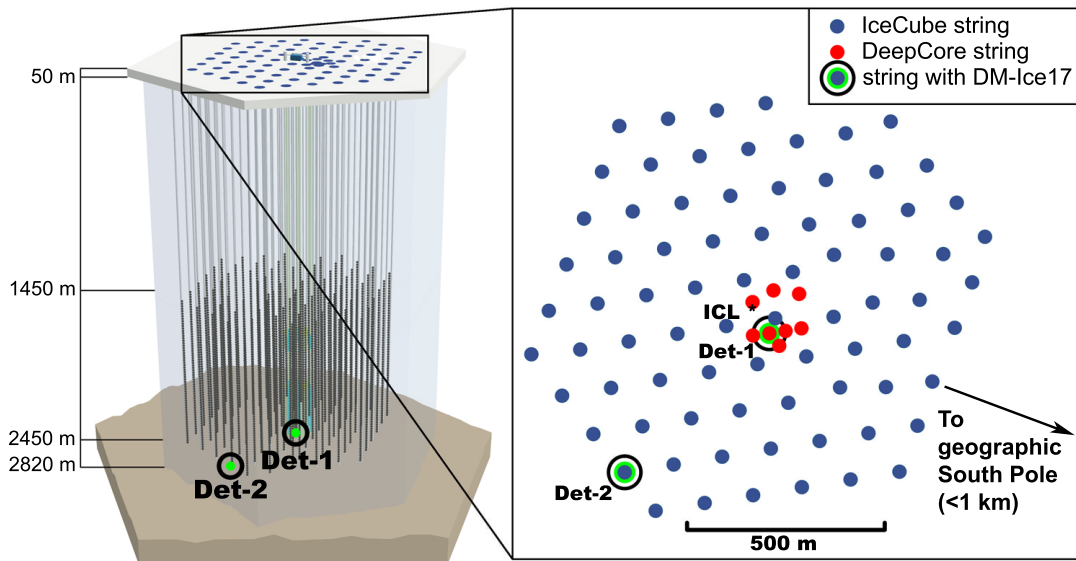


Figure 5.5: Location of DM-Ice17 within the IceCube array [24]. The two DM-Ice17 detectors, Det-1 and Det-2, are located at the bottoms of strings 79 and 7, respectively.

inter-string spacing is decreased to 42–72 m and 50 of the 60 optical sensors are at depths of 2100–2450 m with vertical spacing of 7 m [179].

The IceTop array is the air shower detector located on the surface. It consists of two tanks of frozen water located at the top of each IceCube string. Each tank is instrumented with two optical sensors (identical to those in-ice) running in different gain modes. IceTop is designed to be sensitive to primary cosmic rays of energy 100 TeV – 1 EeV [180].

The DOMs of these three arrays all digitize the PMT signals *in situ* using the same electronics boards [173]. The IceCube and IceTop arrays were constructed in parallel in phases from 2005–2010 as the South Pole operation season allowed.

The two DM-Ice17 detectors were deployed in December 2010 during the final season of IceCube construction. Det-2 was installed first on December 12 at the bottom of IceCube string 7 (IceCube array edge). Det-1 was installed four days later on Dec 16 at the bottom of IceCube strain 79 (IceCube array center, DeepCore infill). The IceCube cables are equipped with a 61st connection point, the “special devices breakout,” which DM-Ice17 utilizes to establish power, timing, and communication.

5.2.2 Ice Drilling

In order to deploy the DOMs to depths of 2450 m, specialized drilling equipment was designed and shipped to the South Pole. The top layer of ice is firm, a porous and less dense ice which requires a separate drill from the deeper ice. Both drills were designed by the Physical Sciences Laboratory (PSL) of University of Wisconsin – Madison.

The independent firm drill starts every hole by melting the ~ 50 m firm layer. It uses a glycol/water drill fluid which is circulated without loss between heaters and the drill head. It runs on 150 kW of electric heating and can be operated independently of the main drill to speed the drilling process.

The enhanced hot water drill (EHWD) is the main drill and produces the required holes of 60 cm diameter down to 2500 m. It sprays a high-pressure jet of water at 48 m/s from the drill head at temperatures of 66–85 °C (varies with depth). Holes were demonstrated to be drilled in as little as 27 hours. The water is recirculated from the hole and reheated during drilling, but an additional 30 L/min must be added to the drill to account for volume reduction from ice to water. The EHWD has a heating plant supplying 5 MW of thermal power and using just over 15000 L of jet fuel per hole [181, 182].

After drilling of a hole is complete, the 60 DOMs are connected in sequence as the string is lowered into the hole. The holes take several weeks to finish freezing, at which point the DOMs are turned on and begin data taking. The ice temperature continues to drop over a several month timespan as the hole ice equilibrates with the surrounding glacial ice.

5.2.3 Ice Properties

The properties of the ice at the South Pole have been measured using laser dust loggers to depths of up to 2500 m on eight separate holes [183]. At 2450 m, the dust concentration is ~ 40 ppb. Correlating the dust layers to those measured in ice cores from Dome C, the age of the ice at 2450 m is ~ 95 kyr.

The radioactive contamination levels of the glacial ice can be estimated assuming typical volcanic dust concentrations of 1 ppm of ^{238}U and ^{232}Th and 1000 ppm of ^{nat}K [183]. These estimates are consistent with the U concentration measured in the Vostok ice core [184] (0.1 pg U/g for 97 kyr sample [185]) using inductively coupled plasma sector field mass spectrometry. The EPICA Dome C ice core [186] has also been used to demonstrate consistency of dust across Antarctica [187].

The density of the South Pole ice from depths of 600–2500 m is ~ 0.92 g/cm³. The resulting overburden for DM-Ice17 is ~ 2200 m.w.e. (meters water equivalent), a depth comparable to some other underground facilities used for dark matter experiments (*cf.* Soudan at 2090 m.w.e., Kamioka at 2700 m.w.e, and Boulby at 2805 m.w.e.).

The temperature of the South Pole ice sheet varies with depth from -50°C at the surface to -6°C at the bedrock. At the 2457 m depth of DM-Ice17, the ice temperature is -18°C . NaI(Tl) crystals at this temperature have much longer decay times and comparable light output.

5.3 Experiment History

The NaI(Tl) crystals currently operating as DM-Ice17 were previously a part of the NaIAD array and collected physics data as part of 2002–2003 run [172]. They remained inoperative and sealed in dry nitrogen boxes from the 2003 until they were recommissioned in July 2010 for use in DM-Ice17. During recommissioning at the Boulby Underground Laboratory, the detectors took data using both the original NaIAD DAQ and IceCube MBs like the ones that would be used in-ice; the commissioning runs verified the comparable performance of the IceCube DAQ and provides the first set of source calibration run data.

The crystals, PMTs, and lightguides were brought to the surface and shipped to Madison, WI in September 2010. When anomalous behavior was observed in PMT dark tests, an additional two PMTs were retrieved. The four PMTs with the most consistent response were incorporated in the DM-Ice17 array. After the detectors were assembled, several days of characterization and source calibration runs were taken on the surface at PSL from 29 October–3 November 2010.

The detectors were then packed in the custom shipping crates and departed from PSL on 5 November. The detectors arrived at the South Pole on 1 December and ran a series of surface runs from 3–6 December. The surface runs at the South Pole had higher rates than at PSL, in agreement with expectation of the

cosmic ray rate at elevation. The surface runs did not include source calibration because of South Pole regulations.

Following deployment, the detectors were powered on for brief intervals throughout the remainder of December 2010 to monitor the freezing progress. As a precaution against the possibility that water might have leaked into the electronics region of the detectors, time spent powered up was minimized until the hole froze. The detectors were powered up on 5 January 2011 to begin collecting continuous data.

Chapter 6

DM-Ice17 Performance and Operations

Following the DM-Ice17 deployment, the detectors were turned on and began collecting data in January 2011. Following a commissioning period during which optimized run settings were established, a physics run at consistent settings was taken from June 2011 to January 2015. The detectors operated stably and continuously throughout the physics run, accumulating a dataset spanning over three-and-a-half years with an integrated exposure of 60.8 kg·yr.

This chapter describes the operation of the detectors and the run settings for the physics dataset. The isolated environment of the South Pole ice allows for long periods of uninterrupted running and an uptime of greater than 99%. Monitoring data collected regularly throughout the dataset has confirmed the stability both of the environmental conditions and the detectors. The dataset collected constitutes the longest and most complete in any NaI experiment after DAMA, and the livetime fraction is much higher than that achieved by other dark matter experiments.

6.1 Detector Operation

The DM-Ice17 hub located on the surface at the South Pole interfaces with the mainboards (MBs) located in the ice and serves as the controller of the detectors and access point for operator intervention. A twisted pair of copper wires runs between the hub and each MB providing communication and power. The hub is responsible for keeping universal time, for defining the beginning and end of runs, and for querying the MBs for their data. The single hub handles communication with all four MBs and aggregates their data; the data received in a run is categorized into ‘streams’ - hit, monitoring, and time calibration. The run settings and communication logs are also saved with the data for each run to preserve a complete detector image.

The MBs located in the upper compartment of the detectors (see Sect. 5.1.2) digitize the data *in situ*. When queried by the hub, they transmit the requested data to the surface in tagged binary packets; header bytes mark the data stream and MB of origin to allow efficient sorting at the hub..

A run begins with the hub querying the MBs to ensure they are in a responsive state. Following their response, the hub transmits the individual run settings to each MB (*e.g.*, trigger conditions, photomultiplier

tube (PMT) high voltage (HV), and sampling rate). When all the MBs have communicated a ready status, the hub logs the run start and begins querying for data; the MBs continue collecting and transmitting data until the hub sends the stop signal. Non-synchronous run starts and stops are introduced mainly by processing delays with negligible contribution from cable delays (~ 3 ms); these are corrected against in livetime calculations (see Sect. 6.4.2) and any recorded events are removed in processing by applying a software local coincidence condition (see Sect. 7.2.1).

The MBs maintain their settings between runs unless external intervention is made to run the boot sequence; this results in the PMTs holding the operating HV point continuously and minimizes instability at run transitions. In the downtime between runs (see Sect. 6.4.2), neither hit nor time calibration data is recorded by the MB; monitoring information, however, continues to be collected and buffered by the MB, awaiting a new query from the hub. In rare cases of extended detector idleness (see Sect. 6.4.3), the MBs may continue recording and buffering hours of monitoring data.

Only in the rare case of a reset of the MB are the buffered monitoring data lost and the PMT HV turned off. The HV remains at 0 V and no monitoring data is recorded until a new run is initialized. MB resets must be performed at least every two months to prevent buffer overflows crashing the DAQ (see Sect. 6.4.3).

6.2 Run Schedule

All DM-Ice17 physics data presented in this thesis is from the ‘standard run settings’ dataset spanning 1323 calendar days. This dataset began on 16 June 2011 when the run parameters were finalized (see Sect. 6.3) and concluded on 28 January 2015 when the PMT HV settings were altered. The vast majority of the dataset (99.93%) consists of the 31443 local coincidence (LC) runs; all energy spectra presented are based on the LC data subset. Regular runs taken with different trigger conditions comprise the ‘DarkNoise’ and ‘Pedestal’ subsets of data; these subsets are used for detector characterization (see Sect. 7.3.4) and waveform correction (see Sect. 7.1.2).

The LC runs employ the full set of trigger conditions, requiring a local coincidence condition between the two PMTs of a single detector. LC settings prescribe a 3600 s run duration, and the control program on the hub automatically transitions between LC runs in a continuous loop. To utilize the full dynamic range of the detectors, all four channels are digitized for every hit. Analysis of event timing allows a data-based assessment of variation in the run duration and downtime associated with the run transitions (see Sect. 6.4.2).

The DarkNoise runs employ relaxed trigger conditions with no local coincidence condition between PMTs. Since most scintillation events produce many photons (38 photons/keV nominal [188]) and will trigger both PMTs, the additional events recorded under DarkNoise settings are nearly exclusively low-energy - a mixture of single photoelectron (SPE) and noise events. DarkNoise runs are taken in pairs - one with the same trigger threshold used in LC runs and one at a lower threshold. Comparing the spectra of the runs, it is possible to

evaluate the SPE response of the PMTs (see Sect. 7.3.4). DarkNoise settings prescribe a 600 s run duration to obtain sufficient statistics of triggered events. Because only the low-energy events are of interest in DarkNoise runs, only ATWD0 and FADC channels are digitized; this makes the event data smaller which increases the buffer capacity of the MB and thus the maximum record rate.

The Pedestal runs employ an automatic trigger that completely bypasses all standard triggering conditions. Because the recorded waveforms do not correspond to real over-threshold triggers, pedestal waveforms are a probe of the natural baseline levels and fluctuations of each bin of the capacitors and digitizers. Pedestal settings prescribe a 60 s run duration to obtain sufficient statistics on the waveform variation. Waveform correction using pedestal runs is a part of the data treatment (see Sect. 7.1.2), requiring all channels to be digitized.

Manual interruptions of LC run looping are scheduled twice per month for a combined characterization run set. This schedule was implemented starting in November 2012 for the pair of DarkNoise runs, and in February 2013 for Pedestal runs. Prior to these dates, characterization run interruptions were performed on an intermittent and infrequent basis.

6.3 Run Parameters

The commissioning period lasted from 5 January – 16 June 2011, dates corresponding to detector turn-on and establishment of standard run settings. During this period, the run settings were optimized to ensure stable detector performance and maximized rates of relevant data. The settings for ATWD sampling rate, PMT HV, and trigger threshold were all adjusted to accomplish this. Other considered detector settings (*e.g.*, coincidence window) were determined to already be operating at optimal settings.

6.3.1 Sampling Rate

The sampling rate setting is a tradeoff between timing resolution and sample duration given the 128 sample digitization limit of the ATWD channels. Unexpectedly, the initially selected ATWD sampling rate (~ 120 MHz, for $> 1 \mu\text{s}$ records) frequently failed to collect pre-pulse samples, with digitization beginning partway up the leading edge of the pulse of some waveforms (see Fig. 6.1).

Increasing the ATWD sampling rate gradually decreased the waveform clipping phenomenon; the new setting was selected to maximize the sample duration while minimizing clipping (see Fig. 6.2). The ATWD sample windows are $\{596, 584, 649, 575\}$ ns, based on the $\{215, 219, 197, 222\}$ MHz sampling rates. The sampling rate was set to an identical digital-to-analog converter (DAC) setting for each MB, which produced the observed variation in the calibrated setting (see Sect. 6.6 on DOMcal calibration routine). The sampling rate is drifting minutely faster over time, resulting in a total decrease in the total ATWD window for each MB of $\lesssim 1$ ns over a four year period extending beyond the physics dataset. The comparatively short ATWD

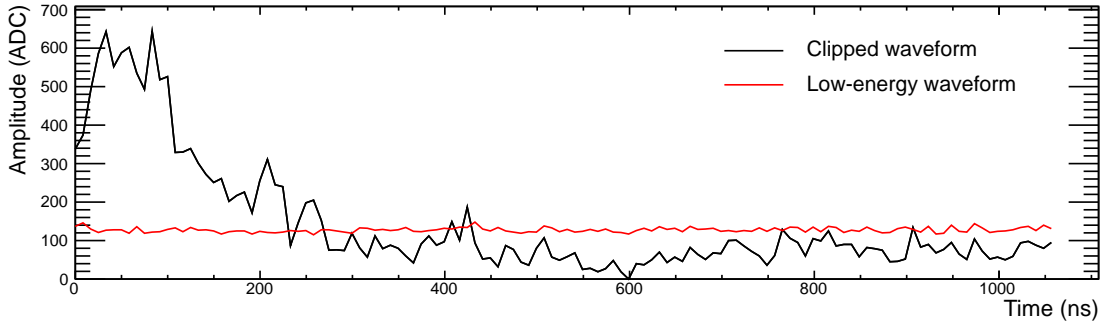


Figure 6.1: Waveform leading edge clipping as found in a sample Det-1a event. Digitization of the scintillation waveform (black) began after the signal began and has therefore lost some information. A low-energy waveform (red) is provided to illustrate the approximate baseline level of the uncorrected waveforms. The x -axis is calibrated to real time units, while the y -axis is in raw ADC units.

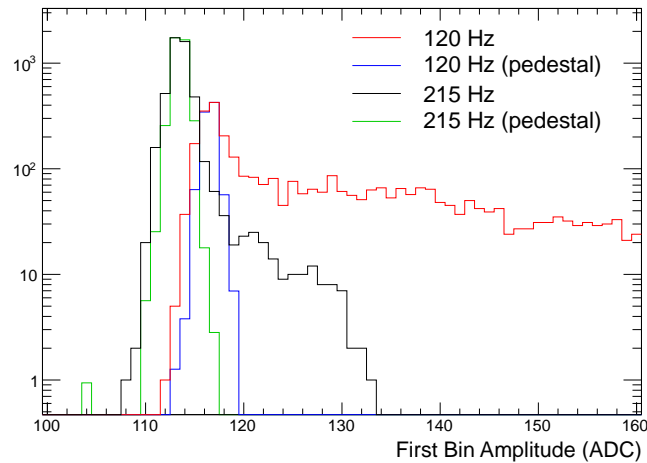
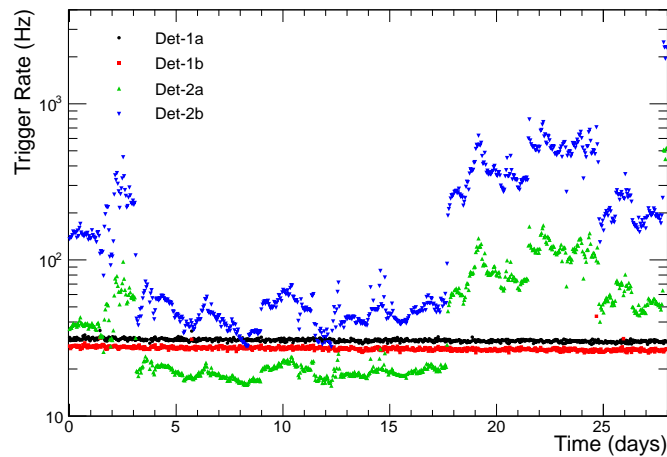


Figure 6.2: Demonstrated improvement in waveform leading-edge clipping effect at higher sampling rate; the tail in the distribution is indicative of more waveform clipping. The tail behavior is much stronger in the hour-long LC run at 120 Hz (black) than at 215 Hz (red) taken the same day. A pedestal run distribution is provided for each sampling rate (green, blue) to demonstrate the natural spread due to the baseline; the pedestal distribution is scaled to match the height of the max-bin of the matching data histogram. The few-ADC shift in the baseline amplitude between the two sampling rates is an unrelated effect caused by automatic corrections of the FPGA.

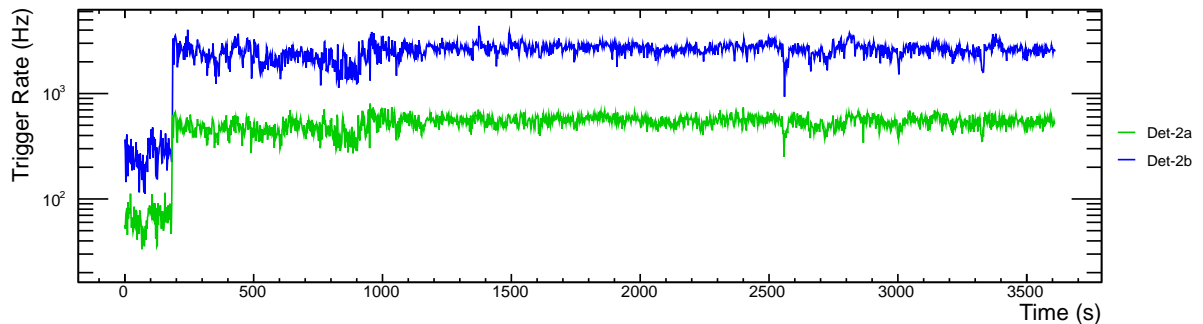
sampling window is complemented by the much longer FADC sampling window of $6.375 \mu\text{s}$ at its slower sampling rate of 40 MHz.

6.3.2 Photomultiplier Tube High Voltage

The PMT HV setting is a tradeoff between gain and longevity, stability, and high-energy pulse linearity. At the initial run settings, Det-2b displayed a large spread in the monitored HV value, and both Det-2 MBs exhibited periodic correlated spikes in monitored trigger rate (see Fig. 6.3); Det-2b was hypothesized to be the culprit because of the stronger rate spike effect and possible association with HV variation. Fearing PMT sparking which could damage the PMT over time and would produce a new class of background events, the Det-2b PMT HV was reduced until the rate spikes were eliminated. At its lower setting, the Det-2b monitored HV variation has decreased but remains much larger than for any other PMT (see Sect. 6.5.3).



(a) Average trigger rate for hour-long LC runs of February 2011.



(b) Trigger rate throughout a single run in February 2011.

Figure 6.3: Monitored trigger rates from February 2011 at initial Det-2b PMT HV value. In contrast to Det-1, both Det-2 detectors show erratic behavior which is highly correlated both over the course of a single run and when averaged. Reducing the Det-2b PMT HV completely eliminated this correlated behavior.

The PMT setting on the remaining PMTs were also reduced following the Det-2b adjustment to bring their setting below the nominal manufacturer recommendation (1100V and 2.7e6 gain). The HV was coarsely scanned down to find a lower set point which still maintained single photoelectron (SPE)-noise separation. The PMT HV settings which achieved our criteria were {1000, 1000, 1100, 950} V. Det-2a had consistently exhibited lower gain than any other PMT, so it required the highest HV setting. With these settings, Det-1a and Det-1b significantly differ in gain with saturation points for the ATWD0 (highest gain) channel at 2050 and 1400 keV; Det-2a and Det-2b are well gain-matched but run at significantly lower gain, reaching saturation for the ATWD0 channel at 2900 and 2800 keV.

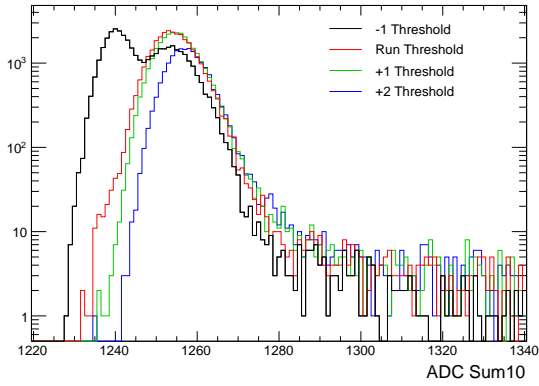
6.3.3 Trigger Threshold

The trigger threshold is a tradeoff between low-energy trigger efficiency and data rates (and corresponding deadtime). Threshold scans were taken first with DarkNoise trigger conditions to characterize the low-energy spectrum and the efficiency of collecting SPE and noise events (see Fig. 6.4). For each MB, the operating threshold selected optimizes the collection efficiency of SPE events for DarkNoise trigger conditions by establishing a sub-SPE level trigger threshold while maintaining minimal DAQ rate saturation. At lower threshold settings (-1 DAC units) a clear noise peak emerges for all MBs which dominates the event sample for all but Det-2b.

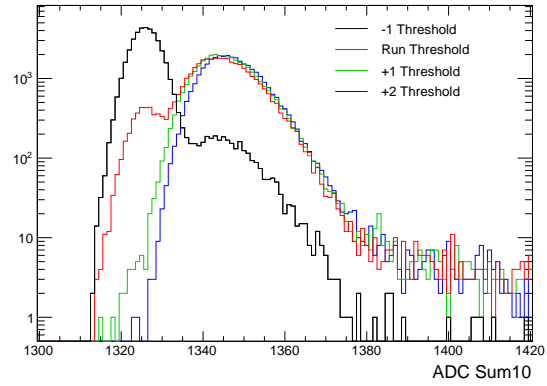
The selected operating threshold exhibits similar acceptance of most SPE events to higher thresholds but better acceptance of smaller-sum SPE events. Because the total event rate is below 100 Hz for all MBs except Det-2b at the operating threshold, the rate saturation effect is minimized for these MBs. Det-1b which has the highest rate of these three has the strongest indication of some SPE event loss on the higher-sum side of the distribution. Det-2b, whose event rate is ~ 120 Hz at the operating threshold exhibits clear event loss from rate saturation, but there is no significant presence of noise events at this threshold leading to its selection.

Following selection of the operating threshold, LC threshold scan runs were taken around the selected operating threshold to ensure the accidental coincidence rate of noise events was small. The total event rate observed is ~ 3 Hz for both detectors. This significantly reduced rate of events passing the trigger condition removes the rate saturation effect.

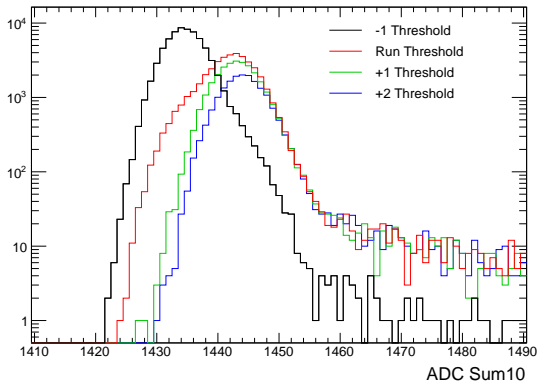
The precise trigger efficiency is not established from data for several reasons. Knowledge of the distribution shape is limited by the granularity of the DAC threshold scan, which cannot resolve a gradual transition between SPE-dominated and noise-dominated regimes (an effect most strongly seen in Det-2). The noise distribution can be inferred from the Pedestal runs, but no LED-calibration is included to assess the SPE distribution. Secondly, the trigger threshold controls an analog discriminator level against the raw signal, but the digitized signal can have additional noise from passage through the delay board, storage on



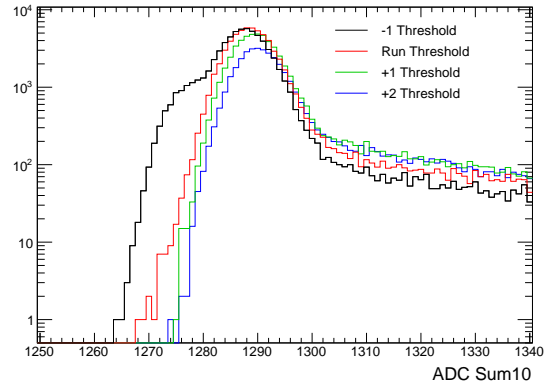
(a) Det-1a



(b) Det-1b



(c) Det-2a



(d) Det-2b

Figure 6.4: DarkNoise threshold scan runs producing single photoelectron (SPE) and noise spectra for all MBs at low-threshold (black), operating-threshold (red), and higher-threshold (green, blue) settings. The trigger threshold is set to optimize acceptance of SPE events while rejecting most noise. The SPE-noise separation power of the MBs follows their gain ordering, $\text{Det-1b} > \text{Det-1a} > \text{Det-2}$. Summing only the first ten bins (ADC Sum10) of the uncorrected waveform provides optimal separation of the two features. Rate saturation of the DAQ in the low threshold run suppresses the recorded rate of the SPE peak. Spectra shown have no waveform corrections applied (see Sect. 7.1), resulting in zero-offsets which vary by MB.

capacitors, and measurement by digitizing electronics. Although the trigger threshold setting is calibrated in charge units during the DOMcal routine, the error on the calibration places all threshold settings within error of zero charge.

6.3.4 Coincidence Window

The coincidence window is a tradeoff between noise reduction and signal acceptance. The coincidence window between the MBs of a single detector is set at ~ 350 ns (see Fig. 6.5). Due to poorly understood irregularities in the electronics response, event pairs are still digitized with partial acceptance for ~ 150 ns beyond the coincidence cutoff. Scanning the coincidence window parameter demonstrated that the the two shoulders at 350 and 500 ns moved together while the central distribution was unchanged.

The scintillation events are strongly concentrated within ± 100 ns while SPE-like noise events are the dominant contribution to the exponential tails (see Fig. 6.6). By maintaining a hardware coincidence window much wider than expectation for scintillation allows flexibility for offline analysis to assess the effect of varying window on removal of noise accidental coincidences.

The coincidence window is longer than the decay time observed in data of ~ 300 ns (somewhat slower at -20°C than the ~ 230 ns decay time at room temperature), allowing for photons from even low-energy events to reach both PMTs; the time for a photon to traverse the crystal, ~ 5 ns, is negligible in comparison. The coincidence window length also ensures that the two ATWD digitization windows, ~ 600 ns each, will overlap.

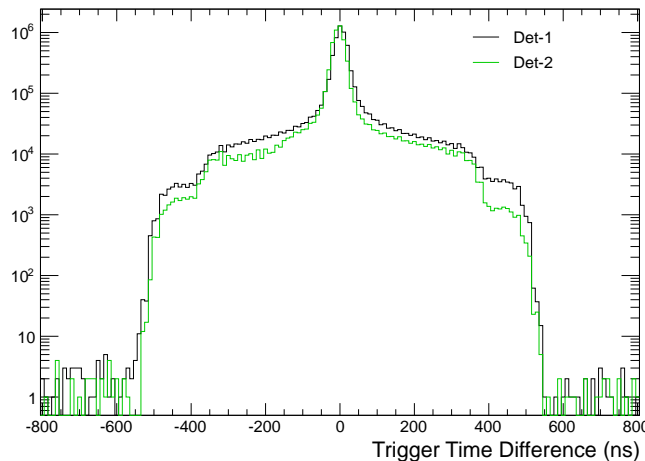


Figure 6.5: Trigger time differences for one month of data from both detectors of DM-Ice17. The coincidence setting allows full acceptance of all events with trigger time differences < 350 ns, and partial acceptance out to ~ 500 ns. The signal (scintillation) events are concentrated in the strong central peak (see Sect. 7.2.1) with complete acceptance; low-energy noise triggers are responsible for the broad shoulders.

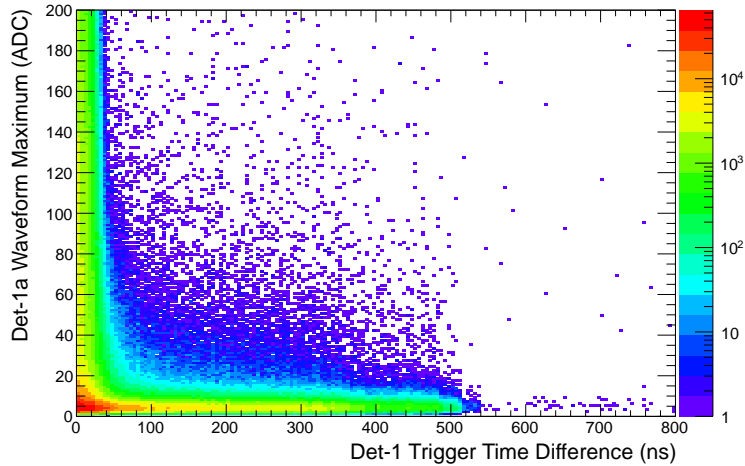


Figure 6.6: Distribution of waveform maxima and trigger time differences for one month of Det-1a data. High-amplitude waveforms (scintillation events) are concentrated below 100 ns, although their distribution widens at lower maxima. The high trigger time difference events are dominated by events with waveform maxima at SPE level, characteristic of SPE-like noise.

6.4 Livetime

DM-Ice17 detectors operate with uptime better than 99% (see Fig. 6.7) and livetime better than 98.8%. The loss of livetime experienced by the detectors comes from a combination of ‘regular’ and ‘acute’ sources. Regular loss is comprised of hit deadtime and run transition downtime, amounting to 10–20 s for each run, as well as characterization run interruptions occurring every two weeks and lasting 21 min. Acute loss is unexpected downtime comprised of runs which fail data quality checks and time when the hub and MBs are not communicating. The efficient operation of DM-Ice17 has allowed the accumulation of a total 60.8 kg·yr exposure in the physics dataset.

6.4.1 Deadtime

Hit deadtime is introduced because there is a minimum time required for the DAQ to be ready to record a subsequent event following digitization. The observed hit deadtime of $\sim 730 \mu\text{s}$ is significantly longer than the MB design specifications indicate. Tests using an upgraded DAQ software found that the hit deadtime could be reduced by a factor of six with the same MBs and digitizing chip configuration (only using ATWD chip 0 for event digitization). In order to maintain a stable and well-characterized run configuration, the older testDAQ software was maintained throughout the dataset and the hit deadtime quantity is derived from data.

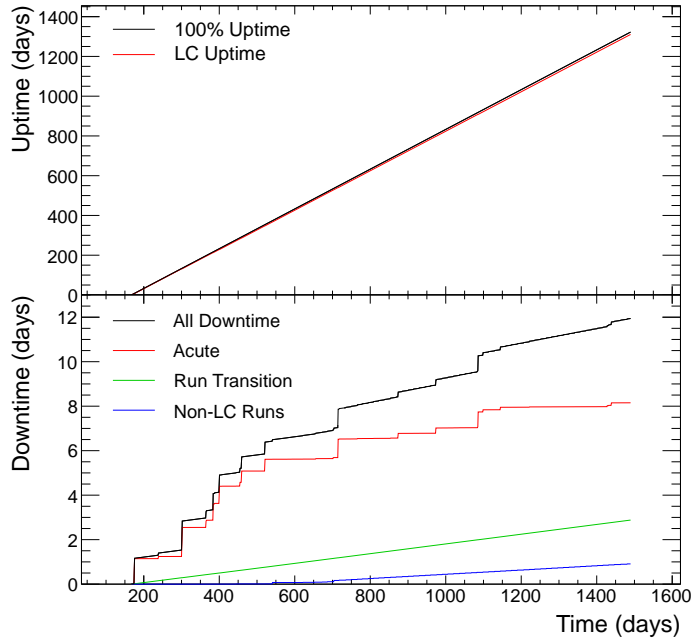


Figure 6.7: Integrated LC exposure for Det-1 of DM-Ice17 (top) and total downtime (bottom) over the three-and-a-half year physics dataset. The LC uptime (red, top) is plotted against the theoretical maximum uptime (black, top); the total downtime (black, bottom) is divided into its various sources (colors, bottom). The uptime fraction for Det-1 is 99.10% for LC data and 99.17% for all data, while the uptime fraction for Det-2 (not plotted) is 99.08% for LC data. The discrepancy between the uptime of two detectors is solely from Det-2 experiencing a slightly longer run transition downtime. The x -axis counts from day 1 as 1 January 2011, with the physics dataset beginning on day 167 (16 June 2011) and ending on day 1489 (28 January 2015).

This analysis characterizes hit deadtime by aggregating monthlong datasets of LC data and analyzing the time difference between each adjacent pair of events for a single MB. Aggregated LC datasets are necessary for this analysis in order to accumulate sufficient statistics at minimal event separation while avoiding irregularities which have been observed when the rate saturates the DAQ capacity. DAQ saturation has been observed to increase the hit deadtime by as much as 25%; this effect is not fully understood given the non-paralyzable nature of the deadtime but difficult to characterize within the limitations of the data transfer rate.

The leading edge of the hit separation distribution can be represented by an offset error function convolved with an exponential distribution:

$$\begin{aligned} f(t) &= A \cdot \left(\operatorname{erf}(B \cdot (t - t_{50})) + \frac{1}{2} \right) \cdot \exp(C \cdot t) \\ &= A \cdot \left(\frac{2}{\sqrt{\pi}} \int_0^x \exp(-B \cdot (t - t_{50})^2) dt + \frac{1}{2} \right) \cdot \exp(C \cdot t) \quad , \end{aligned} \quad (6.1)$$

where B parametrizes the spread in the observed deadtime and t_{50} is the time after a preceding trigger at which the DAQ will be live in 50% of cases (see Fig. 6.8). The error function describes the variation in the deadtime (an ideal DAQ might require modeling with a Heaviside step function), while the exponential describes the Poisson-governed random hit separation timing distribution.

The deadtime has been analyzed for each month of the dataset (see Fig. 6.9) and demonstrated to be stable after correction for two anomalous shifts. The first eight months plotted (July 2011–February 2012) show higher deadtime for both Det-2 MBs; these months correspond to the higher monitoring rate (switched February 28, see Sect. 6.5). The possible connection between monitoring and hit deadtime, as well as its stronger effect on Det-2, are not understood. The Det-2b hit separation distribution shifted towards smaller deadtime for a period from March to May 2013 resulting in fit t_{50} values dropping by 20 μs . The shifts did not correspond to any interruptions in detector operation and similar behavior has not been observed in the other MBs or at any other time in the same detector.

Other cutoff percentages, x , can be evaluated from B and t_{50} using the inverse error function:

$$t_x = \frac{\operatorname{erf}^{-1}(x/50 - 1)}{B} + t_{50} \quad . \quad (6.2)$$

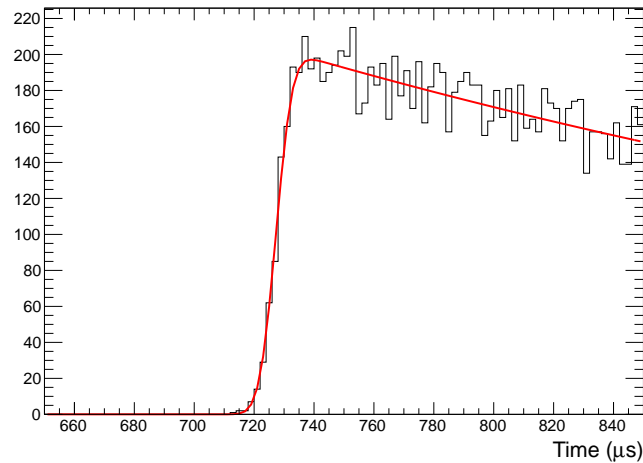


Figure 6.8: Histogram of hit separation for one month of Det-1a LC data with fit to Eqn. 6.1. The hit deadtime for each MB is derived individually from fits to monthlong datasets yielding comparable deadtime estimates of $\sim 730 \mu\text{s}$.

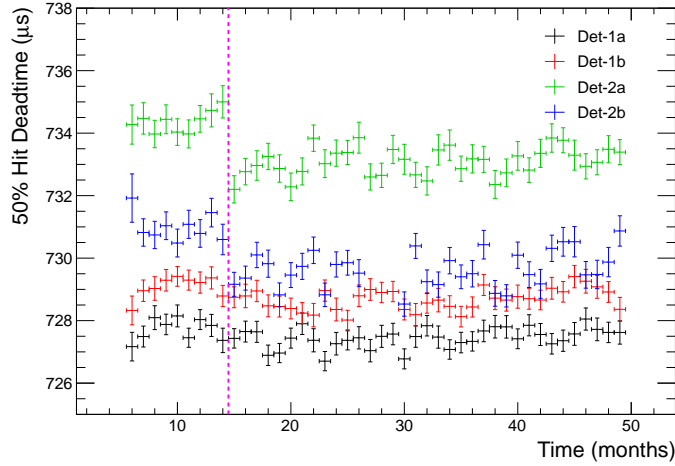


Figure 6.9: Values of t_{50} obtained for each DM-Ice17 MB by fitting monthly hit separation data. Fit data are plotted for the entire physics dataset, June 2011 – January 2015 (months 6 – 49). The dashed magenta line at the end of month 14 indicates when the monitoring frequency was changed. Only the months after the monitoring frequency switch are used in calculating the hit deadtime because of the discontinuity observed. The error bars in y are the fitted parameter errors and in x span the full month.

The larger uncertainty in the fitted value of B drives the increase in uncertainty for calculated t_x values relative to that of t_{50} . The difference between t_{95} and t_{50} is $7-8 \mu\text{s}$, a 1% effect.

The average deadtime (see Tab. 6.1) is calculated as the weighted mean of the fit values and errors after removing anomalous months prior to the monitoring interval change and corresponding to the Det-2b shift. Linear regression fits provide slope estimates consistent with zero with a total effect of the slope over the 35 months less than the calculated deadtime uncertainty. In all cases, the biased weighted sample variance

Table 6.1: Average deadtime values for DM-Ice17 based on fits (see Fig. 6.8) to March 2012 – January 2015 hit separation data. The two reported deadtimes, t_{50} and t_{95} , correspond to times at which the DAQ is live following a digitization in 50 and 95% of cases, respectively. The reported values and errors are the weighted mean and biased weighted sample standard deviation.

	t_{50} (μs)	t_{95} (μs)
Det-1a	727.43 ± 0.32	735.08 ± 1.00
Det-1b	728.67 ± 0.33	736.35 ± 0.72
Det-2a	733.08 ± 0.44	740.46 ± 0.99
Det-2b	729.59 ± 0.57	736.99 ± 1.24

and the sample variance are the same to $< 3\%$, indicating the scatter of the points was random. For all detectors except Det-2b, the calculated deadtime uncertainty closely matches the average of the fit error bars. For Det-2b, the biased weighted sample standard deviation is 25% larger, indicating a possible jitter in the deadtime value. Removal of this jitter would make the Det-2b deadtime uncertainty more closely match the other MBs, but is only a 0.02% effect on the total deadtime. Inclusion of the spring 2013 shifted Det-2b deadtime values would increase the quoted deadtime errors by a factor of 10 for that MB.

A secondary source of hit deadtime may arise from non-coincident over-threshold signals. Because these events are not digitized, the deadtime cannot be verified from data and is assumed to follow MB design specification. The secondary hit deadtime of two clock cycles (50 ns) originates from a MB re-preparing to accept a trigger after the coincidence window ends without a coincident trigger from the paired MB. The DarkNoise trigger rates of 100 Hz place an upper limit on this type of hit deadtime of 18 ms; this $< 1\%$ effect is much less than that of primary hit deadtime.

The digitization rate limit of the MBs characterized by the hit deadtime analysis is much larger than the data transfer rate limit of the cable. The transfer rate limit has been observed to be ~ 72 Hz (93 kB/sec) for each MB when all channels are recording; DarkNoise runs operating with fewer channels active have a higher transfer rate limit (~ 115 Hz) on account of the reduced amount of digitized data per event. Given the capability of the MBs to buffer hundreds of events and with typical event rates at standard LC run settings of ~ 3 Hz, the transfer rate limit contributes a negligible amount to the total downtime.

Because the detector event rates have decreased over time, the average hit deadtime per run has decreased by a corresponding amount even for the assumed constant deadtime per hit (see Fig. 6.10). Most of the event rate decrease corresponds to the hardware monitoring setting change in February 2012 and the associated decrease in EMI noise events. Det-1 average rates fall from 11,800 to 9,100 events/run, corresponding to deadtimes of 8.6 and 6.7 s/run. Det-2 average rates fall from 8,900 to 8,300 events/run, corresponding to deadtimes of 6.5 and 6.1 s/run. The total hit deadtime in standard LC runs over the three year dataset is estimated to be 2.6 d for Det-1 and 2.2 d for Det-2, a total loss of $< 0.2\%$ livetime.

6.4.2 Run Transition Downtime

Run transition downtime is introduced because the MBs do not continuously digitize events and seamlessly transition from one run to the next. Communications and processing delays from the hub and MBs cause a gap of several seconds between the end of one run and start of the next. The different response delays of each MB cause the run start and stop to be asynchronous and differ from the prescribed length, which is corrected only with the software LC condition imposed on all data (see Sect. 7.2.1).

Analysis of the distributions of time differences between the first (t_{first}) and last (t_{last}) events of each MB in each LC runs (see Fig. 6.11) allows a determination of both the uptime and downtime per run. The

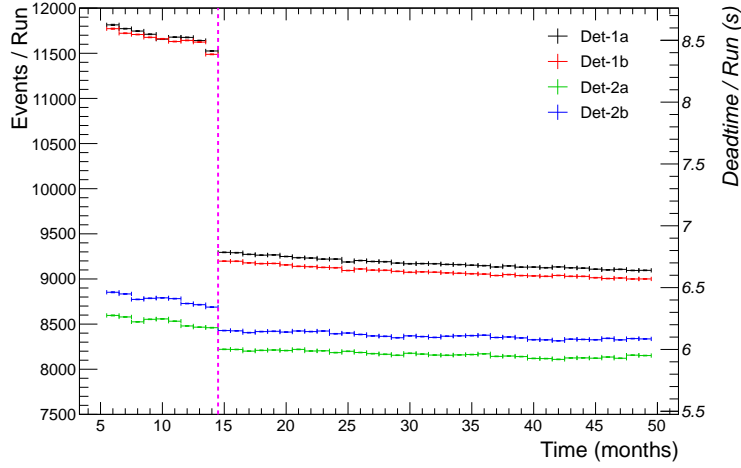


Figure 6.10: Average number of events per run (left axis) and associated deadtime (right axis) for each month of the physics dataset. The sharp drop at the end of month 14 (February 2012, pink dashed line) is due to the decreased EMI noise rate from monitoring (see Sect. 6.5). Statistical y error bars for monthlong averages are < 5 events/run and therefore not evident in this plot.

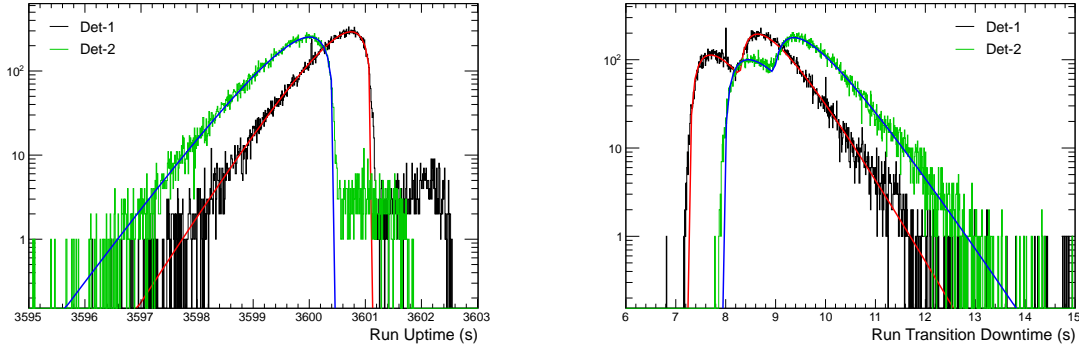
calculated average run transition downtimes are 7.87 and 8.55 s for Det-1 and Det-2, respectively. The run durations (‘uptimes’) are 3601.13 and 3600.45 s for Det-1 and Det-2, respectively.

The important quantity is the combined uptime or downtime for a detector because coincidence is enforced in all analyses by pairing events with the software LC cut. For random physics triggers in a detector, event rates are governed by Poisson statistics, resulting in the arrival time of events relative to the start or end of a run to follow a single exponential distribution. The uptime for a single run (see Fig. 6.11a) follows the expected distribution for sampling from the same exponential distribution for the starting and ending hit:

$$f(t) = \begin{cases} (t_{up} - t) \cdot A \cdot \exp(B \cdot x) & t < t_{up} \\ 0 & t > t_{up} \end{cases}, \quad (6.3)$$

where t is the observed time difference between the later t_{first} and earlier t_{last} for a MB pair and t_{up} is the true run uptime. The downtime between runs (see Fig. 6.11b) follows a similar distribution with switched exponential and cutoff terms. Unexpectedly, the downtime is observed to sample from two distributions, so the fit function identifies two cutoff distributions with the same exponential rate:

$$f(t) = \begin{cases} 0 & t < t_{down1} \\ (t - t_{down1}) \cdot A_1 \cdot \exp(-B \cdot t) & t_{down1} < t < t_{down2} \\ (t - t_{down1}) \cdot A_1 \cdot \exp(-B \cdot t) + (t - t_{down2}) \cdot A_2 \cdot \exp(-B \cdot t) & t > t_{down2} \end{cases}, \quad (6.4)$$



(a) Histogram of time difference between the first and last paired events to characterize run livetime. Both detectors are live for a period longer than the prescribed 3600 s run.

(b) Histogram of time difference between the last paired event of one run and first paired event of the next run to characterize run transition downtime. Two cutoffs are visible for each detector with 42% of runs following the earlier cutoff.

Figure 6.11: Run duration and run transition downtime for DM-Ice17 detectors as derived from all LC physics data taken from June 2011 – January 2015 (31443 LC runs).

where t is the observed time difference between the earlier t_{last} of one run and later t_{first} of the next run for a MB pair and t_{down1} and t_{down2} are the two possible true downtime durations between runs.

The double-downtime distributions have cutoffs that are 1.00 s different from each other, consistent within error of exactly 1 s offset. The data indicate a 42:58 split between the shorter- and longer-downtime distributions. Although the origin of the split distribution is not well understood, it is believed to originate from processing delays from the hub because the run transitions with shorter downtime are correlated, occurring either for all MBs or none. No features are observed in the uptime distribution following the split downtime distribution.

The exponential rate constant, B , of the distributions in Eqn. 6.3 and Eqn. 6.4 should match the event rate of the appropriate detector. This parameter was allowed to float freely in all fits, but results were consistent within error of each other and the event rate for each detector.

The only features of these distributions which have changed significantly over the three year dataset are caused by monitoring noise events and diminished accordingly when the monitoring rate was decreased; the effects are only visible in Det-1 because of its stronger monitoring pickup. A peak in the uptime distribution at 3600.04 s and a corresponding peaks at 8.00 and 10.00 s in the downtime distribution were observed in the first eight months of data as $\sim 70\%$ excesses above background. The features are diminished in Fig. 6.11 by combination with the full dataset.

Dividing the data into subsets to assess time evolution confirms that the t_{up} and t_{down} cutoffs are stable over the dataset. The exponential rate constants of the distributions change consistent with the known event rate decrease over time and especially with the hardware monitoring rate change. The monitoring pickup features visible in Det-1 are only present in data prior to the monitoring rate change.

A similar analysis of the same distributions for single MBs reveals patterns in the asynchronous run starts and stops, with Det-2a records 57% of the first hits in a run and Det-1b records 85% of the final hits. The run durations range from 3600.5 s for Det-2a to 3601.5 s for Det-1b, while the total duration that at least one MB is recording is 3602 s. The run transition downtimes range from 9 s for Det-2a to 8 s for Det-1b, while the full dead window with no MBs recording hits is 7.5 s. These inconsistencies between the run timing of different MBs reinforce the necessity of detector-based analysis.

For the three year dataset from June 2011–January 2015 there were 31443 LC of 31648 total runs. This number of run transitions accounts for a total of 2.9 days of downtime for Det-1 and 3.1 days for Det-2.

6.4.3 Acute Downtime

Acute downtime encompasses all the unexpected losses of data taking, primarily due to extended cessation in data taking (see Fig. 6.12). This downtime is further subdivided into buffer crashes, power outages, and run coordination issues; the remainder are rare instances when a run fails data quality checks during processing. This source of downtime exceeds all others, accounting for 8.1 of the total 11.9 days.

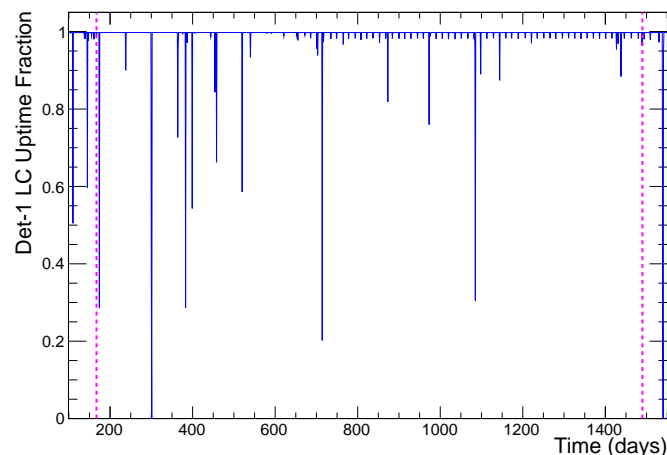


Figure 6.12: Daily Det-1 LC uptime fraction. Since beginning the standard settings run, there have been 14 occasions of $< 90\%$ uptime. The small downward spikes starting at day ~ 600 are interruptions for biweekly characterization runs. The x -axis counts from day 1 as 1 January 2011, with the physics dataset beginning on day 167 (16 June 2011) and ending on day 1489 (28 January 2015) as marked by pink dashed lines.

Buffer crashes are caused by an unforeseen behavior in the hub-DAQ communication causing the MBs to become unresponsive after 1500 hr of operation. This electronics effect will impact the MBs non-simultaneously, but in consistent order of Det-1b, Det-1a, Det-2a, Det-2b. In the event of this MB failure, it is necessary to reset the hub and MBs to resume data taking. In total there have been five instances of detector crashes ranging from June 2011 – June 2012 accounting for 3.4 days of downtime. All five crashes occurred during the standard running dataset as detector resets accompanying power cyclings were more common during the commissioning phase. Preventive measures in place since June 2012 to reset the MBs preemptively on a regular schedule have avoided further outages of this type.

At the South Pole, all power is generated at the central power station to control fire risk in the low humidity environment. All hubs in the ICL receive backup power from uninterruptible power supplies (UPSs) to mitigate the effects of short-duration power fluctuations. In total there have been eight instances of complete power loss to the hub (and consequently also to the MBs) accounting for a combined 3.4 days, three from power outages to the ICL lasting longer than the UPS battery, two from faulty fire alarms causing the hub to immediately shut down, and three related to UPS upgrades.

Run coordination downtime is a combination of human error and the complications of operating detectors which are only accessible over an intermittent satellite connection. In total there have been four instances of extended (> 300 s) run coordination downtime accounting for a combined 1.1 days: two from detector stops associated with the IceCube detector and two from early termination of a satellite connection. The combined effect of short interruptions for detector operation ($\lesssim 60$ s) introduced during every manual interruption of data taking for characterization runs is responsible for the remaining small fraction of the acute deadtime.

Data quality checks for DM-Ice17 are a simple sequence to ensure that the DAQ was operating properly with all MBs reporting and the data timestamps are accurate. Most cases of failure stem from a timing calibration issue between the hub and MB, with a subset caused by early termination of data from any number of MBs. To ensure that the standard dataset contains only good data and for simplicity of analysis, partial good runs are removed completely from the dataset rather than adjusting on a detector-by-detector basis for differing uptimes. If necessary, parts of this data could be recovered for future analysis.

6.5 Monitoring

Detector stability is a critical feature for any dark matter experiment, especially for those searching for a time-varying signal. To characterize operational stability, the DAQ collects regular monitoring information. This data is digitized *in situ* and sent to the hub marked for the monitoring stream. Once the monitoring intervals are set, all monitoring information is collected and buffered by the MB without further prompt from the hub.

The most commonly referenced monitoring quantities are all from the hardware monitoring; these are temperature, pressure, PMT HV, and trigger rate. In addition, the hardware monitoring also contains records the voltage and current throughout the MB, as well as the programmable DAC settings. No deviations from expected values have been observed for any of these values, although they remain additional data quality metrics.

Noise waveforms showing evidence of electromagnetic interference (EMI) were discovered in the data in early 2012. Following the positive correlation of this noise with hardware monitoring events, the monitoring interval was increased from 2 s to 63.13 s on 28 February 2012; the new non-integer interval was a consequence of the setting being stored as a unsigned long integer number of 40 MHz MB clock ticks, and the requested interval overflowing the byte allocation. When the discrepancy was confirmed, the monitoring interval was decreased to 60 s on 23 June 2012. This EMI pickup can be effectively removed from data with cuts or assessed by timing correlation with known monitoring event times, and has been demonstrated to have no effect on the spectrum above 4 keV (see Sect. 7.2.2).

The other information within the monitoring data stream which is recorded includes configuration monitoring reports and status updates. The configuration monitoring is performed on a 60 s interval throughout the dataset and tracks control software versions. The status updates occur at the beginnings of runs to report DAC states, ends of runs to report the total number of events, and in the middle to report the number of recorded waveforms and buffer status. When monitoring data is referenced elsewhere throughout this thesis, it refers only to the subset of hardware monitoring data

6.5.1 Temperature

The temperature is recorded by a sensor located on the MB (see Sect. 5.1.2). The temperature is reported with 0.0625°C precision and the sensor range covers the normal operation of the MBs in ice and at room temperature. The recorded temperature is expected to be warmer than that of the surrounding ice (and the crystals) because each MB dissipates ~ 3.5 W of power, corresponding to a $\sim 10^\circ\text{C}$ increase in the local temperature [173].

The temperature over the entire recorded period (see Fig. 6.13) has been very stable and well understood. The initial decreasing temperature is characterized by two exponentials – the faster one as the drill water column freezes ($\tau \sim 10$ d) and the slower one as the injected heat from drilling dissipates into the glacial ice ($\tau \sim 100$ d). Over the course of the presented three-year dataset, the temperature has decreased only 0.25–0.31°C and the average daily RMS temperature deviation is $< 0.025^\circ\text{C}$.

The temperature of the crystals is expected to track the general exponential trend recorded by the MBs, but at a colder temperature closer to that of the ice and less subject to fluctuations. The two MBs of a single detector are enclosed together in the 6200 cm³ upper volume of the pressure vessel, ~ 0.4 m separated

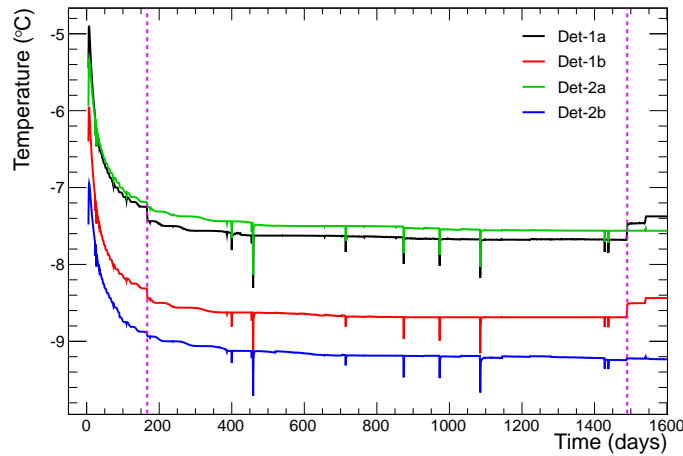


Figure 6.13: Average daily temperature recorded by the DM-Ice17 mainboards. The temperature has been very stable over the three year dataset, showing a decrease of only $0.25\text{--}0.31^\circ\text{C}$ and daily RMS temperature deviation $< 0.025^\circ\text{C}$. The discrepancy between the measured values of adjacent paired MBs is due to the effect of heating by MB components. The x -axis counts from day 1 as 1 January 2011, with the physics dataset beginning on day 167 and ending on day 1489 (pinked dashed lines).

from the crystal. The discrepancy between the readings of the two MBs in a single pressure vessel is because the temperature sensor of the upper mainboard (Det-1a or Det-2a) is located directly above the DC-DC converter of the lower MB; the DC-DC converter is the component which is known to dissipate the most heat [173].

The deviations from exponential behavior observed in Fig. 6.13 are all related to MB heating. The initial fast rise (day 5) corresponds to when the detectors were turned on and the MBs began dissipating heat and warming themselves above the temperature of the surrounding ice. The nine brief downward spikes (*e.g.*, days 400 and 459) correspond to the subset of acute downtime periods (see Sect. 6.4.3) when the MBs lost power and ceased warming the surrounding ice. The step discontinuities (*e.g.*, day 167 and 1489) corresponds to the lowering of the PMT HV setting which initiated the standard settings run; the discontinuity is less pronounced in Det-2 because the Det-2b PMT HV was adjusted previously to address its instability (see Sect. 6.3).

An estimate of the magnitude of the MB heating effect is made by tracking the temperature following extended periods when the MBs were without power (see Fig. 6.14). Of these events, the most pronounced effect is seen on 3 April 2012 (day 459) following a power outage at the ICL because of a fire alarm. The MBs all record a temperature of $\lesssim -16^\circ\text{C}$ as their initial reading ~ 2 min after powering on; their initial rate of temperature increase of $0.3^\circ\text{C}/\text{min}$ suggests an ice (and crystal) temperature of roughly -17°C . The warming

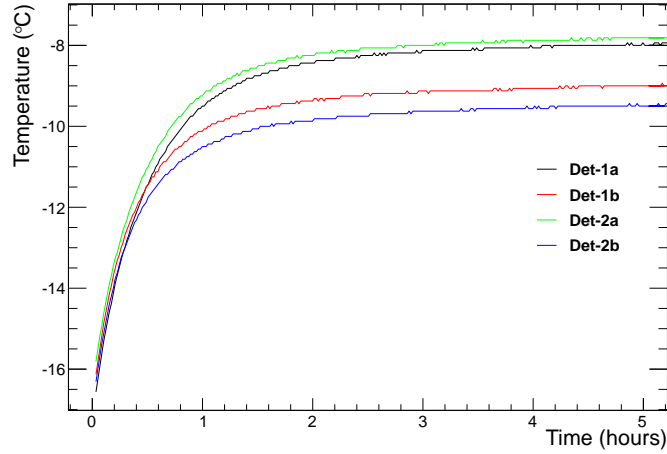


Figure 6.14: Temperature of DM-Ice17 mainboards following an extended power outage. This data indicates a stable ice temperature of the crystals of roughly -17°C . Without their steady power dissipation, the MBs thermalized to the ice temperature, then rewarmed over several hours. The x -axis is in hours since power was restored to the MBs.

is characterized by two exponentials with time constants of $\tau_1 \approx 9$ min and $\tau_2 \approx 2$ hrs; the MBs have all returned to within 2°C of equilibrium at the end of the first hourlong run and within 1°C at the end of the second run.

6.5.2 Pressure

The pressure is also recorded by a sensor located on the MB. It is reported with 0.11 kPa precision, resulting in a ‘steppier’ measurement than that of temperature. The pressure over the entire dataset (see Fig. 6.15) shows an exponential decrease consistent with that observed in the temperature.

The upper pressure vessel volume where the MBs are located was sealed during assembly with atmospheric pressure of air at room temperature (see Sect. 5.1.3); it is isolated both from the lower volume and the outside. Because the two pressure vessels were sealed on different days, the ~ 1 kPa difference in the measured values is consistent with variability of atmospheric pressure in Wisconsin. A similar difference was also observed in monitoring data from pre-deployment tests in Wisconsin and at the South Pole.

The cause of the Det-1 pressure readings matching while the Det-2 pressure readings differ by 0.7 kPa is not known but probably indicates a systematic offset in at least one sensor. The pressure sensors are located next to the temperature sensors on the MB and may exhibit response variation with temperature.

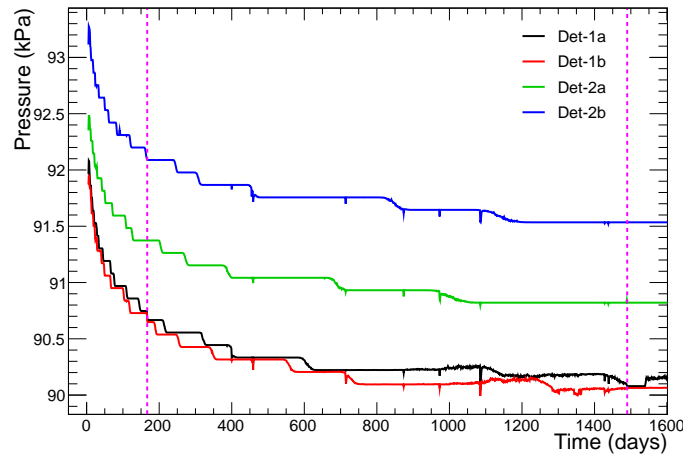


Figure 6.15: Average daily pressure for all DM-Ice17 mainboards. The observed exponential decrease mirrors that of the temperature as the air volume cools. Discrepancy between the value measured by the two detectors is consistent with sealing air volumes on different days, but the difference measured by the two Det-2 MBs is not understood. The x -axis counts from day 1 as 1 January 2011, with the physics dataset beginning on day 167 and ending on day 1489 (pinked dashed lines).

6.5.3 PMT High Voltage

The HV supplied to the PMT as well as the HV set point (DAC value) are reported by the HV supply board; both are reported with 0.5 V precision. The HV set point shows no variation, so all reported variation in the monitored HV is due either to a faulty sensor or instability in the HV supply.

The monitored HV values for both Det-1a and Det-1b are distributed near the set point, while both Det-2a and Det-2b are offset by a few volts (see Fig. 6.16). Both Det-1b and Det-2a exhibit centered nearly-Gaussian distributions, while both Det-1a and Det-2b exhibit tail-favored distributions. The unfavorable characteristics of both distribution spread and offset are most strongly displayed in Det-2b. The source of these irregularities is not understood, but their effect on data is minimal; a study of monitored HV and trigger rate revealed no correlation (see Fig. 6.17).

For the period with 2s monitoring (16 June 2011–28 February 2012), the daily weighted average HV deviations ($HV_{\text{monitored}} - HV_{\text{setpoint}}$) were $\{-0.07, -0.08, -1.88, -3.24\}$ V and the average RMS deviations were $\{0.8, 0.4, 0.8, 9.3\}$ V. For the period with 60s monitoring (23 June 2012–28 January 2015), the daily weighted average HV deviations were $\{0.04, 0.01, -1.79, -3.12\}$ V and the average RMS deviations were consistent with before. This small positive shift in monitored HV for all MBs is much larger than the uncertainty on the average deviation and remains unexplained.

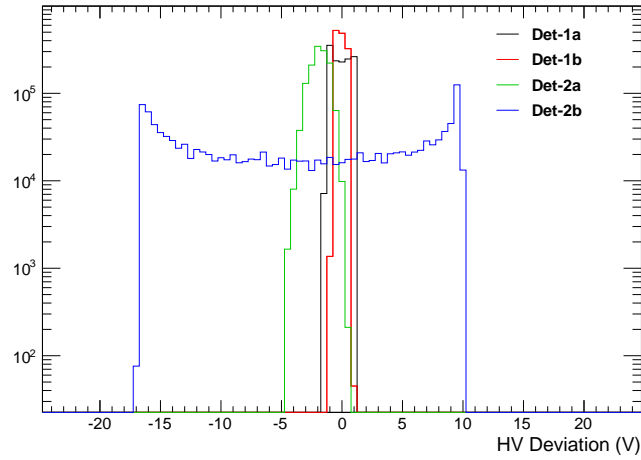


Figure 6.16: PMT HV deviation ($HV_{\text{monitored}} - HV_{\text{setpoint}}$) for one month of DM-Ice17 data. Det-1a and Det-1b both have < 10 mV average deviations, whereas Det-2a and Det-2b have > 1 V deviations and larger spread.

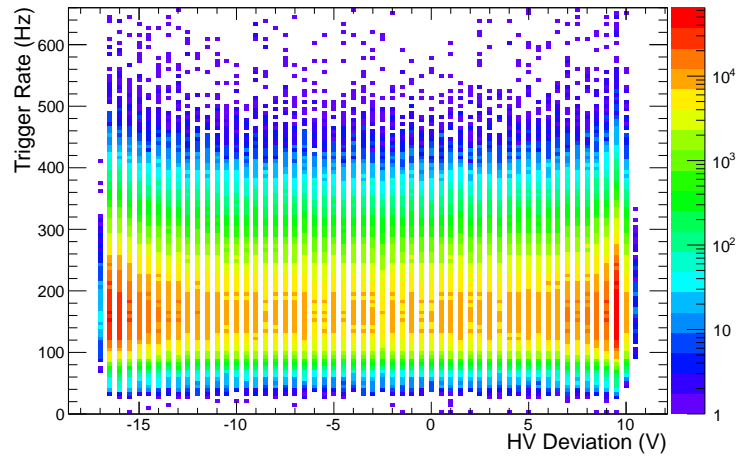


Figure 6.17: Relation between HV deviation and trigger rate (see Sect. 6.5.4) for Det-2b for all data. No correlation is observed between the two quantities, indicating the HV fluctuations do not introduce a systematic variation in the detector response.

6.5.4 Trigger Rate

Each MB is equipped with a scalar which counts the number of discriminator crossings which occurred in the last 900 ms. This scalar counter is converted to a frequency and used to estimate the true trigger rate for the operating threshold of each MB. The monitored trigger rate is higher than the data record rate for either LC (by construction) or DarkNoise runs despite its trigger condition matching that of the (non-coincident)

DarkNoise runs. The only known difference is the lack of hit deadtime in the scalar measurement, which may indicate PMT afterpulses or correlated sequential triggers are present and contributing to the monitored quantity.

Two triggers are implemented on the MB as a result of the IceCube design goals, these are referred to as the SPE and MPE (multiple photoelectron) discriminators. The MPE trigger allows trigger condition flexibility by bypassing the coincidence condition for sufficient signal levels received by a single PMT; because such signals would be unphysical for the DM-Ice17 setup of two PMTs coupled to the same scintillator, the MPE setting is always kept high and therefore only contributes redundant triggers. The trigger rate discussed is only from the SPE scalar measurement, which was adjusted during the commissioning phase (see Sect. 6.3.3).

The monitored trigger rates show an exponential decrease over the three year dataset (see Fig. 6.18). The increased spread in the daily averages on day 424 (28 February 2012) is a real effect associated with the lower hardware monitoring rate. The quasi-periodic switching between two trigger rates in Det-1b is not understood and is difficult to diagnose because of the small nature of the jump and the spread in the monitored trigger rate distribution.

The erratic behavior of the Det-2b trigger rate masks all trends. It is reminiscent of the erratic behavior observed during commissioning, but lacks the extreme fluctuation of up to a few kHz observed at higher PMT HV. The Det-2b fluctuations are large enough to observe clearly in daily averages (see Fig. 6.19). The entire

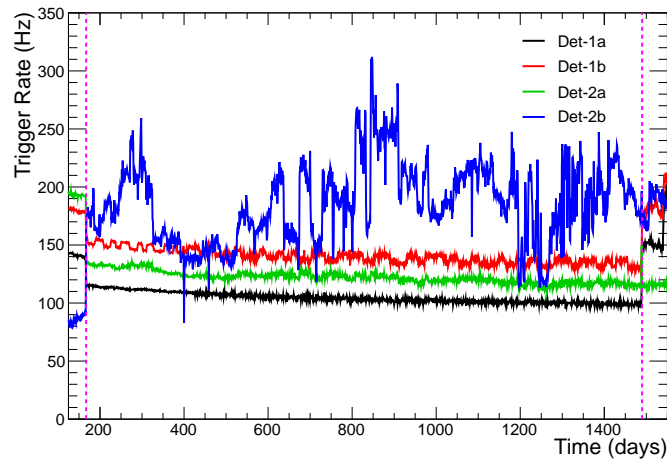


Figure 6.18: Average daily trigger rate for all DM-Ice17 mainboards. Three MBs show an exponential decrease in the trigger rate, while Det-2b shows erratic behavior masking any trend. The x -axis counts from day 1 as 1 January 2011, with the physics dataset beginning on day 167 and ending on day 1489 (pinked dashed lines). Jumps at the start and end and end of the physics dataset correspond to changing HV and threshold settings.

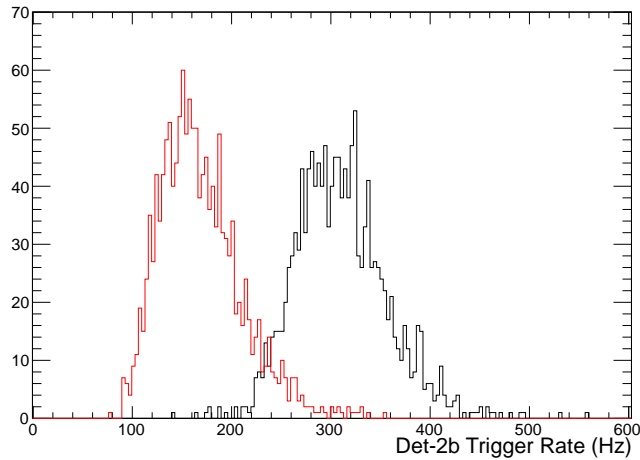


Figure 6.19: Daily monitored trigger rate distributions for Det-2b on days 843 (red) and 845 (black). The erratic behavior of the monitored Det-2b trigger rate stems from significant shifts in all SPE scalar measurements.

distribution of monitored values is observed to shift; the fluctuations are not an artifact of a few outlier scalar readings. Comparison with rate analysis of DarkNoise runs is difficult because of the infrequent scheduling of characterization run sets, but large fluctuations in Det-2b rates are also seen in that data (see Sect. 7.3.4).

These variations in the trigger rate may indicate an instability in the SPE discriminator level over time for Det-2b and to a lesser extent for Det-1b. No corresponding variation is observed in the recorded LC data rate, and no impact has been observed in spectrum. This may be due to the efficiency of noise removal by cuts (see Sect. 7.2) or may indicate that the SPE scalar values are susceptible to additional noise which is not recorded as it is restricted to the deadtime window.

6.6 Calibration

The calibration data taken by DM-Ice17 consists of two primary types – ‘tcal’ timing calibration and the ‘DOMcal’ calibration routine. Both were designed by IceCube to ensure consistency between the 5000+ detectors of their array [173]. The tcal is performed every two seconds during data taking and constitutes one of the three data streams recorded for every run. The DOMcal calibration routine is performed approximately once a year by manual interruption of detector running and is a valid calibration for many runs.

The tcals provide reference between the 40 MHz MB clock, 20 MHz hub clock, ICL Master Clock, and UTC time. A GPS receiver on the ICL synchronizes the ICL Master Clock with the UTC master clock at the US Naval Observatory. The Master Clock timing is distributed through a fan-out and matched signal paths

to each hub with accuracy of less than 1 ns. These timing synchronizations are automatically performed within the IceCube operations framework and serve as the reference for DM-Ice time [173].

The reciprocal active pulsing calibration (RAPcal) method is used to synchronize the MB and hub clocks. The calibration requires the hub to send a bipolar pulse to the MB and the MB to send an identical return pulse to the hub to account for signal delays from differing cable lengths (2500 and 2995 m for Det-1 and Det-2). The tcal data events contain the local timestamps and digitized received waveforms from both the hub and MB. The process is instigated by the hub every two seconds and takes several milliseconds; it interrupts other data transfers but does not interrupt hit digitization. The data extraction routine ensures consistency of the timing calibration by buffering hundreds of tcal records and rejecting any anomalous timing data.

The DOMcal routine performs a series of calibrations on the MB components. Because the MB response changes very slowly, DOMcals can be executed on an annual basis and still adequately track its reported quantities. The timing calibration is used to convert the DAC ATWD sampling rate into MHz; over the three year dataset the sampling rates for each MB have increased by less than 0.2%. The FADC channel samples with the 40 MHz MB clock and requires no timing calibration. Because only one ATWD chip active, the secondary timing calibration is not used and there is no variation in ATWD sample length for a single MB.

The other calibrations of DOMcal are not incorporated in data processing, but provide verification of run settings and calibration. Each bin of each ATWD channel is individually calibrated to convert between mV signal and ADC readout. The zero offsets are independently confirmed by pedestal runs which are taken more frequently to track smaller variation (see Sect. 7.1.2). The relative gain of each digitizing channel is measured; this verifies the scaling between calibrations obtained from fitting contamination lines (see Sect. 7.3.1). The SPE trigger discriminator DAC is also calibrated into charge units; unfortunately the error on the measurement only allows affirmation that we are operating near the zero-point.

Chapter 7

DM-Ice17 Data

Events passing the trigger condition in DM-Ice17 are digitized with 10-bit precision, with the same signal being digitized by up to three ATWD channels and one FADC channel at multiple gain levels and over different sampling windows (see Sect. 5.1.2). All digitized events are saved and the data are sent to Madison, WI for storage and offline analysis. The goal of analysis is to reduce the full dataset to real scintillation events and accurately calibrate from ADC units recorded into energy deposited in the crystal.

Each waveform is first corrected for electronic effects to accurately correspond to the mV signal level reaching the digitizer. Analysis then begins with a series of physically-motivated cuts to remove the noise events; these cuts are highly successful at extending the spectrum downward from ~ 20 keV to below 5 keV with negligible loss of scintillation events.

The energy of an event is determined by integrating the signal from both PMTs and calibrating to known internal contamination lines. Across the entire energy range, the observed spectrum matches expectation based on Monte Carlo simulation. DM-Ice17 detectors exhibit comparable performance to other previous-generation NaI detectors in total background, light yield, gain stability, and energy resolution, verifying the ability to run detectors at the South Pole with no degradation in performance.

7.1 Waveform Corrections

The goal of waveform processing is to translate the digitized signals into an estimator of integrated charge from the PMT anode. To take advantage of the full dynamic range of the digitizers, this must be accurate over five decades of signal, from < 1 pC SPE signals to > 10 nC for muon events. Two corrections, baseline and pedestal, account for digitizer effects. The final correction, droop, accounts for the effect of a passband filter in the passive electronics. The integrated charge estimator obtained after all corrections is more proportional to the energy deposited in the crystal.

7.1.1 Baseline

A uniform ADC offset, termed the ‘baseline,’ is incorporated across all bins of the digitized waveforms. The specific value is determined individually by the FPGA for each channel of each MB to maximize the dynamic range; the offsets range between 110 and 145 ADC units (of the 1024 ADC unit range). Since the quantity of interest is a waveform sum (integrated charge estimate), this offset ensures that symmetric noise fluctuations will correctly sum to zero contribution and allows for waveform undershoot due to an impedance mismatch to be corrected (see Sect. 7.1.3).

The first waveform treatment is a simple baseline adjustment, using the first bin value to determine the integer offset for the entire waveform. The simplest and best estimator of the integer baseline is the mode of first bin values; floating point correction is not allowed until the pedestal correction. Including more bins in the baseline estimator was found not to help because DAQ does not record a consistent number of pre-trigger bins. The long time constant of NaI does not allow time for the signal level to return to zero before the end of the sample window.

To speed data processing while providing consistency during a run, the data is buffered in 1000 s blocks and the baseline for a block is based on all events from the beginning of the file until the next block. For a standard 3600 s run, the baseline is determined in three blocks - 0–2000 s are read in and that calculated baseline is applied to only the first 1000 s; then 2000–3000 s are read in the combined calculated baseline is applied to 1000–2000 s; finally the last 600 s are read in and the total baseline is applied to the last 1600 s).

The baseline obtained from this method is robust for all channels of all MBs except ATWD0 of Det-2a. For Det-2a, the simple baseline calculation will yield a 1 ADC offset in $\sim 15\%$ of cases; for this channel the baseline is verified and corrected by analyzing low energy events.

7.1.2 Pedestals

Each digitizing channel of each MB has characteristic noise offset for each bin, this bin-by-bin offset we term the ‘pedestal.’ The offsets are strongly correlated between channels of the same digitizer (one ATWD chip digitizes ATWD0, ATWD1, and ATWD2), but completely uncorrelated between the ATWD and FADC digitizers on the same MB (see Fig. 7.1). The similarity of the ATWD pedestals indicates that the course structure (up to 30 ADC units) of the pedestal is a digitizer effect, while the small deviation between ATWD channels indicates a smaller variation (up to 5 ADC units) introduced by the signal-storing capacitors.

By construction of the baseline, all pedestal waveforms are expected to have a first bin value close to zero; this forces the ATWD pedestals to appear to deviate over the course of the waveform. The pedestal makes the baseline an unnecessary step, as it can also account for a uniform offset, but the baseline is maintained because it simplifies swift checks of the data.

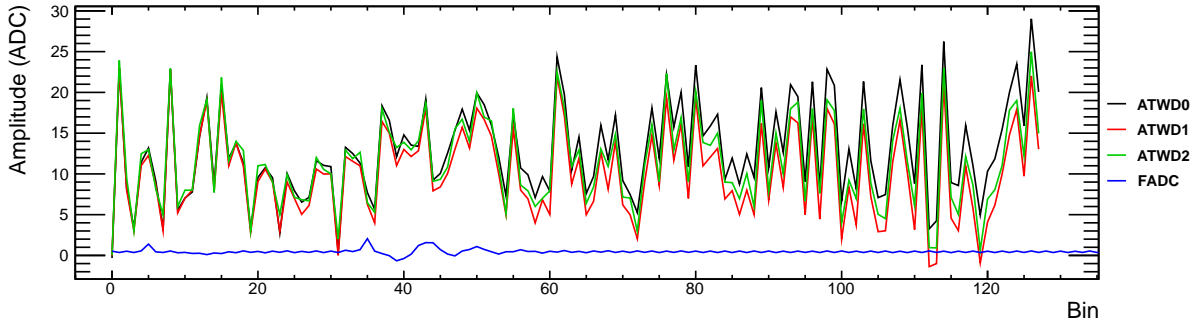


Figure 7.1: Average pedestal waveforms for Det-1a. The ATWD pedestals display their characteristic similarity between channels and large total variability (up to 30 ADC units). The FADC pedestal, by contrast, is mostly flat with only a small feature deviating by 1 ADC unit at bin 40; for clarity of the ATWD pedestals, the FADC pedestal is truncated.

The pedestal is collected by taking brief (60 s) runs which trigger on an internal heartbeat rather than on a threshold crossing. The data from these runs is thus a sample of the digitizer offset, and can be used to establish the pedestal correction for triggered data. Because the pedestal correction is constructed as the average of many (~ 4300 events) integer bin values, this is the first non-integer data correction.

The highest gain channels, ATWD0 and FADC, have the largest RMS variation in per-bin pedestal values; the RMS is approximately constant for all bins (see Fig. 7.2). The lower gain ATWD1 and ATWD2 channels have significantly smaller RMS variation than ATWD0, while exhibiting large fluctuation in RMS between bins (up to a factor of five difference between adjacent bins). The larger fluctuation of the high gain channels can be attributed to noise level fluctuations on the signal line. When the signal noise is suppressed

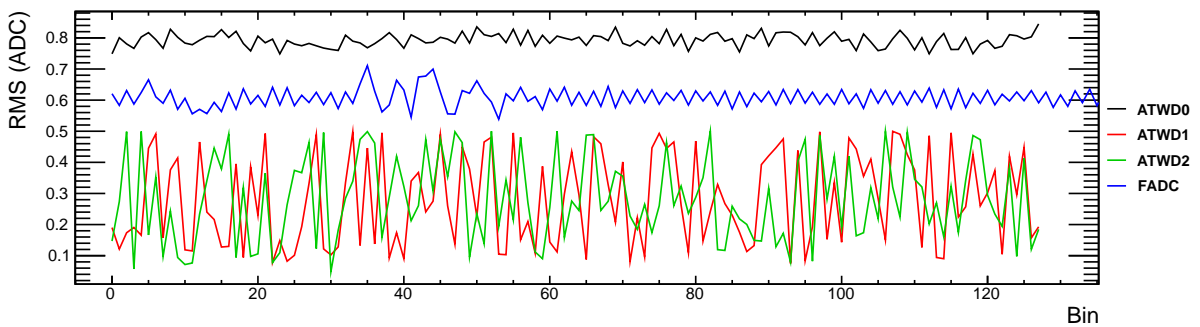


Figure 7.2: RMS variation in the per-bin pedestal values for Det-1a. ATWD0 and FADC, the highest gain channels, exhibit the largest and approximately constant RMS probably limited by noise on the signal line. ATWD1 and ATWD2 exhibit smaller and more variable RMS probably limited by capacitor stability. The FADC error is truncated to match the ATWD range, but shows similar behavior out to bin 255.

in the lower gain channels, the remaining noise is uncorrelated between the bins of ATWD1 and ATWD2 indicating it originates mostly in the capacitors and not the digitizers.

There is a positive correlation in the bin values of pedestal waveform leading to the spread in the pedestal sum being larger than expected by naively adding the per-bin variation in quadrature. The distributions remain Gaussian, but the ATWD0 and FADC sum errors are double the quadrature expectation, while the ATWD1 and ATWD2 sum errors are 3–4 times the quadrature expectation.

The ~ 4300 waveforms collected in a pedestal run provide sufficient statistics to limit the uncertainty in the per-bin pedestal value to < 0.014 ADC units. With the correlated behavior, the uncertainty on the pedestal waveform sum is < 0.5 ADC units.

Based on data collected before deployment, during commissioning, and in the full standard run settings dataset, the effects of temperature, time, and run settings on the pedestal have been studied (see Fig. 7.3). Even for most changes in run settings, the shift in the pedestal full sum is small, less than 1 keV. The sampling rate change illustrates further unexpected behavior in possessing the largest shift (even after removing the effect of changing baseline).

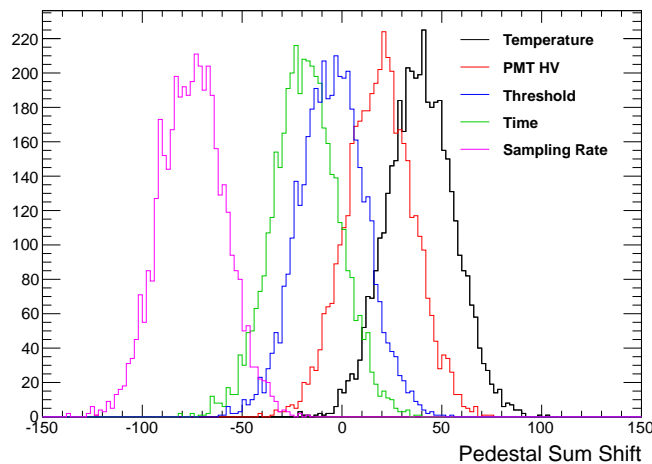


Figure 7.3: Pedestal sum shift for Det-1 ATWD0 due to environment and setting changes. Any change in conditions over a two week period between pedestal runs (due only to HV fluctuations, temperature stabilizing, and time drift) should produce a shift in the pedestal sum of less than 1 ADC bin, which will be undetectable within the statistics of pedestal runs. The pedestal drift is demonstrated here for temperature (10°C change over 50 days during commissioning), PMT high voltage (100 V difference between sequential runs), trigger threshold (50 DAC unit change between sequential runs), time (two years of data collection after freeze-in), and sampling rate (setting change during commissioning).

Over two years, the ATWD0 pedestal drifts by ~ 20 ADC, corresponding to an ~ 0.5 keV shift if uncorrected. Since this drift was not anticipated at deployment, no regular pedestal collection schedule was established until late 2012; the longest time between pedestals in the dataset presented is nine months. An alternative method has been validated against these pedestal runs to extract pedestal information on an hourly run basis for the lowest-energy analysis.

7.1.3 Droop Correction

The analog PMT signal passes through an isolation transformer (MiniCircuits FTB-1-1*A15+) prior to reaching the MB. This decouples the DC reference of the PMT signal from the MB ground, but also introduces a bandpass filter to the signal line. In DM-Ice17 data, only the low-frequency cutoff is observed as the high-frequency cutoff of the filter is above the sampling frequency. This effective high-pass filter distorts the signal shape and can introduce an undershoot, or ‘droop,’ in the recorded waveforms (see Fig. 7.4). If the sampling window is long enough to capture the entire droop, the integral of the undershoot will exactly match the integral of the positive pulse so that all uncorrected events would integrate to zero charge and energy.

Correcting the droop effect out of recorded waveforms requires extrapolating its continuous behavior out of the periodic sampling of the digitizers. The true signal for a bin (S_i) is recovered:

$$S_i = \frac{1}{\tau(1 - e^{-1/\tau})} R_i + (1 - e^{-1/\tau}) D_i \quad , \quad (7.1)$$

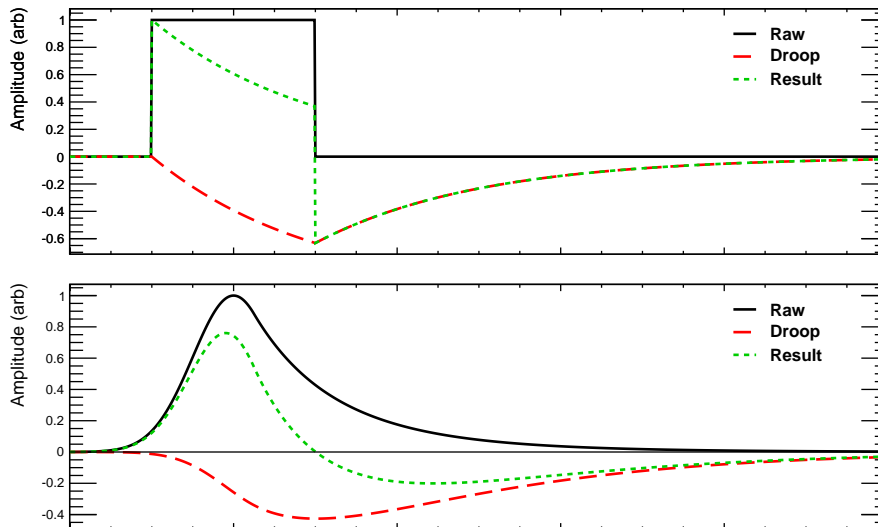


Figure 7.4: Model waveforms to demonstrate the distorting effects of droop. The recorded waveform (green, dotted) requires correction by a droop amount (red, dashed) in order to reconstruct the raw signal input (black, solid).

where τ is the droop time constant (in bins), R_i is the recorded signal, and D_i is the droop effect:

$$D_i = \begin{cases} 0 & i = 0 \\ S_{i-1} + e^{-1/\tau} D_{i-1} & i \geq 1 \end{cases} .$$

The droop time constant is extracted from physics data by examining the noise events (“thin pulses,” see Sect. 7.2.3) with fast decay timing. Scintillation events are unsuitable for determining the droop time constant because their decay time constant is of a similar magnitude. The observed droop time constants of the four MBs differ by $\sim 10\%$ about an average value of ~ 300 ns. The DM-Ice17 spectra is relatively insensitive to variation of the droop time constant used in correction; no significant variation in the energy resolution is observed for droop time constants deviating by up to a factor of two from the preferred values. The lower gain ATWD1 and ATWD2 channels are insensitive to thin pulse analysis, and so they adopt the ATWD0 droop time constant value; the FADC channel has the signal pass through shaping electronics and so sees a different effective droop time constant value.

An identical data acquisition setup operating at room temperature was used to further investigate the droop behavior by recording model pulses from a signal generator. At the higher operating temperatures, the droop time constant was a factor of ~ 3 higher than that found in-ice; this behavior is consistent with previous observations by IceCube [189]. The time constant of the room temperature tests matches the quoted 3 dB cutoff frequency of 0.2 MHz for the transformer. Since no pulse generator studies at low temperature were performed with the DM-Ice17 MBs prior to deployment, the accurate determination of the droop time constant relies on analysis of the physics dataset.

The droop correction must be the last step of the waveform corrections because it will build erroneous features into the corrected waveform based on an incorrect baseline or missing pedestal (*e.g.*, a baseline offset will be droop corrected into a line with non-zero slope). Waveform saturation, either positive or negative, will result in an under-correction of the droop because the droop scales with the input signal level (voltage) while the digitized signal is capped at an arbitrary value.

7.2 Cuts and Associated Noise

The raw recorded data rate of up to 3.3 Hz (for Det-1 in July 2011) contains < 1 Hz of scintillation data. A series of three cuts is used to downselect to good events and remove the noise events. The cuts variables are motivated by real characteristics of the waveforms, and so they are analyzed after waveform corrections so that known electronics effects are already accounted for.

A software local coincidence cut primarily ensures that all events can be paired between PMTs of a single crystal so that the total energy of the event can be summed. The other two cuts target specific types of noise events which profoundly reshape the spectrum below 20 keV (see Fig. 7.5).

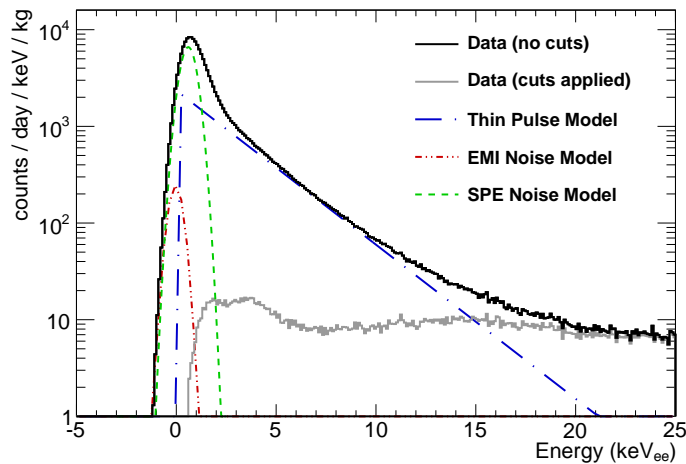


Figure 7.5: Energy spectrum of Det-1 before and after data selection cuts with contributions of individual noise sources identified [24]. No noise-removal cuts are required for analysis down to 20 keV, and only thin pulse removal is necessary for analysis down below 5 keV. This spectrum from December 2012 has the lower rate of EMI noise following the increase in hardware monitoring interval.

7.2.1 Software Local Coincidence

The first cut applied to the data ensures is a software local coincidence window of 800 ns. Because the digitization LC window is ~ 550 ns, this removes almost no events, but does ensure that all events can be paired for summing energy between PMTs on the same crystal. The main effect on data is a reduction in uptime so that the paired PMTs match.

The trigger time difference of scintillation events above 20 keV is Gaussian-distributed with mean < 5 ns (the ATWD sampling interval) and standard deviation ~ 11.5 ns (see Fig. 7.6). Lower energy scintillation events should follow the same distribution until the photon arrival time spread becomes significant at a few keV. Below 20 keV, it is necessary to apply cuts to extract the scintillation events from the noise. This reinforces the assertion that our ~ 550 ns digitization coincidence window is conservative.

The software local coincidence cut removes 4–7% of recorded events from every run, corresponding to 300–800. Det-1a and Det-2b are more strongly impacted due to their higher rates than the corresponding paired PMTs (see Fig. 6.10).

7.2.2 Electromagnetic Interference

The most readily identifiable class of noise events is due to electromagnetic interference (EMI). The waveforms are characterized by their oscillatory behavior and close to zero integrated charge (see Fig. 7.7).

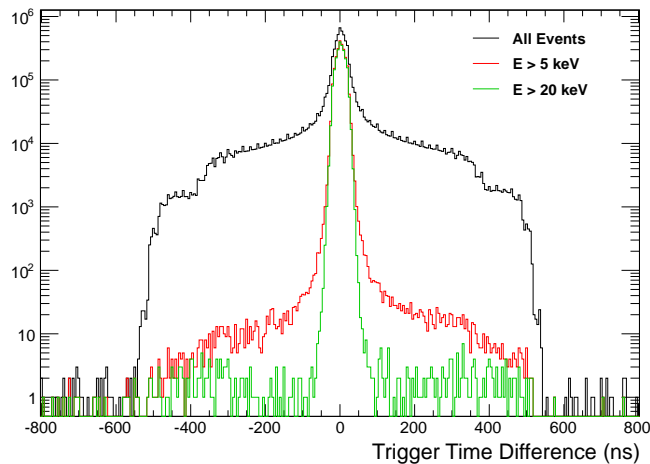


Figure 7.6: Trigger time difference for one month of data from Det-1. A pure scintillation event sample, obtained by sampling only events above 20 keV, exhibits a Gaussian distribution with standard deviation ~ 11.5 ns; no signal is expected to be removed with the 350 ns digitization coincidence window.

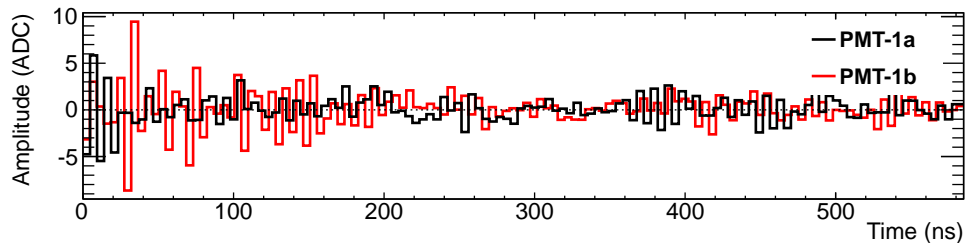


Figure 7.7: Electromagnetic interference waveforms recorded by Det-1 of DM-Ice17 [24]. These noise events have energies centered at 0 keV and can be removed from the data by identifying their oscillatory pattern.

These events are identified in data by taking an effective second derivative:

$$R_{EMI} = \sum_{n=1}^{N-1} ((S_{n+1} - S_n) - (S_n - S_{n-1}))^2 . \quad (7.2)$$

These noise events are strongly correlated with the hardware monitoring query (see Sect. 6.5) and therefore occur at predictable periodic intervals throughout the dataset. The two detectors have very different pickup efficiencies for this noise, $\sim 60\%$ in Det-1 and $\sim 10\%$ in Det-2; since the monitoring event times are not perfectly synchronized, each detector can record up to two EMI noise events per monitoring interval.

The R_{EMI} cut variable allows EMI events to be removed from the dataset with 99.98% efficiency while preserving 99.99% of non-EMI events (see Fig. 7.8). The cut efficiency was validated by analyzing an event sample of triggers near to the hardware monitoring time.

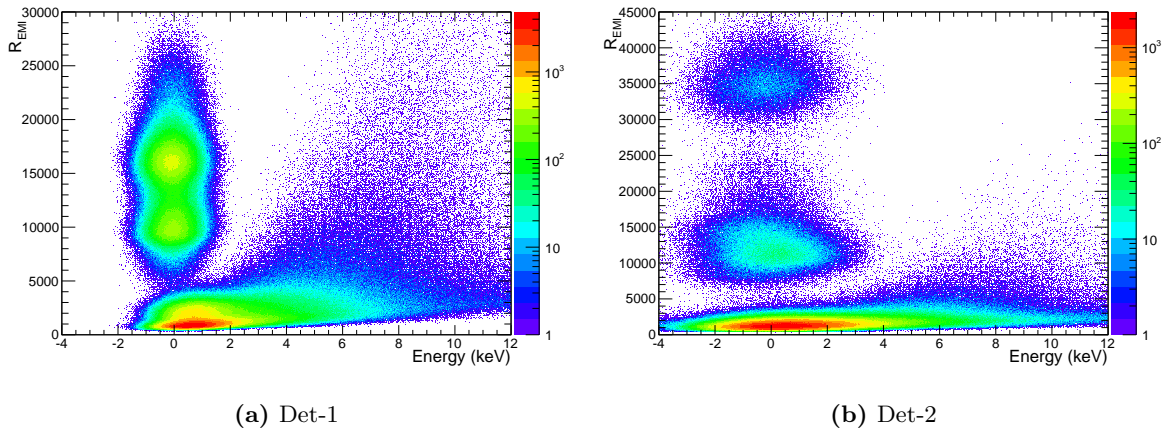


Figure 7.8: Identification of EMI events in one month of DM-Ice17 data with the R_{EMI} cut variable. No EMI events have calibrated energies above 5 keV and so they are completely removed from the cosmogenics dataset. Det-2 with its much lower rate of EMI pickup has a fraction of the events seen in Det-1.

The event rate of EMI noise changes at two points in the dataset corresponding to the changes in hardware monitoring interval in 2012 (see Sect. 6.5). For Det-1, EMI accounts for ~ 0.6 Hz in the early data, and ~ 0.02 Hz in the later data; for Det-2, it accounts for ~ 0.1 Hz and ~ 0.003 Hz. The hardware monitoring interval increase by a factor of 30 in February 2012 caused a significant drop in the total event rate, particularly for Det-1 (see Fig. 6.10).

7.2.3 Thin Pulses

A second class of noise events are “thin pulses,” so named because their decay tail ($\tau < 100$ ns) is much shorter than for crystal scintillation ($\tau \sim 300$ ns). Thin pulses also typically have very asymmetric energy deposition between the two PMTs of a single crystal (see Fig. 7.9).

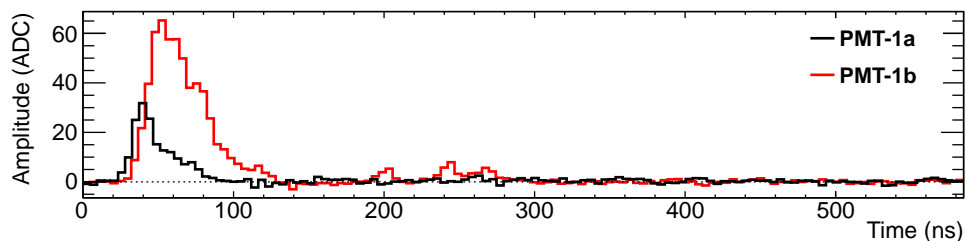


Figure 7.9: Thin pulse waveforms recorded by Det-1 of DM-Ice17 [24]. These noise events have energies below 20 keV and can be identified by the ratio of their height to integral.

Thin pulses can be identified in data without fitting the decay tail time constant by their anomalous ratio of ATWD0 height per ATWD0 integral. The simplest cut variable is,

$$R_{Thin} = \max(ATWD0) \quad , \quad (7.3)$$

with a combined R_{Thin} summing the contribution from each PMT providing the best separation due to the asymmetry of events. This variable provides good identification of thin pulse events down to ~ 5 keV, where the event populations begin to bleed together (see Fig. 7.10).

Thin pulse events are theorized to originate from interactions in the PMTs or light guides, possible either Cherenkov or quartz scintillation. These mechanisms would be consistent with the highly asymmetric energy deposition between the two PMTs and fast decay time.

Thin pulses account for ~ 0.75 Hz in both detectors. Thin pulses are the only noise type visible in the spectrum above 2 keV; they must be removed for any analysis below 20 keV. Above 12 keV, scintillation events outnumber thin pulse events, and by 25 keV thin pulse events have fallen to 0.5% of the spectrum.

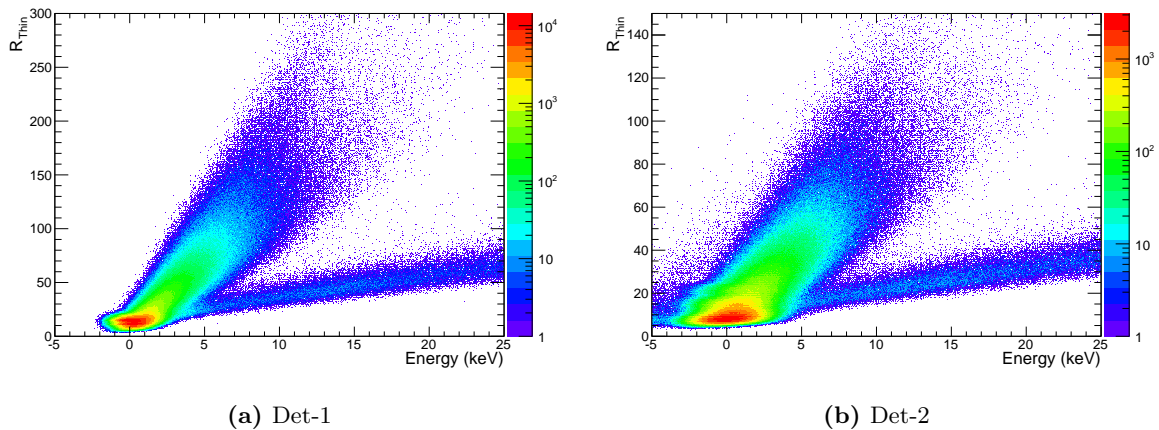


Figure 7.10: Identification of thin pulse events in one month of DM-Ice17 data with the R_{Thin} cut variable. The thin pulse event population is strongly separated from the scintillation event population above 10 keV and thus can be completely removed from the cosmogenics dataset. Det-2 with its lower gain has smaller R_{Thin} values and poorer separation at low energy.

7.2.4 SPE-Like Noise

The final class of noise events is labelled “SPE-like noise” because the only waveform feature is a single photoelectron (SPE) from each PMT. The ~ 1 Hz rate of events, however, is a factor of ~ 100 higher than would be expected from the ~ 100 Hz SPE rate observed in the DarkNoise runs of these PMTs (see Sect. 7.3.4).

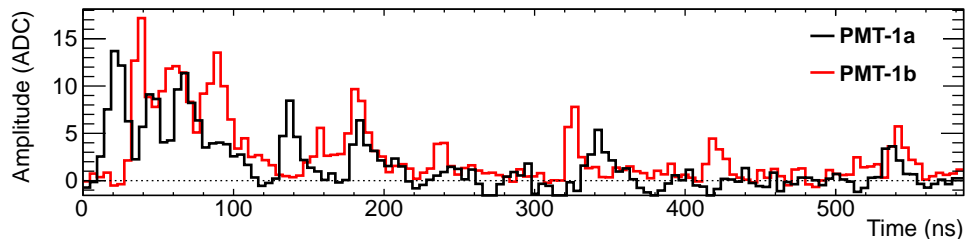
Both SPE-like noise and thin pulses are removed together from data by identifying the number of “peaks” in a given waveform. The peak-identifying algorithm counts the number of bins that are both higher than their neighbors and above a threshold; the threshold is tuned for each PMT to be below the standard SPE height and above the typical noise level. By requiring multiple peaks in each PMT, both SPE and thin-pulse waveforms are strongly removed because their waveforms only have a single peak feature. Scintillation events, however, will contain a series of SPE features dispersed in time following an exponential timing distribution. Monte Carlo simulation indicates scintillation events should be able to pass the peak number cut down to ~ 2 keV, depending on light collection efficiency and SPE-noise separation.

7.3 Energy Spectrum

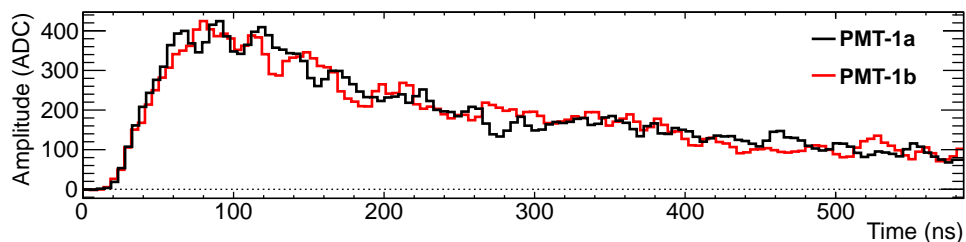
7.3.1 Energy Calibration

After cuts are applied to select only scintillation events, the remaining $\lesssim 1$ Hz of data is analyzed to produce the energy spectrum. Calibrating the detectors requires translating the raw information of the corrected scintillation waveforms (see Fig. 7.11) into a corresponding amount of energy deposited in the crystal.

The first step of calibration is summing the entire waveform from a particular PMT; this ADC-sum is an estimator of the total charge collected at the PMT anode. The waveforms are truncated because the



(a) Low-energy (~ 7 keV) scintillation event



(b) Medium-energy (~ 700 keV) scintillation event

Figure 7.11: Scintillation event waveforms recorded by ATWD0 channel of Det-1 PMTs after waveform corrections [24]. Det-1b waveforms have been scaled down by a factor of 0.76 to achieve an approximate gain match.

digitization window is only $\sim x2$ the crystal decay time, but the lost information should be an approximately constant fraction of the total integral.

The ADC-sum spectrum for each channel of each PMT is then calibrated into energy using internal contamination lines. Each ATWD channel of each PMT must be separately calibrated to account for gain differences and nonlinearities of the crystal and PMTs. The non-linearity of NaI crystals necessitates that the spectrum below 100 keV be treated with its own calibration. The three ATWD channels have broadly overlapping dynamic ranges, allowing the calibration from one channel to always be verified by another except at the lowest energy. For the spectra discussed in this thesis, the following calibrations were applied:

$$E[keV_{ee}] = a + b * (ADC-sum) \quad . \quad (7.4)$$

Table 7.1: Single-PMT calibration fit parameters (see Eqn. 7.4) used for low- and high- energy cosmogenic analysis.

Channel		Det-1a	Det-1b	Det-2a	Det-2b
ATWD0 (< 100 keV)	a	$(-7.893 \pm 1.02) \cdot 10^{-1}$	$(-9.254 \pm 0.997) \cdot 10^{-1}$	0	$(-4.26 \pm 10.7) \cdot 10^{-2}$
	b	$(2.473 \pm 0.006) \cdot 10^{-2}$	$(1.855 \pm 0.004) \cdot 10^{-2}$	$(4.355 \pm 0.007) \cdot 10^{-2}$	$(4.226 \pm 0.010) \cdot 10^{-2}$
ATWD1 (> 100 keV)	a	$(-2.979 \pm 0.61) \cdot 10^1$	$(-4.926 \pm 0.078) \cdot 10^1$	$(-6.136 \pm 0.065) \cdot 10^1$	$(-4.593 \pm 0.073) \cdot 10^1$
	b	$(2.386 \pm 0.001) \cdot 10^{-1}$	$(-1.861 \pm 0.0001) \cdot 10^{-1}$	$(4.393 \pm 0.002) \cdot 10^{-1}$	$(-4.188 \pm 0.002) \cdot 10^{-1}$

After the individual PMTs are calibrated, the final spectrum (see Fig. 7.12) is constructed by averaging the calibrated energy deposited in each PMT for a single event. When the detector resolution is photo-statistics limited, this yields a $\sqrt{2}$ improvement in resolution.

The energy calibration used below 100 keV does have a non-zero intercept, resulting in events with zero ADC-sum being calibrated to negative energies. Analysis of low-energy noise events indicates this is a problematic interpretation, and a more robust calibration should fix the zero-crossing. It is likely the discrepancy arises because of the shifted peak positions of the 3 keV ^{40}K -peak and 14 keV ^{210}Pb -peak. Since the cosmogenics analysis is based mostly on features > 50 keV, a calibration offset of < 1 keV can adjust the peak rates by a maximum of 2%, and since the final rates are integrated over energy will see no effect.

7.3.2 Gain Stability

The gain stability of DM-Ice17 can be assessed in tracking the positions of the uncalibrated peaks. This is primarily of interest for cosmogenics analysis because it informs the necessity of correcting for time evolution of the spectra when comparing data from several years apart.

The stability is primarily tracked for the 46.5 keV ^{210}Pb and the 609 keV ^{214}Bi peaks. For both peaks, most PMTs see a few-percent decrease in the peak position over the full dataset; Det-2b is the only PMT

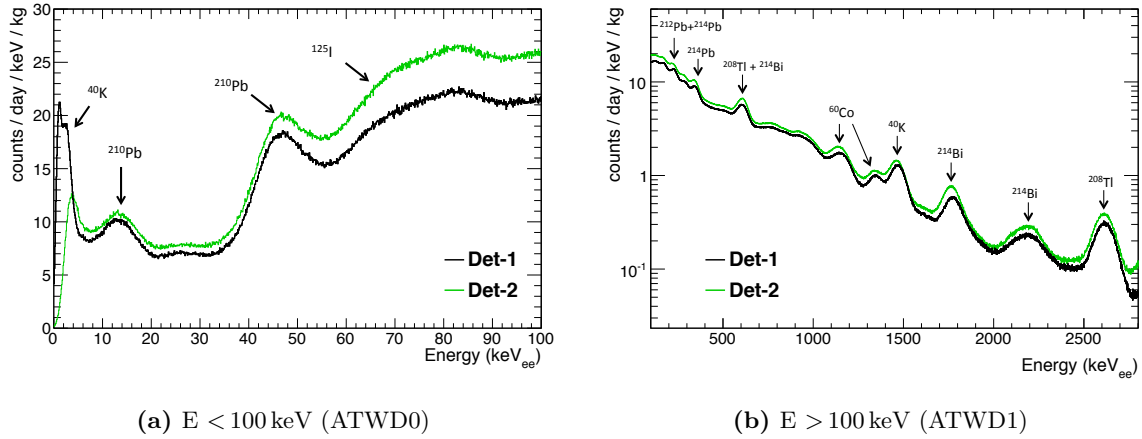


Figure 7.12: DM-Ice17 calibrated energy spectrum with internal lines noted [24]. To account for NaI light response non-linearity at low energy, a continuous calibration cannot be applied over the entire energy range. The spectra here are stopped above the last gamma line (^{208}Tl at 2615 keV) because the dominant spectral feature at higher energy is alpha events whose energy appears lower because of quenching.

which appears to escape this diminishing gain (see Fig. 7.13). Despite the more erratic behavior of the Det-2b high voltage (see Sect. 6.5.3), the relative gain has equivalent error bars and trend stability is comparable to the other PMTs.

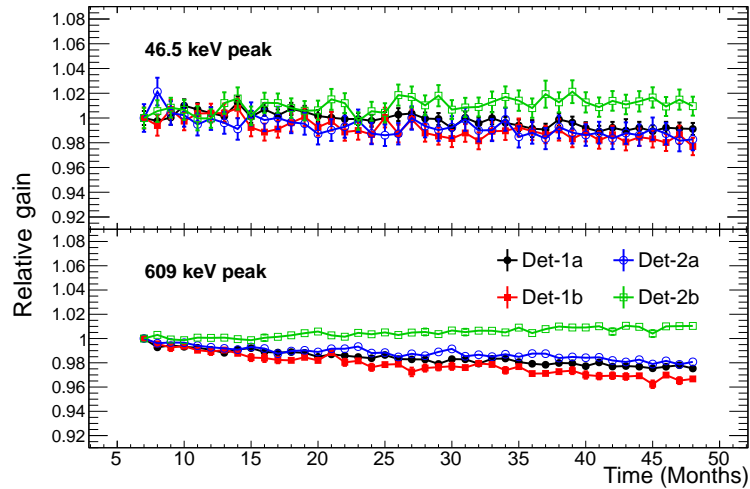


Figure 7.13: Gain stability of individual DM-Ice17 PMTs as determined by peak locations of 46.5 keV ^{210}Pb and 609 keV ^{214}Bi in uncalibrated ADC-sum spectra. There is a ~ 2 -3% gain loss possibly related to light loss in all PMTs except Det-2b over the full 42 month dataset across all energies; Det-2b sees a small 1% increase in gain. The plotted error bars are obtained from the error in the fitted peak mean, which is convolved with the error of the first month measurement for a relative metric.

This effect indicates either that the PMT gain is decreasing or the photon collection efficiency is deteriorating. The PMT voltage is constant over the dataset, so any PMT gain related effect originates in the multiplication stage effecting the SPE size. Alternatively the photon collection efficiency could be related to a decreased light production from the crystal or worsening optical coupling at the interfaces of the crystal, lightguides, or PMTs. The error on the DarkNoise SPE fits are large enough that no definitive statement can be made from SPE analysis to resolve the root cause.

At low energy, only the trend of Det-2b is distinguishable within the error of the peak fitting. At high energies, the peak location are well-resolved by fitting and the Det-1b exhibits the worst gain loss. At all energies, Det-2b exhibits different behavior with a statistically significant increase in gain. The trends of all strong high-energy peaks were tracked, with equivalent results seen for the ^{214}Bi 609 keV, ^{40}K 1461 keV, ^{214}Bi 1764 keV, and ^{208}Tl 2615 keV peaks.

For cosmogenics analysis below 100 keV, the energy resolution is sufficiently broad (see Sect. 7.3.3) that the gain stability is unlikely to be noticeable in comparisons across the entire dataset. For analysis above 600 keV, the energy resolution is at or below 3% so some time evolution of the calibration is necessary to accurately track spectral differences over two years or longer timescales.

7.3.3 Energy Resolution

Mapping the energy resolution of the detectors is important both to compare the performance of DM-Ice17 to other NaI detectors and to produce an accurate simulation spectrum (see Sect. 7.3.5). Because the DM-Ice17 detectors are inaccessible after deployment, the resolution must be determined from science run data instead of dedicated source calibration runs; in this way our determination differs from other experiments (see Fig. 7.14). Our method requires fitting to a non-zero background and is therefore more susceptible to complications than calibration runs; only the 65.3 keV ^{125}I could be fit background-free (see Sect. 8.3.1.1). Repeated manual fits with varied background functions (*e.g.* linear, exponential) and fitting ranges were used to converge to a best fit width. Only a single month of data was included in the fits to prevent artificial broadening due to gain instability.

The functional form which provided the best fit to the resolution data was:

$$\left(\frac{\sigma}{E}\right)^2 = \frac{a}{E} + b \quad . \quad (7.5)$$

The best-fit parameters for Det-1 used in producing simulation spectra are $a = (0.317 \pm 0.016)$ keV and $b = (4.05 \pm 0.20) \cdot 10^{-4}$. The Det-2 resolution was not separately modeled because the resolution is comparable at all but the lowest energies where cut efficiency effects dominate.

There are two resolution points which appear at significantly larger σ/E than predicted by the fit function. At low energy is the ~ 14 keV feature; this is believed to originate from multiple L-shell X-ray lines from

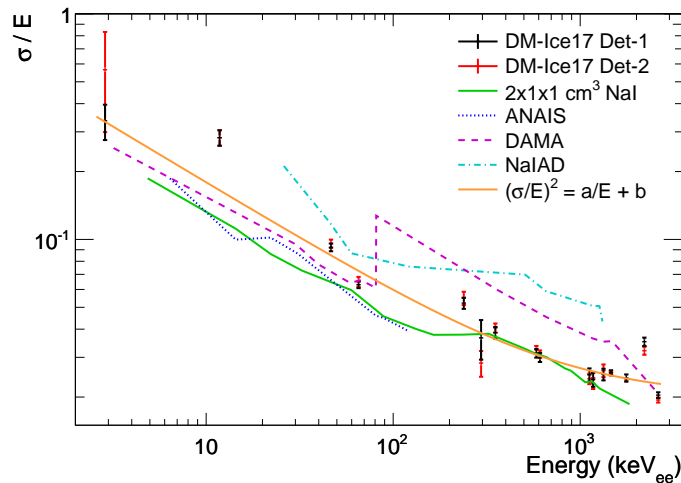


Figure 7.14: Energy resolution of DM-Ice17 detectors as determined from Gaussian fits to internal contamination lines. In comparison with other NaI detectors, DM-Ice17 performs favorably over the entire energy range.

^{238}U -chain isotopes and is wide because of the broadness of the L-shell lines and misalignment of lines between different isotopes. At high energies is the $\sim 2200\text{ keV}$ gamma of ^{214}Bi ; this feature in our spectrum is broadened by its proximity to the Compton edge of the 2615 keV of ^{208}Tl . Although these are the most distorted resolution fits, there is a general expectation of overestimating the peak widths in our method because of overlapping spectral features being treated as a single peak.

The resolution of the DM-Ice17 detectors compares favorably with other NaI detectors. DM-Ice17 outperforms the resolution of NaIAD [190], the experiment from which the crystals and optical assemblies were inherited; the published NaIAD resolution is for a different crystal in their set, the digitizing electronics are completely different, and the operating temperature is different. The DAMA/LIBRA crystals [191] are approximate contemporaries of the NaIAD crystals; their resolution function contains a discontinuity when switching between low- and high-energy DAQs. The ANAIS-25 crystals [122] are a decade newer; they have higher light yield and better resolution. An older measurement with a much smaller crystal ($2\times 1\times 1\text{ cm}^3$) is provided because its smaller dimension provides near-complete light collection, but the older phototubes have significantly lower quantum efficiency.

The dynamic ranges of the ATWD channels overlap extensively (*e.g.* ATWD0 and ATWD1 over $100\text{--}1000\text{ keV}$) which allows us to investigate the effect of digitizing channel on the resolution. In all cases, the higher gain channel exhibited marginally superior resolution; the relative improvement was always less than 5%.

7.3.4 Single Photoelectron Response

The biweekly DarkNoise and Pedestal characterization run sets help track any drift in the response of the detectors. The DarkNoise run pair is necessary in order to collect both an SPE-dominated spectrum at run setting and a noise-dominated spectrum at lower threshold. The Pedestal run collects a pure noise event sample by imposing a continuous trigger which ignores the threshold condition. The Pedestal run confirms that the low-threshold DarkNoise run is identifying the true location of the noise peak and is not being skewed in its noise selection (see Fig. 7.15).

Different summation ranges were applied to the waveform to achieve the best separation of the noise and SPE features, using the ATWD0 sum10 (sum of first 10-bins of ATWD0 waveform) was found to be optimal for all detectors. The resulting spectrum for low-threshold DarkNoise can be accurately represented by a double-Gaussian fit representing the noise and SPE peaks; because no light source was used and a small fraction of the waveform is being summed, no multiple-PE peak is present. More complicated models and fitting functions [192, 193] were considered, but deemed unnecessary largely due to the simpler spectrum present due to SPE calibration without a triggered photon source.

The derived light yield of the two crystals is 5.9 ± 0.1 pe/keV for Det-1 and 4.3 ± 0.1 keV for Det-2; this was calculated from the position of the 65.3 keV ^{125}I peak. For both detectors, the light collection is approximately comparable between the two PMTs. A lower light yield for Det-2 is consistent with

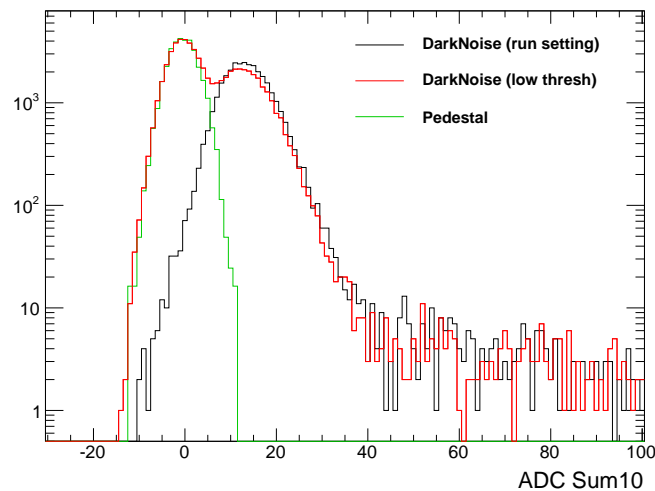


Figure 7.15: Example SPE height determination for Det-1a from DarkNoise and Pedestal spectra after pedestal correction. The location and width of the noise and SPE peaks are well-constrained using the combination of the three runs. The pedestal spectrum has been scaled up to have equivalent uptime.

observations of the crystals prior to construction - the Det-2 crystal had several small cracks and minor delamination of the quartz window which could diminish the light collection.

Analyzing the ΔT distribution between triggers for a single PMT in DarkNoise runs provides an independent crosscheck of the trigger rate scalar monitoring variable (see Sect.6.5.4). For all PMTs, the dominant feature is the exponential distribution of the random trigger arrival times (see Fig.7.16). The rates vary by PMT over the range 50–150 Hz; these rates are $\sim 55\%$ of those reported by the monitoring variable (see Fig.6.18). There is an additional increase beyond the dominant exponential at $\Delta T < 2$ ms which is not understood, but constitutes a small fraction of the total event rate ($< 1\%$); this could be from higher rate correlated events or a DAQ effect following the deadtime period. In all low-threshold and Det-2b standard-threshold DarkNoise runs, the trigger rate exceeds the maximum transferable data rate (~ 100 Hz) and saturation effects strongly distort the distribution.

DarkNoise runs have been taken at least at monthly intervals since October 2012, providing a 2.25 year dataset over which to track changes in the ΔT distribution (see Fig.7.17). For the three PMTs with well-fit rates, this period shows a gradual 5–10 Hz decrease; for Det-2b no trend is visible given the large fluctuations in the fit result. Comparing spectra over the years, the dominant feature shift is a decrease in the amplitude of the SPE peak, indicating a decrease in the SPE rate; there is no significant evidence of a drifting trigger level or of variation in the SPE or noise distribution widths.

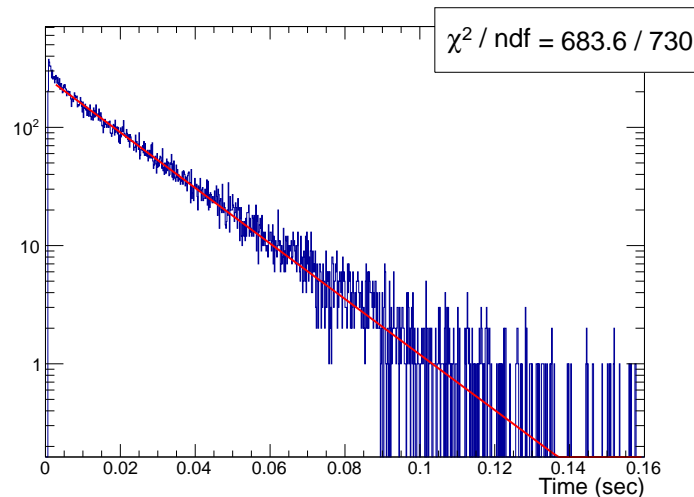


Figure 7.16: PMT non-coincidence trigger (dark) rate determination by fitting the ΔT distribution of Dark-Noise run events with standard trigger. Data are fit with a two-parameter model (exponential with floating normalization) to obtain an unbiased estimate of the rate corrected for DAQ deadtime effects.

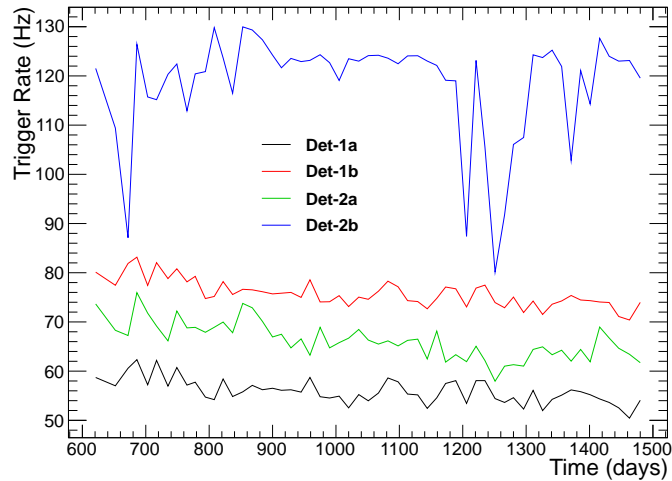


Figure 7.17: Stability of PMT non-coincidence trigger (dark) rate from ΔT fitting. Det-1a, Det-1b, and Det-2a all show a gradual 510 Hz decrease in the PMT dark rate over the 2.25 yr (October 2012–January 2015) period regular DarkNoise runs; Det-2b fitting determination is unreliable due to DAQ irregularities when recording data rates above saturation (~ 100 Hz). All trends mirror, but at different magnitude, the trends seen in the monitored trigger rate quantity (see Fig. 6.18).

7.3.5 Comparison to Simulation

The Monte Carlo simulation of the radioactive backgrounds in the DM-Ice17 detectors is performed within a framework called DMIceSim. This application is based on the 4.9.5-p01 release of the GEANT4 toolkit [194, 195]. The physics list is modeled off the “rdecay02” example which utilizes standard electromagnetic processes; the low-energy atomic de-excitation processes (*e.g.*, Auger e^-) based on the Livermore physics lists [196] are enabled to accurately reproduce the low-energy spectrum.

DMIceSim is adapted from versions originally developed by collaborators at Sheffield to simulate backgrounds in DAMA, NaIAD, and other NaI detectors [197]. The implementation of the precise DM-Ice17 geometry (see Fig. 7.18) as well as the development of DMIceSim were important components of this thesis work.

The DMIceSim package only simulates the energy deposition, and does not consider scintillation, photon propagation, noise, or detector effects. The raw simulated energy deposition is transformed into the simulated spectrum by applying Gaussian smearing based on the resolution function obtained from data (see Sect. 7.3.3).

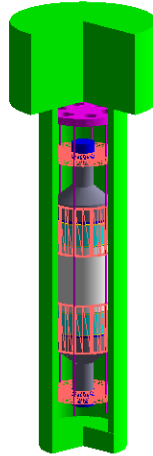


Figure 7.18: OpenGL visualization of DM-Ice17 geometry as implemented in DMIceSim. This pressure vessel cutaway displays the interior volumes color-coded by material: white (crystal), cyan (quartz), gray (PMT), magenta (copper), orange wireframe (PTFE), green (steel).

7.3.5.1 Background Model

Every detector component in the lower pressure vessel with definite geometry and mass of at least 15 g was included in the simulation; this excludes the signal and HV cables, O-rings, springs and nuts. The background model is fixed to expectation based on radio-assays and manufacturer reported levels where available, not based on fits to data. This was not possible for the NaI crystals, where no general information existed and the background levels had to be set by matching spectral features. A single alteration was made to the ^{238}U level in the PMT glass to correct a gross deviation in the simulation-data agreement.

When available, extra components after detector assembly were sent to SNOLAB for counting; the background levels of the steel, copper, silicone gel, and PTFE were obtained in this manner. Samples of the drill ice were collected during drilling which were also counted at SNOLAB; eleven 1 L samples were collected at different depths from multiple holes over two seasons, the weighted average of these eleven samples was taken for the drill ice contamination level. The quartz background level was set to match the ILIAS database for ‘Spectrosil B silica rod;’ no information remains from NaIAD on which product of quartz was used, but quartz is a subdominant component of the total background and this represented an intermediate quality option. The PMT background level for the low-background ETL 9390 UKB tubes was reported in the provided datasheet; a factor of 2 increase in the ^{238}U level was motivated as a single modification which could resolve significant discrepancy in the data-simulation agreement. The glacial ice contamination is determined by optical analysis of the dust concentration. The background model contamination levels for all non-crystal components is summarized in Tab. 7.2.

Table 7.2: Contamination levels of DM-Ice17 detector components in mBq/kg as included in simulation. Components were counted at SNOLAB when possible (indicated by *); other levels were taken from ILIAS database (quartz), manufacturer data sheet (PMTs), or *in situ* ice measurements. Components contributing negligibly to the total background and therefore not shown in Fig. 7.19 are indicated by †.

Material	^{40}K	^{232}Th	^{238}U (^{234}Th)	^{238}U (^{226}Ra)	^{235}U	^{60}Co
Quartz Light Guides	0.50 ± 0.03	< 4.9	12	—	—	—
ETL 9390B PMT	9300	1000	2400	—	—	—
Steel Pressure Vessel *	13.77 ± 6.38	6.49 ± 0.96	118.31 ± 60.11	2.28 ± 0.72	8.79 ± 1.68	7.19 ± 0.82
Drill Ice *	3.71 ± 1.36	0.55 ± 0.17	6.69 ± 3.02	0.39 ± 0.14	0.38 ± 0.21	0.12 ± 0.05
Silicone Optical Gel * †	39.50 ± 18.60	< 0.12	2.08 ± 1.10	38.50 ± 61.00	0.96 ± 1.30	0.32 ± 0.42
PTFE Supports * †	0.34 ± 5.09	0.52 ± 0.44	< 0.41	24.46 ± 21.37	1.92 ± 0.72	< 0.089
Copper Plate * †	< 5.13	< 1.22	0.17 ± 0.92	< 0.67	3.56 ± 1.79	< 0.12
Glacial Ice †	$\sim 3 \times 10^{-4}$	$\sim 4 \times 10^{-4}$	$\sim 10^{-4}$	—	—	—

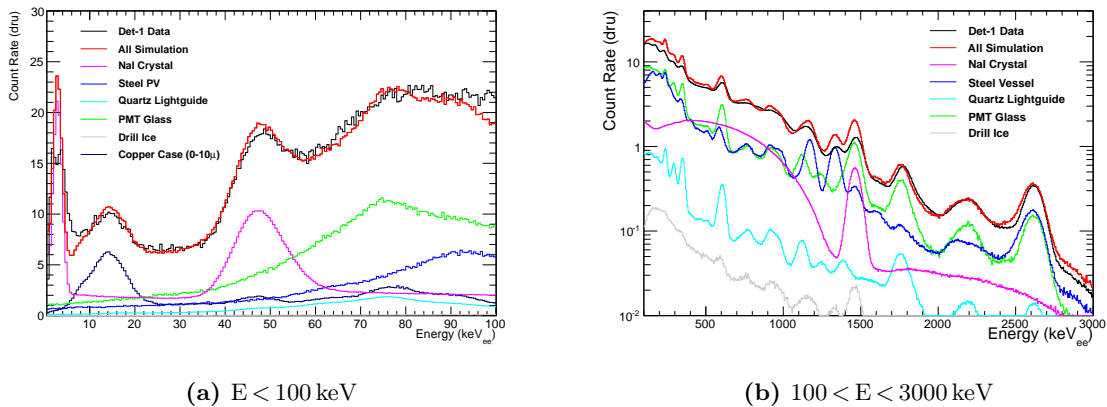


Figure 7.19: Simulated background model for DM-Ice17 with comparison to Det-1 data over beta/gamma region [24]. Simulation is broken separated by detector component and is in good agreement with data.

The background level of the NaI crystal was estimated solely based on comparison with spectral features seen in data. The ^{232}Th - and ^{238}U -chain isotope concentrations were determined from their alpha spectrum over the range 4–9 MeV_r (see Fig. 7.20); alpha energies are quenched in NaI, so the calibrated energy of these Det-1 events has to be scaled up by:

$$E_{\alpha} = \frac{0.435E_{\gamma}}{1 - 0.039E_{\gamma}} \quad , \quad (7.6)$$

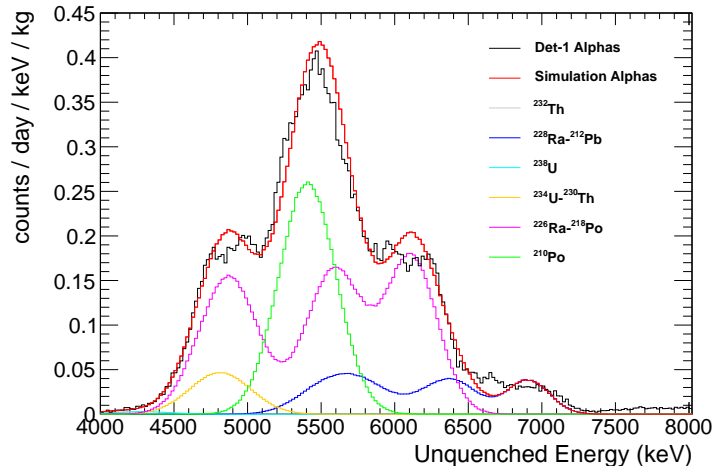


Figure 7.20: Simulated background model for DM-Ice17 with comparison to Det-1b data over alpha region [24]. Alpha background is separated by broken chain segment; all alpha events arise from contaminants in the NaI crystal. Matching the alpha region spectrum sets the ^{232}Th - and ^{238}U -chain contamination levels for the crystal.

where E_α is the true event energy and E_γ is the calibrated energy. The chains are allowed to be maximally broken, where every isotope with half-life greater than five years having a different concentration than its parent; only ^{234}U ($t_{1/2} = 2.5 \cdot 10^5 \text{ yr}$) and ^{230}Th ($t_{1/2} = 7.5 \cdot 10^4 \text{ yr}$) are not broken because their alpha energies are indistinguishable within the energy resolution.

After fixing the NaI ^{232}Th - and ^{238}U -chain concentrations, the ^{40}K and ^{129}I concentrations were fixed to match the shape of their beta shoulders. The ^{129}I concentration was set to match the abundance used by DAMA/LIBRA [191], ANAIS-0 [198], and ANAIS-25 [122]. Having an *a priori* expectation of the ^{129}I abundance is very important because its spectral feature overlaps strongly with the ^{210}Pb peak at 46.5 keV; the ^{210}Pb concentration can be fixed from the alpha region as the ^{210}Po secular equilibrium is supplied by ^{210}Pb decays, giving a second handle. A surface contamination of ^{238}U -chain was also required to match the broad X-ray peak at $\sim 14 \text{ keV}$; a 40 mBq contamination of the full chain distributed uniformly through the inner $10 \mu\text{m}$ of the copper encapsulation is used in the presented simulation. Since multiple isotopes of the ^{238}U -chain contribute to this feature, including a break in the chain for this contamination allows the concentration to be adjusted and the peak center to move. The total NaI contaminant levels as determined for Det-1 are summarized in Tab. 7.3; the levels estimated for Det-2 are consistent within the $\sim 30\%$ errors of the matching technique.

Table 7.3: Contamination in the DM-Ice17 NaI crystals as determined by simulation comparison to data spectral features. Comparison with contaminant levels for ANAIS-0, a contemporaneously-grown NaI crystal, is provided to illustrate similarity in background levels.

Isotope	Subchain	Activity (mBq/kg)	
		DM-Ice17	ANAIS-0
^{40}K		17	12.7
^{129}I		1	0.96
^{232}Th	^{232}Th	0.01	0.013
	$^{228}\text{Ra} - ^{208}\text{Tl}$	0.16	0.035
^{238}U	$^{238}\text{U} - ^{234}\text{Pa}$	0.017	0.075
	^{234}U	0.14	0.075
	^{230}Th	0.14	0.023
	$^{226}\text{Ra} - ^{214}\text{Po}$	0.90	0.098
	$^{210}\text{Pb} - ^{210}\text{Po}$	1.5	0.188

Chapter 8

Activation of DM-Ice17

The time spent in shipment and storage by the DM-Ice17 detectors resulted in production of cosmogenically activated isotopes in both the crystals and pressure vessel. Reconstructing the activation timeline of the detectors allows for a prediction of the abundance of these isotopes in the science dataset. Analysis of time-varying regions of the DM-Ice17 allows for identification of cosmogenic isotopes and verification of the activation predictions.

Cosmogenic activated isotopes contribute to the background spectrum of the detectors and must therefore be incorporated in the Monte Carlo simulation to accurately reproduce the data spectrum. Understanding the decay of cosmogenic spectral features contributes to the detector calibration and characterization by providing unambiguous identification of source peaks and more accurate energy resolution estimates.

8.1 Exposure History

The accurate exposure timeline will capture the location and altitude of the detector components over time. This information can be used to construct the unitless ‘activation factor’ (F_{tot}) which is the scaling factor modifying the cosmic ray flux and thus the activation rate experienced by the detectors:

$$F_{tot} = F_{alt} \cdot F_{BSYD} \quad , \quad (8.1)$$

where F_{alt} (see Eqn. 4.4) accounts for the exponential dependence on atmospheric depth (derived from altitude) and F_{BSYD} (see Eqn. 4.6) accounts for the complicated dependence on altitude, geomagnetic rigidity (derived from latitude), and solar activity. A simple metric to compare the effect of different stages of transportation and storage is the ‘cumulative activation,’ calculated as the time-integrated F_{tot} . This metric does not include any allowance for radioactive decay (see Eqn. 4.9), making it independent of isotope and half-life, but also places an over-emphasis on earlier stages.

8.1.1 Air Shipment

The timescale for constructing and deploying DM-Ice17 necessitated that all long-distance shipment be done by air in order to meet the tight deadlines. The brief periods the detectors or individual components

spent in transit represent a large fraction of their total activation history because of the high altitudes (up to 40,000 ft) often coupled with low geomagnetic shielding. They are also likely to introduce the most uncertainty into the activation scaling calculations because they extend the neutron scaling beyond the tested altitude ($\sim 10,000$ ft) [156] and no record is available of the exact trajectory taken.

In total, five flight segments were investigated as impacting either an individual component or the completed detectors; flight details are summarized in Tab. 8.1. The tube steel for the pressure vessel body was sourced from Sandvik, a vendor based in Sandviken, Sweden and shipped to Stoughton, WI, USA for detector assembly; the flights investigated were direct from Stockholm, SWE to Chicago, IL, USA, both airports being within several hours drive away from the origin and destination. The crystals and lightguides had been stored deep underground at the Boulby Laboratory in Yorkshire, GBR; the flights investigated were direct from London, GBR to Chicago. After the detectors were assembled they were shipped by land to California, and from there were commercially shipped to Christchurch, NZL; this sequence requires at least two flights to accomplish, with the primary flight from Los Angeles, CA, US to either Auckland, NZL or Sydney, AUS, and then connecting on to Christchurch. The first polar flight was on a US Air Force C-17 Globemaster, transporting the detectors from Christchurch to McMurdo Station, Antarctica. The second polar flight was on a New York Air National Guard LC-130, transporting the detectors from McMurdo Station to the South Pole Station.

For the commercial shipments, realistic trajectories (see Fig. 8.1) were modeled based on publicly-available flight-tracking data ¹; this database includes location and altitude data at regular time intervals (≤ 1 min). Interpolation of the geomagnetic rigidity grid for the geographic coordinates of each step provided the R_c , and the F_{tot} was calculated as in Eqn. 8.1. Data from multiple flights along the same route and some alternate

¹ <https://flightaware.com>

Table 8.1: Flight activation stages investigated for DM-Ice17 detector components. The activation rate is suppressed for two of the flights; to New Zealand because of the high geomagnetic shielding received at equatorial latitudes, and to the South Pole because of the lower cruising altitude. The reported $\overline{F_{tot}}$ is the time-weighted average of individual F_{tot} values.

Origin	Destination	Cruising Altitude (ft)	Geomagnetic Rigidity (GV)	Duration (hrs)	$\overline{F_{tot}}$	Component
Stockholm, SWE	Chicago, USA	34,000–38,000	0.1–2.0	8	460	Steel
London, GBR	Chicago, USA	34,000–38,000	0.6–3.0	8	440	NaI, Quartz
Los Angeles, USA	Christchurch, NZL	34,000–38,000	2.6–15	13	100	All
Christchurch, NZL	McMurdo Station	34,000–38,000	0.0–2.6	5	450	All
McMurdo Station	South Pole Station	26,000	0.0–0.1	3	140	All

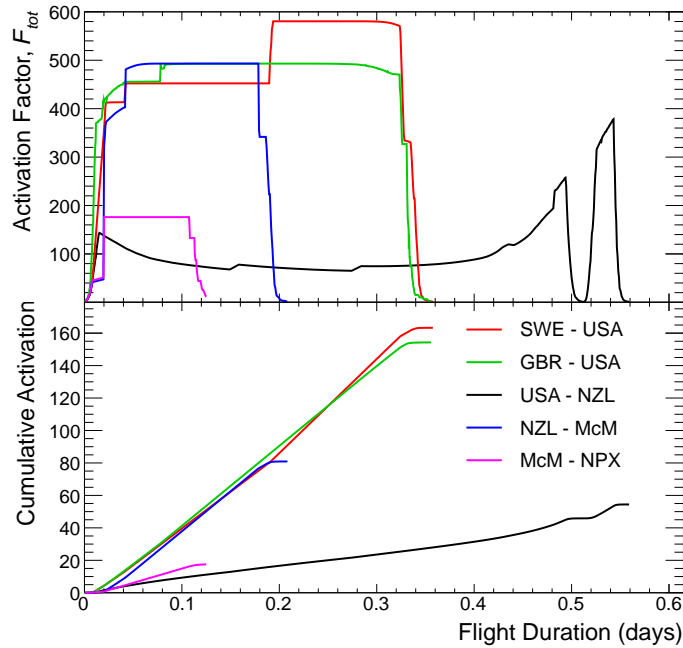


Figure 8.1: Activation scaling factor (top, see Eqn. 8.1) and integrated activation factor (bottom) for the flight segments of individual components and completed detectors. The activation factor scales strongly with altitude, but may be offset by geomagnetic shielding at equatorial latitudes (*e.g.* USA - NZL). The high-latitude flights (SWE-USA for steel and GBR-USA for crystals and lightguides) sourcing detector components are the most damaging for activation because of their combination of high altitude and low geomagnetic shielding received. The lower-altitude flight to the South Pole (McM - NPX) has a much lower activation rate because of the lower service ceiling for a loaded C-130. Abbreviations used are SWE (Sweden), USA (United States of America), NZL (New Zealand), McM (McMurdo Station), and NPX (South Pole Station).

routes were analyzed to assess the average value of cumulative activation and anticipated variation. The effect of geomagnetic shielding can clearly be seen in the USA - NZL flight segment, where the F_{BSYD} can provide up to a factor of 5 suppression in F_{tot} .

For the polar flights, trajectories were extrapolated from commercial data because the military flights are not logged in commercial flight databases. The C-17 flight to McMurdo was assumed to follow an altitude pattern comparable to that of commercial high-latitude flights as it has a similar service ceiling. The LC-130 flight to Pole was assumed to operate at a much lower altitude, as its service ceiling may be as low as 23,000 ft when fully loaded; the 26,000 ft cruising altitude assumed is a conservative allowance. For both flights the trajectory was assumed to follow a straight-line path between the origin and destination coordinates to establish the rigidity.

8.1.2 Total Exposure

The remainder of the exposure assumed for the activation calculation occurs at a much lower rate due to time detector components spent on the surface during storage, construction, or testing (see Fig.8.2). Because the exposure time is much longer than for the flights, the cumulative activation of these periods can be comparable or even greater. Additionally, the scaling calculation is much less error-prone because the highest activation storage location, 9,301 ft at the South Pole, is within the elevation range tested within the Gordon neutron scaling [156], albeit at a lower rigidity.

The first activation stage, experienced only by the pressure vessel steel, is a year of surface storage assumed at the vendor location (see Tab. 8.2). This activation history is built-in at the lower level of the amount found

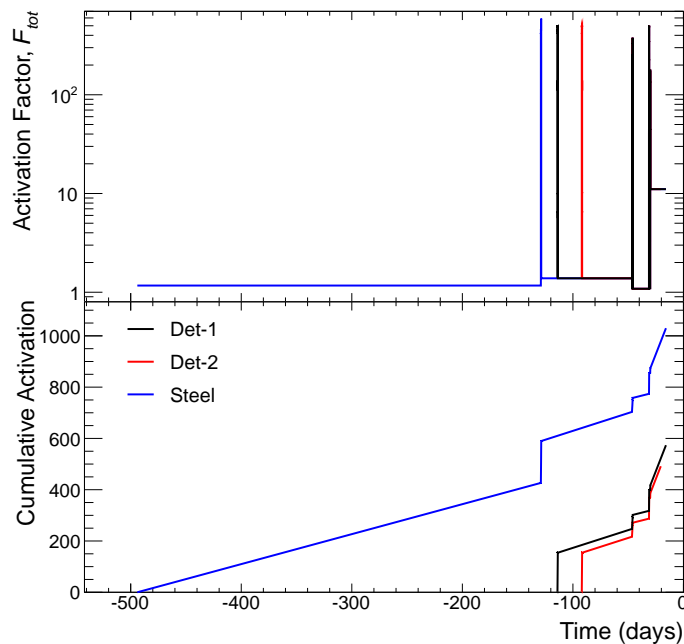


Figure 8.2: Activation scaling factor (top, see Eqn. 8.1) and integrated activation factor (bottom) to establish the activation timeline for the individual detector components. The activation is characterized by long periods of low activation rate punctuated by brief extreme levels due to the flights. The steel experiences the highest cumulative activation because of the assumed one year surface exposure. The NaI crystals and lightguides, in contrast, had been stored underground at the Boulby Laboratory for almost a decade and are assumed to have no historical exposure. Det-2 received the smallest activation mostly because it was deployed 5 days earlier than Det-1 and thus received 33% less Pole activation. The x -axis counts towards day 1 as 1 January 2011 as in previous chapters, with the deployments occurring on days -20 and -15.

Table 8.2: Storage activation stages investigated for DM-Ice17 detector components. The South Pole is the most activating stage because of the cosmic flux enhancement at its altitude of 9,301 ft. Some durations are variable because detector components arrived at different times (Stoughton) or because of the detector deployments were five days apart (South Pole).

Location	Altitude (ft)	Geomagnetic Rigidity (GV)	Duration (days)	F_{tot}	Component
Sandviken, SWE	230	1.22	365	1.17	Steel
Stoughton, USA	876	1.78	45–82	1.38	All
Christchurch, NZL	123	2.66	15	1.08	All
McMurdo Station	18	0.00	1	1.10	All
South Pole Station	9,301	0.03	9–14	11.07	All

in previous measurements [139]. The detector components were all brought together in Stoughton, WI, USA for assembly; the steel arrived first in late August and the Det-2 NaI crystal and lightguides arrived last in early October.

After assembly, the detectors were shipped together and are assumed to have identical activation histories until deployment. The commercial shipment process took two weeks for the detectors to reach Christchurch (mid-November); since no information exists regarding where the detectors spent time, this activation period is attributed to additional time in Stoughton for the purpose of this calculation in order to put the flight at the right time. After arriving in Christchurch, the detectors were transferred to the polar freight queue and idled for an additional two weeks at the US Antarctic Program facilities. During shipment to the South Pole, they experienced a brief stay at McMurdo station on the coast of Antarctica. The time at the South Pole prior to deployment was very limited, allowing for brief performance checks, and both detectors were deployed in under two weeks. The exposure histories of detectors terminate with their deployments on Dec 11 (Det-2) and Dec 16 (Det-1), after which they rest under a 2200 m.w.e. overburden of ice.

For the steel, the historic surface activation in Sweden is the most significant period, accounting for 41% (Det-1) of the cumulative activation. Of the remaining steel cumulative activation, roughly half is from the flights and a quarter from the time at the South Pole. Since the activation period is undocumented, the uncertainty in the historic exposure may be taken to be half a year from previously measured values [139], for a 50% uncertainty in the historic exposure period and a 20% uncertainty on the cumulative activation. The uncertainty in the total activation of specific isotopes from the historic activation will be mitigated by the decay of these isotopes over the remaining exposure time.

Since the crystals are assumed to have no historic exposure, the flights dominate their activation, accounting for 54% (Det-1) and 62% (Det-2). The time at the South Pole is the next largest contributor to the activation at 27% (Det-1) and 21% (Det-2). Because of the additional time both at Stoughton and the South Pole, Det-1 received an additional 17% cumulative activation over Det-2. The historic surface activation of the steel is the primary driver for the Det-1 steel receiving an additional 80% cumulative activation over Det-1 crystal.

8.2 Activation Rate Expectation

The activation rate over the pre-deployment history of the detectors can be calculated from the reference (sea-level) activation rate, R_0 (see Eqn. 4.1), and the activation scaling factor, F_{tot} . When combined with activation timeline and decay half-life, the total activation of every isotope of interest can be estimated.

The reference activation rates were taken from published results of previous measurements when available. Unfortunately these have only been rigorously investigated for steel and copper, with recent preliminary results available for NaI crystals. For investigations of the NaI crystals and quartz lightguides, studies were made using activation codes. The cross section calculations used by the activation codes were benchmarked against experimental data and major *ab-initio* libraries for the primary isotopes of interest. All half-life information was obtained from the NuDat 2.6 database.²

8.2.1 Activation Codes

Several common activation codes exist, including COSMO [148], YIELDX [147], and ACTIVIA [149]. These codes all use the semi-empirical formulae of Silberberg and Tsao [146, 147] as the basis of the cross section calculation. The formulae are designed for activation by protons so the cross sections are only accurate for target isotopes whose proton and neutron activation cross sections are comparable. The codes convolve the calculated cross section with the cosmic ray neutron flux spectrum and integrate over the energy range of interest.

The more recent activation codes have the advantage of using the most updated cross-section formulae and corrections from beyond the scope of the Silberberg and Tsao model. For this study, v1.2 of ACTIVIA was adopted as the primary code,³ with comparison made to COSMO. The ACTIVIA cosmic spectrum was updated to follow the parameterization of Gordon [156], a much more recent and widely accepted model [199, 200, 201, 202, 203]. The Gordon model parameterization is valid from 1 MeV–10 GeV and has an increased differential flux near 100 MeV but lower flux at low and high energy relative to other models.

² National Nuclear Data Center, Brookhaven National Laboratory, <http://www.nndc.bnl.gov/nudat2/>

³ Publicly released for download at <http://universityofwarwick.github.io/ACTIVIA/index.html>

Benchmarking tests of ACTIVIA have found that typical calculations agree with measurements within a factor of two, but in rare cases the discrepancy may be as high as a factor of 10. Disagreement between the different codes has also been demonstrated, with ACTIVIA demonstrating a factor of 10 improvement over COSMO and factor of two improvement over YIELDX for certain isotopes. Calculations by ACTIVIA can be further improved by using *ab-initio* calculation tables as inputs; however this requires first validating the calculation results [149].

The code was used to estimate production from sodium (Na) or iodine (I) targets for the crystal and from silicon (Si) or oxygen (O) targets for the quartz. The activation code calculates activation rates for each target isotope, and the results are balanced for isotopic abundance and mass fraction of atoms. The calculation was run for the entire energy range of the Gordon flux model, 1 MeV – 10 GeV; the cross section models have a typical cutoff of 10 MeV and the integrated flux drops off three orders of magnitude by 10 GeV, so this range does not affect the calculation result.

8.2.1.1 NaI Crystals

Both target elements of the crystal have only one naturally abundant isotope, so the activation code assumed 100% abundance of ^{23}Na or ^{127}I for the two calculations. The generated activation rates are kg^{-1} , so the raw rates were scaled by the mass fraction of 0.153 (Na) or 0.847 (I). The reference activation rates of interest are summarized in Tab. 8.3.

All proton-capture activation products are susceptible to gross overestimate of the reference activation rate; this is only $^{127}\text{I}(\text{p}, \text{n})^{127}\text{Xe}$ for the isotopes listed in Tab. 8.3. While the proton capture cross section calculation may be accurate, it is an inadequate estimator for an incident neutron flux. The proton spectrum has significantly lower flux than the neutron spectrum out to ~ 1 GeV. Since the ^{127}Xe cross section is strongly peaked at 30 MeV, the reference activation rate is likely overstated by more than an order of magnitude.

The cross section calculation does assume that neutron and proton cross sections are equivalent, so production of isotopes which would be impossible under proton capture (*e.g.*, $^{127}\text{I}(\text{n}, \gamma)^{128}\text{I}$ or $^{127}\text{I}(\text{n}, \text{p})^{127}\text{Te}$) are calculated from the corresponding allowed reactions (*e.g.*, $^{127}\text{I}(\text{p}, \gamma)^{128}\text{Xe}$ or $^{127}\text{I}(\text{p}, \text{p})^{127}\text{I}$). This assumption allows the full range of possible isotopes to be simulated, but with the associated error that production by neutron and proton capture may differ significantly.

A second failing of the ACTIVIA calculation for NaI is in cases of long-lived metastable states ($^{119\text{m}}\text{Te}$, $^{121\text{m}}\text{Te}$, $^{123\text{m}}\text{Te}$, $^{125\text{m}}\text{Te}$, and $^{127\text{m}}\text{Te}$). The cross section calculation is completely insensitive to whether an excited or metastable state is produced, so the above table assumes duplicate production of both (so ^{121}Te and $^{121\text{m}}\text{Te}$ both appear with the full reference activation rate). If the production is split between the two states, the reference activation rate will be reduced.

Table 8.3: Activated isotopes in the Det-1 NaI crystal identified by ACTIVIA with activation rate greater than 4 /kg/day and half-life $1 < t_{1/2} < 10^4$ days. The initial (on 1 January 2011) and 6-month (on 1 July 2011) decay rates are reported to provide scale of activation. The upper list contains isotopes with half-lives longer than 50 days which may persist into the DM-Ice17 dataset, while the lower list contains shorter-lived isotopes potentially of interest to future searches. Isotopes whose activation calculation is particularly susceptible to inflation are noted in italics.

Isotope	$t_{1/2}$ (days)	R_0 (#/kg/day)	Initial Rate (decays/kg/day)	6-Month Rate (decays/kg/day)
^3H	4500	26	2.3	2.3
^7Be	53.22	2.4	9.4	0.9
^{22}Na	951	66	27	24
^{109}Cd	461.4	4.8	3.8	2.9
^{113}Sn	115.09	9.0	23	7.7
^{121m}Te	<i>164.2</i>	<i>93</i>	<i>180</i>	<i>83</i>
^{123m}Te	<i>119.2</i>	<i>52</i>	<i>130</i>	<i>44</i>
^{125m}Te	<i>57.40</i>	<i>74</i>	<i>280</i>	<i>31</i>
^{127m}Te	<i>106.1</i>	<i>93</i>	<i>250</i>	<i>76</i>
^{125}I	59.400	221	820	100
^{118}Te	6.00	31	57	0.0
^{119m}Te	<i>4.70</i>	<i>57</i>	<i>64</i>	<i>0.0</i>
^{121}Te	<i>19.17</i>	<i>93</i>	<i>260</i>	<i>0.4</i>
^{124}I	4.176	32	27	0.0
^{126}I	12.93	128	530	0.0
^{127}Xe	<i>36.4</i>	<i>93</i>	<i>410</i>	<i>14</i>

Not included in the ACTIVIA result is cosmogenic ^{129}I , because it is inaccessible to single-nucleon capture processes on ^{127}I . This isotope, however, is expected to be present in the crystals based on its trace abundance ($^{129}\text{I}/^{127}\text{I} = 1.5 \cdot 10^{-12}$ [204]) in natural iodine which would be included during the crystal growth process. Because of its long half-life ($1.57 \cdot 10^7$ yr) and origin in the crystals prior to transport, this isotope is included in the standard background model and not the cosmogenic model.

The energy spectrum of activated decays in the NaI crystal presents a rich series of spectral lines still present at the start of the physics dataset (see Fig. 8.3). The strongest line is at 65.3 keV from ^{125}I decays produced mostly through (n, 3n) process; this is the most easily identified line in the data because of its high large event rate at the beginning of the dataset and short half-life (see Sect. 8.3.1). At lower energies, several

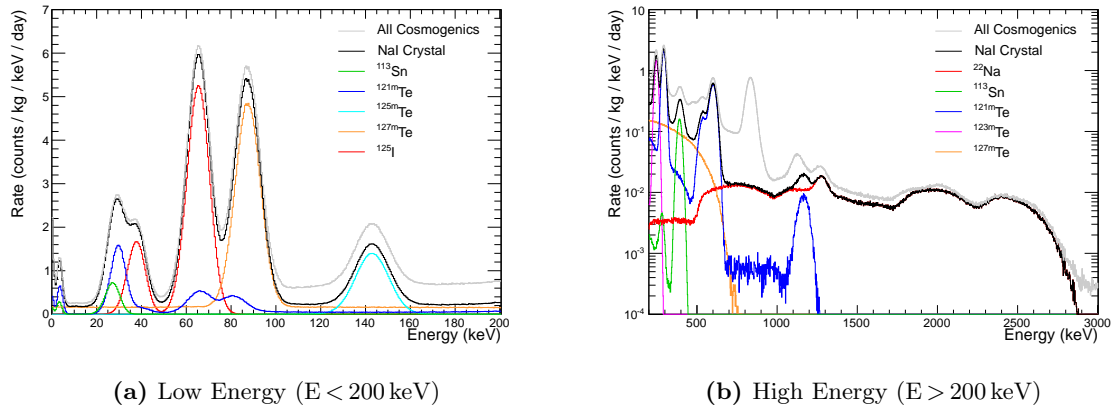


Figure 8.3: Simulated spectrum from activation in the NaI crystal (black) expected in July 2011 with breakdown by isotope (colors). Spectral lines from activated isotopes in the crystal are the dominant features in the activated spectrum out to ~ 650 keV and the flat background from ^{22}Na dominates the activated spectrum above 1 MeV. Including contribution from metastable tellurium isotopes, the contribution to the spectrum from 2–5 keV is 1 counts/day/keV/kg.

isotopes have X-ray lines in the 25–40 keV region, making it difficult to disentangle their relative contributions. In the region of interest for dark matter searches, 2–6 keV, several decays with Auger electrons may add up to 1 counts/day/keV/kg to the total count rate. Above 1.2 MeV, the decay of ^{22}Na is the dominant cosmogenic background (see Fig. 8.4) providing an approximately flat background at 0.01 counts/day/keV/kg due to the combination of 511 keV escape and Compton scatters of the 1275 keV gamma. Because of the long half-life of ^{22}Na a small decay in this background will be invisible in data.

Above the ^{125}I line, all four long-lived metastable tellurium isotopes have lines with simulated peak rates above 0.5 counts/day/keV/kg; additionally these peaks could all be strongly suppressed if the production of the ground state is stronger than the metastable. Only the lowest energy peak, 88 keV at the full deexcitation energy of ^{127m}Te is a promising candidate to identify in our data; the possible 5 counts/day/keV/kg expected rate would clearly protrude over the 22 counts/day/keV/kg background. The next three peaks – at 145 keV (^{125m}Te), 247 keV (^{123m}Te), and 294 keV (^{121m}Te) – are all in a high-energy calibration region where the calibration points require background subtraction using a steep region of the spectrum, making them susceptible to a shifted calibration and difficulty in correcting for time variation; the peak rate is also $\sim 10\%$ of the constant background. The final peak is at ~ 600 keV from the decay of ^{121}Te (in equilibrium with ^{121m}Te by the start of data taking in July 2011); because this falls under the ~ 609 keV ^{214}Bi , it will also be difficult to identify this decay.

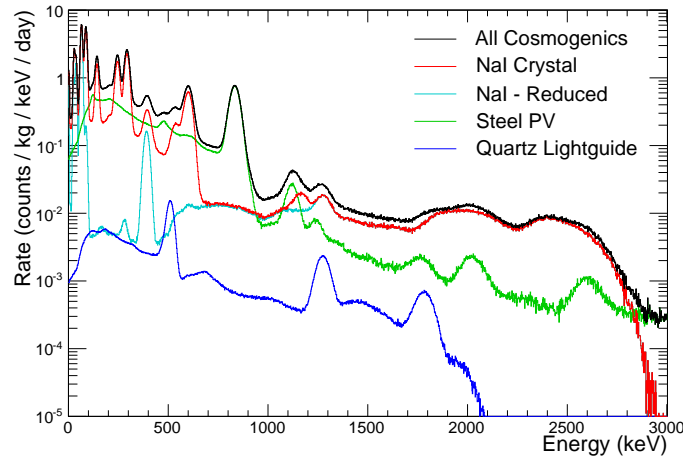


Figure 8.4: Simulated spectrum from all activation products (black) expected in July 2011 with breakdown of contributions from different activation regions (colors). The “reduced” NaI simulation (cyan), without ^{127}Xe and metastable tellurium isotopes, removes the majority of the identifiable spectral features coming from activation products in the crystal.

8.2.1.2 Quartz Lightguides

Adjacent to the crystal on both sides is a 2” quartz lightguide, separated by only a thin layer of optical coupling consisting of silicone grease and gel. The 3.6-kg of quartz are the nearest material of any significant mass which could possibly be activated.

Quartz is a crystal with chemical formula SiO_2 . Naturally occurring oxygen is dominated by ^{28}Si (92.23%) with the remainder ^{29}Si and ^{30}Si ; natural oxygen is dominated by ^{16}O (99.76%), with the remainder ^{17}O and ^{18}O . The isotopic abundances are provided to ACTIVIA so that the output is correctly scaled for each element. The results are scaled by the mass fraction of 0.467 (Si) or 0.533 (O). The reference activation rates are summarized in Tab. 8.4.

All three isotopes with $A < 30$ and $1 < t_{1/2} < 10^6$ days are simulated to have significant activation rates. However, the small mass of the quartz and the poor detection efficiency for these decays results in a cosmogenic contribution an order of magnitude below that of the activation products in the crystal (see Fig. 8.5).

8.2.2 Steel

Direct measurement of activation in steel was performed by collaborators of the GERDA experiment based on activation at altitude measured at the Laboratori Nazionali del Gran Sasso (LNGS) [139]. For this thesis, the PR_{LNGS} value is adopted and independently scaled to a reference activation, as their scaling factor does not account for geomagnetic rigidity and was based on the older scaling rules of Ziegler [138]. A

Table 8.4: Activated isotopes in the quartz lightguides identified by ACTIVIA with any activation rate and half-life $1 < t_{1/2} < 10^6$ days. Because few radioactive isotopes exist with low-Z and favorable half-lives, the quartz is expected to contribute negligibly to the cosmogenic spectrum. The initial (on 1 January 2011) and 6-month (on 1 July 2011) decay rates are reported to provide scale of activation.

Isotope	$t_{1/2}$ (days)	R_0 (#/kg/day)	Initial Rate (decays/kg/day)	6-Month Rate (decays/kg/day)
^3H	4500	46	3.8	3.7
^7Be	53.22	38	150	14
^{22}Na	951	40	16	14

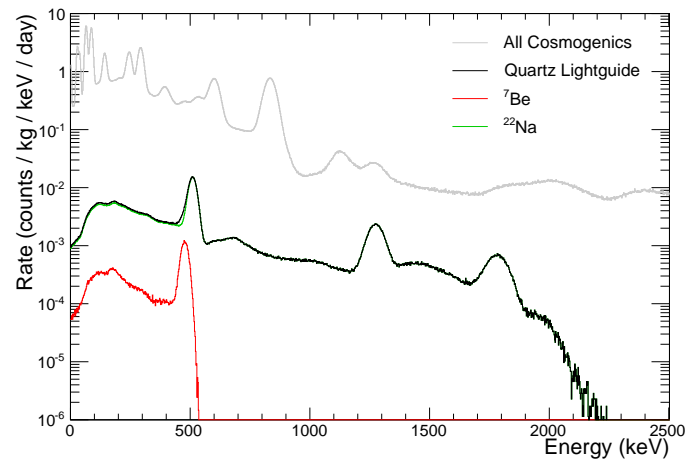


Figure 8.5: Simulated spectrum from activation in the quartz lightguides (black) expected in July 2011 with breakdown by isotope (colors). The background spectrum from quartz activation is orders of magnitude below the total cosmogenic background and contributes negligibly to the total detector background.

revised scaling factor of 2.0 is obtained based on a rigidity of 6.0, altitude of 3230 ft, and conditions near the solar maximum (as was the case in 2009); the scaling factor reported by the group was 2.4.

The reference activation rate must also be scaled from the steel composition measured to the Sandvik 2205⁴ composition used in DM-Ice17 (see Tab. 8.5). The individual activation rates are scaled appropriately by the composition ratios based on the activation channel (*e.g.* ^{54}Mn is produced by $(n, p2n)$ and $(\mu^-, \nu 2n)$ reactions on ^{56}Fe , so the reference activation rate must be scaled by the iron composition ratio).

⁴<http://www.smt.sandvik.com/en/materials-center/material-datasheets/tube-and-pipe-seamless/sandvik-saf-2205/>

Table 8.5: Comparison of steel composition between that measured at LNGS [139] and Sandvik 2205 used in DM-Ice17. The elemental composition ratios are necessary to scale the different reference activation rates (see text).

	Fe	Cr	Ni	Mo	Mn	Si	N	C	P	S	Ti
LNGS measured	69.11	16.62	10.55	2.03	0.83	0.47	0.012	0.03	0.025	0.003	0.32
Sandvik	66.5	22	5	3.2	< 2	< 1	0.18	< 0.030	< 0.030	< 0.015	-

Because steel is an alloy composed of many elements, the activation products are more varied than would be expected from iron alone. The reference activation rates are summarized in Tab.8.6. The iron content (primarily ^{56}Fe) drives the production of manganese isotopes; the nickel content (primarily ^{58}Ni and secondarily ^{60}Ni) drives production of cobalt and nickel isotopes; and the chromium content (primarily ^{52}Cr) drives production of lighter chromium and vanadium isotopes.

The LNGS measurement also attempted to identify cosmogenic ^{57}Co and ^{60}Co in the samples. ^{57}Co was obscured because its gamma lines (122 and 136.5 keV) lie at low energy and are obscured in the Compton spectrum of other lines; this was included in the simulation at its production upper limit level. Activated ^{60}Co ($t_{1/2} = 1925.28\text{days}$) was obscured by the anthropogenic contamination intrinsic to the sample; this was

Table 8.6: Activated isotopes in the steel pressure vessel measured at LNGS.[139] The published reference activation rates have been rescaled to sea level (see text) and Sandvik SS 2205 elemental composition. The initial (on 1 January 2011) and 6-month (on 1 July 2011) decay rates are reported to provide scale of activation. The upper list contains isotopes with half-lives longer than 50 days which may persist into the DM-Ice17 dataset, while the lower list contains shorter-lived isotopes.

Isotope	$t_{1/2}$ (days)	PR_{LNGS} (mBq/kg)	R_0 (#/kg/day)	Initial Rate (decays/kg/day)	6-Month Rate (decays/kg/day)
^7Be	53.22	10.9	478	1990	188
^{46}Sc	83.79	0.53	22	79	18
^{54}Mn	312.20	6.5	274	452	302
^{56}Co	77.24	0.57	11.8	43	8.5
^{57}Co	271.74	< 1.7	< 35.3	< 64	< 40
^{58}Co	70.86	1.5	31	118	20
^{48}V	15.97	0.88	51	230	0.1
^{51}Cr	27.70	4.9	284	1350	15
^{52}Mn	5.591	0.9	36	59	0.0
^{56}Ni	6.075	0.4	8.3	16	0.0

omitted from the cosmogenics simulation because it was identified in the SNOLAB counting and is included in the standard background simulation. If additional ^{60}Co was activated after construction at the same rate as measured for ^{58}Co , it would produce an increase in the ^{60}Co activity above the SNOLAB radioassay measured value of 1%.

The spectrum expected from steel cosmogenic decays is dominated by ^{54}Mn decays (see Fig. 8.6); all other cosmogenic peaks lie an order of magnitude lower than the static background level. At low energy, the Compton spectrum from the ^{54}Mn still dominates. The total contribution from steel isotopes is 0.06–0.07 counts/day/keV/kg in the 0–10 keV region.

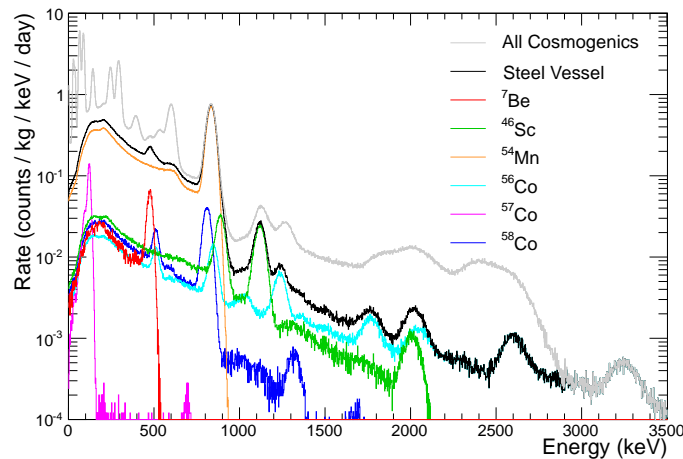


Figure 8.6: Simulated spectrum from activation in the steel pressure vessel (black) expected in July 2011 with breakdown by isotope (colors). The contribution from ^{54}Mn is expected to dominate other activated isotopes in the steel with both the largest total event rate and the most visible spectral feature with its 835 keV gamma line.

8.3 Cosmogenic Activation Products Observed in DM-Ice17 Data

Based on the simulation, the most promising isotopes to identify in data are ^{125}I at 65.3 keV and ^{54}Mn at 835 keV. A secondary search for metastable tellurium isotopes from 88 to 600 keV has also been performed. Based on their features at higher energy, X-ray features below 30 keV are explained; because multiple decays can contribute to the X-rays, half-life and rate measurements of the data features are not attempted.

8.3.1 Activation Products in the Low-Energy Spectrum

The primary expected low-energy decay is that of ^{125}I to stable ^{125}Te with half-life of 59.4 days. The decay occurs via electron capture (followed by up to 31.7 keV in X-rays and Auger electrons) to a 35.5 keV excited state which immediately decays (see Fig. 8.7). The full decay energy is 67.2 keV.

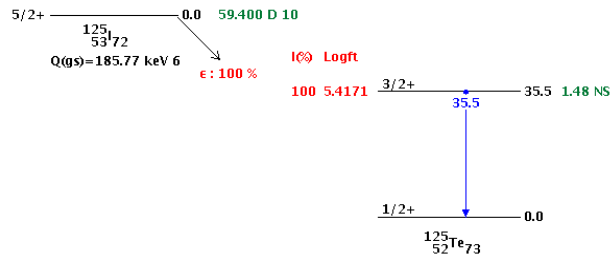


Figure 8.7: Decay scheme for ^{125}I . The electron capture of the decay causes an X-ray or Auger e^- of up to 31.7 keV, and the prompt deexcitation of the $^{125}\text{Te}^*$ daughter releases 35.5 keV via conversion electrons or a gamma. Energy level schema from Nudat 2.6.

The simulated spectrum of these decays has a primary peak at 65.3 from the full energy deposit (see Fig. 8.8). The full energy peak appears at 2 keV below the full decay energy because the simulated Auger electron deexcitation releases up to 9 keV less energy than the full X-ray energy. Because the conversion electron process is preferred to the 35.5 keV gamma for the $^{125}\text{Te}^*$ deexcitation, the lower-energy Auger electron can occur twice causing the doubly-split peaks observed in raw simulation. After applying energy

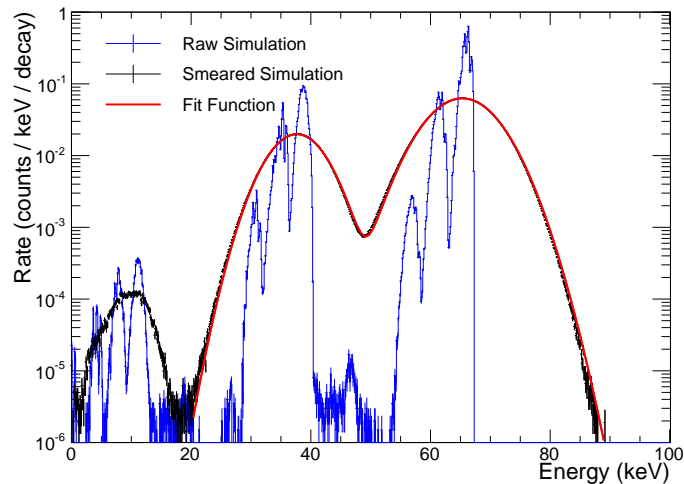


Figure 8.8: Normalized simulated spectrum of activated ^{125}I in NaI crystal (black). The simulation data can be well represented by two Gaussian functions (red) – at the L-shell capture energy of 37.6 keV and at the full energy of 65.3 keV. The ratio of the peak areas is 1:4 with 100% of events depositing energy, resulting in 79.6% of decays in the full energy peak. The triple splitting of both peaks in the unsmeared simulation (blue) is due to energy lost to binding energy in the Auger electron releases; the ratio of the split peak areas follows the Auger versus X-ray deexcitation probability. Statistical rate (y -axis) error bars are included but are negligible.

resolution smearing (Gaussian sigma of 4.7 keV at 65 keV) to the raw simulation, the resulting peaks are well modeled by Gaussian functions with 79.6% of decays in the full energy peak.

A secondary peak appears in the simulated spectrum at 37.6 keV. The majority of these events are from L- or M-shell electron captures, simulated to occur in 19% of decays; capture from L-shell orbital is expected to decrease the total decay energy by 28 keV, consistent with the simulated energy.

In investigating low-energy cosmogenic decays in the DM-Ice17 data, the low-energy calibration was applied out to 150 keV. No time-varying correction was applied to the calibration because the 7% energy resolution at 65 keV is significantly larger than any spectral shift. Since the lowest energy feature expected is above 20 keV, no cuts were applied to the data to remove any possibility of skewing the data; this results in a strong increase in the spectrum and residuals below 15 keV (see Fig. 8.9).

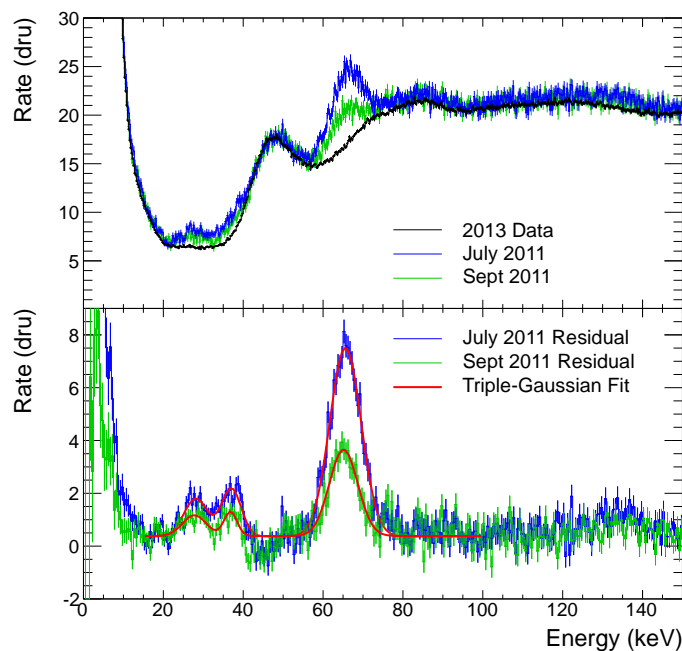


Figure 8.9: Activation lines of ^{125}I revealed in 2011 low-energy Det-1 data (blue and green); comparison is made to all 2013 data (black) to allow time for cosmogenic decay but limit calibration shift. The residual data is fit to a triple-Gaussian function with background offset; this identifies the full-energy (65.3 keV) and L-capture (37.6 keV) peaks of ^{125}I , as well as an additional tellurium or tin X-ray peak at 28 keV. The small feature at 135 keV is consistent with the energy of the ^{125m}Te deexcitation. The spectrum below 20 keV and residual spectrum below 15 keV turn sharply up because the data shown has no cuts applied after LC coincidence. The y -axis variable (dru) is counts/day/keV/kg, and the plotted error bars assume Poisson statistics.

As expected, the strongest feature in the low-energy residuals is the full-energy peak of ^{125}I visible at 65.69 ± 0.18 keV. The Gaussian width (sigma) of this peak is 4.02 ± 0.09 keV, tighter than the 5.05 keV expected from the smeared simulation (4.74 keV width expected for a mono-energetic feature, but the spread in simulated deposited energy further widens the peak); this is consistent with expectation based on the fit result (see Fig. 7.14). The Gaussian fit parameters were all allowed to float, with both a decreasing mean (0.9 keV over 5 months) and sigma (0.6 keV over 5 months) being observed. Because of apparent shift in the fit parameters, only data through August 2011 is used in the quoted peak mean and sigma.

The next feature at lower energy is the L-capture peak of ^{125}I visible at 36.97 ± 0.60 keV; the energy resolution of the detectors causes this peak to overlap somewhat with an X-ray peak, believed to be from tellurium or tin at 28.02 ± 0.51 keV. The L-capture ^{125}I peak has a Gaussian width of 2.18 ± 0.19 keV, much narrower than the 4.05 keV width predicted by simulation. The X-ray peak has a Gaussian width of 2.93 ± 0.63 keV, close to the 3.03 keV width predicted; the simulated width could be broadened if this peak is formed with significant contributions from multiple X-rays (possibly ^{121m}Te and ^{113}Sn). Both peaks exhibit a moderate decrease in mean and sigma parameters at a similar level to that seen in the full energy peak.

The area ratio between the two ^{125}I peaks is 6.63 ± 0.89 , larger than the 3.9:1 expected from simulation. The discrepant peak area ratio and L-capture peak width may be linked to the small calibration shift; the L-capture peak width is primarily set by the high-energy edge, which is possibly sharpened by the undershoot in the residual spectrum at 40 keV from the ^{210}Pb peak. If, however, the simulation incorrectly predicted the peak ratio, this will lead to a systematic error being introduced in estimating the total ^{125}I rate from only the full energy peak.

Between the two ^{125}I peaks the residual spectrum has negative values. This effect is caused by a small calibration shift from the gain decrease over the two years between the reference 2013 data and 2011 data plotted. The ^{210}Pb peak appears at 46.5 keV; a small shift in the peak location to lower energy over time will cause the reference spectrum to have higher rate below 46.5 keV.

The ^{127m}Te deexcitation peak at 88 keV is conspicuously absent, indicating the proposed activation rate is overestimated by at least an order of magnitude (a 0.5 counts/day/keV/kg peak rate would be clearly resolved within the statistical error of the residual spectrum). The ^{125m}Te deexcitation peak at 145 keV is also much lower than the proposed activation rate. The small rise in the residual spectrum below 140 keV could be from this decay; extending the low-energy calibration above its valid range is expected to result in calibrated energies below the true value (see Sect. 7.3.1).

8.3.1.1 Iodine-125 Rate Analysis

The analysis studying the ^{125}I full-energy peak was performed on bimonthly spectra beginning with June 2011 to provide better identification of its 59.4 day half-life. In fitting the full energy peak, residuals were

constructed by subtracting off a 12-month average spectrum constructed from all 2013 data; by January 2013, the ^{125}I rate had fallen to 0.11% of the rate in July 2011.

The peak was analyzed both by fits to a Gaussian function and energy-range integration (see Tab. 8.7), both with various background models. Three fit models are presented - a triple Gaussian with offset over 15–100 keV (see Fig. 8.9), a single Gaussian with offset over 50–100 keV, and a single Gaussian without offset over 50–100 keV. The fit range was set to avoid at low energy either the noise turn on at 15 keV (triple Gaussian) or ^{210}Pb peak shift undershoot at 45 keV, and at high energy to cover a region of flat background. The integration methods both use an energy range of 52–80 keV, one background subtracted using the 80–100 keV range to estimate the flat background and the other with no background but an offset term added to the exponential decay fit. The integration range was selected to cover $\pm 3.5\text{-}\sigma$ around the peak center to give full $3\text{-}\sigma$ (99.7%) peak coverage despite small shifts in the peak location; integration ranges down to $1\text{-}\sigma$ yielded consistent peak area estimates after correcting for Gaussian peak coverage, while single-sided preferred a longer half-life for the left-side integration (consistent with expectation of a shifting peak).

Table 8.7: Initial rate determination and fit parameters for exponential decay of ^{125}I full-energy peak. The fit methods for Det-2 (indicated in italics) all failed to converge in later months, making the obtained parameters less reliable. The methods which did not account for background provided better agreement with the known half-life of 59.4 days. The ‘Integral’ method was adopted for the quoted activation level because of the better fit performance; a systematic uncertainty is introduced from the uncorrected background contribution.

	Method	Floating $t_{1/2}$			Fixed $t_{1/2}$	
		$t_{1/2}$ (days)	Initial Rate (counts/kg/day)	χ^2/DOF	Initial Rate (counts/kg/day)	χ^2/DOF
Det-1	Triple-Gaussian	52.2 ± 1.8	955 ± 94	11.7/22	677 ± 13	25.9/23
	Gaussian + BG	47.9 ± 1.7	1130 ± 122	17.1/22	615 ± 13	55.6/23
	Gaussian	59.6 ± 2.1	779 ± 68	6.8/22	787 ± 14	6.8/23
	Integral	59.2 ± 1.8	802 ± 11	24.5/27	803 ± 11	24.5/28
	Integral - BG	52.1 ± 2.4	978 ± 112	22.3/27	719 ± 15	30.4/28
Det-2	<i>Triple-Gaussian</i>	76.4 ± 4.0	349 ± 37	$72.1/22$	607 ± 14	$95.5/23$
	<i>Gaussian + BG</i>	56.1 ± 2.5	644 ± 78	$20.4/22$	556 ± 14	$22.0/23$
	<i>Gaussian</i>	73.4 ± 5.8	446 ± 61	$48.8/22$	668 ± 18	$57.0/23$
	Integral	60.9 ± 2.6	615 ± 56	24.8/27	648 ± 12	25.2/28
	Integral - BG	48.2 ± 2.9	912 ± 152	19.0/27	547 ± 16	30.2/28

For each method, the bimonthly points were fit with an exponential function (see Fig. 8.10) both with fixed and floating half-life; the results of the fits are summarized in Tab. 8.7. The Gaussian fits could not be made to converge after 12 months (rate is 1.2% of 1 July 2011 rate) with some problematic fits as early as 8 months; all fit parameters were allowed to float, but fit convergence was not significantly improved by fixing mean and/or sigma parameters. To present consistent data, the integration method was truncated at 15 months (rate is 0.4% of 1 July 2011 rate).

The ‘Integral’ method for both detectors obtained an exponential decay with a rate parameter matching within error the ^{125}I half-life. For Det-1 the simple Gaussian fit without background offset also matched the rate parameter; the Det-2 simple Gaussian fit failed in later months and the exponential fit is not representative of the data.

All more complicated models attempting to account for background changes result in half-lives shorter than expected for ^{125}I . For all three background-subtracted methods (‘Triple-Gaussian,’ ‘Gaussian + BG,’ and ‘Integral - BG’) the background follows an exponential trend with half-lives of 150–200 days; no faster decaying exponential background component is expected to pull the data in this direction. The residuals

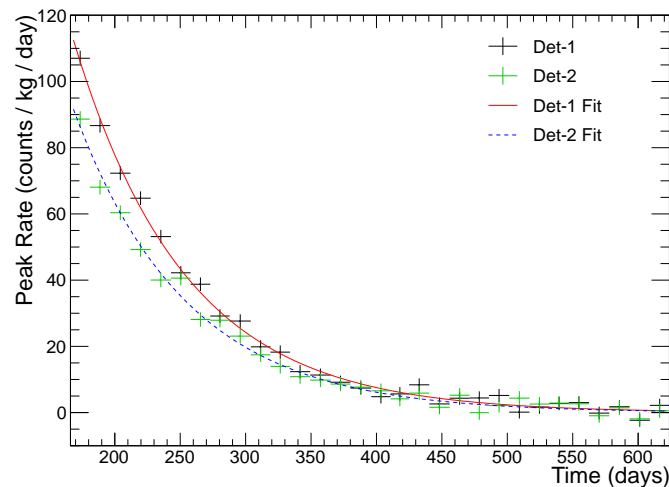


Figure 8.10: Observed rate in 52–80 keV range of low-energy spectrum to identify the decaying 65.3 keV peak of ^{125}I . Det-1 (black) observes a 24% higher initial rate of ^{125}I decays than Det-2 (green), consistent with expectation based on exposure histories. Fits to the decaying rate are consistent with the 59.4 day half-life of ^{125}I for both Det-1 (red, solid) and Det-2 (blue, dashed). Data is binned in time (x -axis) matching the variable livetime of bimonthly intervals and the plotted rate (y -axis) error bars statistical; the y -axis variable (dru) is counts/day/keV/kg. Since the static background level is different in the two detectors, the data was fit to an exponential plus offset and the data have been shifted by the fit offset value.

from the fits, background-subtracted or not, are consistent within errors of flat and show no significant behavior to indicate preference of one fit method over the others.

Comparing the results from the fixed $t_{1/2}$ ‘Integral’ method to the simulation expectation, the initial (1 January 2011) rates after scaling for full-energy peak efficiency are 1010 and 814 counts/kg/day (11.7 and 9.42 mBq/kg) for Det-1 and Det-2, respectively. These rates are consistent within error to the simulation expectation of 817 and 715 counts/kg/day. The quoted data rates are possibly overestimated given the systematic uncertainty from excluding the background estimation; different accounting methods for the background were shown to reduce the measured rate by 10–20%.

8.3.2 Activation Products in the High-Energy Spectrum

The primary expected high-energy decay is that of ^{54}Mn to stable ^{54}Cr with half-life of 312.2 days. The decay occurs via electron capture to a 834.8 keV excited state which immediately deexcites to ground via release of a single gamma. The energy deposited in the crystal is either the full gamma energy or from its Compton spectrum (see Fig. 8.11). The gamma peak in simulation is well-modeled a Gaussian function on a linear background which is centered 1.3 keV below the full energy due to the non-flat background;

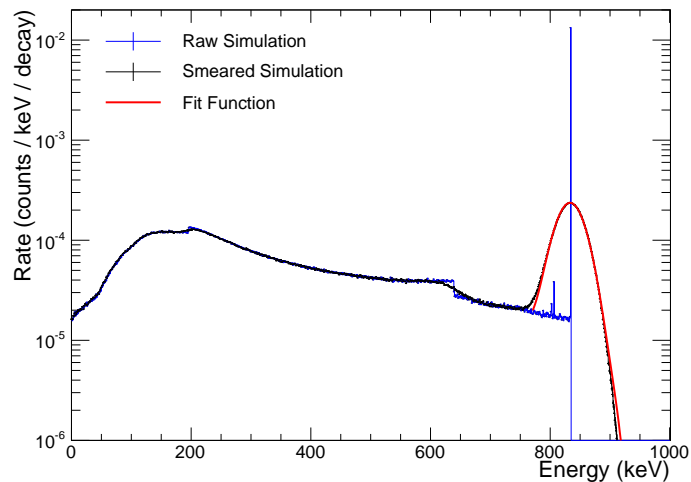


Figure 8.11: Simulated spectrum of activated ^{54}Mn in steel pressure vessel (black). The gamma line at 835 keV is well represented by a Gaussian function (red) on a linear background which skews the peak center lower in energy by 1. keV. Only 6.0% of decays (lower pressure vessel only) result in any energy deposition in the crystal, with 1.3% depositing the full gamma energy. All energy deposited in the crystal is from one gamma, with Compton edges at 639 and 196 keV visible in the unsmeared simulation (blue).

its predicted width is 23.3 keV, matching the resolution function smearing at this energy. The detection efficiency for this decay is 1.3% for the full energy peak and 6.0% for any energy.

In investigating high-energy cosmogenic decays in the DM-Ice17 data, the high-energy calibration was applied; time-varying corrections were applied because the few-percent gain shift over the full dataset are larger than the energy resolution at the highest energy (2%). The reference spectrum is the all-2014 time-calibrated data average; the reference data has 1% statistical error bars for 1 keV binning at 800 keV. For the preliminary analysis, the time binning utilizes quarter-year increments (see Fig. 8.12).

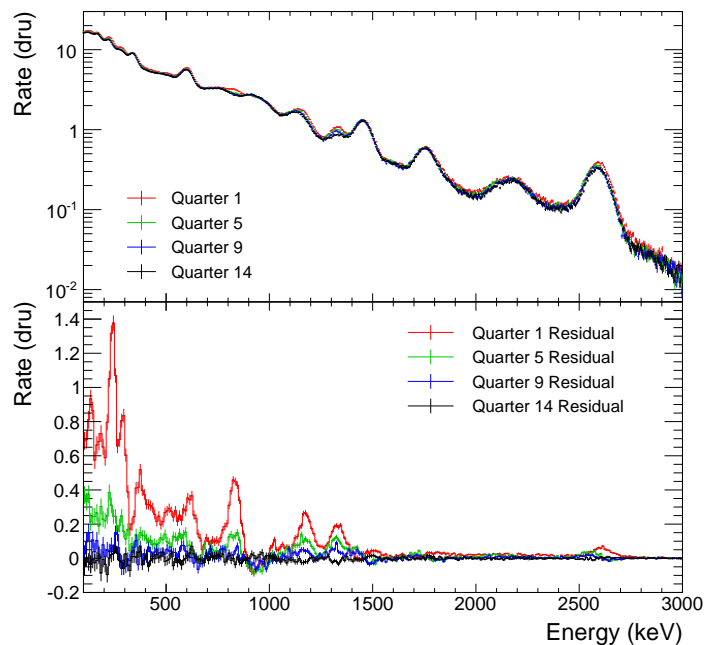


Figure 8.12: High energy Det-1 data (top) and data residual (bottom); comparison for residuals is made to all-2014 reference spectrum to allow time for the 312.2 day decay half-life of ^{54}Mn . The primary cosmogenic peak visible is the 835 keV ^{54}Mn gamma. Higher energy features correspond to ^{60}Co (1173 and 1332 keV gammas) and ^{208}Tl (2615 keV gamma) decays in the pressure vessel; these decays are included in the standard background simulation. Lower energy features are primarily attributed to decays of activated metastable tellurium isotopes. Quarter 1 is July–September 2011 and Quarter 14 is October–December 2014. The y -axis variable (dru) is counts/day/keV/kg, and the plotted error bars assume Poisson statistics.

At energies above the ^{54}Mn peak, three peaks from decays of isotopes in the steel pressure vessel present in the standard background model dominate the residual spectrum (see Sect. 8.3.3). These can be well-modeled by ^{60}Co (1173 and 1332 keV) and ^{208}Tl (2615 keV). The deficit above 900 keV also comes from the pressure vessel, where the broken ^{232}Th -chain gives rise to an increasing ^{228}Ac concentration.

At energies below the ^{54}Mn peak, the dominant features are expected to arise from metastable tellurium decays. Two peaks will arise from ^{121m}Te decays; one at 294 keV from the metastable state deexcitation and the other near 600 keV through the decay of its shorter-lived daughter ^{121}Te . The last peak expected is at 247 keV from the deexcitation of ^{123m}Te decaying to stable ^{123}Te .

Analyzing the ^{54}Mn fitted Gaussian peak parameters from the first six-months of data yields a mean of 837.0 ± 1.0 keV and width 21.9 ± 0.6 keV. Both of these fit parameters are possibly impacted by the presence of the residual deficit from ^{228}Ac at immediately higher energy; an overlapping negative peak would decrease the observed mean energy and width of the ^{54}Mn peak, while uncorrected distortion of the background shape could have the opposite effects.

8.3.2.1 Manganese-54 Rate Analysis

The time-varying correction for the high-energy spectra involved a gain loss of 0.8%/yr for Det-1 and 0.2%/yr for Det-2. Gaussian fits were performed over 700–900 keV, a range capturing the flat background region below the peak and truncating before the deficit at higher energy; fits were attempted both on quarterly and monthly data intervals. Integration was performed over 1- ($811\text{--}859$ keV) and $2\text{-}\sigma$ ($787\text{--}883$ keV) ranges around the predicted peak location in both symmetric and single-sided intervals; integration ranges were selected to not include the deficit region at higher energy. The Gaussian fits showed similar behavior independent of the background model (none, flat, or linear) and all failed to converge for most data intervals after 15 months; even in the early periods, the fit suffered from the irregular background shape and had poor goodness-of-fit.

The integral data shows a clear exponential decay (see Fig. 8.13), but always with a half-life shorter than the expected 312.2 days; values ranged from 260–305 days. The extrapolated initial rate estimates from different fitting ranges were consistent within error, but the high energy single-sided integrations consistently returned a higher half-life than the low energy side.

In the Det-2 data, months 12–16 (June–October 2012) exhibited a shift in the spectrum to higher energy even in the non-time-corrected calibration; the effect of this shift is a Gaussian-like bump in the exponential decay spanning the effected months. The fit function was modified with a floating Gaussian feature to prevent this data from pulling the other fit parameters. The effect of unexplained spectral behavior from gain shifts on the reported activation rate is treated as an additional systematic uncertainty.

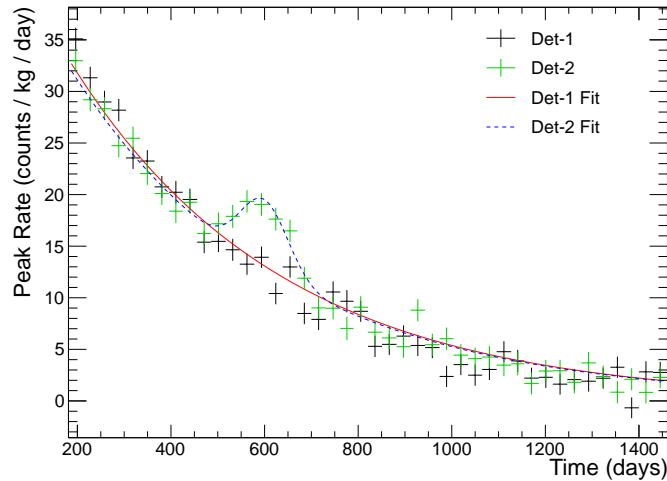


Figure 8.13: Observed rate in 52–80 keV range of low-energy spectrum to identify the decaying 65.3 keV peak of ^{125}I . Det-1 (black) observes a 7% higher initial rate of ^{54}Mn decays than Det-2 (green), consistent with expectation based on exposure histories. Fixed half-life fits to the decaying rate are shown for both Det-1 (red, solid) and Det-2 (blue, dashed) as the fits with floating half-life consistently prefer half-lives a month shorter than the 312.2 days expected. The bump in the Det-2 decay near day 600 is attributed to a spectral shift in those months, the cause of which is not understood. Data is binned in time (x -axis) matching the variable livetime of monthly intervals and the plotted rate (y -axis) error bars statistical. Since the static background level is different in the two detectors, the data was fit to an exponential plus offset and the data have been shifted by the fit offset value.

Fit values for the initial rate in the $2\text{-}\sigma$ integration window are 53.4 ± 0.9 and 50.1 ± 1.0 counts/kg(crystal)/day for Det-1 and Det-2, respectively. Correcting for detection efficiency in this energy interval (1.4%) and mass ratio of steel to crystal (10.3), rates of 380 and 356 counts/kg(steel)/day are obtained. These are consistent within error of the simulation expectation of 452 and 422 counts/kg/day.

The dominant systematic uncertainty for ^{54}Mn arises from the unknown historical exposure of the steel; because of the with its 312 day half-life, this exposure accounts for 31% (140 counts/kg/day initial rate for either detector) of the total ^{54}Mn activation. Additional systematic uncertainty is introduced by the unaccounted-for background causing the best-fit half-life to be lower than expected for ^{54}Mn and the spectral shift uncertainty demonstrated by the Det-2 bump.

8.3.3 Simulation Agreement

A qualitative assessment of the agreement in the data residuals has been made by combining the cosmogenic simulation with the few isotopes of the standard background simulation which are known or hypothesized to have changing decay rates. The comparison was made from high to low-energy in order to

isolate the most unique features of each isotope or decay chain. Both difference spectra are constructed as the difference between the ‘Quarter 1’ (July–September 2011) and all-2014 data, with the high-energy using a time-corrected calibration and the low-energy applying no correction.

At energies above 700 keV, individual peaks exist in the difference spectra which enable unambiguous identification of the decaying components (see Fig. 8.14). Components from the standard background simulation are ^{60}Co and ^{232}Th -chain (represented by ^{228}Ra – ^{228}Ac and ^{228}Th – ^{208}Tl); components from the cosmogenic simulation are ^{54}Mn and ^{58}Co .

Reproducing the spectral features requires a maximally-broken out of equilibrium ^{232}Th -chain, allowing the ^{208}Tl and ^{228}Ac rates to float independent of each other; this can be accomplished by breaks at ^{228}Ra

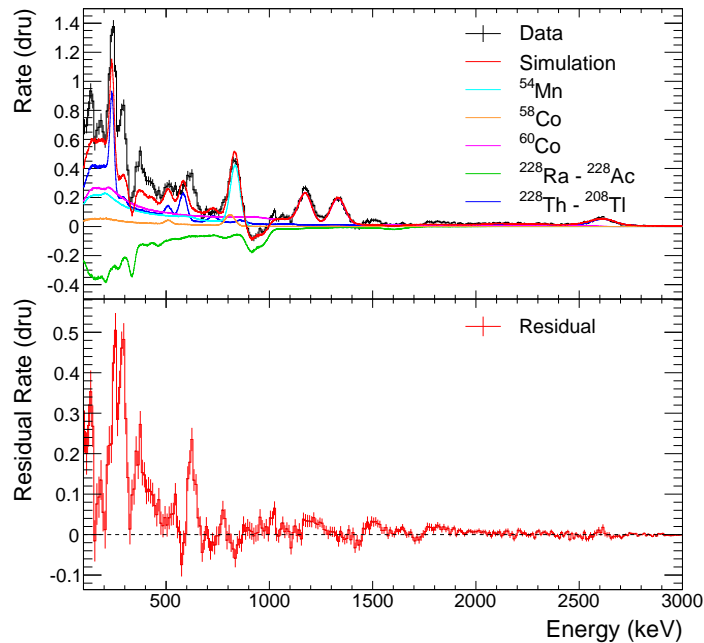


Figure 8.14: High energy Det-1 data difference spectrum between Quarter 1 and all-2014 (top) and residual from simulation contributions (bottom); all simulated features can be modeled by gammas emitted by pressure vessel isotopes. A maximally-broken ^{232}Th -chain gives rise to a decaying ^{208}Tl rate (2615 keV peak) and a rising ^{228}Ac rate (~ 900 keV). The ^{60}Co concentration in the pressure vessel decaying with 5.27 yr half-life gives rise to the pair of peaks at 1173 and 1332 keV. The cosmogenic ^{54}Mn concentration decaying with 312 day half-life gives rise to the 835 keV peak. A small concentration of cosmogenic ^{58}Co giving rise to a gamma line at 811 keV improves agreement with data on the low-energy side of the ^{54}Mn peak. The five highest-energy peaks set the concentrations of these isotope and chain decays, setting the rates of less definitive lines below 700 keV and Compton spectra. The y -axis variable (dru) is counts/day/keV/kg, and the plotted error bars (data and residual) assume Poisson statistics.

($t_{1/2} = 5.75$ yr) and ^{228}Th ($t_{1/2} = 1.912$ yr). Although the steel pressure vessel and PMT are simulated with approximately equivalent contributions to the ^{208}Tl peak (see Fig. 7.19), breaking the chain in the pressure vessel provides better agreement with data because the age of the PMT glass (~ 10 yr at DM-Ice17 deployment) strongly limits the relative rates. The ^{208}Tl decay gives rise to the peak at 2615 keV and the increasing ^{228}Ac decay gives rise to the broad negative feature above 900 keV (from gammas of energies 911, 965, and 968 keV); the ^{232}Th must be decaying at a much higher rate to populate the ^{228}Ra portion of the chain, but this no energy from the alpha decay reaches the crystal. The simulated rates of these decays to reproduce the peaks are 2.7 mBq/kg of ^{228}Th – ^{208}Tl and -2.7 mBq/kg of ^{228}Ra – ^{228}Ac ; these activities are realistic values given the SNOLAB steel assay measurement of 6.49 mBq/kg (^{208}Tl line activity) made in November 2010.

The ^{60}Co decay ($t_{1/2} = 1925.28$ days) gives rise to a pair of peaks at 1173 and 1332 keV. The gamma lines are equal in intensity, but the lower-energy line appears at 20% higher rate due to underlying Compton features. The simulated rate in the difference spectrum is 1.6 mBq/kg, 20% lower than expected based on the 7.19 ± 0.82 mBq/kg (in November 2010) measured initial concentration of ^{60}Co . A lower ^{60}Co rate is also preferred by the general simulation agreement (see Fig. 7.19).

The cosmogenic ^{54}Mn decay ($t_{1/2} = 312.2$ days) gives rise to the gamma line at 835 keV (see Sect. 8.3.2.1). The simulated rate in the difference spectrum is 2.0 mBq/kg, 20% lower than the expected 2.9 mBq/kg; this discrepancy is of similar magnitude to that obtained from the exponential fit to the peak rate.

A cosmogenic ^{58}Co decay ($t_{1/2} = 70.86$ days) was also included in the model to produce better agreement with the data match on the low-energy edge of the ^{54}Mn peak. This isotope decays via electron capture to excited states of ^{58}Fe and produces an 811 keV gamma in every decay. The simulated rate in the difference spectrum is 0.4 mBq/kg, considerably higher than the expected 0.2 mBq/kg.

The residual shows good agreement between the simulation model and data. A small mismatch visible at the 2615 keV ^{208}Tl peak is due to the resolution; the simulated peak is broader and shorter than data, producing an oscillatory pattern in the residual. This mismatch is expected given the resolution function overestimates the observed width at 2615 (see Fig. 7.14). Other variations in the residual down to 700 keV may also arise from resolution or else from small variation in the calibration which generate aberrant features in the difference spectrum.

Applying the high-energy contributions down to 100 keV, the low-energy limit of the calibration validity, the data residual exhibits the need for additional contributions (see Fig. 8.15). Potential cosmogenic contributions to this region of the energy spectrum are dominated by metastable tellurium isotopes and ^{113}Sn , all from the crystal. Both ^{123m}Te and ^{125m}Te produce mono-energetic lines from their deexcitation to effectively stable ($t_{1/2} > 10^{15}$ yr) ground states; these peaks can appear at 247 and 145 keV, respectively. ^{121m}Te , the other medium-energy metastable isotope, decays with 88.6% probability to the ground state and

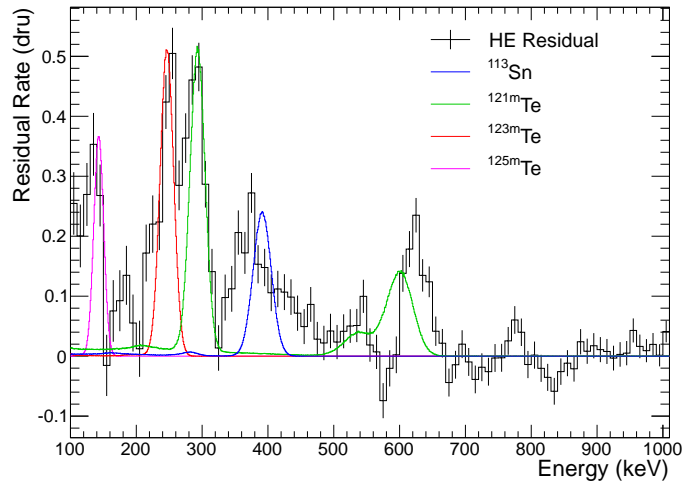


Figure 8.15: Medium energy Det-1 data difference spectrum residual (black) and comparison to possible cosmogenic decays from the NaI crystal (colors); the simulation contribution from high-energy components (see Fig. 8.14) have been removed from the residual. The sharpest features are the peaks at 250 and 300 keV, which can be reproduced by ^{123m}Te and ^{121m}Te , respectively; this ^{121m}Te decay rate would also produce a peak at 600 keV which is not reproduced in the data. Decay of ^{113}Sn could account for some of the excess at 400 keV, but the shape of the data spectrum is poorly matched to a single gamma line. Decay of ^{125m}Te could produce the excess at 150 keV. Because this data corresponds to the Compton shoulder of the spectrum, small variations in detector response can give rise to disproportionate features in the residual, making quantitative analysis of this region beyond the scope of this work. The y -axis variable (dru) is counts/day/keV/kg, and the plotted error bars (data and residual) assume Poisson statistics.

then via electron capture to ^{121}Sb ; the two decays will be in equilibrium by the start of the dataset because of the short ($t_{1/2} = 19.17$ days) half-life of ^{121}Te . The primary features expected of these decays are the deexcitation line at 294 keV and a peak at 600 keV corresponding to the full ^{121}Te decay energy; smaller features exist at 540, 30, and 3 keV. ^{113}Sn decays via electron capture primarily to the 391.7 keV metastable state of ^{113}In ($t_{1/2} = 99.476$ min) which then deexcites to the stable ground state; these results in a line at the metastable deexcitation energy and X-ray features from the electron capture at the K- and L-shell energies of 28 and 3 keV respectively.

These medium energy lines lie under the Compton shoulder of the energy spectrum, where the event rate is the highest and the background most difficult to model. The calibration stability limits the confidence of cosmogenic matching in this region, both because small shifts in the calibration under the rapidly varying non-linear background can rapidly generate false features and because the background shape adds uncertainty to the calibration. Within these limitations, cosmogenics decays of reasonable rate can improve the agreement

in this region; the simulation levels of 0.12, 0.21, 0.16, and 0.08 mBq/kg for ^{113}Sn , ^{121m}Te , ^{123m}Te , and ^{125m}Te (see Fig. 8.15) correspond to 175, 27, 41, and 37% of the predicted rates.

The only cosmogenic isotopes remaining with concentrations to be set by the low-energy region are ^{125}I and ^{127m}Te (see Fig. 8.16). The ^{127m}Te deexcitation to the ground state would produce a mono-energetic peak at 88 keV; the absence of any feature only allows a weak limit to be placed on the ^{127m}Te production rate of 10% the quoted ACTIVIA level. The ^{125}I decay produces a pair of peaks at 65 and 38 keV with area ratio of 4:1 (see Sect. 8.3.1.1); these are reproduced with activity 0.75 mBq/kg, 5% higher than the predicted

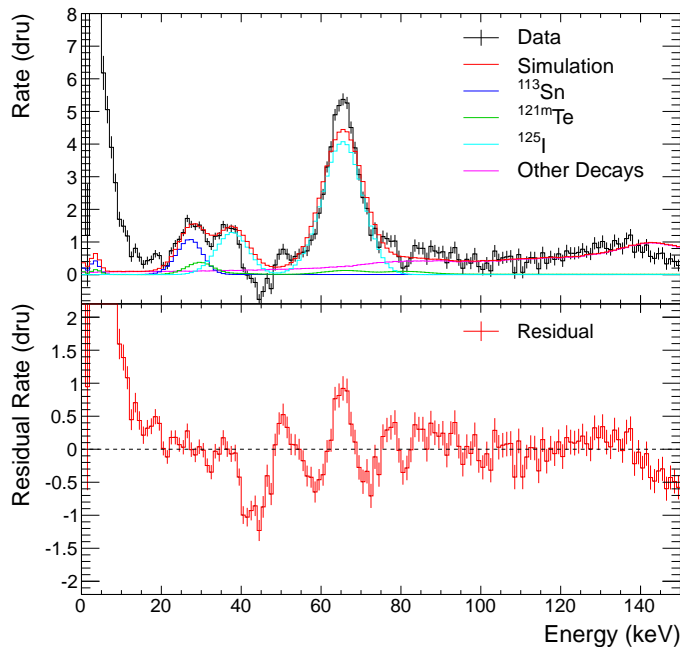


Figure 8.16: Low energy Det-1 data difference spectrum between Quarter 1 and all-2014 (top) and residual from simulation contributions (bottom); contributions from crystal cosmogenic decays dominate the difference spectrum in this region. Cosmogenic ^{125}I with full energy peak at 65.3 keV and L-capture peak at 37.6 keV is the only decaying isotope which does not have higher energy (> 100 keV) features to constrain its rate. Cosmogenic ^{113}Sn and ^{121m}Te , whose rates are weakly indicated by peaks from 200–600 keV, both contribute to the X-ray peaks at 3 keV and 28 keV. The low-energy calibration used is valid up to 100 keV, giving rise to the observed discrepancy above 120 keV. Oscillations in the residual around 65 keV are indicative of the discrepancy in energy resolution around the ^{125}I full-energy peak. Discrepancy around 45 keV is caused by calibration shift around the ^{210}Pb peak at 46.5 keV. The rising spectrum below 15 keV is an artifact of the uncut data used in this analysis, in which thin pulse noise events dominate at low energy. The y -axis variable (dru) is counts/day/keV/kg, and the plotted error bars (data and residual) assume Poisson statistics.

level. Decays of ^{113}Sn and ^{121m}Te , whose rates were set by intermediate-energy spectral features, contribute both to the X-ray peaks below 30 and at 3 keV. The impact of all decaying on the low-energy region is a change of 1.8 counts/kg/day over 2–6 keV (0.45 counts/day/keV/kg average) with 83% of this rate coming from the ^{113}Sn and ^{121m}Te decays; the events are peaked at 3.5 keV.

The low-energy match between data and simulation has several shortcomings. The resolution mismatch gives rise to an oscillation in the residual around the 65 keV full-energy ^{125}I peak, where matching the peak area produces a shorter and wider peak. Above the 38 keV ^{125}I L-capture peak is a deficit in the difference spectrum which is increased in the residual; no increasing components of the spectra are expected in this region from broken decay chains, making this likely tied to a shift in the calibration around the 46.5 keV ^{210}Pb peak. The upturn observed at low-energy is from noise events which were not removed from the analyzed spectrum; cut efficiency below 5 keV has sufficient uncertainty that no clarity on the 3 keV peak could be gained. The deficit above 140 keV is a result of undercalibrating the energy of events beyond the low-energy calibration validity limit of 100 keV.

8.4 Comparison to Other NaI Detectors

Cosmogenic activation products have also been reported by the ANAIS [199], DAMA [191], and KIMS [23] NaI(Tl) dark matter experiments; only ANAIS presents a quantitative discussion. The DAMA spectrum clearly demonstrates the decay of ^{125}I after a period of underground storage, and they briefly discuss the limits on ^{24}Na and ^3H . KIMS also illustrates the decay of ^{125}I over two months in spectra that also exhibits the lower-energy Te/Sn X-ray line; coincidence between multiple crystals allows identification of ^{22}Na events as well, although this decay is not yet apparent in the dataset available.

ANAIS collected spectra over 200 days immediately after moving new crystals underground; these crystals had been grown at an altitude of 5000 ft and so had an extensive activation history. By analyzing the decay of spectral features, they positively identified the signatures of eight isotopes; for all cosmogenic isotopes identified they also assessed *ab-initio* libraries and experimental data to calculate the expected production rate. The libraries referenced do distinguish between production of metastable and ground states. These results are summarized in Tab. 8.8 and compared to the ACTIVIA predictions.

For ^{125}I , the decay rates calculated and measured match the ACTIVIA prediction within error, with simulation preferring a 10% higher value. The DM-Ice17 measurement of ^{125}I is 15–25% higher than the simulation prediction; a moderately higher production rate would improve agreement, but there is no tension between the measurements. The DM-Ice17 measurement based only on matching of simulation residuals over the entire dataset is in much closer agreement with the ANAIS calculation and measurement. No discussion is made by ANAIS of analysis on the L-capture peak.

Table 8.8: Comparison of measured cosmogenic activation rates from NaI isotopes. Values generated for this analysis are ACTIVIA simulation (from Tab. 8.3) and DM-Ice17 measurement. ANAIS performed both a calculation based on *ab-initio* cross section calculations and measurements based on 200 days of data after an extended activation period. [199]. The ACTIVIA estimates of metastable tellurium isotopes (noted in italics) are prone to overestimate. The DM-Ice17 values are all based on simulation matching except ^{125}I , which has an additional measurement (in parentheses) based on the analysis of the decaying full-energy peak (see Sect. 8.3.1.1). Systematic errors of $> 10\%$ dominate the DM-Ice17 measured values. Agreement between DM-Ice17 and ANAIS measured values is within $1\text{-}\sigma$ errors for all isotopes except ^{123m}Te and ^{127m}Te . The upper list contains isotopes with half-lives longer than 50 days which persist into the DM-Ice17 dataset, while the lower list contains shorter-lived which decayed away during the six-month commissioning period and are not accessible to DM-Ice17 analysis.

		DM-Ice17		ANAIS	
Isotope	$t_{1/2}$ (days)	ACTIVIA (#/kg/day)	Measurement (#/kg/day)	Calculation (#/kg/day)	Measurement (#/kg/day)
^{22}Na	951	66	-	53.6	45.1 ± 1.9
^{113}Sn	115.09	9.0	16	-	-
^{121m}Te	164.2	<i>93</i>	25	23.8	23.5 ± 0.8
^{123m}Te	119.2	<i>52</i>	21	33.2	31.6 ± 1.1
^{125m}Te	57.40	<i>74</i>	27	41.9	28.2 ± 1.3
^{127m}Te	106.1	<i>93</i>	< 9	7.1	10.2 ± 0.4
^{125}I	59.400	221	230 (273)	242.3	220 ± 10
^{121}Te	19.17	<i>93</i>	-	8.4	9.9 ± 3.7
^{126}I	12.93	128	-	297.0	283 ± 36

The metastable tellurium isotopes are all calculated and measured to have significantly lower production rates than the ACTIVIA prediction. For the long-lived isotopes discussed, the ratios of the ANAIS measured value to ACTIVIA predictions are 25%, 61%, 38%, and 11% for ^{121m}Te , ^{123m}Te , ^{125m}Te , and ^{127m}Te , respectively. These are in very good agreement with the estimates made when attempting to match the data residual peaks (27%, 41%, 37%, and $< 10\%$, see Sect. 8.3.3). It is somewhat surprising that the mono energetic ^{123m}Te feature would be underestimated by 33%, but some issue is clear in the energy calibration from the ^{121m}Te features near 600 keV.

In addition to the cosmogenics observed in DM-Ice17, ANAIS was able to measure ^{22}Na , ^{121}Te , and isoI126 through coincidence features between adjacent crystals. Because the two DM-Ice17 crystals are physically removed from each other, this powerful reduction technique was not available for this analysis.

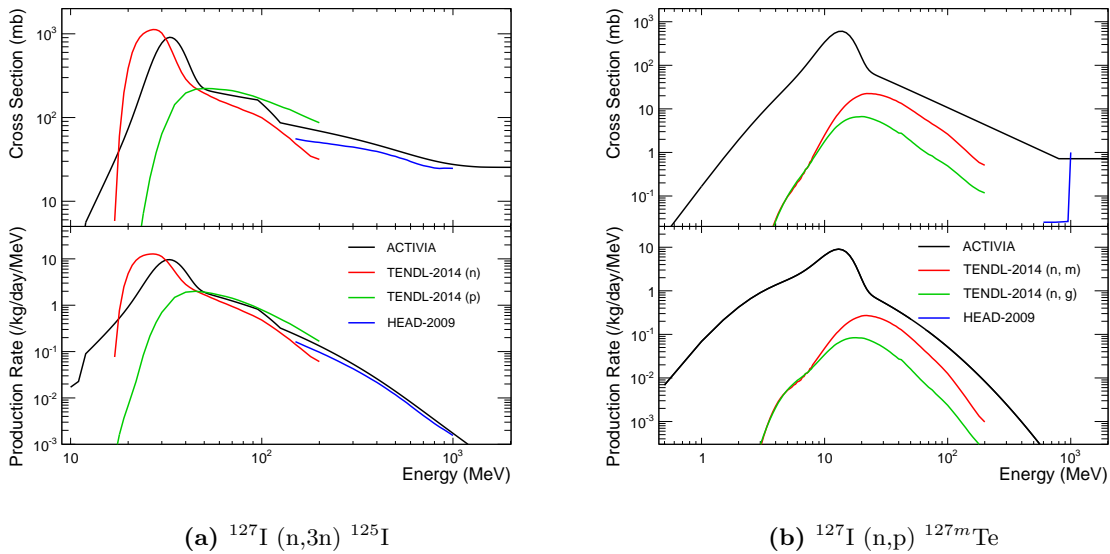


Figure 8.17: Comparison of cross section (top) and differential production rate (bottom) predictions for ^{125}I (left) and ^{127m}Te (right). The differential production rate convolves the cross section data with the cosmic ray neutron spectrum from Gordon. Cross section values from ACTIVIA (black), TENDL-2014 (p) library (green), and HEAD-2009 library are all based on proton activation. The ANAIS study found the best agreement with data for most isotopes by combining TENDL data (up to 200 MeV) with HEAD-2009 (150–1000 MeV). In ^{125}I production, the ACTIVIA cross section calculation departs from the TENDL proton calculations below 50 MeV and better reproduces the TENDL neutron calculation which yields a much more accurate activation estimate. In ^{127m}Te production, the ACTIVIA calculation exceeds the total TENDL prediction at all energies, yielding an activation overestimate by a factor of ten. Calculating production of ^{127m}Te also caused problems for the HEAD calculation, forcing the ANAIS calculation to use an extrapolation from TENDL data.

The isotopes identified by this analysis in DM-Ice17 but absent in ANAIS are ^{58}Co , ^{54}Mn , and ^{113}Sn ; the ^{58}Co and ^{54}Mn are produced in the steel pressure vessel and therefore not be expected in their data. ^{113}Sn , however, is expected equivalently in all NaI detectors, and is an important omission.

Activation of ^{113}Sn requires loss of 3 protons and 12 neutrons (assuming neutron capture), and so has a much higher nucleon difference to the target than all other activation products discussed by the ANAIS study. It is produced both directly and via decays of the chain $^{113}\text{I} \rightarrow ^{113}\text{Te} \rightarrow ^{113}\text{Sb} \rightarrow ^{113}\text{Sn}$, with ^{113}Sb production contributing 40% of the total.

The < 100 keV spectrum of ^{113}Sn is significant because it decays by electron capture to a metastable indium state with half-life 99.5 min (with 99.79% probability). The long-lived metastable daughter state allows the prompt decay emission to only consist of low-energy X-ray or Auger electron deexcitation of the

electron capture-induced vacancy. The energy of the first decay is 3 or 28 keV depending on the shell of the electron capture, the energy of the delayed deexcitation is the 392 keV state energy.

Since this decay was not identified in the ANAIS study, it is important to validate the cross section calculation from ACTIVIA. Adopting the same libraries as used by ANAIS, TENDL-2014⁵ [144] neutron data up to 200 MeV and HEAD-2009⁶ [142] proton data over 200–1000 MeV (see Fig. 8.18) are used. The overall agreement of the ACTIVIA cross section calculation with these libraries is poor across the entire energy ranging, differing by up to an order of magnitude above 100 MeV. The calculated ^{113}Sn production rate is 7% higher than that calculated by ACTIVIA.

⁵ Publicly released at <ftp://ftp.nrg.eu/pub/www/talys/tendl2014/tendl2014.html>

⁶ Made available by Prof. Korovin

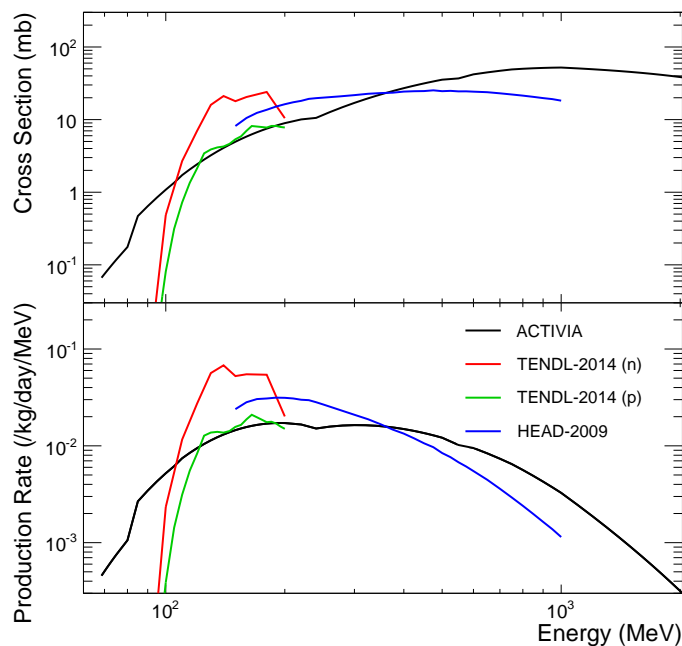


Figure 8.18: Comparison of cross section (top) and differential production rate (bottom) predictions for ^{113}Sn . The differential production rate convolves the cross section data with the cosmic ray neutron spectrum from Gordon. Cross section values from ACTIVIA (black), TENDL-2014 (p) library (green), and HEAD-2009 library are all based on proton activation. The ANAIS study found the best agreement with data for most isotopes by combining TENDL data (up to 200 MeV) with HEAD-2009 (150–1000 MeV). Although the ACTIVIA cross section calculation consistently mismatches the data at all energies, the total production rate calculation only underestimates the value obtained from TENDL + HEAD by 7%.

The DM-Ice17 measured ^{113}Sn production rate from simulation match remains 60% above the simulated rate even after adopting the cross sections adopted from the data libraries. The error on the cross section values appears higher for this production channel than in others, with different alternate libraries predicting a wide spread in values. Because this production requires loss of 15 nucleons after capture, no experimental results exists in the EXFOR database. Constraining this production rate is important open question moving forward.

8.5 Summary

Based on the analysis of cosmogenics in DM-Ice17 data, the simulation procedure has been validated for estimating the production of cosmogenic isotopes in the detector components. The measured rates in DM-Ice17 agree within errors with those obtained by ANAIS. Systematic errors dominate this analysis, emerging in the discrepancies of the ^{125}I rate based on different estimation methods as well as the calibration and background uncertainty in analyzing the 100 – 700 keV region. The exposure history can be better constrained for future measurements by utilizing GPS trackers to reduce uncertainty in the simulation prediction.

The most damaging activation stage varies by detector component and isotopic half-life. For ^{54}Mn ($t_{1/2} = 312$ days) in the steel, the simulation prediction estimated 31% of activation from the historical exposure (with data indications this is an overestimate), 20% from the time at the South Pole, and 37% from the combined exposure during flight segments. For ^{125}I ($t_{1/2} = 59$ days) in the crystal, the simulation prediction estimated 38% of activation from the time at the South Pole and 47% from the combined exposure during flight segments. For ^{113}Sn ($t_{1/2} = 115$ days) in the crystal, the component with the largest contribution seen in DM-Ice17 data at low energy, the simulation prediction estimated 33% of activation from the time at the South Pole and 50% from the combined exposure during flight segments (see Fig. 8.19). All above estimates are for Det-1 activation, with Det-2 receiving 33% less South Pole exposure time.

There is a natural synergy between the calibration and characterization of the detector and the cosmogenics analyses of DM-Ice17. After appropriate correction for time-varying calibration, the residual spectra used in the cosmogenic analysis provide simpler spectral features over an approximately flat background. This is in contrast to the standard characterization based on stable intrinsic radioisotopes which must makes assumptions of the underlying complex background shape in fitting the intrinsic spectral features. The cosmogenics analysis can also inform the detector background model by providing insight into broken decay chains and an independent measurement (in addition to SNOLAB radioassays) of the decaying background levels. In turn, a more precisely calibrated and stable spectrum will reduce systematic uncertainty in identification and verification of cosmogenic isotopes.

Overall, this analysis demonstrates a very strong match of the cosmogenic production rates to those measured by ANAIS or calculated based on *ab-initio* methods. The DM-Ice17 analysis was able to achieve

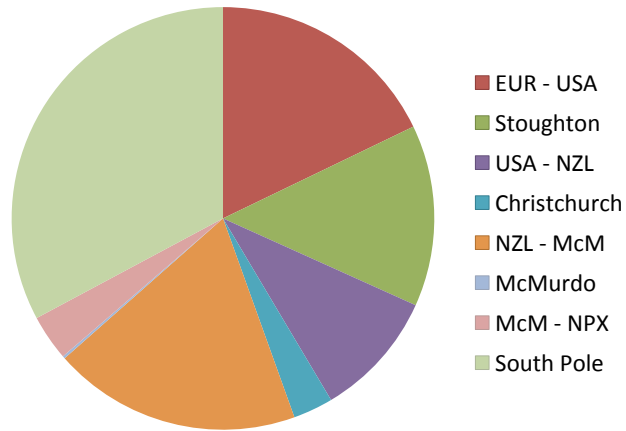


Figure 8.19: Contributions to the total cosmogenic rate of ^{113}Sn ($t_{1/2} = 115.09$ days) by exposure stage for Det-1 crystal. The single most damaging stage is the time spent at the South Pole prior to deployment, accounting for 33% of the total rate. The most damaging combined contribution is from the four flight segments, accounting for 50% of the total rate

this agreement despite background levels up to an order of magnitude higher than those in ANAIS. Adding to the previous work, this analysis has identified an additional cosmogenic isotope, ^{113}Sn , with low-energy spectral features (3 keV Auger electron or X-ray deexcitation) and long half-life ($t_{1/2} = 115$ days) with potentially significant impact on data in the region of interest for future dark matter searches.

Chapter 9

Future DM-Ice Experimental Stages

With DM-Ice17 having demonstrated the feasibility of deploying and operating low-background NaI(Tl) crystals deep in the South Pole, the potential of next generation deployments has been investigated. A proposed full-scale concept, DM-Ice250, has the potential to fully investigate the DAMA-reported dark matter modulation signal. Applying the lessons from DM-Ice17, we assess the background levels achievable in DM-Ice250, the cosmogenic activation contributions to the background, and mitigation strategies. The ongoing research and development (R&D) work being performed by the DM-Ice collaboration is discussed within the context of achieving the DM-Ice250 design goals.

9.1 DM-Ice250

9.1.1 Experimental Concept

The DM-Ice250 experiment is designed with the requirement of having the sensitivity to unambiguously test the DAMA signal. The design goal is to achieve a background level at or surpassing that of the DAMA/LIBRA apparatus. Sensitivity studies have shown that high-significance tests can still be performed within two years at a higher background (see Fig. 9.1).

For the null-hypothesis scenario (see Fig. 9.1a), the DAMA quenching factors ($q_{Na} = 0.3$ and $q_I = 0.09$) were assumed to compare results accurately. The sensitivity for low-mass WIMPs (< 15 GeV) is dominated by signal from recoils on sodium while the sensitivity for all higher-mass WIMPs is dominated by signal from recoils on iodine; lower-mass WIMPs have more efficient energy transfer to the lighter sodium nucleus while higher-mass WIMPs scatter preferentially on iodine due to the A^2 cross section enhancement. For low-mass WIMPs, the sensitivity is strongly dependent on the energy threshold of the experiment; a 1 keV analysis threshold extends the iodine-recoil dominated region to below the low-mass DAMA preferred region and delays the sharp upturn in the sodium-recoil exclusion to below 5 GeV. For high-mass WIMPs, the sensitivity is driven by the dark matter abundance; for a fixed dark matter density, higher-mass dark matter particles will have a smaller number density and thus decrease the signal rate. The loss of sensitivity above 100 GeV is an artifact of the energy binning which is sensitive to the location of the zero-crossing of the

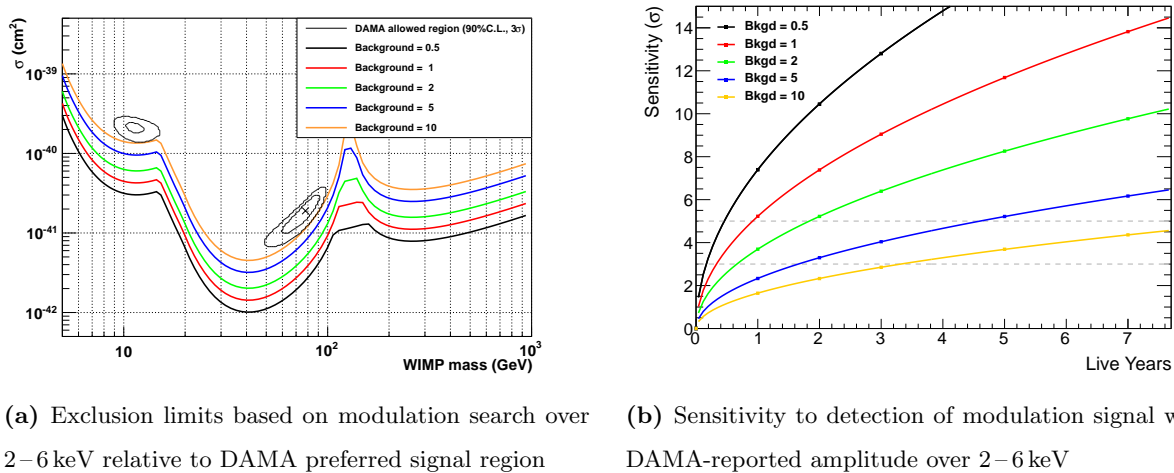


Figure 9.1: Potential of full-scale DM-Ice250 experiment to either exclude the DAMA preferred signal region (left) or detect DAMA modulation (right) based on Monte Carlo simulation. The exclusion limits plot in WIMP dark matter parameter space (cross section vs. mass) the 90% confidence level exclusions for a 500 kg·yr DM-Ice exposure. The sensitivity curve demonstrates the ability of a 250 kg DM-Ice detector to unambiguously measure a dark matter modulation with the amplitude reported by DAMA; the 3- σ (“evidence”) and 5- σ (“discovery”) targets are drawn as shaded lines. As expected, the sensitivity scales as the square root of exposure divided by background. For both simulations, various background scenarios were considered to investigate their impact on DM-Ice sensitivity; for backgrounds of up to 2 counts/day/keV/kg an unambiguous test of DAMA is expected within two years of running.

modulation amplitude. With sufficient statistics and the independent modulation analysis of narrower energy bins this feature is smoothed.

The signal-hypothesis scenario (see Fig. 9.1b) is a simpler Monte Carlo projecting the sensitivity to measuring a modulating signal with the DAMA-reported amplitude; in this way it is a completely dark matter model-independent Monte Carlo simulation. For a 5- σ result within two years, background levels of 2 counts/day/keV/kg or better are required; for a 3- σ result within two years, background levels as high as 5 counts/day/keV/kg are allowable. As expected, the sensitivity for both scenarios scales as $\sqrt{S/B}$.

9.1.2 Geometry

The geometry proposed for the DM-Ice250 detectors is modular, allowing for phased deployment and variable configurations. The detector configuration utilizes a close-packed array of crystals to take advantage of anti-coincidence cuts to characterize and eliminate background. The entire array must be capable of enclosure in pressure vessel(s) (see Fig. 9.2) for deployment at the South Pole, but allowance has also been made for a preceding Northern Hemisphere run.

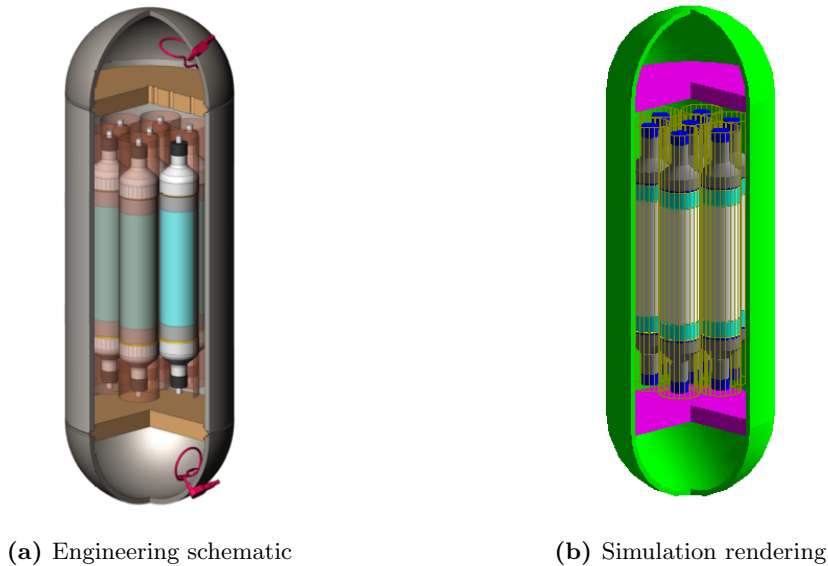


Figure 9.2: Proposed full-scale DM-Ice geometry as engineering schematic (left) and as rendered in Geant4 simulation (right). Seven cylindrical NaI(Tl) crystals in a close-packed array provides 125 kg of target mass and opportunities for coincidence studies between crystals. Electronics for digitization and PMT power supplies can be housed in the isolated hemispherical volumes at either end.

The crystals are 5 inch diameter and 15.5 inch length, a length dimension limited to maintain uniform light collection at a 3:1 aspect ratio. This radius is also well-matched to 5 inch PMTs and allows reasonable photocathode coverage for 3 inch PMTs. An array of smaller 3 inch diameter crystals was also considered, but has been discarded because either the length would need to be significantly reduced or else the aspect ratio would be very elongated resulting in less uniform response along the z -axis.

These crystal dimensions remain operable within the pressure vessel requirements imposed by a South Pole deployment. The pressure vessel is designed with an outer diameter of 22 inch, the maximum tested in a hole drilled with the IceCube enhanced hot water drill, and a wall thickness of 0.875 inch, set by to achieve guaranteed resilience to a 10^4 psi freezing pressure. The interior diameter of 20.25 allows ample room for the crystals, encapsulation, and support structure with additional space allowing for low-background copper shielding to reduce background from the pressure vessel, as necessary.

Each pressure vessel can hold an array of seven crystals, allowing for a target mass of 130 kg. The pressure vessel length dimension is unconstrained to allow for lightguides (if included), PMTs, and vibration-isolating support structure. The hemispherical endcaps provide space for digitizing and control electronics to be deployed with the detectors *in situ*. Radiation shields of clean copper are incorporated in the design to isolate the electronics regions.

A preliminary run of DM-Ice250 at a Northern Hemisphere deep underground laboratory, termed DM-Ice250N (see Fig. 9.3a), will afford the opportunity to fully characterize the performance of the DM-Ice250 array. Having access to the array will allow regular calibration with radioactive sources and LEDs to characterize the PMT response, energy resolution, and energy calibration over time. Various underground laboratories meet the requirements for this deployment phase; these include deployment inside the recently-vacated XENON10 shield at LNGS, the same laboratory where DAMA operates.

If the DM-Ice250N experimental run sees a statistically significant modulation signal, either at the level of DAMA or below, a Southern Hemisphere follow-up run will be necessary to fully assess possible seasonal systematics. Although new deep underground laboratory spaces in the Southern Hemisphere have been proposed [205, 206], the South Pole remains the only existing deployment location with demonstrated viability for detector operation [24] (see Fig. 9.3b). The South Pole deployment would be targeted for the bottom-center of the IceCube array inside DeepCore, near the Det-1 detector of DM-Ice17. Possible deployment synergy exists with the PINGU experiment, pending aligned experimental timelines.

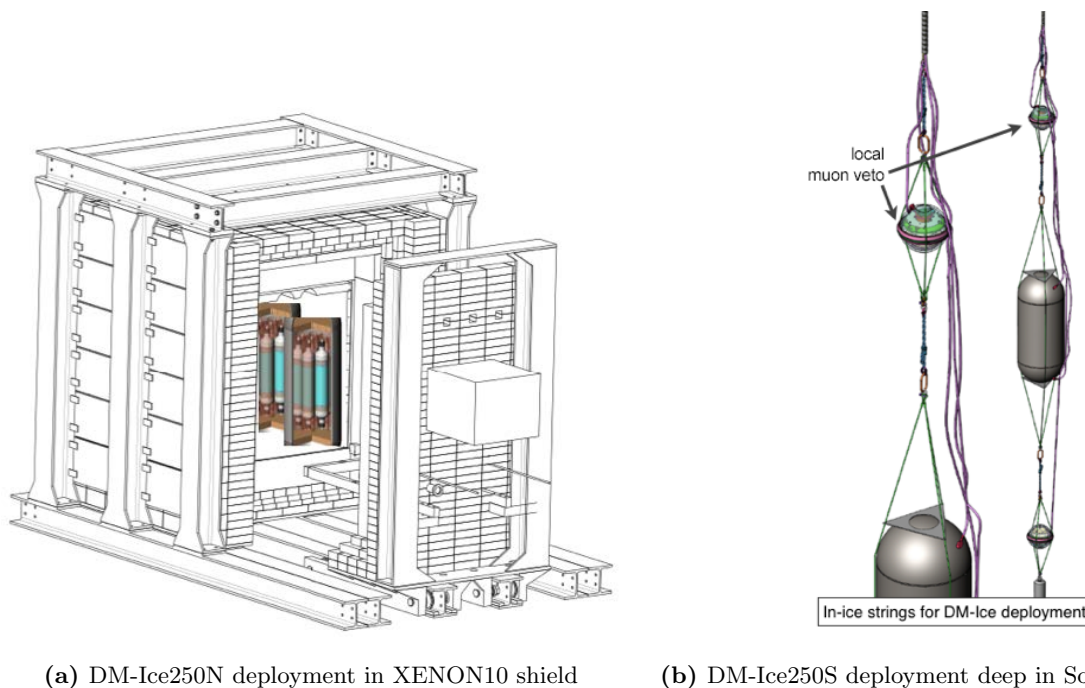


Figure 9.3: Deployment scenarios for DM-Ice250 detector modules. A Northern Hemisphere deployment could be conducted at various underground labs, with an allowable configuration inside the XENON10 shield at LNGS depicted (left). The Southern Hemisphere deployment is currently only feasible at the South Pole (right), but future laboratory spaces have been proposed. The same fully-characterized detector modules could be run in the South if the initial two year data run in the North saw a modulation signal.

The DM-Ice250N run affords the advantages taken for granted by most dark matter experiments – ability to service malfunctioning components, possibility of upgrades, and regular calibrations. It also lowers the cost of the two year science run and provides a less technically challenging deployment. If a Southern Hemisphere deployment is required, this experimental plan allows the same detectors to be relocated, only then incurring the additional deployment cost of drilling and operations at the South Pole after the hardware has been completely demonstrated. In this way, the phased approach of the DM-Ice experimental plan maintains the advantages of the Southern Hemisphere deployment of reduced systematics and stable environment, while coupling them to the advantages of accessibility afforded by a Northern Hemisphere deployment.

9.1.3 Intrinsic Background

A background model for the detector components has been constructed based on demonstrated contamination levels (see Tab. 9.1) and implementation of the DM-Ice250 geometry into DMIceSim (see Sect. 7.3.5). The contamination levels adopted are either values from DM-Ice17 or else a conservative estimate based on a compilation of measurements taken by other low-background experiments. The simulation demonstrates that the most important component for reducing the total experimental background is the NaI crystal (see Fig. 9.4).

The NaI crystal contamination follows the ^{129}I and broken chains of ^{232}Th and ^{238}U of DM-Ice17 but adopts the ^{40}K measurement from new crystals of ANAIS-25 [122]. ANAIS has reported an alpha rate attributed entirely to ^{210}Po (^{238}U -chain bottom) a factor of two larger than the DM-Ice17 ^{210}Po concentration,

Table 9.1: Contamination levels simulated for DM-Ice250 detector components in mBq/kg. Contamination levels adopted from DM-Ice17 background model are indicated by * with broken chains following the DM-Ice17 breakdown indicated by †. The remaining contamination levels match measurements made by other low-background experiments.

Material	Simulated Activity (mBq/kg)				
	^{40}K	^{232}Th	^{238}U	Other	Other
NaI(Tl) Crystal	1.25	0.16 ^{†*}	1.5 ^{†*}	1.25* (^{129}I)	
Quartz Lightguides	0.31	0.81	2.47		
R12669 PMT	540	100	430		
Steel Pressure Vessel	13.77*	6.49*	118.31 ^{†*}	7.19* (^{60}Co)	8.79* (^{235}U)
PTFE Reflector	0.34*	0.52*	0.5		
Copper Encapsulation	0.4	0.064	0.065		
Gel Optical Coupling	39.50*	0.12*	38.50*		
Copper Shield	5.13*	1.22*	0.67*		

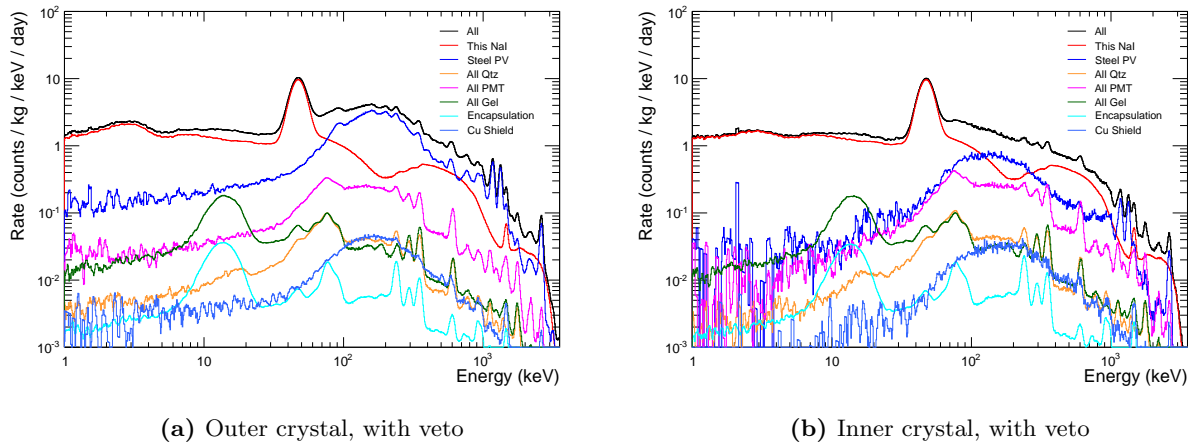


Figure 9.4: Background spectrum for both outer (left) and inner (right) crystals of DM-Ice250. Background model includes low-background 3 inch PMTs, demonstrated crystal contamination, and steel contaminant levels as in DM-Ice17. After application of an anti-coincidence veto (for $E > 2$ keV in any other crystal), a background level of 2 counts/day/keV/kg is achieved in the 2–6 keV region of interest for both crystals. The background contribution from ^{40}K and ^{210}Pb in the crystal dominate at low energies.

with no measurable alpha contribution from other parts of either the ^{232}Th - or ^{238}U -chain. The reduction of the ^{210}Po portion of the chain (which also includes ^{210}Pb is an active area of work by the crystal vendors, and so the contaminant levels for the broken chains is expected to be conservative.

The quartz lightguide contamination levels are adopted from the upper limited of the supplier-quoted range for Heraeus ‘Suprasil B.’ The PMT contamination levels are matched to the average measured value by DAMA of their R6233MOD 3” PMTs [207]; this model is the basis for the 3 inch Hamamatsu R12669 being investigated. The steel pressure vessel, OFHC copper shield, and gel optical coupling contamination levels were all taken from SNOLAB counting results performed on DM-Ice17 components. The PTFE reflector followed the measurements performed by DM-Ice ^{40}K and ^{232}Th , but adopted the value from LUX for ^{238}U [202]. The copper encapsulation was taken as the higher-contamination level value in comparison of CUORE and EDELWEISS measurements [208].

Under these background model assumptions, the NaI contaminant backgrounds dominate the total spectrum, with the ^{210}Pb -chain portion dominating at most energies (see Fig. 9.5). At low-energy (< 10 keV), the ^{210}Pb decay generates a flat background of 1 counts/day/keV/kg for the assumed 1.5 mBq/kg contamination. Because the Q-value of this β -decay isotope is 63.5 keV, the veto removes almost none of the contribution. The ^{40}K contribution at low-energy is dominated by the 3 keV K-shell Auger deexcitation peak. The 3 keV deexcitation follows all electron capture decays (10.72% probability) but are mostly accompanied by a 1460 keV

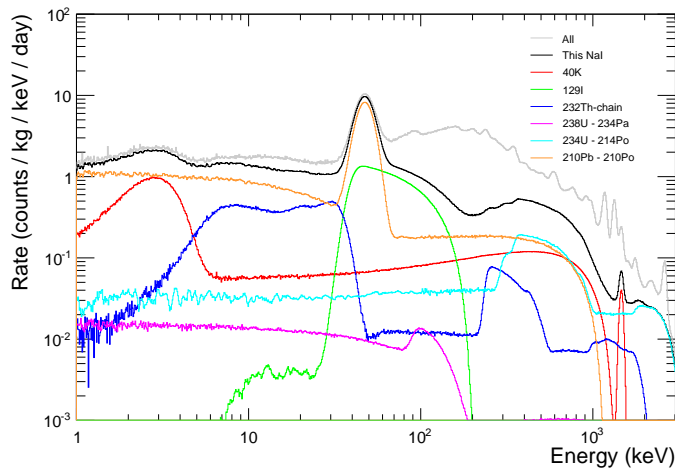


Figure 9.5: Background simulation for DM-Ice250 outer crystal after veto (black). The event rate below 10 keV is dominated by ^{210}Pb and ^{40}K decays. Whereas the ^{40}K 3 keV peak is reduced by 40% (outer crystal) or 70% (inner crystal with the multi-crystal veto, the flat background from ^{210}Pb is reduced by less than 10% leaving it the dominant background. This simulated background combines the ANAIS-25 ^{40}K level with the other DM-Ice17 contamination levels.

gamma; a rare (0.2% branching ratio) forbidden decay directly to the ground state, which has been postulated but never measured, is included in the simulation and allows the 3 keV deexcitation unaccompanied by the high-energy gamma [209].

9.2 DM-Ice250 Cosmogenic Discussion

The two deployment locations of DM-Ice250 present very different cosmogenic activation scenarios. As the concerns for a Northern Hemisphere deployment have been addressed separately [199], this analysis focuses only on DM-Ice250S. DM-Ice250S faces similar exposure challenges to DM-Ice17, but with the additional flexibility afforded by time and planning. The cosmogenic impact on the science potential of DM-Ice250S is first considered under the assumption of an identical exposure scenario to DM-Ice17, followed by a discussion of feasible modifications to reduce the background from activated isotopes.

9.2.1 Cosmogenic Impact

For cosmogenic production in DM-Ice250S, it is useful to consider the decay rates from deployment. In this way the minimum allowable time for the detectors to “cool” following their pre-deployment exposure can be investigated under various exposure scenarios. The commissioning period of DM-Ice17 lasted for six months following deployment, making the previous analysis blind to many short-lived cosmogenic isotopes.

This analysis uses revised production rate estimates based on the best available measurements or calculations where necessary; these are summarized in Tab. 9.2. The bulk of these production rates come from the ANAIS analysis [199], which are in good agreement with the DM-Ice17 analysis values (see Chap. 8) but with better controlled error due to the shorter cooling window and lower crystal background. The remaining production rates are ^{113}Sn from this DM-Ice17 analysis, as well as ^7Be and ^{109}Cd from ACTIVIA calculations.

The spectrum of these cosmogenic isotopes has been simulated at one month after deployment (see Fig. 9.6). This simulation presents an indication of the background spectrum after a much shorter commissioning period than used for DM-Ice17. At this time, the MB temperature measurements are within 2°C of their stable operating point and are still dominated by the fast exponential freezing time scale (see Fig. 6.13); as the detectors have not yet stabilized in temperature, this would be an early start to the physics run but a helpful point in characterizing the cosmogenic background. Since isotopes in the crystal dominate the total rate, only the NaI cosmogenic spectrum is shown.

The most significant difference seen in these cosmogenic spectra compared with those for DM-Ice17 is the presence of ^{126}I , whose 12.93 day half-life made it too short-lived to persist into the DM-Ice17 dataset.

Table 9.2: Production rates of cosmogenic isotopes in NaI assumed for DM-Ice250 simulation. Measured values with best error are adopted where available, with ^{113}Sn coming from DM-Ice17 analysis and others measured by ANAIS [199]; ^7Be and ^{109}Cd are based on ACTIVIA estimate in the absence of any measured value. All isotopes are previously discussed in Tab. 8.8 or Tab. 8.3.

Isotope	$t_{1/2}$ (days)	Production Rate (#/kg/day)
^7Be	53.22	2.4
^{22}Na	951	45.1
^{109}Cd	461.4	461.4
^{113}Sn	115.09	16
^{121}Te	19.17	9.9
^{121m}Te	164.2	23.5
^{123m}Te	119.2	31.6
^{125m}Te	57.40	28.2
^{127m}Te	106.1	10.2
^{125}I	59.400	220
^{126}I	12.93	283

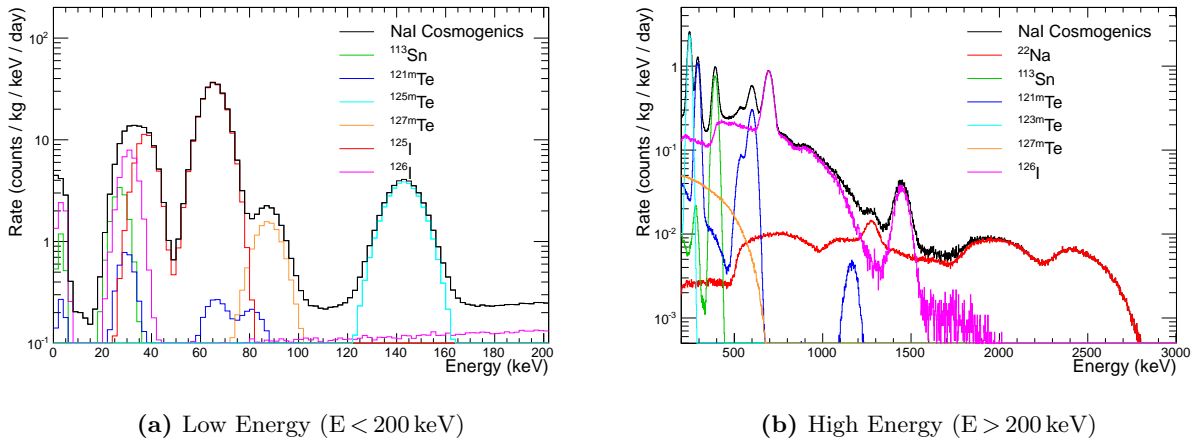


Figure 9.6: Simulated spectrum from activation in the NaI crystal (black) expected one month after deployment with breakdown by isotope (colors). Eight cosmogenic isotopes are expected to produce spectral lines with peak rates exceeding 0.5 counts/day/keV/kg providing additional calibration points out to 700 keV for the initial data. Below 10 keV the contributions from 3 keV deexcitations in ^{126}I ($t_{1/2} = 12.93$ days) and ^{113}Sn ($t_{1/2} = 115.09$ days) dominate, producing a cumulative average 3.1 counts/day/keV/kg in the 2–6 keV region.

The possible decay modes for ^{126}I are electron capture to ^{126}Te and β^- -decay to ^{126}Xe , both of which are stable. The two high-energy spectral lines arise from electron capture to the 666.3 keV and 1420.2 keV excited states, with observed energies higher from the addition of a K-shell deexcitation. At low-energy, the primary contributions of ^{126}I are from the electron capture decay directly to the ground state of ^{126}Te (19.5% probability); the only energy observed from these decays is from the K-shell (32 keV) or L-shell (3 keV) deexcitation. The decay of ^{126}I is expected to be the dominant contribution to the region of interest.

Over the first year of DM-Ice250S data, the cosmogenic features see significant decay (see Fig. 9.7). The main isotopes can be roughly classed into three categories – short-lived ^{126}I with half-life 12.93 days, medium-lived ^{125}I and ^{125m}Te with two month half-lives, and long-lived ^{113}Sn , ^{121m}Te , ^{123m}Te , and ^{127m}Te . The rapid decay of ^{126}I leads to an initial quick decrease in the rate at 3 keV (see Fig. 9.8) and 30 keV; allowing for a longer 3 month commissioning period will see this contribution mostly vanish. Medium-lived isotopes will see significant loss over the first six months of data, with the 145 keV ^{125m}Te peak falling into obscurity, but the ^{125}I will persist through the first year because of its initial intensity. After a year, the cosmogenic decay spectrum will have fallen entirely below 0.6 counts/day/keV/kg peak rate at all energies (highest at the ~ 30 keV deexcitation) and below 0.3 counts/day/keV/kg in the 2–6 keV region of interest.

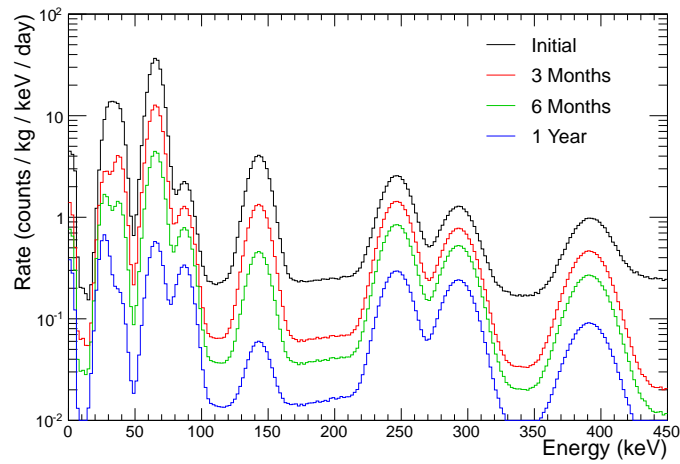


Figure 9.7: Evolution of background spectrum from cosmogenic isotopes below 450 keV over first year of DM-Ice250S under baseline exposure scenario and allowing one-month commissioning period. The initial rapid decrease in the 2–6 keV region of interest and at the broad 30 keV deexcitation peak are related to the decay of ^{126}I ($t_{1/2} = 12.93$ days). By one year into the proposed dataset, the largest spectral feature is 0.6 counts/day/keV/kg at the 30 keV deexcitation peak and the contribution to the region of interest is < 0.3 counts/day/keV/kg.

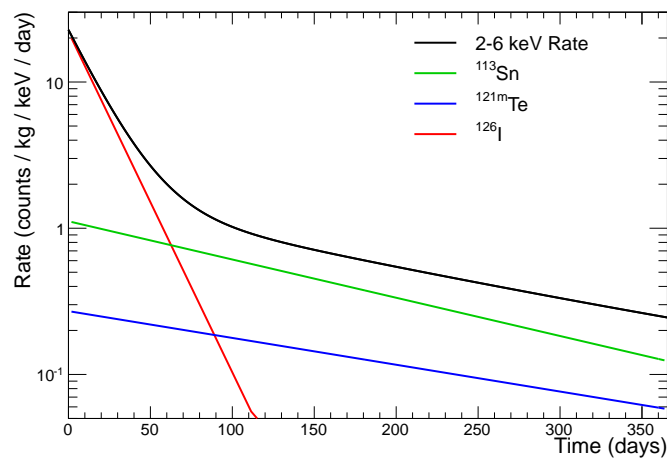


Figure 9.8: Decay of cosmogenic contribution in 2–6 keV region of interest. This initial exponential decay is dominated by ^{126}I ($t_{1/2} = 12.93$ day), with ^{113}Sn ($t_{1/2} = 115.09$ day) becoming the largest contribution after two months. The cosmogenic rate in the region of interest drops below 1 counts/day/keV/kg after 103 days and below 0.5 counts/day/keV/kg after 217 days.

9.2.2 Cosmogenic Exposure and Mitigation Strategies

The DM-Ice250S baseline activation scenario assumed exposure identical to Det-1 of DM-Ice17 involving four flight stages and surface exposure totaling 100 days prior to deployment. This cosmic ray exposure was influenced by the constraints of the South Pole deployment, but also by the rapid deployment timeline. While this scenario is reasonable for future deployments, a number of modifications are possible to reduce the total exposure.

The total exposure received during all the flight stages dominated the total activation for both crystals, with the high-altitude and latitude flights having the largest effect. For each of these flight segments alternative transport methods exists. The commercial flight segments can be completely circumvented by transporting only by boat and overland; this alteration may add several weeks of surface activation time but could be further mitigated by including additional shielding in the shipping containers. A boat transport option is also available from Christchurch, NZL to McMurdo Station, but an icebreaker only reaches McMurdo once and quite late during the season; this option is disfavored as it would require wintering the detectors on the surface at McMurdo for nine months. An overland traverse of detectors is possible between McMurdo and South Pole Stations; this option is also disfavored as the standard traverse lasts 6 weeks, which would result in a larger cumulative exposure (two days at the South Pole are more damaging than the flight, and significant time would be spent on the high Antarctic plateau during the traverse).

The exposure from time spent at the South Pole prior to deployment is the second largest contributor to the total exposure. As demonstrated by the Det-2 DM-Ice17 deployment, this can be reduced from 14 days to 9 days without any impact on the deployment logistics. The minimal exposure scenario is set by the amount of time necessary to characterize the detectors following transport; as a reasonable baseline we estimate 7 days – 5 days to calibrate and 2 days to drill the hole.

Based on these possible reductions, a new reduced exposure baseline scenario for DM-Ice250S can be established; this is summarized in Tab. 9.3. In order to maintain a conservative estimate of the total activation, the initial stages include transport from a European deep underground lab where DM-Ice250N was operating and a two month stop in Stoughton, WI, USA for detector servicing and modification for an in-ice deployment.

The individual contributions of each exposure stage have been assessed for ^{126}I and ^{113}Sn (see Fig. 9.9, the dominant contributors to the low-energy event rate in the 2–6 keV region of interest. The reduction in cosmogenic decay rate at deployment relative to the DM-Ice17 exposure scenario is 25.7% for ^{126}I and 38.8% for ^{113}Sn ; the reductions from the commercial flight stages are primarily experienced for the long-lived ^{113}Sn . For both isotopes, the time at the South Pole and the high-latitude, high-altitude flight (NZL – McM) remain dominant contributors to the total rate at deployment. The time at the South Pole is reduced a week from

Table 9.3: Baseline activation scenario for DM-Ice250S with reduced exposure. Reductions come primarily from replacing commercial flights with ocean shipment and reduced time at the South Pole.

Location	Duration (days)	\overline{F}_{tot}
EUR – USA	15	1
Stoughton, WI, USA	60	1.4
USA – NZL	30	1
Christchurch, NZL	15	1.1
NZL – McM	5/24	457
McMurdo Station	7	1.1
McM – NPX	3/24	140
South Pole Station	7	11

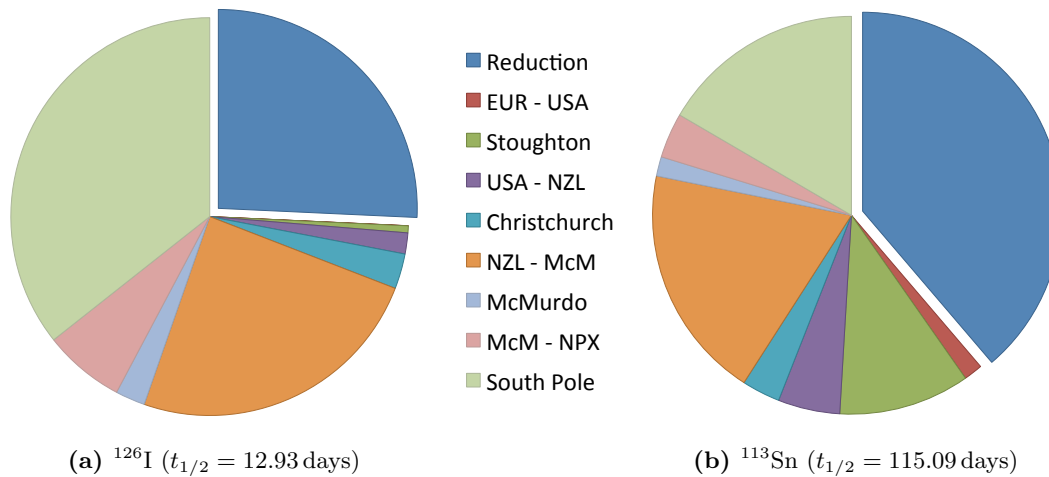


Figure 9.9: Contributions to the total cosmogenic rate at deployment of ^{126}I and ^{113}Sn by exposure stage; the reduction relative to the DM-Ice17 exposure model is broken off (blue). For both isotopes, the most damaging stages remain the time spent at the South Pole prior to deployment and the high-altitude, high-latitude flight (Christchurch, NZL to McMurdo Station). For short-lived ^{126}I the cosmogenic activation is concentrated in the later stages due to decay of earlier activation, while for longer-lived ^{113}Sn the activation is more evenly distributed.

the DM-Ice17 activation scenario, but the NZL – McM flight remains the same. With these modifications, the cosmogenic event rate in the region of interest will have fallen below 0.6 counts/day/keV/kg within 100 days of deployment.

Further reductions in the activation rate are still possible, but require more complicated deployment and shipping profiles. These reductions can be achieved by targeting the most significant stages - Stoughton (^{113}Sn only), NZL – McM flight, and South Pole.

The time at Stoughton is built in as a precaution for the possible DM-Ice250N deployment scenario where the NaI detectors are not operated in their pressure vessel modules. Under this scenario, the detectors will need to be packaged prior to shipment to the South Pole. If the modifications are performed at the DM-Ice250N underground location or the testing following work is moved to a nearby underground site, this 10% contribution can be mostly eliminated.

The NZL – McM flight assumes the cargo is taken on a C-17, the primary workhorse of the Polar programs cargo delivery, to Antarctica. An alternative delivery via one of the LC-130 aircraft is possible, but would require special processing of the cargo. The LC-130s operates at lower altitude than the C-17s, allowing for a reduction in the total exposure of 50%; the 70% reduction in the average activation factor ($\overline{F_{tot}}$) is partially offset by an increase in flying time from 5 to 8 hours due to the lower cruising speed of an LC-130.

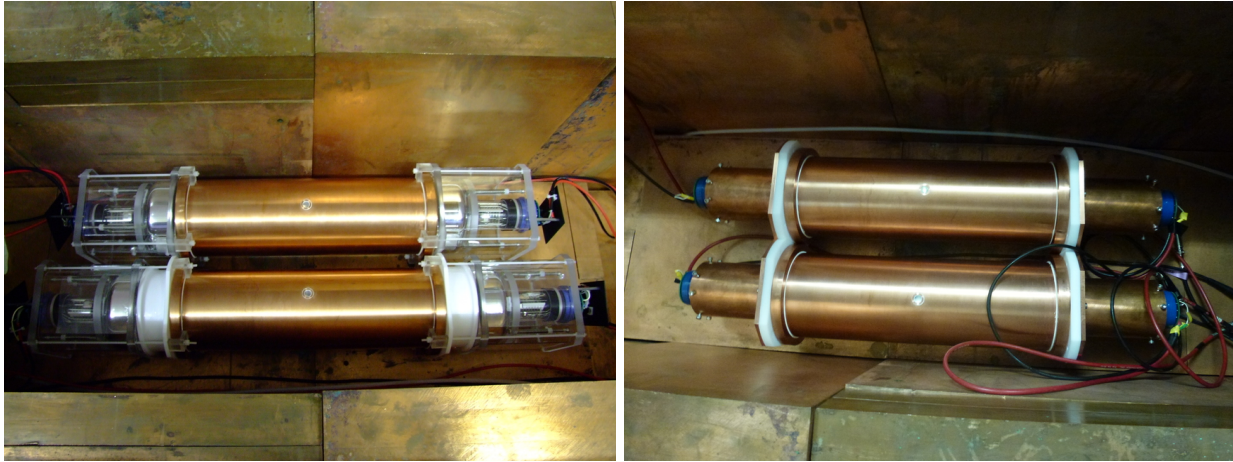
Reduction in the South Pole time is difficult, as the detectors must be on-site and fully tested before drilling commences. A reduction in the received exposure remains feasible by immediately storing and testing the detectors in a location of maximum storage. The most effective location identified is the tunnel system, which reaches depths of 50 ft under the firn and potentially a reduction in the neutron flux of over an order of magnitude (see App. A).

9.3 DM-Ice Research and Development

In order to demonstrate the current background level of achievable in DM-Ice250-like detectors, an active R&D campaign is underway. The first phase of this R&D involves running two new 18.28 kg NaI(Tl) crystals, causing the setup to be dubbed DM-Ice37 following its total target mass of 36.56 kg. These detectors have been running at the Boulby Underground Laboratory in the UK since December 2014.

These detectors have served as a testbed for PMT and lightguide configurations (see Fig. 9.10). The initial configuration operated with 5 inch Hamamatsu R877-100 (super-bialkali high-QE photocathode) PMTs, with one crystal having standard background PMTs coupled through 2 inch lightguides of Heraeus Suprasil quartz and the other crystal having low-background glass PMTs coupled directly to the crystal with no lightguides. A second configuration is now operating with 3 inch Hamamatsu R12669SEL PMTs (high-QE, low background) coupled directly to the crystal; a PTFE baffle covers the crystal window around the PMT to provide diffusive reflection and improve light collection.

The crystals were grown at an elevation of 4,600 ft (1,400 m) in Grand Junction, CO, USA by Alpha Spectra. After receipt from the vendor, the crystals were rapidly moved to a shallow underground at Fermilab in April of 2014. They remained underground until November when they were readied for shipment



(a) First configuration, 5" PMTs

(b) Second configuration, 3" PMTs

Figure 9.10: DM-Ice37 has tested several configurations of PMTs and lightguides for background and light collection. The initial configuration (left) had high-QE 5 inch R877 PMTs, one set with low-background glass coupled directly to the crystal and the other with normal glass coupled through 2 inch quartz lightguides. The second configuration (right) had low-background high-QE 3 inch R12669 PMTs coupled directly to the crystals.

to England. In shipment, the crystals were intentionally given very different exposures, as one by shipped by air while the other was shipped by sea.

Preliminary analysis of the alpha backgrounds in the crystals confirm that the ^{210}Po rate is 33% higher than in DM-Ice17, which will translate into a > 1 counts/day/keV/kg flat background from ^{210}Pb in the crystal. Resolution of ^{210}Pb contamination in the NaI powder, probably arising from ^{222}Rn leak, is a topic being pursued with the vendor. Ongoing analysis is pursuing a complete background model of these detectors to particularly assess the ^{40}K contamination in the crystal and total background contribution from the R12669 PMTs. The light yield of this detector geometry is of particular interest, to see if it can match the 15 pe/keV measured in smaller crystals from the same vendor; if attained despite poorer photocathode coverage this would validate the use of fewer larger crystals. Performance of the PMTs is also being considered to optimize tradeoff between noise separation, gain, and non-linearity at high-energy.

A cosmogenics analysis following the methods in Chap. 8 of this thesis is intended once at least six months of data are accumulated. With the lower total background rate of DM-Ice37 relative to DM-Ice17, as well as the faster start of the dataset, an analysis of more cosmogenic peaks should be possible. Of particular interest to this analysis will be measuring the total ^{113}Sn level and extrapolating its reference production rate.

9.4 Summary

DM-Ice250 is a proposed experiment with the sensitivity required to unambiguously test the DAMA dark matter signal claim within two years of running. Its modular detector structure provides multi-crystal anticoincidence veto opportunity and affords the advantages of phased deployment of identical detectors. It is designed with the flexibility to operate the same detectors sequentially in the Northern and then Southern Hemispheres, allowing a full characterization of the detectors and reduction in systematic uncertainties.

Sensitivity studies demonstrate that the full science potential of DM-Ice250 can be achieved with a background rate of 2 counts/day/keV/kg in the 2–6 keV region of interest; this is a factor of two higher than the level reported for the DAMA/LIBRA detectors. Simulation of the proposed detector geometry indicates that a total average background rate of 2 counts/day/keV/kg is achievable in the region of interest after application of an anticoincidence veto between crystals. This simulation is based on measured and available intrinsic contamination levels for all detector components.

Additional background introduced by cosmogenic activation of medium half-life ($10 < t_{1/2} < 1000$ days) isotopes has the potential to directly impact the rate in the region of interest. With no mitigation strategies implemented, the initial rate is expected to be 20 counts/day/keV/kg in the region of interest (dominated by ^{126}I) falling to below 1 counts/day/keV/kg after 100 days of running (dominated by ^{113}Sn). Opportunities to reduce the total cosmic ray exposure have been investigated yielding estimated improvements of 50% or more in the region of interest cosmogenic event rate after 100 days.

To validate the DM-Ice250 design and background model, an active phased R&D campaign is currently underway. The present phase is DM-Ice37, currently operating at the Boulby lab. The two crystals and four PMTs of DM-Ice37 are the same models as proposed for DM-Ice250, allowing for verification of the simulated background model and demonstration of detector performance. The DM-Ice37 R&D apparatus is also well poised to validate the cosmogenic production rates projected to impact DM-Ice250.

Chapter 10

Conclusion

DM-Ice17 has successfully complete a three-and-a-half year physics data run in a stable run configuration. During this period it has demonstrated the feasibility of deploying a sensitive low background detector, the ability to remotely operate and calibrate such a detector, and the favorable conditions afforded by the South Pole ice environment. In this way it has completed or surpassed its design goals.

This analysis first established the extent and quality of the DM-Ice17 dataset. The detector uptime has been demonstrated to be $> 99\%$ during the physics data run, with over 50% of the cumulative downtime occurring in the first year. The environmental temperature has been stable to within 0.3°C over the dataset with daily fluctuations $< 0.025^\circ\text{C}$. The contribution of the surrounding ice to the detector background is subdominant by two orders of magnitude. Small decreases in the raw trigger and coincidence data rates are consistent with quieting of the PMTs and reduction of known backgrounds.

The extreme exposure history of the DM-Ice17 detectors during their shipment to and storage at the South Pole makes them an excellent study for cosmogenic activation. Analysis of the time-varying spectrum of DM-Ice17 has identified clear features of six cosmogenically-activated isotopes – ^{54}Mn from the pressure vessel and ^{113}Sn , ^{121m}Te , ^{123m}Te , ^{125m}Te , and ^{125}I from the crystal. The measured abundance of these isotopes in data validates the complex modeling performed of the exposure history, an extension beyond that attempted by other groups in the low background detector community. The ratios of cosmogenic isotope production measured are in good agreement with values obtained by calculation and measured by other groups.

One previously unmeasured cosmogenic product of NaI, ^{113}Sn , was identified in this analysis. This isotope is especially of concern for dark matter experiments as it contributes strongly to the rate at low energy with a 3 keV deexcitation peak. The measured contribution of this isotope is higher than predicted by *ab initio* cross section calculations, meriting further investigation.

This cosmogenics analysis has also provided valuable feedback to the low-level DM-Ice17 data analysis. By identifying unique decaying features of known energy, the absolute energy calibration scale has been validated. Additionally, the analysis of peak shapes in residual spectra provides a background-subtracted estimate of the

energy resolution; this data indicates that the energy resolution function adopted for simulation overestimates the typical peak width at a range of energies. This information is especially valuable for a remote experiment like DM-Ice17 which cannot be directly calibrated with radioactive sources.

The successful operation of DM-Ice17 has generated momentum towards a full-scale experiment, DM-Ice250. This next-generation experiment is designed to have the sensitivity to definitively evaluate the DAMA modulation signal within two years of running. Simulations performed as part of this analysis indicate that the background rate expected from intrinsic radioactive contaminants may be within a factor of two of those reported by DAMA, a level sufficient for the test. Backgrounds expected from cosmogenic activation of the detectors following a South Pole deployment can be mitigated so that they provide a negligible rate contribution in the 2–6 keV region of interest within four months of operation. This work has therefore helped set the stage for the next-generation DM-Ice250 experiment to deploy in both the Northern and Southern Hemispheres.

The operation of intermediate-stage R&D detectors at the Boulby lab is seeking to support the discussed DM-Ice250 studies by demonstrating the required detector performance, measuring more precisely the cosmogenic production rates, and validating the cosmogenic production scaling under high cosmic flux conditions. In this way, the DM-Ice experimental family is pushing towards resolving a decade-old controversy in the dark matter field and helping to illuminate the nature of dark matter.

LIST OF REFERENCES

- [1] Ade, P. *et al.* Planck 2013 results. XVI. Cosmological parameters. *Astron.Astrophys.* **571**, A16 (2014). 1303.5076.
- [2] Olive, K. *et al.* Review of Particle Physics. *Chin. Phys.* **C38**, 090001 (2014).
- [3] Zwicky, F. Die Rotverschiebung von extragalaktischen Nebeln. *Helv.Phys.Acta* **6**, 110–127 (1933).
- [4] Goodman, M. W. & Witten, E. Detectability of Certain Dark Matter Candidates. *Phys.Rev.* **D31**, 3059 (1985).
- [5] Ahlen, S. *et al.* Limits on Cold Dark Matter Candidates from an Ultralow Background Germanium Spectrometer. *Phys.Lett.* **B195**, 603–608 (1987).
- [6] Cushman, P. *et al.* Working Group Report: WIMP Dark Matter Direct Detection (2013). 1310.8327.
- [7] Bernabei, R. *et al.* Final model independent results of DAMA/LIBRA-phase1 and perspectives of phase2. *Phys.Part.Nucl.* **46**, 138–146 (2015).
- [8] Bernabei, R. Dark Matter Particles in the Galactic Halo 10–19 (2014). 1412.6524.
- [9] Akerib, D. *et al.* First results from the LUX dark matter experiment at the Sanford Underground Research Facility. *Phys.Rev.Lett.* **112**, 091303 (2014). 1310.8214.
- [10] Aprile, E. *et al.* Dark Matter Results from 225 Live Days of XENON100 Data. *Phys.Rev.Lett.* **109**, 181301 (2012). 1207.5988.
- [11] Xiao, X. *et al.* Low-mass dark matter search results from full exposure of PandaX-I experiment (2015). 1505.00771.
- [12] Agnese, R. *et al.* Search for Low-Mass Weakly Interacting Massive Particles with SuperCDMS. *Phys.Rev.Lett.* **112**, 241302 (2014). 1402.7137.
- [13] Angloher, G. *et al.* Results on low mass WIMPs using an upgraded CRESST-II detector. *Eur.Phys.J.* **C74**, 3184 (2014). 1407.3146.
- [14] Kim, S. *et al.* New Limits on Interactions between Weakly Interacting Massive Particles and Nucleons Obtained with CsI(Tl) Crystal Detectors. *Phys.Rev.Lett.* **108**, 181301 (2012). 1204.2646.
- [15] Behnke, E. *et al.* First Dark Matter Search Results from a 4-kg CF₃I Bubble Chamber Operated in a Deep Underground Site. *Phys.Rev.* **D86**, 052001 (2012). 1204.3094.

- [16] Aalseth, C. *et al.* CoGeNT: A Search for Low-Mass Dark Matter using p-type Point Contact Germanium Detectors. *Phys.Rev.* **D88**, 012002 (2013). 1208.5737.
- [17] Angloher, G. *et al.* Results from 730 kg days of the CRESST-II Dark Matter Search. *Eur.Phys.J.* **C72**, 1971 (2012). 1109.0702.
- [18] Agnese, R. *et al.* Silicon Detector Dark Matter Results from the Final Exposure of CDMS II. *Phys.Rev.Lett.* **111**, 251301 (2013). 1304.4279.
- [19] Bernabei, R. *et al.* Dark Matter investigation by DAMA at Gran Sasso. *Int.J.Mod.Phys.* **A28**, 1330022 (2013). 1306.1411.
- [20] Klinger, J. & Kudryavtsev, V. Muon-induced neutrons do not explain the DAMA data. *Phys.Rev.Lett.* **114**, 151301 (2015). 1503.07225.
- [21] Amar, J. *et al.* From ANAIS-25 towards ANAIS-250. *Phys.Procedia* **61**, 157–162 (2015). 1404.3564.
- [22] Cherwinka, J. *et al.* A Search for the Dark Matter Annual Modulation in South Pole Ice. *Astropart.Phys.* **35**, 749–754 (2012). 1106.1156.
- [23] Kim, K. *et al.* Tests on NaI(Tl) crystals for WIMP search at the Yangyang Underground Laboratory. *Astropart.Phys.* **62**, 249–257 (2014). 1407.1586.
- [24] Cherwinka, J. *et al.* First data from DM-Ice17. *Phys.Rev.* **D90**, 092005 (2014). 1401.4804.
- [25] Wigner, E. P. The unreasonable effectiveness of mathematics in the natural sciences. *Communications on Pure and Applied Mathematics* **13**, 1–14 (1960). URL <http://dx.doi.org/10.1002/cpa.3160130102>.
- [26] Bessel, F. W. On the variations of the proper motions of Procyon and Sirius. *Monthly Notices of the Royal Astronomical Society* **6**, 136–141 (1844).
- [27] Kapteyn, J. C. First Attempt at a Theory of the Arrangement and Motion of the Sidereal System. *Astrophysical Journal* **55**, 302 (1922).
- [28] Oort, J. H. The Force Exerted by the Stellar System in the Direction Perpendicular to the Galactic Plane and Some Related Problems. *Bulletin of the Astronomical Institutes of the Netherlands* **6**, 249 (1932).
- [29] Oort, J. H. Some Problems Concerning the Structure and Dynamics of the Galactic System and the Elliptical Nebulae NGC 3115 and 4494. *Astrophysical Journal* **91**, 273 (1940).
- [30] Volders, L. M. J. S. Neutral Hydrogen in M 33 and M 101. *Bulletin of the Astronomical Institutes of the Netherlands* **14**, 323 (1959).
- [31] Rubin, V. C. & Ford, J., W. Kent. Rotation of the Andromeda Nebula from a Spectroscopic Survey of Emission Regions. *Astrophys.J.* **159**, 379–403 (1970).
- [32] Corbelli, E. & Salucci, P. The Extended Rotation Curve and the Dark Matter Halo of M33. *Mon.Not.Roy.Astron.Soc.* **311**, 441–447 (2000). [astro-ph/9909252](https://arxiv.org/abs/astro-ph/9909252).
- [33] Kowalski, M. *et al.* Improved Cosmological Constraints from New, Old and Combined Supernova Datasets. *Astrophys.J.* **686**, 749–778 (2008). 0804.4142.

- [34] Penzias, A. A. & Wilson, R. W. A Measurement of Excess Antenna Temperature at 4080 Mc/s. *Astrophysical Journal* **142**, 419–421 (1965).
- [35] Ade, P. *et al.* Planck 2013 results. I. Overview of products and scientific results. *Astron.Astrophys.* **571**, A1 (2014). 1303.5062.
- [36] Bennett, C. *et al.* Nine-Year Wilkinson Microwave Anisotropy Probe (WMAP) Observations: Final Maps and Results. *Astrophys.J.Suppl.* **208**, 20 (2013). 1212.5225.
- [37] Das, S. *et al.* The Atacama Cosmology Telescope: temperature and gravitational lensing power spectrum measurements from three seasons of data. *JCAP* **1404**, 014 (2014). 1301.1037.
- [38] Reichardt, C. *et al.* A measurement of secondary cosmic microwave background anisotropies with two years of South Pole Telescope observations. *Astrophys.J.* **755**, 70 (2012). 1111.0932.
- [39] Naess, S. *et al.* The Atacama Cosmology Telescope: CMB Polarization at $200 < \ell < 9000$. *JCAP* **1410**, 007 (2014). 1405.5524.
- [40] Ade, P. *et al.* BICEP2 / Keck Array V: Measurements of B-mode Polarization at Degree Angular Scales and 150 GHz by the Keck Array (2015). 1502.00643.
- [41] Ade, P. *et al.* A Measurement of the Cosmic Microwave Background B-Mode Polarization Power Spectrum at Sub-Degree Scales with POLARBEAR. *Astrophys.J.* **794**, 171 (2014). 1403.2369.
- [42] Keisler, R. *et al.* Measurements of Sub-degree B-mode Polarization in the Cosmic Microwave Background from 100 Square Degrees of SPTpol Data (2015). 1503.02315.
- [43] Adam, R. *et al.* Planck Intermediate Results. XXX. The Angular Power Spectrum of Polarized Dust Emission at Intermediate and High Galactic Latitudes (2014). 1409.5738.
- [44] Ade, P. *et al.* Detection of B-Mode Polarization at Degree Angular Scales by BICEP2. *Phys.Rev.Lett.* **112**, 241101 (2014). 1403.3985.
- [45] Ade, P. *et al.* Joint Analysis of BICEP2/Keck Array and Planck Data. *Phys.Rev.Lett.* **114**, 101301 (2015). 1502.00612.
- [46] Eisenstein, D. J. *et al.* Detection of the baryon acoustic peak in the large-scale correlation function of SDSS luminous red galaxies. *Astrophys.J.* **633**, 560–574 (2005). astro-ph/0501171.
- [47] Percival, W. J. *et al.* Baryon Acoustic Oscillations in the Sloan Digital Sky Survey Data Release 7 Galaxy Sample. *Mon.Not.Roy.Astron.Soc.* **401**, 2148–2168 (2010). 0907.1660.
- [48] Beutler, F. *et al.* The 6dF Galaxy Survey: Baryon Acoustic Oscillations and the Local Hubble Constant. *Mon.Not.Roy.Astron.Soc.* **416**, 3017–3032 (2011). 1106.3366.
- [49] Blake, C. *et al.* The WiggleZ Dark Energy Survey: mapping the distance-redshift relation with baryon acoustic oscillations. *Mon.Not.Roy.Astron.Soc.* **418**, 1707–1724 (2011). 1108.2635.
- [50] Padmanabhan, N. *et al.* A 2 per cent distance to $z=0.35$ by reconstructing baryon acoustic oscillations - I. Methods and application to the Sloan Digital Sky Survey. *Mon.Not.Roy.Astron.Soc.* **427**, 2132–2145 (2012). 1202.0090.

- [51] Anderson, L. *et al.* The clustering of galaxies in the SDSS-III Baryon Oscillation Spectroscopic Survey: Baryon Acoustic Oscillations in the Data Release 9 Spectroscopic Galaxy Sample. *Mon.Not.Roy.Astron.Soc.* **427**, 3435–3467 (2013). 1203.6594.
- [52] Perlmutter, S. *et al.* Measurements of Omega and Lambda from 42 high redshift supernovae. *Astrophys.J.* **517**, 565–586 (1999). astro-ph/9812133.
- [53] Riess, A. G. *et al.* Observational evidence from supernovae for an accelerating universe and a cosmological constant. *Astron.J.* **116**, 1009–1038 (1998). astro-ph/9805201.
- [54] Humphreys, E., Reid, M. J., Moran, J. M., Greenhill, L. J. & Argon, A. L. Toward a New Geometric Distance to the Active Galaxy NGC 4258. III. Final Results and the Hubble Constant. *Astrophys.J.* **775**, 13 (2013). 1307.6031.
- [55] Clowe, D. *et al.* A direct empirical proof of the existence of dark matter. *Astrophys.J.* **648**, L109–L113 (2006). astro-ph/0608407.
- [56] Markevitch, M. *et al.* 1E 0657-56: NASA Finds Direct Proof of Dark Matter. url: <http://chandra.harvard.edu/photo/2006/1e0657/> (2006). URL <http://chandra.harvard.edu/photo/2006/1e0657/>. Accessed: 9 May 2012.
- [57] Babul, A. & Veillet, C. Dark Matter Core Defies Explanation. <http://www.cfht.hawaii.edu/en/news/DarkMatterCore/> (2012). URL <http://www.cfht.hawaii.edu/en/news/DarkMatterCore/>. Accessed: 9 May 2012.
- [58] Jee, M. *et al.* A Study of the Dark Core in A520 with Hubble Space Telescope: The Mystery Deepens. *Astrophys.J.* **747**, 96 (2012). 1202.6368.
- [59] Harvey, D., Massey, R., Kitching, T., Taylor, A. & Tittley, E. The non-gravitational interactions of dark matter in colliding galaxy clusters. *Science* **347**, 1462–1465 (2015). 1503.07675.
- [60] Thompson, R., Dav, R. & Nagamine, K. The rise and fall of a challenger: the Bullet Cluster in Λ Cold Dark Matter simulations (2014). 1410.7438.
- [61] Kraljic, D. & Sarkar, S. How rare is the Bullet Cluster (in a CDM universe)? *JCAP* **1504**, 050 (2015). 1412.7719.
- [62] Milgrom, M. A Modification of the Newtonian dynamics as a possible alternative to the hidden mass hypothesis. *Astrophys.J.* **270**, 365–370 (1983).
- [63] Bekenstein, J. D. Relativistic gravitation theory for the MOND paradigm. *Phys.Rev.* **D70**, 083509 (2004). astro-ph/0403694.
- [64] Freese, K., Fields, B. & Graff, D. Limits on stellar objects as the dark matter of our halo: nonbaryonic dark matter seems to be required. *Nucl.Phys.Proc.Suppl.* **80**, 0305 (2000). astro-ph/9904401.
- [65] Feng, J. L. Dark Matter Candidates from Particle Physics and Methods of Detection. *Ann.Rev.Astron.Astrophys.* **48**, 495–545 (2010). 1003.0904.
- [66] Roszkowski, L. Particle dark matter: A Theorist’s perspective. *Pramana* **62**, 389–401 (2004). hep-ph/0404052.
- [67] Peccei, R. & Quinn, H. R. CP Conservation in the Presence of Pseudoparticles. *Phys.Rev.Lett.* **38**, 1440–1443 (1977).

- [68] Weinberg, S. A New Light Boson? *Phys.Rev.Lett.* **40**, 223–226 (1978).
- [69] Wilczek, F. Problem of Strong p and t Invariance in the Presence of Instantons. *Phys.Rev.Lett.* **40**, 279–282 (1978).
- [70] Arik, M. *et al.* New solar axion search in CAST with ^4He filling (2015). 1503.00610.
- [71] Asztalos, S. *et al.* A SQUID-based microwave cavity search for dark-matter axions. *Phys.Rev.Lett.* **104**, 041301 (2010). 0910.5914.
- [72] Shokair, T. *et al.* Future Directions in the Microwave Cavity Search for Dark Matter Axions. *Int.J.Mod.Phys.* **A29**, 1443004 (2014). 1405.3685.
- [73] Irastorza, I. *et al.* Towards a new generation axion helioscope. *JCAP* **1106**, 013 (2011). 1103.5334.
- [74] Cahill-Rowley, M. *et al.* Complementarity of dark matter searches in the phenomenological MSSM. *Phys.Rev.* **D91**, 055011 (2015). 1405.6716.
- [75] Aad, G. *et al.* Search for dark matter in events with a hadronically decaying W or Z boson and missing transverse momentum in pp collisions at $\sqrt{s} = 8$ TeV with the ATLAS detector. *Phys.Rev.Lett.* **112**, 041802 (2014). 1309.4017.
- [76] Aad, G. *et al.* Search for dark matter in events with heavy quarks and missing transverse momentum in pp collisions with the ATLAS detector. *Eur.Phys.J.* **C75**, 92 (2015). 1410.4031.
- [77] Khachatryan, V. *et al.* Search for the production of dark matter in association with top-quark pairs in the single-lepton final state in proton-proton collisions at $\sqrt{s} = 8$ TeV (2015). 1504.03198.
- [78] Boyarsky, A., Ruchayskiy, O., Iakubovskiy, D. & Franse, J. Unidentified Line in X-Ray Spectra of the Andromeda Galaxy and Perseus Galaxy Cluster. *Phys.Rev.Lett.* **113**, 251301 (2014). 1402.4119.
- [79] Bulbul, E. *et al.* Detection of An Unidentified Emission Line in the Stacked X-ray spectrum of Galaxy Clusters. *Astrophys.J.* **789**, 13 (2014). 1402.2301.
- [80] Adriani, O. *et al.* An anomalous positron abundance in cosmic rays with energies 1.5-100GeV. *Nature* **458**, 607–609 (2009). 0810.4995.
- [81] Fermi-LAT Collaboration. Measurement of Separate Cosmic-Ray Electron and Positron Spectra with the Fermi Large Area Telescope. *Physical Review Letters* **108**, 011103 (2012). 1109.0521.
- [82] Accardo, L. *et al.* High Statistics Measurement of the Positron Fraction in Primary Cosmic Rays of 0.5500 GeV with the Alpha Magnetic Spectrometer on the International Space Station. *Phys.Rev.Lett.* **113**, 121101 (2014).
- [83] Bergstrom, L., Bringmann, T., Cholis, I., Hooper, D. & Weniger, C. New limits on dark matter annihilation from AMS cosmic ray positron data. *Phys.Rev.Lett.* **111**, 171101 (2013). 1306.3983.
- [84] Cholis, I. & Hooper, D. Dark Matter and Pulsar Origins of the Rising Cosmic Ray Positron Fraction in Light of New Data From AMS. *Phys.Rev.* **D88**, 023013 (2013). 1304.1840.
- [85] Vitale, V. & Morselli, A. Indirect Search for Dark Matter from the center of the Milky Way with the Fermi-Large Area Telescope (2009). 0912.3828.

- [86] Goodenough, L. & Hooper, D. Possible Evidence For Dark Matter Annihilation In The Inner Milky Way From The Fermi Gamma Ray Space Telescope (2009). 0910.2998.
- [87] Abazajian, K. N., Canac, N., Horiuchi, S. & Kaplinghat, M. Astrophysical and Dark Matter Interpretations of Extended Gamma-Ray Emission from the Galactic Center. *Phys.Rev.* **D90**, 023526 (2014). 1402.4090.
- [88] Daylan, T. *et al.* The Characterization of the Gamma-Ray Signal from the Central Milky Way: A Compelling Case for Annihilating Dark Matter (2014). 1402.6703.
- [89] Ackermann, M. *et al.* Search for gamma-ray spectral lines with the Fermi large area telescope and dark matter implications. *Phys.Rev.* **D88**, 082002 (2013). 1305.5597.
- [90] Albert, A. Indirect Searches for Dark Matter with the Fermi Large Area Telescope 1. *Phys.Procedia* **61**, 6–12 (2015).
- [91] Ackermann, M. *et al.* Searching for Dark Matter Annihilation from Milky Way Dwarf Spheroidal Galaxies with Six Years of Fermi-LAT Data (2015). 1503.02641.
- [92] Choi, K. *et al.* Search for neutrinos from annihilation of captured low-mass dark matter particles in the Sun by Super-Kamiokande. *Phys.Rev.Lett.* **114**, 141301 (2015). 1503.04858.
- [93] Bovy, J. & Tremaine, S. On the local dark matter density. *Astrophysical Journal* **756**, 89 (2012). 1205.4033.
- [94] Pato, M., Agertz, O., Bertone, G., Moore, B. & Teyssier, R. Systematic uncertainties in the determination of the local dark matter density. *Physical Review D* **D82**, 023531 (2010). 1006.1322.
- [95] Weber, M. & de Boer, W. Determination of the Local Dark Matter Density in our Galaxy. *Astron.Astrophys.* **509**, A25 (2010). 0910.4272.
- [96] Albert, A. *et al.* Search for 100 MeV to 10 GeV γ -ray lines in the Fermi-LAT data and implications for gravitino dark matter in $\mu\nu$ SSM. *JCAP* **1410**, 023 (2014). 1406.3430.
- [97] Kerr, F. J. & Lynden-Bell, D. Review of galactic constants. *Monthly Notices of the Royal Astronomical Society* **221**, 1023 (1986).
- [98] Reid, M. *et al.* Trigonometric Parallaxes of High Mass Star Forming Regions: the Structure and Kinematics of the Milky Way. *Astrophysical Journal* **783**, 130 (2014). 1401.5377.
- [99] Carlin, J. L. *et al.* Kinematics and Chemistry of Stars Along the Sagittarius Trailing Tidal Tail and Constraints on the Milky Way Mass Distribution. *Astrophysical Journal* **744**, 25 (2012). 1111.0014.
- [100] Smith, M. C. *et al.* The RAVE Survey: Constraining the Local Galactic Escape Speed. *Monthly Notices of the Royal Astronomical Society* **379**, 755–772 (2007). astro-ph/0611671.
- [101] Freese, K., Lisanti, M. & Savage, C. Annual Modulation of Dark Matter: A Review. *Rev.Mod.Phys.* **85**, 1561–1581 (2013). 1209.3339.
- [102] Baudis, L. Direct Detection of Cold Dark Matter. *ArXiv e-prints* (2007). 0711.3788.
- [103] Bertone, G., Hooper, D. & Silk, J. Particle dark matter: evidence, candidates and constraints. *Physics Reports* **405**, 279–390 (2004).

- [104] Smith, D. & Weiner, N. Inelastic dark matter. *Physical Review D* **64**, 043502 (2001). [hep-ph/0101138](#).
- [105] Ahmed, Z. *et al.* Results from a Low-Energy Analysis of the CDMS II Germanium Data. *Physical Review Letters* **106**, 131302 (2011). [1011.2482](#).
- [106] Spooner, N. Introduction to dark matter. <https://www.hep.shef.ac.uk/research/dm/intro.php> (2012). URL <https://www.hep.shef.ac.uk/research/dm/intro.php>. Accessed: 5 May 2012.
- [107] Amole, C. *et al.* Dark Matter Search Results from the PICO-2L C₃F₈ Bubble Chamber (2015). [1503.00008](#).
- [108] Agnese, R. *et al.* Search for Low-Mass Weakly Interacting Massive Particles Using Voltage-Assisted Calorimetric Ionization Detection in the SuperCDMS Experiment. *Phys.Rev.Lett.* **112**, 041302 (2014). [1309.3259](#).
- [109] de Boissire, T. Low mass WIMP search with EDELWEISS-III: First Results (2015). [1504.00820](#).
- [110] Bonicalzi, R. M. *et al.* The C-4 dark matter experiment. *Nuclear Instruments and Methods in Physics Research A* **712**, 27–33 (2013). [1210.6282](#).
- [111] Giovanetti, G. *et al.* A Dark Matter Search with MALBEK. *Phys.Procedia* **61**, 77–84 (2015). [1407.2238](#).
- [112] Zhao, W. *et al.* First results on low-mass WIMP from the CDEX-1 experiment at the China Jinping underground Laboratory. *ArXiv e-prints* (2013). [1306.4135](#).
- [113] Kang, K.-J. *et al.* Introduction to the CDEX experiment. *Front.Phys.China* **8**, 412–437 (2013). [1303.0601](#).
- [114] Chavarria, A. E. *et al.* DAMIC at SNOLAB. *Phys.Procedia* **61**, 21–33 (2015). [1407.0347](#).
- [115] Abe, K. *et al.* XMASS detector. *Nucl.Instrum.Meth.* **A716**, 78–85 (2013). [1301.2815](#).
- [116] Yoo, J. *et al.* Scalability, scintillation readout and charge drift in a kilogram scale solid xenon particle detector (2014). [1410.6496](#).
- [117] Calvo, J. *et al.* Status of ArDM-1t: First observations from operation with a full ton-scale liquid argon target (2015). [1505.02443](#).
- [118] Agnes, P. *et al.* First Results from the DarkSide-50 Dark Matter Experiment at Laboratori Nazionali del Gran Sasso. *Phys.Lett.* **B743**, 456–466 (2015). [1410.0653](#).
- [119] Amaudruz, P. A. *et al.* DEAP-3600 Dark Matter Search (2014). [1410.7673](#).
- [120] Rielage, K. *et al.* Update on the MiniCLEAN Dark Matter Experiment. *Phys.Procedia* **61**, 144–152 (2015). [1403.4842](#).
- [121] McKinsey, D. LightWIMP Detection with Liquid Helium. Light Dark Matter Workshop (2013). URL <http://www.umich.edu/~mctp/SciPrgPgs/events/2013/dm2013/>.
- [122] Amaré, J. *et al.* Preliminary results of ANAIS-25. *Nucl.Instrum.Meth.* **A742**, 187–190 (2014). [1308.3478](#).

- [123] Angloher, G. *et al.* Probing low WIMP masses with the next generation of CRESST detector. *ArXiv e-prints* (2015). 1503.08065.
- [124] Archambault, S. *et al.* Constraints on low-mass WIMP interactions on ^{19}F from PICASSO. *Physics Letters B* **711**, 153–161 (2012). 1202.1240.
- [125] Felizardo, M. *et al.* Final Analysis and Results of the Phase II SIMPLE Dark Matter Search. *Physical Review Letters* **108**, 201302 (2012). 1106.3014.
- [126] Battat, J. *et al.* First background-free limit from a directional dark matter experiment: results from a fully fiducialised DRIFT detector (2014). 1410.7821.
- [127] Renner, J. *et al.* Ionization and scintillation of nuclear recoils in gaseous xenon. *Nucl.Instrum.Meth.* **A793**, 62–74 (2015). 1409.2853.
- [128] Armengaud, E. *et al.* Search for low-mass WIMPs with EDELWEISS-II heat-and-ionization detectors. *Physical Review D* **86**, 051701 (2012). 1207.1815.
- [129] CDMS Collaboration *et al.* Search for annual modulation in low-energy CDMS-II data. *ArXiv e-prints* (2012). 1203.1309.
- [130] Collar, J. I. & Fields, N. E. A Maximum Likelihood Analysis of Low-Energy CDMS Data. *ArXiv e-prints* (2012). 1204.3559.
- [131] Agnese, R. *et al.* Maximum Likelihood Analysis of Low Energy CDMS II Germanium Data. *Phys.Rev.D* **D91**, 052021 (2015). 1410.1003.
- [132] Collar, J. Comments on "A Dark Matter Search with MALBEK" (2014). 1407.2581.
- [133] Aprile, E. *et al.* Limits on spin-dependent WIMP-nucleon cross sections from 225 live days of XENON100 data. *Phys.Rev.Lett.* **111**, 021301 (2013). 1301.6620.
- [134] Bellini, G. *et al.* Cosmic-muon flux and annual modulation in Borexino at 3800 m water-equivalent depth. *Journal of Cosmology and Astroparticle Physics* **5**, 15 (2012). 1202.6403.
- [135] Shields, E., Xu, J. & Calaprice, F. SABRE: A New NaI(Tl) Dark Matter Direct Detection Experiment. *Phys.Procedia* **61**, 169–178 (2015).
- [136] Lal, D. Cosmic ray labeling of erosion surfaces - In situ nuclide production rates and erosion models. *Earth and Planetary Science Letters* **104**, 424–439 (1991).
- [137] Beer, J., McCracken, K. & von Steiger, R. *Cosmogenic Radionuclides* (Springer-Verlag Berlin Heidelberg, 2012).
- [138] Ziegler, J. F. Terrestrial cosmic ray intensities. *IBM Journal of Research and Development* **42**, 117–139 (1998). URL http://ieeexplore.ieee.org/xpl/freeabs_all.jsp?arnumber=5389314.
- [139] Laubenstein, M. & Heusser, G. Cosmogenic radionuclides in metals as indicator for sea level exposure history. *Applied Radiation and Isotopes* **67**, 750 – 754 (2009). URL <http://www.sciencedirect.com/science/article/B6TJ0-4VFC7VW-6/2/752802f64c495dce10e074b898c5597b>. 5th International Conference on Radionuclide Metrology - Low-Level Radioactivity Measurement Techniques ICRM-LLRMT'08.

- [140] Shubin, Y. N., Lunev, V. P., Konobeyev, A. Y. & Kitjuk, A. I. Cross-section data library MENDL-2 to study activation as transmutation of materials irradiated by nucleons of intermediate energies. *International Atomic Energy Agency* (1995). URL <https://www-nds.iaea.org/publications/iaea-nds/iaea-nds-0136.htm>.
- [141] Shubin, Y. N., Lunev, V. P., Konobeyev, A. Y. & Kitjuk, A. I. MENDL-2P Proton reaction data library for nuclear activation (Medium Energy Nuclear Data Library). *International Atomic Energy Agency* (1998). URL <http://www.oecd-nea.org/tools/abstract/detail/iaea1376>.
- [142] Korovin, Y. A., Natalenko, A. A., Konobeyev, A. Y., Stankovskiy, A. Y. & Mashnik, S. G. High Energy Activation Data Library (HEAD-2009). *Nucl.Instrum.Meth.* **A624**, 20–26 (2010). 1003.2225.
- [143] Chadwick, M. B. *et al.* ENDF/B-VII.1 Nuclear Data for Science and Technology: Cross Sections, Covariances, Fission Product Yields and Decay Data. *Nuclear Data Sheets* **112**, 2887–2996 (2011).
- [144] Koning, A. J. & Rochman, D. Modern Nuclear Data Evaluation with the TALYS Code System. *Nuclear Data Sheets* **113**, 2841–2934 (2012).
- [145] Barashenkov, V., Konobeev, A., Korovin, Y. & Sosnin, V. Cascade/inpe code system. *Atomic Energy* **87**, 742–744 (1999). URL <http://dx.doi.org/10.1007/BF02673263>.
- [146] Silberberg, R. & Tsao, C. H. Partial Cross-Sections in High-Energy Nuclear Reactions, and Astrophysical Applications. I. Targets With $z \leq 28$. *Astrophys.J.Suppl.* **25**, 315–333 (1973).
Silberberg, R. & Tsao, C. H. Partial Cross-Sections in High-Energy Nuclear Reactions, and Astrophysical Applications. II. Targets Heavier than Nickel. *Astrophys.J.Suppl.* **25**, 335–367 (1973).
- [147] Silberberg, R., Tsao, C. & Barghouty, A. Updated Partial Cross Sections of ProtonNucleus Reactions. *Astrophys.J.* **501**, 911–919 (1998).
- [148] Martoff, C. & Lewin, P. COSMO - a program to estimate spallation radioactivity produced in a pure substance by exposure to cosmic radiation on the earth. *Comput.Phys.Commun.* **72**, 96–103 (1992).
- [149] Back, J. & Ramachers, Y. A. ACTIVIA: Calculation of Isotope Production Cross-sections and Yields. *Nucl.Instrum.Meth.* **A586**, 286–294 (2008). 0709.3472.
- [150] Liskien, H. (n, 3n) processes and the statistical theory. *Nuclear Physics A* **118**, 379 – 388 (1968).
- [151] Qaim, S. & Ejaz, M. Half-lives and activation cross-sections of some radio-isotopes of iodine, tellurium and antimony formed in the interactions of iodine with 14.7 MeV neutrons. *Journal of Inorganic and Nuclear Chemistry* **30**, 2577 – 2581 (1968).
- [152] Kuznetsova, M. Y., Mekhedov, V. N. & Khalkin, V. A. Investigations of (p,pxx) Reactions on Iodine. *Soviet Phys. JETP.* **7**, 759 (1958).
- [153] Ladenbauer, I.-M. & Winsberg, L. Interaction of high-energy protons and alpha particles with iodine-127. *Phys. Rev.* **119**, 1368–1375 (1960).
- [154] Hess, V. F. Über Beobachtungen der durchdringenden Strahlung bei sieben Freiballonfahrten. *Physik. Zeitschr.* **13**, 1084–1091 (1912).
- [155] Simpson, J. A., Fonger, W. & Treiman, S. B. Cosmic Radiation Intensity-Time Variations and Their Origin. I. Neutron Intensity Variation Method and Meteorological Factors. *Physical Review* **90**, 934–950 (1953).

- [156] Gordon, M. S. *et al.* Measurement of the Flux and Energy Spectrum of Cosmic-Ray Induced Neutrons on the Ground. *IEEE Transactions on Nuclear Science* **51**, 3427–3434 (2004).
Gordon, M. S. *et al.* Correction to “Measurement of the flux and energy spectrum of cosmic-ray induced neutrons on the ground”. *IEEE Transactions on Nuclear Science* **52**, 2703–2703 (2005).
- [157] Armstrong, T. W., Chandler, K. C. & Barish, J. Calculations of neutron flux spectra induced in the earth’s atmosphere by galactic cosmic rays. *Journal of Geophysical Research* **78**, 2715–2726 (1973). URL <http://dx.doi.org/10.1029/JA078i016p02715>.
- [158] Gehrels, N. Instrumental background in balloon-borne gamma-ray spectrometers and techniques for its reduction. *Nuclear Instruments and Methods in Physics Research Section A: Accelerators, Spectrometers, Detectors and Associated Equipment* **239**, 324 – 349 (1985). URL <http://www.sciencedirect.com/science/article/pii/0168900285907326>.
- [159] Sato, T., Yasuda, H., Niita, K., Endo, A. & Sihver, L. Development of parma: Phits-based analytical radiation model in the atmosphere. *Radiation Research* **170**, 244–259 (2008).
- [160] Stephens, S. A. An Examination of Zenith Angle Dependence of Spectrum at Sea-Level. *International Cosmic Ray Conference* **10**, 90 (1979).
- [161] Gaisser, T. K. *Cosmic Rays and Particle Physics* (Cambridge University Press, New York, 1990).
- [162] Cruz Moreno, J. & Sciutto, S. Characterization of the atmospheric depth profile using the ground-level temperature: The case of malarg ue, argentina. *The European Physical Journal Plus* **128** (2013). URL <http://dx.doi.org/10.1140/epjp/i2013-13104-3>.
- [163] Clem, J. M. & Dorman, L. I. Neutron Monitor Response Functions. *Space Science Reviews* **93**, 335–359 (2000).
- [164] Forbush, S. E. World-Wide Cosmic-Ray Variations, 1937-1952. *Journal of Geophysical Research* **59**, 525–542 (1954).
- [165] Ziegler, J. F. Terrestrial cosmic rays. *IBM Journal of Research and Development* **40**, 19 –39 (1996).
- [166] Mewaldt, R. A. *et al.* Record-setting Cosmic-ray Intensities in 2009 and 2010. *Astrophysical Journal Letters* **723**, L1–L6 (2010).
- [167] Stozhkov, Y. I. *et al.* Cosmic ray modulation in the current 24th solar cycle from the measurements in the atmosphere. *Journal of Physics Conference Series* **409**, 012195 (2013).
- [168] Oh, S. *et al.* Record neutron monitor counting rates from galactic cosmic rays. *Journal of Geophysical Research (Space Physics)* **118**, 5431–5436 (2013).
- [169] Compton, A. H. Variation of the cosmic rays with latitude. *Phys. Rev.* **41**, 111–113 (1932). URL <http://link.aps.org/doi/10.1103/PhysRev.41.111.2>.
- [170] Shea, M. A. & Smart, D. F. personal communication (2014).
- [171] Smart, D. F. & Shea, M. A. Fifty years of progress in geomagnetic cutoff rigidity determinations. *Advances in Space Research* **44**, 1107–1123 (2009).
- [172] Alner, G. *et al.* Limits on WIMP cross-sections from the NAIAD experiment at the Boulby Underground Laboratory. *Phys.Lett.B* **616**, 17–24 (2005). [hep-ex/0504031](http://arxiv.org/abs/hep-ex/0504031).

- [173] Abbasi, R. *et al.* The IceCube Data Acquisition System: Signal Capture, Digitization, and Timestamping. *Nucl.Instrum.Meth.* **A601**, 294–316 (2009). 0810.4930.
- [174] NSF. Amundsen-Scott Station. <http://www.southpole.aq/maps/station.html> (2012). URL <http://www.southpole.aq/maps/station.html>. Accessed: 1 March 2014.
- [175] Carlstrom, J. *et al.* The 10 Meter South Pole Telescope. *Publ.Astron.Soc.Pac.* **123**, 568–581 (2011). 0907.4445.
- [176] Staniszewski, Z. *et al.* The Keck Array: A Multi Camera CMB Polarimeter at the South Pole. *Journal of Low Temperature Physics* **167**, 827–833 (2012).
- [177] Besson, D., Kravchenko, I., Ramos, A. & Remmers, J. Radio Frequency Birefringence in South Polar Ice and Implications for Neutrino Reconstruction. *Astropart.Phys.* **34**, 755–768 (2011). 1005.4589.
- [178] Achterberg, A. *et al.* First Year Performance of The IceCube Neutrino Telescope. *Astropart.Phys.* **26**, 155–173 (2006). astro-ph/0604450.
- [179] Abbasi, R. *et al.* The Design and Performance of IceCube DeepCore. *Astropart.Phys.* **35**, 615–624 (2012). 1109.6096.
- [180] Abbasi, R. *et al.* IceTop: The surface component of IceCube. *Nucl.Instrum.Meth.* **A700**, 188–220 (2013). 1207.6326.
- [181] Benson, T. *et al.* Icecube enhanced hot water drill functional description. *Annals of Glaciology* **55**, 105–114 (2014-12-31T00:00:00). URL <http://www.ingentaconnect.com/content/igsoc/agl/2014/00000055/00000068/art00014>.
- [182] Halzen, F. & Klein, S. R. IceCube: An Instrument for Neutrino Astronomy. *Rev.Sci.Instrum.* **81**, 081101 (2010). 1007.1247.
- [183] Aartsen, M. G. *et al.* South Pole glacial climate reconstruction from multi-borehole laser particulate stratigraphy. *Journal of Glaciology* **59**, 1117–1128 (2013).
- [184] Petit, J. R. *et al.* Climate and atmospheric history of the past 420,000 years from the Vostok ice core, Antarctica. *Nature* **399**, 429–436 (1999).
- [185] Gabrielli, P. *et al.* Trace elements in Vostok Antarctic ice during the last four climatic cycles [rapid communication]. *Earth and Planetary Science Letters* **234**, 249–259 (2005).
- [186] Augustin, L. *et al.* Eight glacial cycles from an Antarctic ice core. *Nature* **429**, 623–628 (2004).
- [187] Marteel, A. *et al.* Climate-related variations in crustal trace elements in dome c (east antarctica) ice during the past 672kyr. *Climatic Change* **92**, 191–211 (2009). URL <http://dx.doi.org/10.1007/s10584-008-9456-3>.
- [188] Knoll, G. F. *Radiation Detection and Measurement* (Wiley, 2010), 4th edn.
- [189] Wendt, C. personal communication (2011).
- [190] Ahmed, B. *et al.* The NAIAD experiment for WIMP searches at Boulby mine and recent results. *Astropart. Phys.* **19**, 691–702 (2003). hep-ex/0301039.

- [191] Bernabei, R. *et al.* The DAMA/LIBRA apparatus. *Nucl. Instrum. Methods Phys. Res., Sect. A* **592**, 297–315 (2008). 0804.2738.
- [192] Lang, K. *et al.* Characterization of 1600 Hamamatsu 16-anode photomultipliers for the MINOS Far detector. *Nucl.Instrum.Meth.* **A545**, 852–871 (2005).
- [193] Bellamy, E. *et al.* Absolute calibration and monitoring of a spectrometric channel using a photomultiplier. *Nucl.Instrum.Meth.* **A339**, 468–476 (1994).
- [194] Agostinelli, S. *et al.* GEANT4: A Simulation toolkit. *Nucl.Instrum.Meth.* **A506**, 250–303 (2003).
- [195] Allison, J. *et al.* Geant4 developments and applications. *IEEE Trans.Nucl.Sci.* **53**, 270 (2006).
- [196] Guatelli, S., Mantero, A., Mascialino, B., Nieminen, P. & Pia, M. Geant4 atomic relaxation. *IEEE Trans. Nucl. Sci.* **54**, 585–593 (2007).
- [197] Kudryavtsev, V., Robinson, M. & Spooner, N. The expected background spectrum in NaI dark matter detectors and the DAMA result. *Astropart.Phys.* **33**, 91–96 (2010).
- [198] Cebrián, S. *et al.* Background model for a NaI (Tl) detector devoted to dark matter searches. *Astropart.Phys.* **37**, 60–69 (2012).
- [199] Amaré, J. *et al.* Cosmogenic radionuclide production in NaI(Tl) crystals. *JCAP* **1502**, 046 (2015). 1411.0106.
- [200] Mei, D.-M., Yin, Z.-B. & Elliott, S. Cosmogenic Production as a Background in Searching for Rare Physics Processes. *Astropart.Phys.* **31**, 417–420 (2009). 0903.2273.
- [201] Cebrián, S. *et al.* Cosmogenic activation in germanium and copper for rare event searches. *Astropart.Phys.* **33**, 316–329 (2010).
- [202] Akerib, D. *et al.* Radiogenic and Muon-Induced Backgrounds in the LUX Dark Matter Detector. *Astropart.Phys.* **62**, 33–46 (2015). 1403.1299.
- [203] Wang, B. S. *et al.* Cosmogenic-neutron activation of TeO₂ and implications for neutrinoless double-beta decay experiments (2015). 1503.02095.
- [204] Moran, J. E., Fehn, U. & Teng, R. T. Variations in ¹²⁹I/¹²⁷I ratios in recent marine sediments: evidence for a fossil organic component. *Chemical Geology* **152**, 193 – 203 (1998). URL <http://www.sciencedirect.com/science/article/pii/S0009254198001065>.
- [205] Bertou, X. The ANDES Deep Underground Laboratory. *ArXiv e-prints* (2013). 1308.0059.
- [206] Barberio, E. Search for Dark matter in the southern hemisphere. CPPM Seminar (2015). URL <https://indico.in2p3.fr/event/11261/>.
- [207] Bernabei, R. *et al.* Performances of the new high quantum efficiency PMTs in DAMA/LIBRA. *JINST* **7**, P03009 (2012).
- [208] Armengaud, E. *et al.* Background studies for the EDELWEISS dark matter experiment. *Astropart.Phys.* **47**, 1–9 (2013). 1305.3628.
- [209] Pradler, J., Singh, B. & Yavin, I. On an unverified nuclear decay and its role in the DAMA experiment. *Phys.Lett.* **B720**, 399–404 (2013). 1210.5501.

- [210] Cherwinka, J. personal communication (2011).
- [211] Severinghaus, J. P., Grachev, A. & Battle, M. Thermal fractionation of air in polar firn by seasonal temperature gradients. *Geochemistry, Geophysics, Geosystems* **2**, 1048 (2001). URL <http://dx.doi.org/10.1029/2000GC000146>.
- [212] Bai, X. *et al.* Muon flux at the geographical South Pole. *Astropart.Phys.* **25**, 361–367 (2006). [astro-ph/0602381](http://arxiv.org/abs/astro-ph/0602381).
- [213] Kuivinen, K. C., Koci, B. R., Holdsworth, G. W. & Gow, A. J. South Pole ice core drilling, 1981-1982. *Antarctic Journal of the U.S.* **17**, 89–91 (1982). URL <http://www.coldregions.org/ajus.htm>.
- [214] Broeke, M. v. d. Depth and density of the antarctic firn layer. *Arctic, Antarctic, and Alpine Research* **40**, pp. 432–438 (2008). URL <http://www.jstor.org/stable/20181806>.
- [215] Miyake, S. Empirical formula for range spectrum of cosmic ray μ mesons at sea level. *Journal of the Physical Society of Japan* **18**, 1093–1093 (1963). URL <http://dx.doi.org/10.1143/JPSJ.18.1093>.
- [216] Spindler, W. J. More about those ice tunnels... <http://www.southpolestation.com/trivia/00s/utilidor2.html> (2008). URL <http://www.southpolestation.com/trivia/00s/utilidor2.html>. Accessed: 7 May 2015.

GLOSSARY

ACTIVIA	software package for estimating the rate of cosmogenic activation for arbitrary target isotopes; first released in 2008
ADC	<i>Analog to Digital Converter</i>
ANAIS	<i>Annual modulation with NAI Scintillators</i> dark matter experimental program operating NaI detectors at Canfranc; experimental phases include ANAIS-0 and ANAIS-25
ATWD	<i>Analog Transient Waveform Digitizer</i> analog to digital converter chip used by DM-Ice17; the same chip records the signal at three different gain levels and these data are referred to as ATWD0, ATWD1, ATWD2
axion	dark matter candidate particle in mass range $1 \mu\text{eV} - 1 \text{eV}$
Boulby	<i>Boulby underground laboratory</i> deep underground science laboratory in England with 2850 m.w.e. overburden
Canfranc	<i>laboratorio subterráneo de Canfranc</i> deep underground science laboratory in Spain with 2450 m.w.e. overburden
CMB	<i>Cosmic Microwave Background</i> relic thermal radiation leftover from the Big Bang
COSMO	software package for estimating the rate of cosmogenic activation for arbitrary target isotopes; first released in 1992
DAC	<i>Digital to Analog Converter</i> arbitrary units used in setting run parameters requiring calibration and conversion into standard units

DAQ	<i>Data AcQuisition</i>
DAMA	<i>DARk MATter</i> dark matter experimental program operating NaI detectors at LNGS; experimental phases include DAMA/NaI and DAMA/LIBRA (<i>Large sodium Iodide Bulk for RAre processes</i>)
Det-1	detector of DM-Ice17 deployed at bottom center (string 79) of IceCube array
Det-2	detector of DM-Ice17 deployed at bottom edge (string 7) of IceCube array
DM-Ice	<i>Dark Matter in Ice</i> dark matter experimental program operating NaI detectors at the South Pole; experimental phases include DM-Ice17, DM-Ice37, and DM-Ice250
FADC	<i>Flash Analog to Digital Converter</i> analog to digital converter chip used by DM-Ice17
firn	layer of compacted and recrystallized snow near surface at the South Pole with density increasing with depth
FPGA	<i>Field Programmable Gate Array</i>
Geant4	<i>GEometry ANd Tracking</i> Monte Carlo simulation tool for used to estimate spectra of radioactive backgrounds
HEAD-2009	<i>High Energy Activation Data library</i> nuclear data library including calculated neutron and proton capture cross sections over 150–1000 MeV formed from the HEPAD-2008 (<i>High-Energy Proton Activation Data</i>) and IEAF-2009 (<i>Intermediate Energy Activation File</i>) libraries; released in 2009
HV	<i>High Voltage</i> adjustable setting of DM-Ice17 PMTs affecting detector gain
IceCube	<i>IceCube Neutrino Observatory</i> 1 km ³ neutrino detector at the South Pole
Jinping	<i>China Jinping underground laboratory</i> , also CJPL deep underground science laboratory in China with 6700 m.w.e. overburden

KIMS	<i>Korea Invisible Mass Search</i> dark matter experimental program operating CsI and NaI detectors at Yangyang
ΛCDM	<i>Lambda - Cold Dark Matter</i> concordance cosmological model including dark energy (Λ) and cold dark matter
LC	<i>Local Coincidence</i> requirement of coincidence hit between PMTs within a time window in recorded data
LNGS	<i>Laboratori Nazionali del Gran Sasso</i> deep underground science laboratory in Italy with 3400 m.w.e. overburden
MB	<i>MainBoard</i> digitization and control electronics for DM-Ice17
MCA	<i>MultiChannel Analyzer</i>
Modane	<i>laboratoire souterrain de Modane</i> deep underground science laboratory in France with 4800 m.w.e. overburden
m.w.e.	<i>meters water equivalent</i> measure of shielding from cosmic ray muons correcting for density of overburden material
NaI	<i>sodium iodide</i> (chemical abbreviation), also NaI(Tl) detector technology for dark matter searches utilizing thallium-doped sodium iodide scintillating crystals
NaIAD	<i>NaI Advanced Detector</i> dark matter experiment operating NaI detectors at Boulby from 2000–2003
PMT	<i>PhotoMultiplier Tube</i> light sensitive detector used by DM-Ice and many other dark matter experiments
R_c	geomagnetic rigidity cutoff
R&D	<i>Research and Development</i>
ROI	<i>Region Of Interest</i>
SNOLAB	<i>Sudbury Neutrino Observatory LABORatory</i>

deep underground science laboratory in Canada with 6010 m.w.e. overburden

SPE

Single PhotoElectron

minimum observable signal with PMT

TENDL

TALYS-based Evaluated Nuclear Data Library

nuclear data library including calculated neutron and proton capture cross sections up to 200 MeV with new release every year; most recent release is TENDL-2014

UPS

Uninterruptible Power Supply

UTC

Coordinated Universal Time

WIMP

Weakly Interacting Massive Particle

dark matter candidate particle in mass range 1 GeV – 1 TeV

Yangyang

Yangyang underground laboratory

deep underground science laboratory in Korea with 2000 m.w.e. overburden

YIELDX

software package for estimating the rate of cosmogenic activation for arbitrary target isotopes; first released in 1999

APPENDIX

Portable Muon Detector

The relative cosmic ray fluxes at various potential storage locations at the South Pole were measured using a portable muon detector. This detector was designed and constructed in Fall 2011 and then operated at the South Pole in January 2012. The design, construction, and operation of the detector are discussed in this appendix, along with the data analysis which supports the conclusions in Sect. 9.2.2.

A.1 Design Considerations

The muon detector was designed with the goal of measuring the muon spectrum and flux at any potential storage locations identified at the South Pole. The design constraints formulated to achieve all preconceived deployment requirements were:

- robust (survive shipment to Pole)
- insulated/heated (unaffected by -50°C under-ice temperature)
- autonomous (capable of running for hours untended)
- small (able to reach all deployment locations)
- lightweight (able to be moved around easily)

A.1.1 RodWell Deployment

The most challenging deployment that the detector was designed to make was for measurement inside a ‘Rodrigues well,’ or ‘RodWell.’ At the South Pole rodwells are commonly used to generate meltwater from the ice by continuously injecting heat into a recirculating water. The minimum start depth is ~ 45 m to fully bypass the porous firn region. Over the course of its lifetime, a rodwell gradually swells and deepens, reaching depths of 75 m or more (see Fig. A.1). The RodWells being considered were artifacts of the IceCube drilling campaign, with the largest two being those used in the last three drilling seasons – 2008/2009 or the shared RodWell for the 2009/2010 and 2010/2011 austral summers.

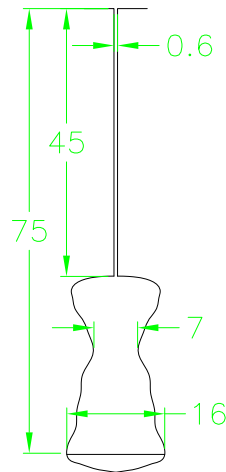


Figure A.1: Estimated profile of a SouthPole RodWell leftover from IceCube drilling (all dimensions quoted in meters) [210]. The RodWell begins 45 m below the ice surface to completely penetrate the porous firn ice layer. The cavern of the RodWell may be tens of meters high and wide. The narrow RodWell ‘neck’ constrains the maximum width of the muon detector package.

Deployment of the muon detector into a RodWell would require the detector be lowered down the ~ 2 ft diameter shaft, limiting the cross-sectional area of the detector. The deployment apparatus would require the ability to lower the muon detector to a depth of at least 75 m and either suspend the muon detector in place or else allow it to tip down and rest on the bottom. The ice temperature at these shallow depths, and thus the trapped air temperature, is -51°C [211], so the detector package requires the capability of handling a 70°C temperature swing between the RodWell and the $+20^{\circ}\text{C}$ station.

A.2 Detector Components

The detector was constrained from the outside in, with the case suffering the most stringent requirements. The sensitive components inside were then designed to fit the constraints of the case. The major design components are summarized in Tab. A.1.

The detector case selected was a ‘1740 Long Case’ from Pelican Products. This satisfied the requirement for both the robustness and size (diagonal of 21.33” for RodWell deployment). Additionally, the exterior design of the case included enough handles and securing points to secure a harness of webbing, allowing the entire detector package to be lowered into a RodWell.

The sensitive volume was constructed of EJ-200 plastic scintillator from Eljen Technology. This common scintillator exhibits fast pulse characteristics (0.9 ns rise time and 2.1 ns decay time) with good light output

Table A.1: Components of Cosmic Ray Detector

Component	Company	Product ID	Comment
Package	Pelican	1740	
Scintillator	Eljen	EJ-200	25 x 15 x 2.5 cm
PMT	ADIT	B51D01	2 in diameter
HV PMT base	Bridgeport Instruments	hvBase-P-B14D10	
DAQ	Bridgeport Instruments	qMorpho-2010	20 MHz, 10 bit ADC

(10 p.e./keV) peaked at 425 nm. Critically, the light output has been measured to exhibit no change over the range -60°C to $+20^{\circ}\text{C}$.

The light was detected by 2 inch B51D01 PMTs from ADIT. The PMTs have 25% photocathode quantum efficiency at 420 nm and a broad response well-matched to the scintillation spectrum of EJ-200. Their 10-dynode stages achieve typical gain of 10^6 gain at 1100 V operating voltage.

The PMT high voltage supply, voltage divider, and monitoring are integrated into a single unit, the hvBase-P-B14D10 from Bridgeport Instruments. This signal is read out by the qMorpho-2010 digitizer (20 MHz, 10-bit ADC), also from Bridgeport Instruments. The digitizer and PMT HV bases function together with the integrated DAQ and control software through an IgorPro C++-based GUI. The DAQ was run on a Lenovo Thinkpad laptop running Ubuntu Linux. The DAQ had flexibility to individually manage the four PMT channels, select data type (save waveforms or spectra), and set trigger masks for (anti-)coincidence settings.

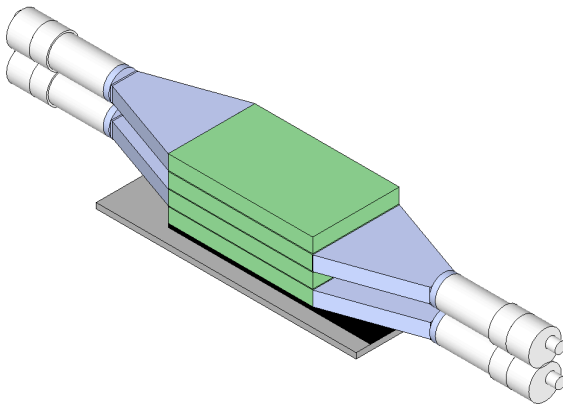
Power was provided to the qMorpho from a 3.7 V, 6.6 A·hr Li-ion battery, and the laptop battery was supplemented by an external battery pack. The detector could run for ~ 8 hrs in freezing conditions before the laptop battery died.

A.2.1 Scintillator Paddles

The dimensions of the scintillator paddles were constrained by the expected muon flux for the RodWell deployment. A measurement with $< 1\%$ statistical error was desired for a 1 hr run, requiring $> 10,000$ events even for the vertical detector configuration.

The muon flux at the South Pole has been measured to be 1.76×10^{-2} muons/sec/cm²/sr for vertical muons with $E_{\mu} > 246$ MeV [212]. This flux will be attenuated by the 53 m of firn (to the top of the RodWell opening), approximately a 30 m.w.e. overburden [213, 214] or 90% flux reduction [215]. A geometry of four stacked scintillator panels of dimensions 2.5 x 15 x 25 cm would give a coincidence rate of $\sim 50,000$ muons/hour.

Each scintillator panel was coupled to its 2" PMT by lightguides of one-inch cast acrylic. The two components of the lightguide were a trapezoidal piece to transport the light into the smaller PMT area, and a circular piece to provide better coupling to the PMT (see Fig. A.2).



(a) Detector design schematic



(b) Assembled detector

Figure A.2: Design and implementation of muon detector. The sensitive detector is comprised of four identical pieces of EJ-200 scintillator (green, left). Light is collected through acrylic lightguides (blue, left) and directed into 2" B51D01 PMTs (white, left). Each scintillator panel, lightguide, and PMT functions as an independent unit; the four units are vertically aligned and close packed to maximize probability of coincident muon trajectories. Rubber padding in between each unit serves to dampen mechanical shock.

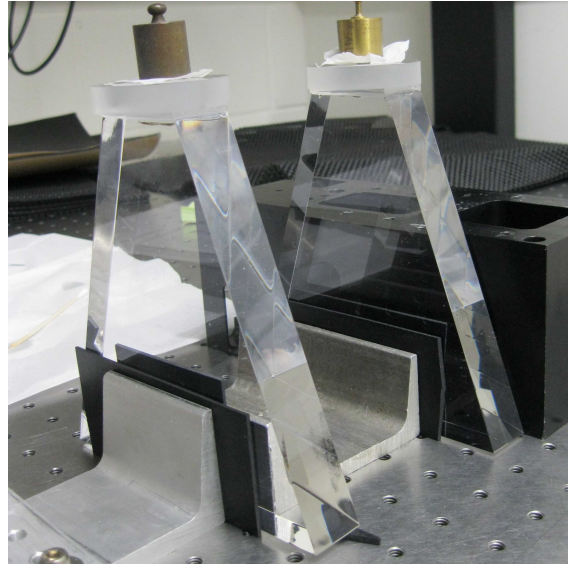
A.3 Detector Construction

To condition the optical surfaces, each scintillator and lightguide component was sanded down to 6000 grit with MicroMesh paper, and then polished with 1 and 0.3 micron aluminum oxide powder from Buehler. After polishing, the lightguide pieces were optically bonded together with EJ-500 optical cement. The scintillator panels were then coupled to the lightguide units with EJ-560 silicone gel. The optical cement produced an excellent interface, but the silicone gel was impossible to manipulate to similar effect; small irregularities in the surfaces and air bubbles led to visible imperfections in the optical coupling (see Fig. A.3). Later tests of optical coupling revealed that the performance of the silicone gel pads could be greatly improved with the addition of a thin layer of optical grease on either side.

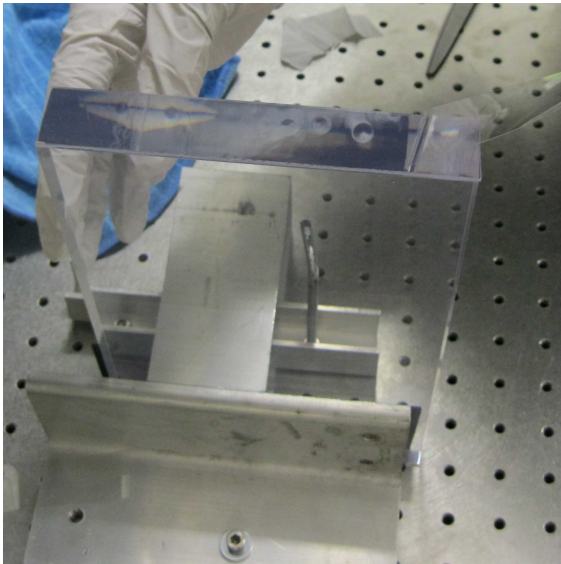
After optical coupling, the entire assembly was wrapped with reflective aluminum foil to increase light collection. The foil was then wrapped with multiple layers of black tape to ensure that scintillator assembly was completely lighttight and no cross-contamination of signal could occur between paddles. Additional tape was tensioned around the edges to provide compressive force on the lightguide-scintillator interface and



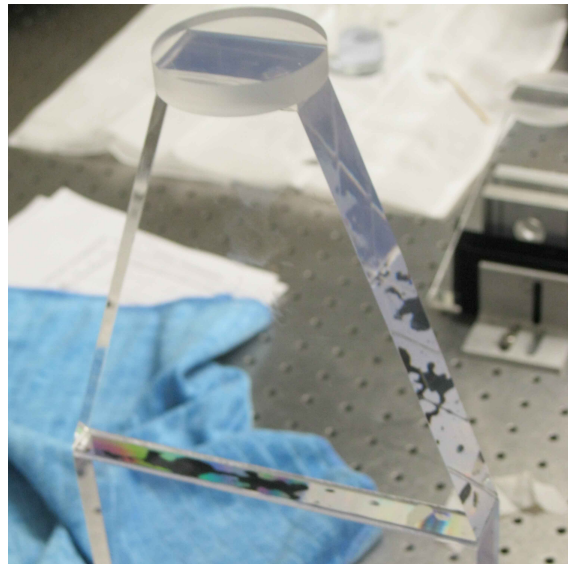
(a) Polished lightguides



(b) Optical cementing of lightguides with EJ-500



(c) Application of EJ-560 silicone gel to scintillator



(d) Optical interfaces in assembly

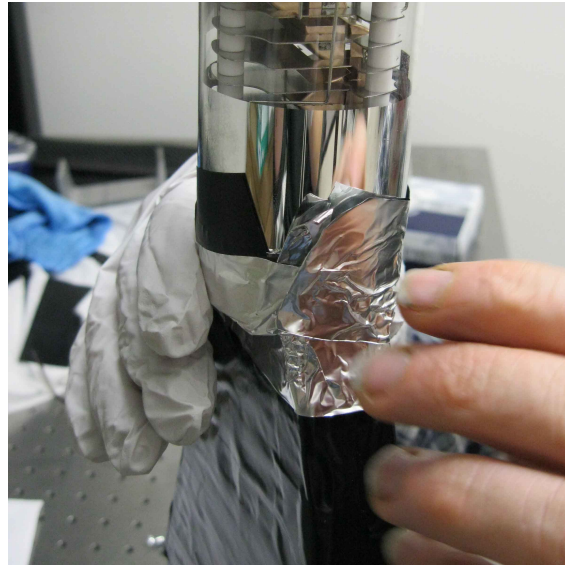
Figure A.3: Assembly of optical interfaces of one scintillator paddle. After polishing all machined optical surfaces the lightguide components were bonded together with EJ-500 optical cement. The scintillator paddles and PMTs (not shown) were optically coupled to the lightguides with EJ-560 silicone gel pads. The optical cement provided a flawless interface whereas the gel allowed small surface irregularities to diminish the coupling.

improve the coupling provided by the gel pad. After the lower section was secure, the PMT was coupled with an additional EJ-560 silicone pad. The PMT was then wrapped on in a similar manner with foil covering all

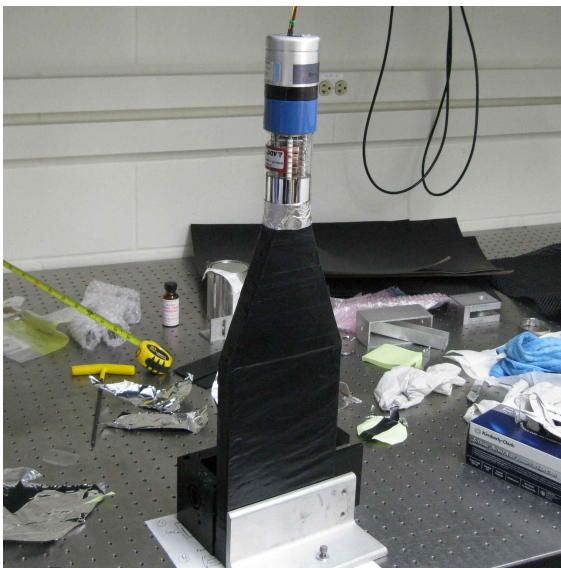
optical surfaces and then the entire assembly wrapped in black tape. Final compression tension was applied to the entire paddle assembly with additional loops of black tape (see Fig. A.4).



(a) After reflective wrap



(b) Adjusting PMT-lightguide interface



(c) After light-tight tape wrap



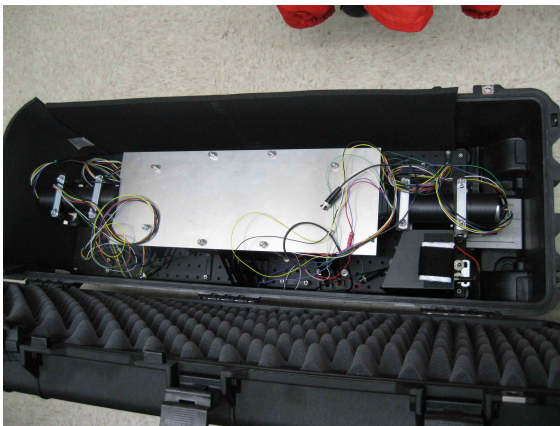
(d) Tensioning full single paddle assembly

Figure A.4: Completion of scintillator paddle assembly. The entire paddle is wrapped in reflective foil to increase light collection and then in black tape to optically isolate each paddle. After completing the optical seal, additional tape was tensioned around the assembly to provide compressive force on the gel optical interfaces.

Once all four panels were assembled following this procedure, they were combined into the final stacked configuration (see Fig. A.2). An aluminum optical breadboard provided the rigid base on which was placed an acrylic spacer to provide clearance between the first PMT and the breadboard. Each paddle was placed down in opposite direction to the previous paddle to provide clearance for the PMTs. Between each paddle was a rubber sheet, aluminum sheet, rubber sheet sandwich to provide friction, strain release, and stability for the assembly. Above the final paddle was a 1/8" aluminum plate which was secured to the breadboard with 1/4-20 threaded rods. All gaps were shimmed with rubber spacers or cardstock to lock all components into place and reduce stress during shipment. Vertical supports barred any lateral motion while the top plate barred vertical motion.

Once the qMorpho digitizer was also secured to the optical breadboard, the entire detector apparatus was moved assembled into the Pelican 1740 case (see Fig. A.5). Rubber feet on the breadboard in addition to the rubber and foam pads between the supports and optical components provided dampening of mechanical shock. All remaining space in the case was filled with insulating foam except for space for the DAQ laptop and battery packs.

For runs at the South Pole, the heat output of the laptop and digitizers did not offset the heat loss to the environment. To mitigate the cooling of the detector, additional warming was provided by chemical hand warmers during outdoor runs. The temperature was monitored throughout the detector using three temperature probes. After every data run all components not bolted down were designed to be removed -



(a) Completed detector in case



(b) Completed detector after packaging

Figure A.5: Completed muon detector in case. After all components were secured to the optical breadboard, the single unit was placed in the case (a) and all remaining room filled with insulation. The DAQ laptop and battery pack were stored at the top for ease of access.

the computer and temperature probes for data retrieval, battery packs for recharging, and all hand warmers were replaced.

A.4 Detector Operation

Detector construction was completed on 22 December 2011. Tests were run during construction to ensure that all PMTs were functioning properly, lighttight, and capable of recording high-amplitude pulses. Freezer tests of the three temperature probes validated the accuracy of their measurements between room temperature and their minimum temperature rating of -40°C .

The data presented in this analysis is all from the qMorpho's spectrum running mode and is referenced by channel according to the multichannel analyzer (MCA) number, MCA0 through MCA3. In this configuration, the qMorpho internally corrects for baseline effects and saves only the ADC value of the waveform's peak amplitude (10-bit precision) or 10 bin peak integral (11-bit precision). Only the spectrum is saved for each active channel and no coincidence pairing information is saved. The spectrum only contains data which did not saturate the 10-bit MCA and there is no 'overflow' spectrum bin or record catching events exceeding the 11-bit range. Analysis of the spectra and features present therein are included in Sect. A.5.

The qMorpho digitizer is also capable of recording waveform traces, but this mode could not be used to continually save all triggered waveforms. Because of this limitation, it was only used in commissioning runs to understand the features observed and optimize the run settings. The qMorpho waveforms are 1024 bins long at 20 MHz sampling frequency (50 ns/bin), of which 100 bins are pre-trigger samples.

The detector commissioning and establishment of the final run configuration was only completed after the detector reached the South Pole, so all comparison spectra are only available from later data collection periods. One detector channel, MCA0, failed during shipment to Christchurch, NZ from the South Pole and is therefore omitted from the analysis because it has no sea-level spectrum for comparison. Detector quality control runs performed at every extended stop of the detectors shipment have indicated no other deteriorations in performance.

A.4.1 Run Parameter Optimization

The commissioning period involved adjustments to the photomultiplier (PMT) high voltage (HV), amplifier transimpedance, trigger threshold, integration window, and coincidence settings. The modification of these settings were enacted to minimize digitizer saturation, maximize signal-to-noise separation, and reduce the total digitized noise. All settings were controlled through the qMorpho interface and required no hardware modifications.

The first parameter adjusted was the amplifier transimpedance, which could be set to one of five discrete values between $100\ \Omega$ and $10,100\ \Omega$. The primary effect of larger impedance settings was an increase in both

the baseline-corrected peak amplitude and the length of the decay tail of the waveform pulses (see Fig. A.6). A secondary effect was a positive shift in the baseline level; this was the result of an automatic shift by the DAQ, although there was no evidence seen in waveforms of undershoot that this would be necessary to correct against. The highest impedance setting ($10,100\ \Omega$) was selected for all further runs because the wider pulses produced larger integrals and gave better separation from any low-energy non-scintillation noise features.

The second parameter adjusted was the PMT HV, which was set individually for each channel. Three of the PMTs were well gainmatched and coarsely adjusted together, but MCA0 required an HV setting several hundred volts higher to achieve equivalent performance. Since pulses either with amplitudes exceeding the 10-bit digitizer range or integrals exceeding the 11-bit spectrum maximum were discarded, the selection criteria for coarse HV was to keep rates below 1 count/30 min in the 10 highest energy bins. After satisfying the more stringent integral limit, the MCA1 and MCA3 channels were found to be well gainmatched and the remaining two channels were adjusted to lower HV to complete the gainmatched set (see Fig. A.7). The resulting HV values used for the four channels were $\{1025, 800, 790, 800\}$. Since the final analysis method utilized a fitting routine instead of a raw sum, the HV limit could have been relaxed to operate the PMTs at higher gain to produce better separation of muon events.

The final parameter to be fine-tuned was the trigger threshold level, which was also set individually for each channel. The threshold could be established as an integer value of ADC units above the average baseline level. As expected, adjusting the trigger level primarily linearly increased the low-energy cutoff and

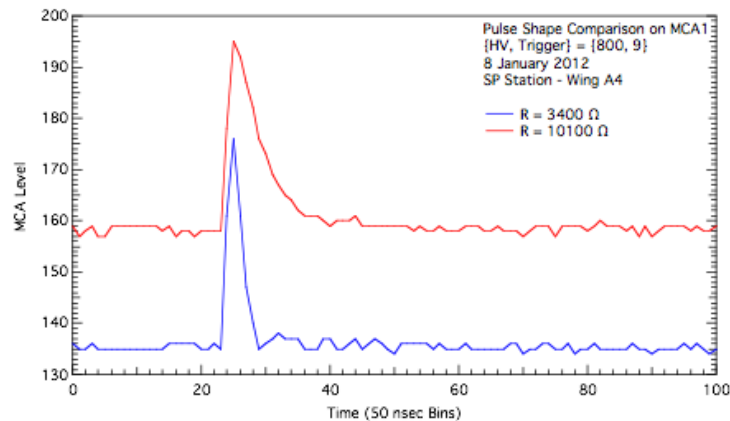


Figure A.6: Sample waveforms of similar peak amplitude recorded at two highest gain resistor settings. Higher transimpedance values result in wider pulses and larger pulse integrals for better noise separation. The vertical shift between the example pulses is a result of the MCA’s automatic baseline adjustment. The time axis has been rescaled to remove most of the 100 pre-pulse bins and truncate the 1024 bin waveform.

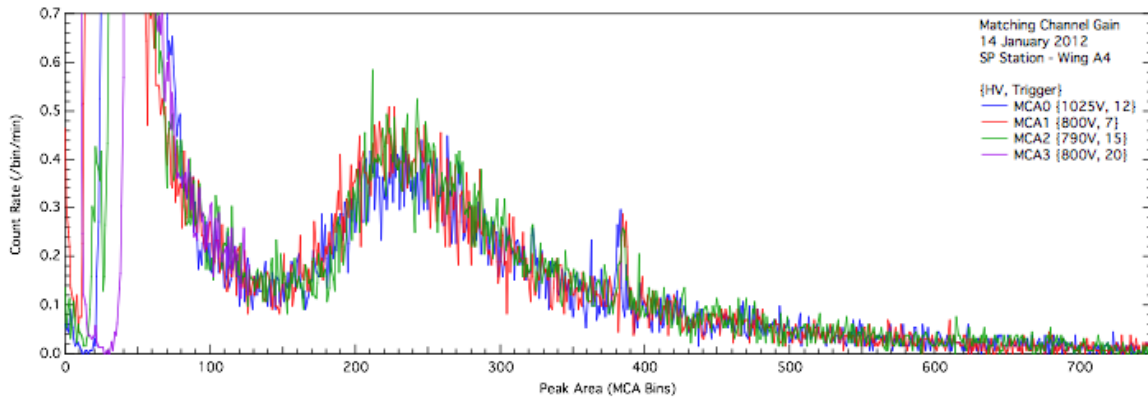


Figure A.7: Example spectrum from commissioning run from all four MCA inputs after PMT HV adjustments for gainmatch. The ‘hot channel’ near integral of 400 for all MCA channels persisted at different HV settings.

removed scintillation events below the region of interest (see Fig. A.8). The rejection power of the threshold for noise events varied on a run-to-run basis, resulting in a well-separated secondary population of events sometimes appearing near zero integral. The operating threshold selected allowed similar total event rates for all channels and minimal hit deadtime ($< 0.1\%$) while preserving enough of the exponential scintillation backgrounds to include in fits.

The coincidence window could be set as integer numbers of 50 ns clock period. No variation in the signal acceptance was senior values between 100 ns and arbitrarily long windows, so the final window choice was set to match the designer recommendation of 250 ns. For coincident runs, the background rates were suppressed and the trigger threshold could be significantly lowered without concern for increased deadtime.

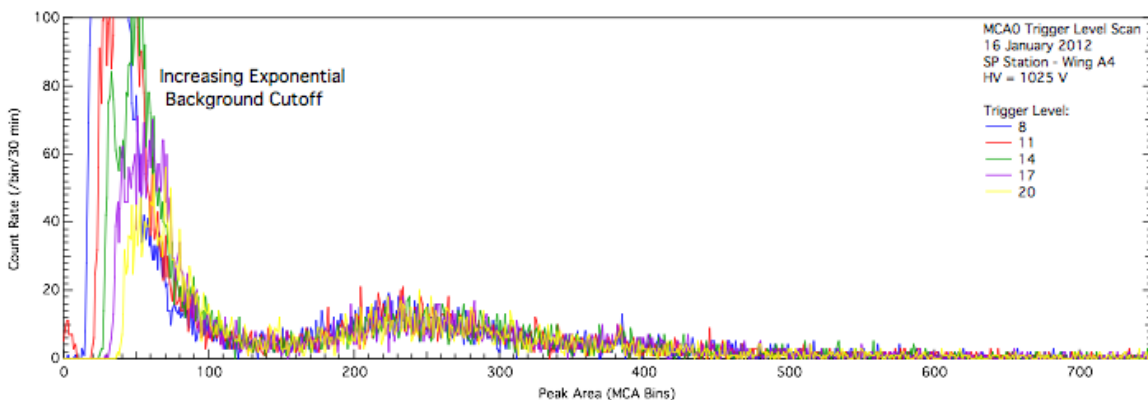


Figure A.8: Spectra illustrating effect of increasing trigger threshold for MCA0. The cutoff of the exponential scintillation background shifts with threshold (< 100), but muon events in the MIP peak (~ 250) is unaffected. Electronic noise (~ 0) is well-separated from signal even when it passes the threshold (*e.g.*, red).

The trigger mask can be customized to allow any combination of channel triggers. The 15 valid triggers (from four single-channel triggers up to one four-channel trigger) can be combined in any of 32,768 combinations to explicitly allow or disallow specific trigger configurations. Commissioning runs exploited this flexibility to investigate coincidence performance by collecting data in non-coincident (each channel self-triggers), coincident (only digitize signals from channels satisfying $N \geq 2$ coincidence), and anti-coincident (only digitize signals with no coincident pairing) settings. These runs revealed that the coincidence setting was successfully rejecting most backgrounds, but also rejecting a large fraction of muon events in the MIP peak (see Fig. A.9). The clear presence of the MIP peak in anticoincidence runs confirmed that muon events were not being lost, but rather were unexpectedly failing the qMorpho coincidence criteria. No improvement in the coincidence acceptance of muon events was observed at longer coincidence window settings.

Distortions in the spectrum were also investigated when running in an end-up configuration that would be required for any vertical deployment. The non-coincident spectra had a much shorter muon feature with significantly stronger tail to high energy, in expectation with longer and less-peaked muon path lengths. The coincidence spectra became almost featureless as the muon feature broadened and weakened.

The adopted run plan was to collect alternating coincidence and non-coincidence data runs. The non-coincidence data had a well understood spectral shape, but had an error contribution from separating the muon signal and background components. The coincidence data had the large systematic uncertainty from the unexpected spectral shape, which it was hoped would be understood in analysis with additional data.

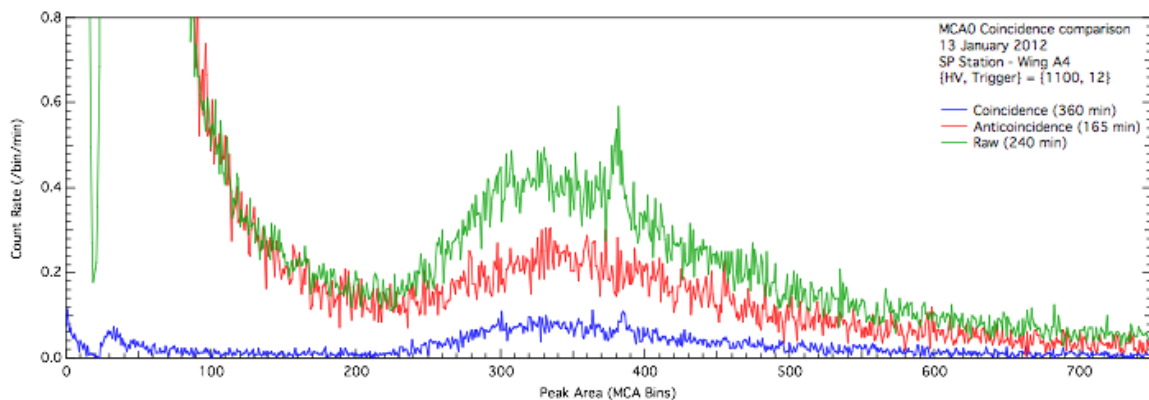


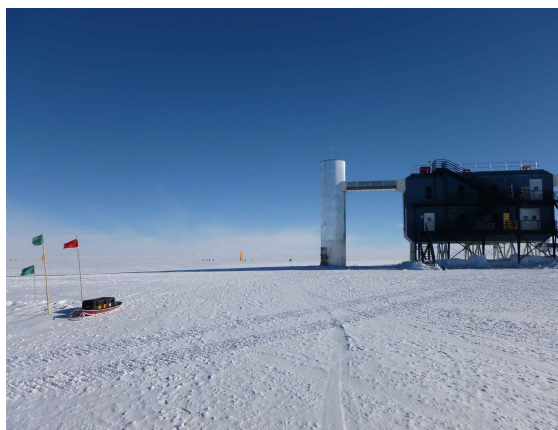
Figure A.9: Spectra taken with different trigger masks for MCA0. The muon peak in coincidence mode is suppressed while still appearing in anticoincidence mode, both in contradiction of expectation. Coincidence mode was successful at suppressing lower-energy backgrounds allowing for a lower trigger threshold.

A.4.2 South Pole Data

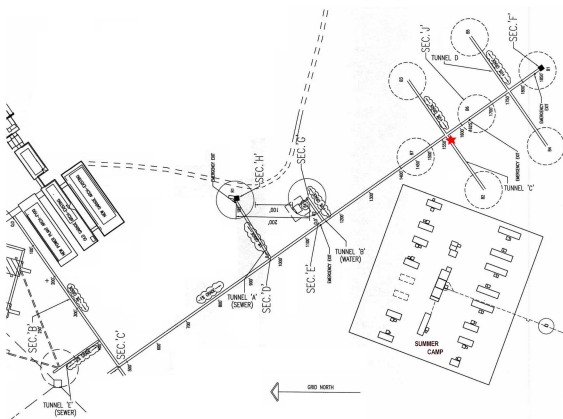
Data runs were taken at various potential overburden locations at the South Pole over the period 20–23 January 2012. The locations successfully measured in these runs include an exposed surface position, under the IceCube Laboratory (ICL), inside the main station, and in the ice tunnels (see Fig. A.10). Two separate datasets were taken in the tunnels to accommodate for the lower muon statistics due to the larger overburden. Additional runs near the station were rejected following failed data quality checks.



(a) Cargo (left) and garage (right) arches; the arches reach peak heights of 8.3 (left) and 9.8 m



(b) IceCube Laboratory and muon detector operating at exposed surface location



(c) Map of South Pole tunnels [216] (simplified); the measurement location is indicated with a red star



(d) Muon detector operating in tunnels at start of tunnel 'C' underneath Amundsen bust

Figure A.10: Potential overburden locations at the South Pole and operation of muon detector. Low density of building material and drifted snow minimize available overburden locations. The only deep firn location near the station with moderate overburden is the water and sewage tunnel system.

No runs were attempted in the RodWells because of constraints imposed by the compact run schedule and uncertainty in the condition of the access holes. An updated survey probably followed by redrilling the shaft to remove encroaching ice will be required prior to utilizing the RodWells as a storage location. Measurements on the polar flights between the South Pole, McMurdo Station, and New Zealand were proposed but would have required additional approval by the polar program officials.

The prospective overburden locations at the South Pole was limited because of the constraints of operation in this remote and harsh environment. The cargo and garage arches (see Fig. A.10a) are unique in their design allowing snow accumulation, but even these structures only gain a small overburden at their peak. The low density of surface snow ($\sim 0.35 \text{ g/cm}^3$ [213]) results in marginal improvement in the overburden. Buildings at the South Pole are constructed out of lightweight materials (*e.g.*, plywood and foam insulation) because of the cost of flying in supplies. Although the major buildings are elevated to mitigate snow accumulation which allows for easy underneath storage (see Fig. A.10b), the two-story structures contribute little overburden.

The most promising location was the tunnel system which carries the under-ice conduits for fresh water and sewage between the station and the station RodWells (see Fig. A.10c). It was known anecdotally that these tunnels reach a depth of ~ 50 ft in the firn at their terminal end near cross-tunnels ‘C’ and ‘D’. The muon detector was positioned at the entrance to the right branch of tunnel C for both tunnel runs (see Fig. A.10d), a distance of 500 m into the tunnel system. While this access route would be untenable for maneuvering a future DM-Ice detector to, station staff confirmed that a new hole could be drilled through the firn to provide direct access to a temporary storage in the tunnel.

Because of the extreme temperatures at all outdoor locations, the detector was prepared and sealed inside the main station with data taking already initiated. The detector was then moved into position and run times were used to reduce the dataset to only good runs. Over the course of a run, the temperatures inside the case would typically drop from the 22°C station temperature to $\sim 0^\circ\text{C}$. Runs in the colder tunnel environment (-50°C) cooled much faster and sapped the laptop battery more rapidly than runs at surface temperature (-30°C). The heat loss to the environment was somewhat offset by the heating of the laptop processor and chemical hand warmers. The hand warmers appeared to stop working over the course of a run and then reactivate once the case was opened indoors possibly due to insufficient airflow when packed in the insulation.

Following each run set, an extended break was necessary to prepare for the next run. The detector was allowed to slowly reequilibrate to room temperature in the station to prevent thermal shock to detector components. The rechargeable batteries for the laptop and DAQ also needed a period of six hours to recharge. Short benchmarking datasets were taken at room temperature to verify that the baseline performance of each channel had not deteriorated.

A.4.3 Post-Pole Data Runs

During the extended layover in Christchurch, New Zealand on the return trip, reference spectra were taken at a near sea level location. A total of 18 hr of data was taken at a minimal overburden location (on the top floor with only a roof overhead). One channel, MCA0, was discovered to be dead on arrival in this data; further analysis upon return to the lab traced the problem to the PMT or base, requiring deconstruction of the full detector to diagnose further.

When the detector returned to Madison, WI, a suite of characterization runs were taken to test the instrumental response. Multiple power sources were tested for both the laptop and qMorpho DAQ to demonstrate that no performance variation was experienced as the batteries drained during the runs at the South Pole. The absolute energy scale for the spectra was established using a ThO_2 source (2.615 MeV ^{208}Tl gamma); runs with a ^{207}Bi source (1.06 MeV gamma) failed to produce a distinguishable feature above the exponential background. Temperature tests of the assembled detector were not possible within the spatial limitations of the available freezers, although the temperature response could be assessed in analysis of the Pole runs. Additional reference spectra were also taken in Madison; both a surface measurement on the roof of the physics building (Chamberlin Hall) and a moderate overburden measurement in the basement of the same were taken.

A.5 Analysis of Spectra

The general features of the recorded spectrum were constant across all runs, with three prominent features – electronic noise, exponential scintillation, and muon events (see Fig. A.11). The muon events are clustered in the minimum ionizing particle (MIP) peak, allowing them to be separated from the two types of background. Only the muon events are of interest to this study, but characterization of the other backgrounds lends confidence in techniques to remove them from the analysis.

Electronic noise makes up the lowest-energy events. The waveforms of these events are characterized by an oscillatory pattern as in the DM-Ice17 EMI noise (see Sect. 7.2.2) with large amplitude and small integral. Their pulse shape makes them difficult to remove with increased trigger threshold setting, but makes them well-separated from true scintillation events.

Low-energy scintillation events make up the next spectral component, possessing a sharp low-energy cutoff and exponential shape to high-energy. These events arise from energy depositions in the scintillator paddles by environmental gammas, but because of the poor energy resolution all spectral peaks are washed out. The highest-energy events in this distribution should be primarily from 2.6 MeV ^{208}Tl gammas. The low-energy cutoff in this distribution is a consequence of the trigger threshold setting; since the gammas have a consistent pulse shape the amplitude cut provides a relatively clean cut on the integral. The size of

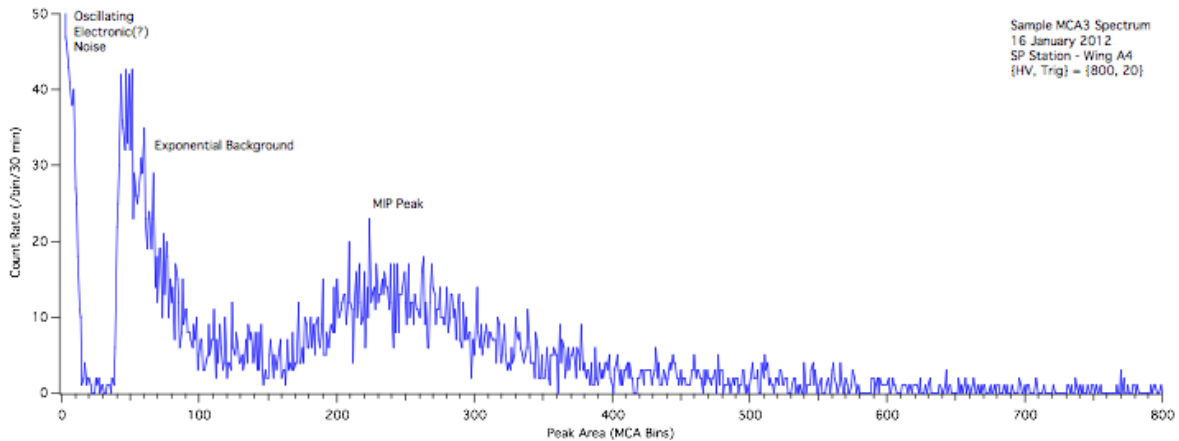


Figure A.11: Example spectrum recorded by MCA3 with major features indicated. The lowest energy events (< 20 MCA) are electronic noise, whose small waveform integral places them below the threshold for scintillation events. The exponential background (40–150 MCA) is composed of scintillation events from environmental gamma radiation. The muon events of interest are responsible for the minimum ionizing particle (MIP) peak (150–400 MCA). The spectrum extends up to bin 2047, but it has been truncated for clarity of demonstrating the spectral features.

this exponential background varies strongly with the detector environment – runs outside at the South Pole having much smaller rates in this feature than runs taken inside buildings in New Zealand or Wisconsin.

The muon signal events appear at the highest energies and are most concentrated in the minimum ionizing particle (MIP) peak. Most muons will have equivalent energy deposition density ($dE/dx \approx 2 \text{ MeV/cm}$), so the variation in their energy spectrum arises from pathlength differences. The most probable trajectory will be approximately downgoing resulting in a 25 mm pathlength, but the distribution will be heavily tailed from muons of higher zenith angle with longer pathlengths. Lower-energy muons can also contribute smaller energy depositions when stopped in the panel, but these signals were modeled to not contribute significant spectral contributions or distinguishable features.

The absolute energy scale of the detectors was established using the ThO_2 source calibration runs taken in Madison. A gamma line was clearly visible on top of the exponential scintillation background (see Fig. A.12) at consistent location across calibration runs taken with varying source positions. The weighted average of the fitted peak location from all source runs was used to establish the energy scale for each channel. Response linearity was assumed in extrapolating from the single calibration point at the 2.615 MeV ^{208}Tl peak. This calibration is consistent with distortions in the exponential shape of the background runs in the Chamberlin lab being caused by the 1.461 MeV ^{40}K and 2.615 MeV ^{208}Tl environmental gammas. It also places the muon peak center at 5–6 MeV, consistent with MIP depositions for a 25 mm pathlength.

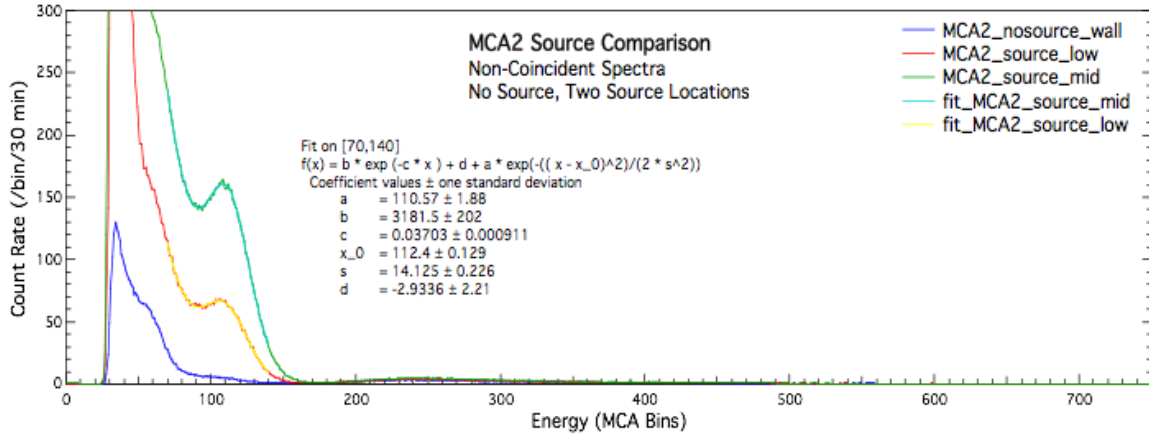


Figure A.12: Spectra from ThO₂ source runs compared with no-source data taken in first floor Chamberlin Hall lab. A strong peak from the 2.615 MeV ²⁰⁸Tl gammas is visible above the exponential background.

Analysis of the event rate in the MIP peak was performed by fitting the data to a Crystal Ball function:

$$f(x; \alpha, n, \bar{x}, \sigma) = N \cdot \begin{cases} \exp\left(-\frac{(x-\bar{x})^2}{2\sigma^2}\right), & \frac{x-\bar{x}}{\sigma} < \alpha \\ \left(\frac{n}{|\alpha|}\right)^n \cdot \exp\left(-\frac{|\alpha|^2}{2}\right) \cdot \left(\frac{n}{|\alpha|} - |\alpha| - \frac{x-\bar{x}}{\sigma}\right)^{-n}, & \frac{x-\bar{x}}{\sigma} \geq \alpha \end{cases} \quad (\text{A.1})$$

This functional form was selected because of its capability to model the high-energy tail of the distribution. To correct for gamma scintillation background leakage from lower-energy energy, an exponential background term was also included in all the fits (see Fig. A.13). All parameters were allowed to float for each fit, accounting for varying dispersion in pathlengths (from the muon zenith distribution) at locations with

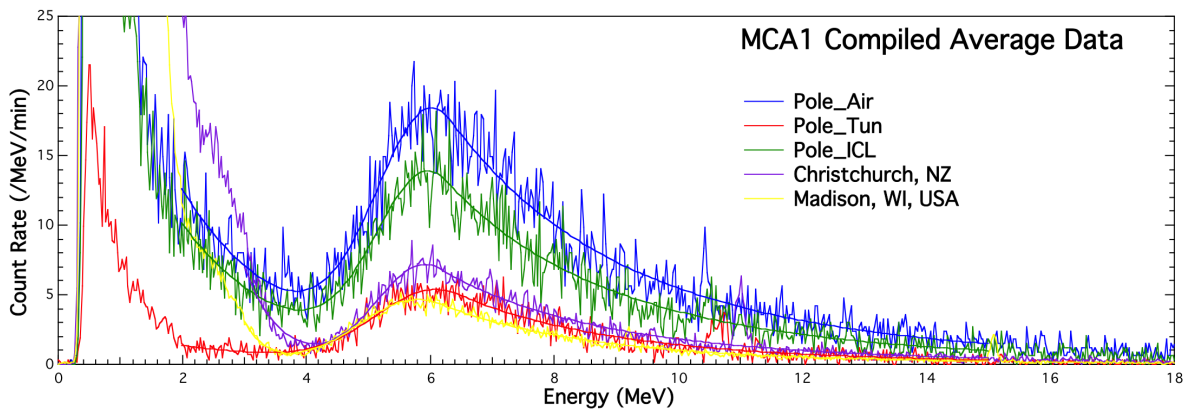


Figure A.13: Comparison of muon detector spectra from South Pole locations with reference spectra. The Crystal Ball plus exponential fit function is overlaid on each dataset. Overburden at the South Pole tunnel location (red) affords a muon flux reduction from the exposed surface level (blue) to below that measured near sea level in Christchurch, NZ (purple).

different overburdens. Pure integration methods and symmetric fit functions produced widely varying peak rate estimates because of their inability to account for such variation.

For all datasets, the internal consistency was established by comparing the fit results for individual 30 min runs. Once the stability of the spectral shape and rate were confirmed, the full dataset was combined and the muon peak fit. Since the best data was obtained from non-coincident runs where there can be no event pairing, the final results are presented for each channel individually (see Tab. A.2). The rates at each location are all normalized to the South Pole exposed surface measurement to provide a relative measurement independent of detector geometry.

The variation of the rates at the various locations observed between the three channels is indicative of a statistical uncertainty at the level of a few percent uncertainty. There is no evidence for a systematic bias to any channel in the scatter of the three measurements.

The coincidence data was also analyzed, with broadly consistent trends observed. The analysis suffered from the statistics for each run were lower resulting in larger scatter between individual MCA channels. One significant trend that emerged in the data was that the South Pole overburden runs (tunnel and ICL) have higher coincident ratios than non-coincident, while the data sets taken outside of Antarctica (in Christchurch and Madison) have significantly lower coincident ratios. Because the response of the coincident DAQ setting was never understood or trusted, the analysis numbers presented in Tab. A.2 are based on the non-coincident data only.

Differences in the spectral shape exist between the different datasets (see Fig. A.13). The environmental radioactive background is higher for runs taken in Christchurch and Madison, which differ from the South Pole runs in that they were taken inside buildings. This higher background with a small ^{208}Tl shoulder forced the fit range for the exponential background to start at higher energy but should not result in significant

Table A.2: Relative muon rates normalized relative to South Pole exposed surface measurement. The station tunnels at the South Pole provided the best shielding environment, reducing the cosmic ray muon rate below the sea level rate. The three columns present the independent measurements made by the three functioning detector channels based on non-coincident runs.

Location	MCA1	MCA2	MCA3
Tunnel	0.298	0.305	0.314
ICL	0.720	0.704	0.762
Christchurch	0.390	0.379	0.384
Ch1115	0.258	0.252	0.262
Madison	0.575	0.456	0.472

error in the muon rate estimate. The valley between the exponential background and muon peak in the South Pole exposed and ICL runs is significantly higher than in the other three datasets. Mismodeling the exponential background in this region would result in an underestimate of the muon rate, which would correspondingly increase the quoted muon flux suppression for the remaining sites. Finally the muon peak centroid for the South Pole tunnel runs appears shifted to higher energy, which may indicate some instability of the detector gain response. Because the muon measurement is a rate measurement with integration over a wide energy range, this is unlikely to impact the quoted results.

Datasets at larger overburden or atmospheric depth (South Pole tunnel, Christchurch, and Madison) had the potential of seeing better agreement between the coincident and non-coincident datasets as the muons became more collimated to smaller zenith angles. This effect was not observed for any of these three datasets, perpetuating the uncertainty in the coincidence performance of this DAQ.

A.6 Conclusions

The data presented here shows a significant reduction in the muon flux observed in measurements taken in the South Pole tunnel system. The reduction observed, to 30% of the exposed surface rate, lowers the cosmic ray flux to below that measured at sea level, corresponding to a factor of 10 reduction in the cosmic ray neutron flux. Identification of this potential storage location for use in conjunction with future DM-Ice detector deployments fulfills the project goals.

The error in these measurements is difficult to quantify within the limits of the unknown systematics introduced because of poorly-understood detector response characteristics. The largest uncertainty arises from the coincidence mode performance of the detectors, whose data prefer a smaller flux reduction (to 43% of the exposed surface muon rate). A possible systematic bias in the quoted non-coincident data which could contribute to this discrepancy is the unresolved valley between the exponential background and muon peak in the exposed surface data which may lead to an underestimate of the surface rate.

Even under pessimistic shielding assessments, the tunnels still afford the best shielding available at the South Pole, with muon flux reductions of a factor of ~ 2 relative to any alternate location. To more accurately assess the cosmogenic effect on a future detector during pre-deployment activities, constant monitoring by an accompanying muon detector could be achieved.

The leftover IceCube RodWells remain a viable storage location despite their omission from the enacted run plan. The cavern roofs are typically a factor of ~ 3 deeper in the firn, which corresponds to a larger increase in the overburden due to the increasing firn density with depth. A unique challenge of the RodWell storage option will be that access to the detectors during storage will be impossible. It also shares in the challenges of tunnel storage both in mitigating temperature shock to the crystals of a future DM-Ice detector during thermalization to -50°C and in requiring logistic support to dig a new hole through the firn.